

AN ABSTRACT OF THE THESIS OF

Masao Fukuda for the degree of Doctor of Philosophy

in Mechanical Engineering presented on December 17, 1981

Title: LAMINAR NATURAL CONVECTION IN VERTICAL TUBES WITH ONE END

CLOSED

Redacted for privacy

Abstract approved:

James R. Welty

The problem of laminar natural convection in a vertical cylindrical enclosure with one end open to a reservoir is solved analytically to obtain a similarity-flow solution and then numerically to obtain non-similarity flow solutions for the Rayleigh-number ranges of $0 < Ra_A < 1300$ and $0 < Ra_L^a < 1000$. The closed-form solution applied here is that originally developed by Lighthill and later modified by Ostrach and Thornton. The numerical solution employs the finite-difference technique with successive-over-relaxation and up-wind methods to achieve acceleration of convergence.

For values of Ra_A between 380 and 1200, similarity flows from numerical calculations well agree with those of the closed-form solution. The numerical solution, in addition, is able to give information about non-similarity flows; four flow regimes were identified with $0 < Ra_A < 1300$ and $0 < Ra_L^a < 1000$. For one of the five flow regimes where a cell formation (or a secondary flow) was present, a

parametric equation correlating the size of cells and the above two Rayleigh numbers has been developed. The numerical solution is also sufficiently general such that it is able to predict those convection flows once investigated by Lighthill, and Ostrach and Thornton as special cases. The comparison made between their solutions and the present numerical solutions indicates good agreement.

©Copyright by Masao Fukuda

December 17, 1981

All Rights Reserved

Laminar Natural Convection in Vertical
Tubes with One End Closed

by

Masao Fukuda

A THESIS

submitted to

Oregon State University

in partial fulfillment of
the requirements for the
degree of

Doctor of Philosophy

Completed December 1981

Commencement June 1982

APPROVED:

Redacted for privacy

~~Professor of Mechanical Engineering~~ in charge of major

Redacted for privacy

~~Head of Department of Mechanical Engineering~~

Redacted for privacy

~~Dean of Graduate School~~

1

Date thesis is presented December 17, 1981

Typed by Barbara Hanson for Masao Fukuda

ACKNOWLEDGMENTS

I would like to thank my major professor and department head, Dr. James R. Welty for his constructive suggestions to my thesis work and financial support during the course of my graduate studies. In addition, the help of my graduate committee members, Dr. Dean E. Booster, Dr. Gunnar Bodvarsson, Dr. Lorin R. Davis, and Dr. Milton B. Larson is most appreciated. I wish also to thank Dr. Gordon M. Reistad for providing technical and extra financial support, Dr. Robert W. Thresher for his moral support, and the Oregon State University Computer Center for providing computer time.

Also, my thanks are extended to Mrs. Barbara Hanson for typing the thesis manuscript, and Mrs. Linda Haygarth for illustration of several figures.

Finally, I would like to extend my special thanks to my wife, Nanae who provided endless support to my graduate study, and my children, Naomi and Masahiro who provided my only precious entertainment.

TABLE OF CONTENTS

I. INTRODUCTION	1
1.1 Problem	2
1.2 Past Work	2
1.2.1 Well Related Studies	4
1.2.2 Turbine Blade Problem	6
1.2.3 Other Related Studies	10
II. ANALYTICAL STUDY	12
2.1 Governing Equations	12
2.2 Analytical Development	14
2.2.1 Modification of Governing Equations	14
2.2.2 Solution Method	17
2.2.3 Average Heat Transfer	32
2.3 Result of Analytical Study	33
III. NUMERICAL STUDY	38
3.1 Modification of Governing Equations	38
3.2 Finite Difference Formulation	41
3.2.1 Energy Equation	42
3.2.2 Vorticity Equation	45
3.2.3 Vorticity and Stream Function Relation	54
3.2.4 Stream Function Equations	55
3.2.5 Average Heat Transfer Coefficient	57
3.3 Programming Consideration	62
3.3.1 Gauss-Seidel Iteration Method	63
3.3.2 Mesh Configuration and Calculation Sequence	65
3.3.3 Nusselt Number Calculation	69
3.3.4 Validation of Numerical Method	70
3.3.5 Effect of Reservoir Boundary Condition and Size	71
3.3.6 Convergence of the Numerical Solution	82
3.4 Result of Numerical Study	90
3.4.1 Flow Characterization	95
3.4.2 Flow Regimes	118
3.4.3 Nusselt Number and Heat Transfer Coefficients	143
3.4.4 Cases of Lighthill and Ostrach	147
IV. CONCLUSIONS AND RECOMMENDATIONS	158
V. BIBLIOGRAPHY	160
VI. APPENDICES	164
A - Modified Numerical Equations	165
B - Computer Codes	172

LIST OF FIGURES

<u>Figure</u>	<u>Page</u>
1.1 Schematic of vertical cylinder above a hot reservoir as considered in this analysis	3
2.1 The predicted velocity and temperature profiles	20
2.2 Relationship between Ra_L^a and α	25
2.3 Relationship between Ra_L^a and Ra_A	26
2.4 Two kinds of flow direction predicted by Ra_L^a and Ra_A relations	27
2.5 Cross plot of Figs. 2.2 and 2.3 in the range $0 < Ra_L^a < 1000$	28
2.6 Temperature profiles	29
2.7 Velocity profiles	31
2.8 Average heat transfer coefficient within the applicable range	35
3.1 The axial velocity gradient illustration; the $\partial U / \partial R$ approaches zero as X approaches $X=L$	51
3.2 Nodal structure used for derivation of Eq. 3.29	53
3.3 Nodal structure used for derivation of Eqs. 3.30 and 3.31	53
3.4 Internal node arrangements for the velocity difference-equations	56
3.5 Node adjacent to boundaries for velocity calculation	58
3.6 Nodal structure used for Eqs. 3.40, 3.41, and 3.41a	61
3.7 Mesh configuration	66
3.8 Flow chart of the program NATCON	68
3.9 The configuration of the problem used by Ref. [26] where $a=b$, $c/a=0.1$, and $T_1 > T_0$	72
3.10 Isotherms of (a) Ref. [26] and (b) the current study	73
3.11 Streamlines of (a) Ref. [26] and (b) the current study	74

<u>Figure</u>	<u>Page</u>
3.12 Comparison of the three temperature boundary conditions	76
3.13 Comparison of the three temperature boundary conditions of the reservoir	77
3.14 Effect of L/L_{RES} at $Ra_A=0$	79
3.15 Effect of L/L_{RES} at $Ra_A \neq 0$	81
3.16 Required number of iterations for various S.O.R. factors and mesh sizes for the same nodal structure	87
3.17 Required number of iterations for various mesh sizes and number of nodes for approximately the same G_r	89
3.18 Comparison of the variation of temperature at a certain node when S.O.R. factor is larger, or smaller than the optimum FAC, or when it is equal to the optimum FAC	91
3.19 Typical variations of T , Ξ , and Ψ when the numerical solution fails to converge due to excessively large mesh distances are used	92
3.20 Typical variations of T , Ξ , and Ψ when the numerical solution converges	93
3.21 The boundary temperature configuration applied to the numerical study where T_0 is the coldest and T_{RES} is the hottest temperature of the system	94
3.22 Ra_A vs. Ra_L^a for $AR =$; (a) 1.0, (b) 2.0, (c) 4.0, (d) 6.0, (e) 12.0, (f) 15.0, (g) 35, and (h) 40.0	99
3.23 Streamlines and axial velocity profiles of Run No. 09	108
3.24 Development of axial velocity profiles at the orifice section for $AR= .25, .5$, and 1.0 at $Ra_A \approx 900$	109
3.25 Variation of the flow parameter α along the cylinder length for $AR=2$ and 15 , and $Ra_L^a=350, 500$, and 600	111
3.26 Isotherms and streamlines of $AR=15$ at $Ra_A=230$	112
3.27 Isotherms and streamlines of $AR=15$ at $Ra_A=850$	113
3.28 Isotherms and streamlines of $AR=15$ at $Ra_A=1580$	114

<u>Figure</u>	<u>Page</u>
3.29 Axial velocity profiles along the centerline of the cylinder	116
3.30 Isotherms and streamlines at AR=50 and $Ra_A = 1000$	117
3.31 Axial velocity profiles along the centerline of the cylinder at AR=40 for various Ra_A	119
3.32 Flow regime map	120
3.33 Illustration of the corrected modified-Rayleigh number when a cell is formed	124
3.34 Correlation of Ra_A , Ra_L^a , and Lc/L in Regime IV	125
3.35 Lc/L vs. Ra_L^a for various Ra_A (extrapolated from Fig. 3.34)	126
3.36 Lc/L vs. Ra_A for various Ra_L^a (extrapolated from Fig. 3.34)	127
3.37 Corrected Ra_L^a for the flows in Regime IV	129
3.38 Cell formation in AR=4 at $Ra_A = 2970$ and $Ra_L^a = 2010$	133
3.39 Development of a cell in AR=4 at $Ra_A = 2970$ where I represents the number of iterations	134
3.40 Region of periodic instability for AR=.83 to 15	136
3.41 Theoretical and numerical flow parameter variations over the applicable Ra_L^a range	140
3.42 Theoretical and numerical velocity profiles within the similarity flow regime	141
3.43 Theoretical and numerical temperature profiles within the similarity flow regime	142
3.44 Net Nu_a vs. Ra_A for AR=2, 15, and 40	144
3.45 Variation of local heat transfer coefficients along the cylinder length at $Ra_A \approx 1000$ for AR=2, 15, 70	146
3.46 Configuration of the model investigated by Lighthill when $A=0$; and later by Ostrach and Thornton when $A \neq 0$	148
3.47 Comparison of similarity flows resulted from the theoretical and from the numerical analysis at AR=15	150

<u>Figure</u>	<u>Page</u>
3.48 Streamlines of non-similarity flows in the Ostrach's configuration at AR=15	151
3.49 The case of Lighthill where $R_A = 0$ at AR=15 for various Ra_L^{α}	152
3.50 Comparison of the theoretical and numerical flow parameters for the cases of Lighthill and Ostrach; $-306 < Ra_L^{\alpha} < 260$, and $255 < Ra_A^{\alpha} < 355$	156

LIST OF TABLES

<u>Table</u>		<u>Page</u>
2.1 Average heat transfer coefficient (Eq. 2.45)		34
3.1 Numerical result of mesh sizing factor C_U and C_V for $\Delta x = .333$ and $\Delta r = .25$		84
3.2 Summary of computer runs		96
3.3 Computer runs made for the evaluation of cell formation in Regime IV		123
3.4 The largest Ra_A without a periodic instability		137
3.5 Temperature and velocity profiles from the numerical and theoretical studies within the similarity flow regime at $AR=15$		139
3.6 Nusselt numbers for various AR's		145
3.7 Computer runs made for the cases of Lighthill and Ostrach		149

NOMENCLATURE

<u>Symbols</u>	<u>Description</u>
a	Radius of cylinder
a_{RES}	Reservoir radius
A	Temperature gradient on the cylinder wall
AR	Aspect ratio of cylinder, (L/a)
$(AR)_M$	Aspect ratio of the main flow at presence of a cell
C_p	Specific heat at constant pressure
C_U, C_V	Mesh sizing factors based on axial and radial velocities, respectively
C'_U, C'_V	Modified C_U and C_V
ζ	Axial centerline of cylinder or a line of symmetry
$f_{i,j}$	Arbitrary variables in the numerical development
FAC	S.O.R. factor ($=\bar{\alpha}$)
\vec{g}	Gravitational-acceleration vector
Gr	Grashof number based on $(T_1 - T_0)$
Gr,RES	Reservoir Grashof number
Gr,ORF	Orifice Grashof number
h	Enthalpy of the fluid
h	Heat transfer coefficient
k	Thermal conductivity
L	Axial length of cylinder
L_{RES}	Axial length of reservoir
L_C	Axial length of cell
Nu_a	Average Nusselt number
p	Dimensionless P
P	Pressure

<u>Symbols</u>	<u>Description</u>
Pr	Prandtl number
r	Dimensionless R
R	Radial coordinate
Ra	Rayleigh number based on the radius and the temperature difference ($T_1 - T_0$)
Ra_A	Modified Rayleigh number based on the radius and the temperature gradient A
Ra_L^a	Modified Rayleigh
$(Ra_L^a)_C$	Corrected Ra_L^a of the main convective flow at presence of a cell
S.O.R.	Successive-Over-Relaxation
t	Dimensionless time variable
t	Dimensionless temperature
T	Temperature
Ta	Cylinder wall temperature in analytical development
T_{BOT}	Bottom wall temperature of cylinder
T_0	Closed-end temperature of cylinder
T_1	Centerline temperature at open-end of cylinder
u	Dimensionless axial velocity
U	Axial velocity
v	Specific volume
v	Dimensionless radial velocity
V	Radial velocity
\vec{V}	Velocity vector
x	Dimensionless axial coordinates
X	Axial coordinate

<u>Greek Symbols</u>	<u>Description</u>
α	Flow parameter in the analytical development
$\bar{\alpha}$	Successive-Over-Relaxation factor in the numerical development
$\bar{\alpha}_{\text{opt}}$	Optimum successive-over-relaxation factor
β	Volumetric expansion coefficient
β_0	β at reference temperature T_0
κ	Thermal diffusivity
μ	Dynamic viscosity
ν	Kinematic viscosity
ξ	Dimensionless vorticity
Ξ	Vorticity
ρ	Density
ρ_0	Density at reference temperature T_0
Φ	Dissipation function
ψ	Dimensionless stream function
Ψ	Stream function

<u>Others</u>	
$(\)_{\text{ave}}$	Average quantity
$(\)_{i,j}$	Quantity at node (i,j)
$(\)_w$	Quantity at the cylinder wall
$(\)_{r=0}$	Centerline quantity
$\Delta(\)$	Finite difference quantity

LAMINAR NATURAL CONVECTION IN VERTICAL
TUBES WITH ONE END CLOSED

I. INTRODUCTION

Natural convection in a vertical cylindrical enclosure with one end open to a reservoir has been of interest to geologists who, for example, deal with ground water within a deep well like that of a geothermal well; by turbine engineers who employ natural convection of this nature for cooling turbine blades; and by engineers and scientists in general who are concerned with natural convection generated in such geometric configurations. Although some interest has existed for several decades, progress in this area of natural convection has been rather slow, due in part to the magnitude of the problem where, for example, one kind of Rayleigh number (a dimensionless temperature parameter) may range from zero to the order of a million, the aspect ratio (a length-to-radius ratio) of the fluid column can vary between 1 and well over 100, and the fluid column can be exposed to several kinds of temperature boundary condition. For these reasons, a general solution is rather difficult to obtain, and the currently existing solutions are often applicable only to specific regions of the problem.

Therefore, the author has attempted here to investigate and understand the fundamental natures of the problem, hoping that the results presented in this thesis will fill the previously undefined and unexamined regions of the problem.

1.1 Problem

The problem investigated in this thesis is the fluid motion resulting from natural convection in a vertical cylindrical enclosure with one end open to a reservoir as shown in Fig. 1.1. The boundary conditions are: (a) the cylinder wall maintains a linearly changing temperature with its length, (b) the fluid is confined within a solid cylinder with one end open to a reservoir without any restriction, and (c) the reservoir is maintained at either the hottest or the coldest temperature of the system depending on the specific situation. Of major interest is the case of the cylinder above a reservoir with the cylinder-wall temperature increasing linearly in the direction of the body force applied to the system. Another case of interest is that where the cylinder is open to a reservoir located above with the body force directed toward the closed-end. In all cases, this study is confined to steady-state laminar flows.

1.2 Past Work

Although the exact problem being considered here has not been treated previously, similar types of problems have been investigated analytically and/or experimentally by a handful of people in the past 40 to 50 years. These previous investigations can be divided into the following three types: a) those related to geothermal and geological wells in which the basic geometry is a long bore hole with or without specified temperature along the well, b) those related to the cooling of a turbine blade where the basic geometry

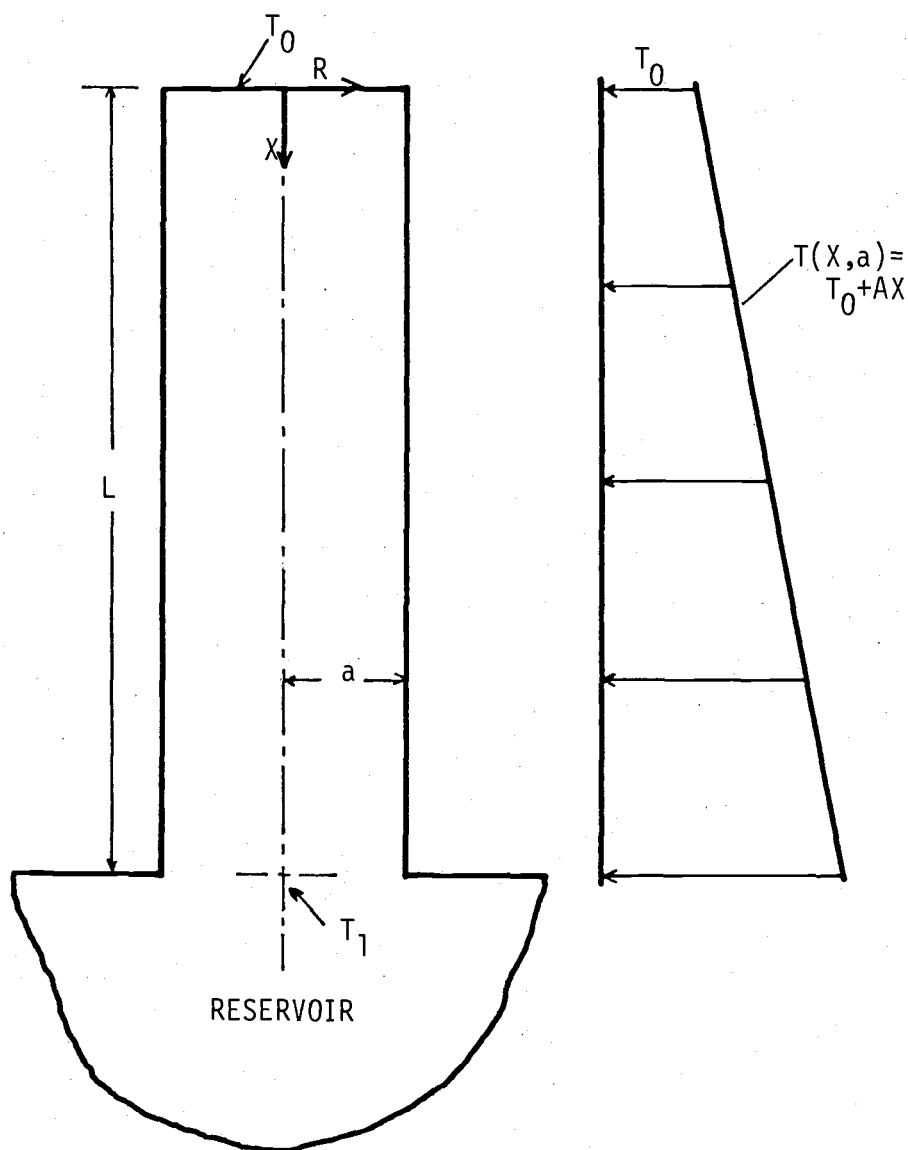


Figure 1.1 Schematic of vertical cylinder above a hot reservoir as considered in this analysis.

consists of a long drilled hole along the axis of a blade with a fluid reservoir at its base, and c) those which do not belong to either of the above two cases but are still related to the problem considered here.

In the following subsections, summaries of these studies are listed in the order described above, and at the same time particular emphasis is given to the information applicable to this proposed study.

1.2.1 Well Related Studies

One of the earliest studies of natural convection in general was that of Benard [1] who studied experimentally the convection phenomena in a thin sheet of fluid heated from below and observed the formation of hexagonal cells. Following his study Lord Rayleigh [2], Jeffreys [3], Hales [4], and Pellew and Southwell [5] treated problems of the same nature. Among these studies, the common interest was to determine the on-set of convective flow (then it was called the problem of instability) in different geometric configurations, however, that of Jeffreys' and Hales' is most closely related to the geometry of the current problem. Jeffreys and Hales each derived the expression which established the condition for the onset of convective flow of water in deep boreholes. Jeffreys expressed the instability of the water by relating the temperature gradient to adiabatic compression, and Hales related the temperature gradient to viscosity. These two expressions were later combined by Krige [6] whose new formula gave an expression for critical temperature gradient (the rate of temperature change with depth),

which is related to the viscosity and compressibility of fluid in the borehole for a given size (or diameter) of well at a given depth. Temperature gradients greater than the critical temperature gradient indicated an unstable condition (the onset of flow) of the fluid in the well. Diment [7] performed an extensive test of temperature measurement of water in a large (length-to-diameter ratio) well at the U.S. Bureau of Mines' West Virginia Laboratory. In addition to measuring temperature as a function of depth, he also recorded the temperature oscillation over a time period of 50 minutes at several different depths of the well. The maximum temperature variation of fluid at a given depth was correlated with the temperature gradient. From this correlation, he suggested that the water movement was in the form of cells or eddies juxtaposed vertically in the well and the height of the cells was no more than several times the well diameter. The completely independent investigations of Gretener [8] yielded similar results in his observation of a large diameter well. Diment also indicated that when thermal instability exists in a large diameter well, temperature oscillations of several hundredths of a degree would be expected at a given depth.

Sammel [9] used two wells of different length-to-diameter ratio, L/D, (63 and 270) to prove the existence of convective flow in a deep well. From temperature oscillation measurements in his field and laboratory tests, Sammel estimated the approximate velocity of the convective flow, which ranged as high as 3 cm/sec, and the size of the cell which ranged from 8cm to 48cm for the well of L/D=270, and a diameter of 4.5cm. From these experiments he concluded that the theoretical critical values of temperature gradient obtained by

use of Krige's formula were close to, but probably higher than the measured values. For these experiments the estimated Rayleigh number based on the fluid temperature gradient ranged from 1.4×10^4 to 4.5×10^6 .

Donaldson [10] performed analytical and experimental studies of a geothermal-well model. His experimental model was a 2.45 cm diameter tube, about 90 cm long with closed-top and -bottom, and with a linearly increasing temperature with depth imposed along the tube wall. The same model was analytically solved to obtain a correlation among the ratio of temperature gradients (along the tube axis and the wall), modified Rayleigh number based on the wall temperature gradient, and the tube radius. He obtained a good agreement between his experimental and theoretical results only when the modified Rayleigh number was less than 300 and greater than 3000. Between the above two values of the modified Rayleigh number, a negative temperature gradient was observed along the axis in his experiment. The given reason for this was that the convective flow generated in the cylinder was probably not symmetric. When the modified Rayleigh number was as large as 10^6 , it was experimentally observed that the temperature of the fluid corresponded closely with that of the wall at the same depth.

1.2.2 Turbine Blade Problem

This type of problem was first treated by Lighthill [11] in a purely theoretical manner. His model was a circular cylinder with a constant wall temperature, closed at the bottom and open at the top to a reservoir. The body force was always directed toward the

closed end, and the hottest and the coldest temperatures of his system were always at the centerline of the top opening and at the cylinder wall, respectively. For this problem he defined the following characteristic non-dimensional parameters; the length-to-radius ratio, L/a (or often called the aspect ratio) of the tube, the two modified Rayleigh numbers, R_a and R_1 (based on the radius a and the length of the tube, respectively), and the Prandtl-number. He established three flow regimes in such a model for laminar flow. They are defined as: i) at small L/a , flow along the tube wall is a type that can be approximated by free convection along a flat vertical wall; ii) for large L/a , the boundary layer mixes with the central flow which fills up the entire tube and the velocity distributions at each section of the tube are similar differing only by some constant (He called this the similarity flow regime, and the solution for this particular flow regime was called the similarity solution.), and iii) if L/a exceeds the critical value of the above regime, the flow does not occur along the entire length of the tube leaving some fluid, within a certain distance from the closed-end, stationary. Regarding these flow regimes, he predicted that the similarity flow regime was bounded by two critical aspect ratios (one borders the first regime and the other borders the third regime), and these two were separated by a factor of order 10. Lighthill solved the field equations for each of the above three regimes by integrating them over each cross-sectional area first, then forming three integral conservation equations. He found expressions for temperature and velocity profiles in each regime and the Nusselt number was related to the

modified Rayleigh number. He concluded that in such configuration the flow is always up along the wall and down along the tube axis, with turbulent flow predicted to occur at a modified Rayleigh number near 10^4 .

In the following year Martin and Cohen [12] performed heat transfer experiments using the same model that Lighthill studied, and found that most of their results agreed with Lighthill's in regard to heat transfer rates. When Martin [13] continued his experiment with a special emphasis on turbulent flow, he found that Prandtl number became significant as to how the turbulent flow was generated while it was insignificant in laminar flow. For Prandtl numbers near unity, he found that transition occurred during laminar impeded-flow regime, and for large Prandtl numbers, transition took place during laminar boundary-layer flow, yielding conventional boundary-layer regime. In his experiment the transition was detected by noting the fluctuation of the orifice temperature, and the transitional modified Rayleigh number was found to be in between $10^{4.4}$ and $10^{4.6}$.

A condition similar to Lighthill's configuration but with a linearly decreasing temperature with depth (or decreasing in the direction of the applied body force) along the wall, was analytically investigated by Ostrach and Thornton [14] for the similarity flow which was previously defined by Lighthill. His solution technique was similar to that of Lighthill's, however, because of the imposed temperature gradient along the cylinder wall, he introduced a new Rayleigh number, Ra_A , based on the wall temperature gradient. Similarity flow could not be specified by one Rayleigh number for

this case while Lighthill stated that similarity flow would occur only when $Ra_L^a = 311$ since Ra_A was always zero. Ostrach and Thornton concluded that similarity flow exists within certain ranges of Ra_L^a and Ra_A values, and defined them to be approximately $0 < Ra_A < 1600$ and $0 < Ra_L^a < 311$, however no explanation was given for these choices of Rayleigh number ranges. Their result also indicated that the flow along the wall was always in the direction of increasing temperature of the wall within defined Rayleigh number ranges.

Hasegawa [15] published the results of his extensive work on heat transfer in an open thermosyphon. In his three part report the last two parts are of interest to the current problem. In these, he discussed the analytical and experimental results of the open thermosyphon in a circular tube. His experimental configuration was very closely related to that of Martin. His results in the similarity flow region agree very closely with Lighthill's analytical work. In particular, the occurrence of a stagnant region as a function of the Rayleigh number based on the top and bottom temperature difference was closely duplicated by Hasegawa. He used a two-dimensional model which enabled him to use a Schlieren system to obtain visual flow profiles. He further noted that where the Rayleigh number was less than a certain value, a portion of the fluid column could be expected to become fairly stagnant. He also observed that the occurrence of turbulence takes place where the shear is maximum, and that turbulence in the down-flowing fluid along the center axis usually precedes that in the up-flow along the wall and eventual turbulence in the entire fluid.

1.2.3 Other Related Studies

Elder [16,17,18] in three reports presented an extensive study of free convection in a vertical slot where the two vertical walls were at different temperatures and its top and bottom were adiabatically closed with solid boundaries. His main concern was to characterize the convective flow in such a geometric configuration by analytical, numerical, and experimental means. In these he reported the existence of secondary and tertiary flows when the Rayleigh number based on slot width and the difference between the two wall temperatures exceeded 10^5 . His numerical solution also indicated the existence of secondary flow at a Rayleigh number as low as 1500. In addition to this, he also experienced a partial numerical instability with a Rayleigh number larger than 1500 in his finite difference and iterative numerical solution. However, he was not able to identify whether the instability was actually of a physical nature or the propagation of a local numerical disturbance.

The same phenomenon observed by Elder was later demonstrated by de Vahl Davis and Thomas [19]. Then, de Vahl Davis and Mallinson [20] concluded that the instability of numerical solutions encountered by Elder, and de Vahl Davis and Thomas was of a physical nature rather than the instability of the numerical method they applied. In Ref. [20], it was mentioned further that the instability was experienced whenever the secondary motion was generated at the center portion of the slot where the shear was thought to be greatest. The stability problem of natural convection in a vertical slot was also studied by Batchelor [21], Vest and

Arpacı [22], and Ostrach and Raghavan [23].

Regarding numerical solutions, Barakat and Clark [24] applied the finite difference method to a natural convection problem in a cylindrical enclosure. A similar application of finite difference methods was also made by Kee, Landram, and Miles [25]. Torrance [26] made a comparison study of five different finite-difference-methods which were applied to a common problem of natural convection in a cylindrical enclosure. Other numerical work related to the current problem to a lesser degree are the following: Powe and Comfort [27] applied a finite difference scheme to natural convection in a spherical enclosure with a cylindrical cavity inside; Newell and Schmidt [28] applied the Crank-Nicholson method to laminar natural convection in a two-dimensional rectangular enclosure; Ozoe, Yamamoto, Churchill, and Sayama [29] developed a general numerical solution using finite difference methods with an alternating direction scheme which was applied to laminar natural convection in a cubic enclosure, the space between two horizontal infinite plates, and a long square channel; Hwang and Cheng [30] used the boundary vorticity method to solve the combined free and forced laminar convection in horizontal tubes; Pepper and Harris [31] applied a strongly implicit procedure to three dimensional natural convection in a rectangular enclosure; and Mallinson and de Vahl Davis [32] used the false transient method for natural convection in a box.

II. ANALYTICAL STUDY

The mathematical development of the problem described in the previous chapter will be considered in this chapter.

The governing equations will be developed, then solved analytically to obtain a closed-form solution. In Chapter III a numerical solution will be presented which allows additional insight beyond that possible in closed form.

2.1 Governing Equations

The governing equations consist of the usual conservation relationships namely: conservation of mass, momentum, and energy. These three equations in vector form are as follows [33,34]:

$$\frac{D\rho}{Dt} + \rho \nabla \cdot \vec{V} = 0 \quad (2.1)$$

$$\rho \frac{DV}{Dt} = \rho \vec{g} - \nabla P + \mu V^2 V \quad (2.2)$$

$$\rho \frac{Dh}{Dt} = \frac{DP}{Dt} + \nabla \cdot (k \nabla T) + \phi \quad (2.3)$$

where $D() / Dt$ indicates the substantial or particle derivatives and can be written out as follows:

$$\frac{D()}{Dt} = \frac{\partial()}{\partial t} + (\vec{V} \cdot \nabla)() \quad (2.4)$$

The first term, $\partial() / \partial t$, in the right hand side of Eq. (2.4) represents a local rate of change of the property in interest and the second term, $(\vec{V} \cdot \nabla)()$, indicates a rate of change due to the

motion of the property, and which is commonly called the convection term. The three conservation equations are written in relatively general form, the conservation-of-momentum equation is for constant viscosity medium and is one form of the Navier-Stokes equation.

In order to reduce these three conservation equations to forms suitable to this problem, the following assumptions are made:

- 1) axisymmetric flow (only two geometric variables; r for radial and x for vertical directions),
- 2) incompressible, steady state flow, and
- 3) constant property liquid medium.

With these assumptions, and the coordinates specified as shown in Fig. 1.1, Eqs. (2.1) through (2.3) reduce to the following forms, respectively:

$$\frac{\partial U}{\partial X} + \frac{\partial V}{\partial R} + \frac{V}{R} = 0 \quad (2.5)$$

$$U \frac{\partial U}{\partial X} + V \frac{\partial U}{\partial R} = -g - \frac{1}{\rho} \frac{\partial P}{\partial X} + \nu \left[\frac{\partial^2 U}{\partial R^2} + \frac{1}{R} \frac{\partial U}{\partial R} + \frac{\partial^2 U}{\partial X^2} \right] \quad (2.6)$$

$$U \frac{\partial V}{\partial X} + V \frac{\partial V}{\partial R} = - \frac{1}{\rho} \frac{\partial P}{\partial R} + \nu \left[\frac{\partial^2 V}{\partial R^2} - \frac{V}{R^2} + \frac{1}{R} \frac{\partial V}{\partial R} + \frac{\partial^2 V}{\partial X^2} \right] \quad (2.7)$$

$$U \frac{\partial T}{\partial X} + V \frac{\partial T}{\partial R} = \kappa \left[\frac{\partial^2 T}{\partial R^2} + \frac{1}{R} \frac{\partial T}{\partial R} + \frac{\partial^2 T}{\partial X^2} \right] \quad (2.8)$$

where $\kappa = k/\rho C_p$, and the direction of the body force is downward.

Eqs. (2.6) and (2.7) are component forms of the conservation of momentum; the former in the axial (x) direction, the latter in the radial (r) direction. The reasons for the disappearance of the pressure term, DP/DT , and the dissipation function, Φ , in the

transition from Eqs. (2.4) to (2.8) are as indicated in the footnote below.

2.2 Analytical Development

In this section, the four governing equations, Eqs. (2.5) through (2.8), established in the previous section are reduced to three governing equations. These are then solved for "similarity" flow.

2.2.1 Modification of Governing Equations

Because of the similarity in geometry of the model (see Fig. 1.1) considered here with that of Ostrach and Thornton [14], the following modification of the three governing equations follows their procedure.

First, the use of the laminar boundary layer approximation is employed. That is; a) U , T , and X are in the order of unity, and b) V and R are in the order of $(\text{Reynolds number})^{-1/2}$. After applying this approximation, several terms can be eliminated from Eqs. (2.5) through (2.8), and the resulting equations for mass, momentum, and energy conservation are as follows:

$$\frac{\partial U}{\partial X} + \frac{\partial V}{\partial R} + \frac{V}{R} = 0 \quad (2.9)$$

$$U \frac{\partial U}{\partial X} + V \frac{\partial U}{\partial R} = -g - \frac{1}{\rho} \frac{\partial P}{\partial X} + \nu \left[\frac{\partial^2 U}{\partial R^2} + \frac{1}{R} \frac{\partial U}{\partial R} \right] \quad (2.10)$$

From the defining thermodynamic relation, enthalpy is written as, $h=u+pv$, where u is the internal energy and v is the specific volume. When we write $dh=CpdT$ and $du=CvdT$ and substitute, we have $CpdT=CvdT+pdv+vdp$. For solid or incompressible media with $Cp \approx Cv$ and $dv=0$, the enthalpy equation reduces to $vdp=0$. Since $v \neq 0$, we have $dp=0$.

Commonly, a "slow" fluid movement indicates the dissipation function to be negligible, however, this becomes clear if one nondimensionalizes the energy equation, Eq. (2.3), to find the coefficient of the dissipation term, ϕ . This coefficient is usually a ratio of Eckert to Reynolds numbers and is small for liquids.

$$\frac{\partial P}{\partial R} = 0 \quad (2.11)$$

$$U \frac{\partial T}{\partial X} + V \frac{\partial T}{\partial R} = \kappa \left[\frac{\partial^2 T}{\partial R^2} + \frac{1}{R} \frac{\partial T}{\partial R} \right] \quad (2.12)$$

The applicable boundary conditions are: $U(0,R)=0$, $V(0,R)=0$, $T(0,R)=T_0$, $U(X,a)=0$, $V(X,a)=0$, $T(X,a)=T_0+AX$, and $T(L,0)=T_1$ where A represents the temperature gradient along the cylinder wall. To eliminate the pressure term from Eq. (2.10), we first apply the velocity boundary conditions, namely, at $R = a$ (at wall), $U = 0$ and $V = 0$ to produce the following equation

$$\left[0 = -g - \frac{1}{\rho} \frac{\partial P}{\partial X} + v \left(\frac{\partial^2 U}{\partial R^2} + \frac{1}{R} \frac{\partial U}{\partial R} \right) \right]_{R=a} \quad (2.13)$$

Then, subtraction of Eq. (2.13) from (2.10) results in,

$$U \frac{\partial U}{\partial X} + V \frac{\partial U}{\partial R} = - \frac{1}{\rho} \frac{\partial P}{\partial X} + \frac{1}{\rho} \frac{\partial P}{\partial X} \Big|_{R=a} + v \left[\frac{\partial^2 U}{\partial R^2} + \frac{1}{R} \frac{\partial U}{\partial R} \right]_{R=a}^{R=R} \quad (2.14)$$

To account for the change of density due only to the temperature, the following steps are taken to obtain the specific volume ($1/\rho$) and temperature relation: first, the specific volume, v , is expanded about v_0 of at some reference temperature by Taylor series as follows,

$$v = \frac{1}{\rho} \approx v(T_0) + \frac{(T-T_0)}{1} \frac{\partial v(T_0)}{\partial T} + \frac{(T-T_0)^2}{2} \frac{\partial^2 v(T_0)}{\partial T^2} + \dots$$

then, the definition of the thermal expansion coefficient,

$$\beta(T_0) \equiv \frac{\partial v(T_0)/\partial T}{v(T_0)}$$

is applied, and finally using only the first two terms, the following relationship is obtained,

$$\frac{1}{\rho} \approx \frac{1}{\rho_0} + (T - T_0) \frac{\beta}{\rho_0} \quad (2.15)$$

where the subscript, 0, indicates the quantity at the wall. With the substitution of Eq. (2.15) together with the hydrostatic pressure change, $\partial P / \partial X \approx \rho_0 g$, Eq. (2.14) becomes,

$$U \frac{\partial U}{\partial X} + V \frac{\partial U}{\partial R} = -(T - T_a) \beta g + v \left[\frac{\partial^2 U}{\partial R^2} + \frac{1}{R} \frac{\partial U}{\partial R} \right]_{R=a}^{R=R} \quad (2.16)$$

where β is the volumetric expansion coefficient and is assumed constant (at wall temperature) throughout the region in question.

Applying the following dimensionless variables to Eq. (2.9), (2.16), and (2.12):

$$\begin{aligned} x &= X/L, r = R/a, u = a^2 U / (\kappa L), v = aV/\kappa \\ t &= \beta g a^4 (T_0 - T) / (\nu \kappa L) \end{aligned} \quad (2.17)$$

the dimensionless equations of mass, momentum, and energy are obtained

$$\frac{\partial u}{\partial x} + \frac{\partial v}{\partial r} + \frac{v}{r} = 0 \quad (2.18)$$

$$\frac{1}{Pr} \left(u \frac{\partial u}{\partial x} + v \frac{\partial u}{\partial r} \right) = t + \frac{\beta g A a^4}{\nu \kappa} x + \left(\frac{\partial^2 u}{\partial r^2} + \frac{1}{r} \frac{\partial u}{\partial r} \right)_{r=1}^{r=r} \quad (2.19)$$

$$u \frac{\partial t}{\partial x} + v \frac{\partial t}{\partial r} = \frac{\partial^2 t}{\partial r^2} + \frac{1}{r} \frac{\partial t}{\partial r} \quad (2.20)$$

and the applicable dimensionless boundary conditions are:

$$u(0, r) = 0, v(0, r) = 0, u(x, 1) = 0, v(x, 1) = 0 \quad (2.21)$$

$$t(0, r) = 0, t(x, 1) = -Ra_A x, t(1, 0) = -Ra \left(\frac{a}{L}\right) \quad (2.22)$$

where $Ra_A = A\beta ga^4/\nu k$ is a modified Rayleigh number based on the radius and the temperature gradient A along the wall, and $Ra = \beta ga^3(T_1 - T_0)/\nu k$ is a Rayleigh number based on the radius and the temperature difference $(T_1 - T_0)$ which is the difference between the bottom and the top temperature of the fluid at the center line.

Thus, Eqs. (2.18) through (2.22) define the problem in a dimensionless manner.

2.2.2 Solution Method

As was done by Lighthill [11] and few years later by Ostrach and Thornton [14], the "similarity" solutions along X-direction for the axial velocity and the temperature are sought. In other words the temperature and axial velocity profiles obtained at a certain value of x should look proportional or "similar" to those obtained at some other value of x .

To accomplish this, Eqs. (2.18) through (2.20) are first integrated along the radius of the cylinder ($r = 0$ to 1) to give the further simplified conservation equations in integral form:

$$\int_0^1 r u dr = 0 \quad (2.23)$$

$$\frac{\partial}{\partial x} \int_0^1 t u r dr = \left. \frac{\partial t}{\partial r} \right|_{r=1} \quad (2.24)$$

$$\frac{1}{Pr} \frac{\partial}{\partial x} \int_0^1 r u^2 dr = \int_0^1 r t dr + \frac{1}{2} \left(\frac{\partial u}{\partial r} - \frac{\partial^2 u}{\partial r^2} \right) \Big|_{r=1} + Ra_A \frac{x}{2} \quad (2.25)$$

Next, Eq. (2.19) is evaluated at the centerline of the cylinder ($r = 0$) to give:

$$\frac{1}{Pr} u \left. \frac{\partial u}{\partial x} \right|_{r=0} = \left(t + Ra_A x \right) \Big|_{r=0} + \left(\frac{\partial^2 u}{\partial r^2} + \frac{1}{r} \frac{\partial u}{\partial r} \right) \Big|_{r=1}^{r=0} \quad (2.26)$$

and Eq. (2.20) is evaluated at both the centerline and the wall to give

$$u \left. \frac{\partial t}{\partial x} \right|_{r=0} = \left(\frac{\partial^2 t}{\partial r^2} + \frac{1}{r} \frac{\partial t}{\partial r} \right) \Big|_{r=0} \quad (2.27)$$

$$\left(\frac{\partial^2 t}{\partial r^2} + \frac{\partial t}{\partial r} \right) \Big|_{r=1} = 0 \quad (2.28)$$

In the preceding process radial flow at the centerline is assumed zero ($v = 0$ at $r = 0$), because of the symmetry about the centerline of the model geometry.

Then, to obtain the solutions for the axial velocity, U , and for the temperature, t , within the cylinder the following two expressions are assumed:

$$u = F(x)(a_0 + a_1 r^2 + a_2 r^4 + a_3 r^6) \quad (2.29)$$

$$t = G(x)(b_0 + b_1 r^2 + b_2 r^4 + b_3 r^6) \quad (2.30)$$

where a_i and b_i for $i=0$ to 3 are unknown at this stage. The even functions which are functions of r only, represent the general shape of intuitively surmised axial velocity and temperature profiles (see Fig. 2.1), and the two functions $F(x)$ and $G(x)$ represent the variation of $u(r)$ and $t(r)$, respectively, along X -axis of the geometry.

To approximate $F(x)$ and $G(x)$, Eqs. (2.29) and (2.30) are substituted into Eq. (2.25) to obtain:

$$\frac{\partial F(x)}{\partial x} \sim \frac{G(x)}{F(x)} \sim \frac{x}{F(x)} \sim \text{constant.}$$

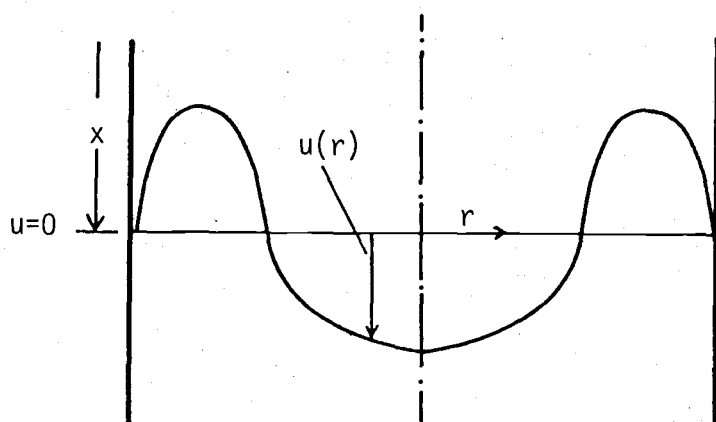
When $F(x)$ and $G(x)$ are denoted by $F(x) \sim x^m$ and $G(x) \sim x^n$, the above expression becomes:

$$mx^{m-1} \sim \frac{x^n}{x^m} \sim \frac{x}{x^m} \sim \text{constant.}$$

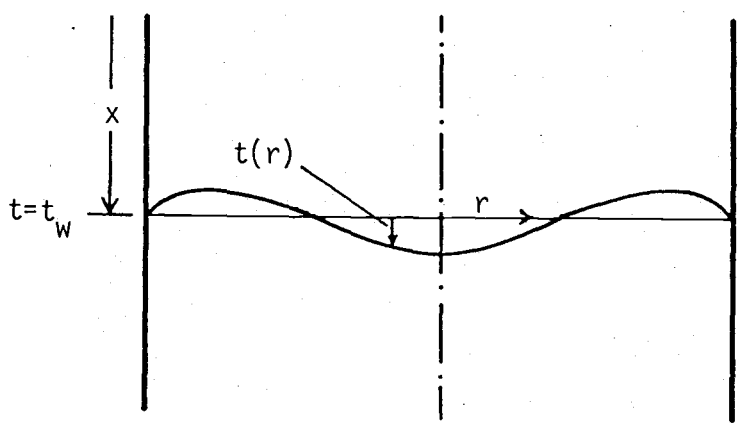
For each of these terms to be proportional to the others in the above expression, by either the first or the third term it can be concluded that $m = 1$, and by second term $n = m$. From this analogy, $F(x)$ and $G(x)$ are determined to be of the form $F(x) \sim x$ and also $G(x) \sim x$.

Using the above result, Eqs. (2.29) and (2.30) can be rewritten as:

$$u = x(a_0 + a_1 r^2 + a_2 r^4 + a_3 r^6) \quad (2.31)$$



a) Axial velocity profile



b) Temperature profile

Figure 2.1 The predicted velocity and temperature profiles.

$$t = x(b_0 + b_1 r^2 + b_2 r^4 + b_3 r^6) \quad (2.32)$$

In order for the unknown coefficients, a_i and b_i , to be found, Eqs. (2.31) and (2.32) are substituted into Eqs. (2.23), (2.26), (2.27), and (2.28) to form four independent equations. Together with three more independent equations which are formed by applying the following boundary conditions: $u(x,1) = 0$, $t(x_1) = -(A\beta g a^4 / \nu k)x$, and $t(1,0) = (T_0 - T_1)\beta g a^4 / \nu k L$, to Eqs. (2.31) and (2.32), the unknown coefficients can be determined and the results are:

$$\frac{u}{x} = \alpha(1 - 6r^2 + 9r^4 - 4r^6) \quad (2.33)$$

$$\begin{aligned} \frac{t}{x} = & -Ra_L^{\frac{a}{L}} - \frac{1}{4}\alpha Ra_L^{\frac{a}{L}} r^2 + [9(Ra_L^{\frac{a}{L}} - Ra_A) + 2\alpha Ra_L^{\frac{a}{L}}] \frac{r^4}{5} \\ & + [16(Ra_A - Ra_L^{\frac{a}{L}}) - 3\alpha Ra_L^{\frac{a}{L}}] \frac{r^6}{20} \end{aligned} \quad (2.34)$$

where α can be taken as a flow parameter yet to be determined.

These last two equations provide profiles of the axial velocity and of the temperature, however, for the actual use of these two equations, additional expressions relating the three parameters, α , $Ra_L^{\frac{a}{L}}$, and Ra_A must be found.

Following the procedure detailed by Ostrach and Thornton, two additional expressions relating, α , $Ra_L^{\frac{a}{L}}$, and Ra_A are achieved by substituting already defined axial velocity and temperature equations, Eqs. (2.33) and (2.34), into Eqs. (2.24) and (2.25), the expressions which result are:

$$\begin{aligned}
& 2B_2 + 4B_3 + 6B_4 \\
& = A_1(B_1 + \frac{1}{2}B_2 + \frac{1}{3}B_3 + \frac{1}{4}B_4) + A_2(\frac{1}{2}B_1 + \frac{1}{3}B_2 + \frac{1}{4}B_3 + \frac{1}{5}B_4) \\
& + A_3(\frac{1}{3}B_1 + \frac{1}{4}B_2 + \frac{1}{5}B_3 + \frac{1}{6}B_4) + A_4(\frac{1}{4}B_1 + \frac{1}{5}B_2 + \frac{1}{6}B_3 + \frac{1}{7}B_4) \\
& \quad (2.35)
\end{aligned}$$

and

$$\begin{aligned}
& \frac{1}{Pr}(A_1^2 + A_1A_2 + \frac{1}{3}A_2^2 + \frac{2}{3}A_1A_3 + \frac{1}{2}A_2A_3 + \frac{1}{5}A_3^2 + \frac{1}{2}A_1A_4 + \frac{2}{5}A_2A_4 \\
& + \frac{1}{3}A_3A_4 + \frac{1}{7}A_4^2) = \\
& \frac{1}{2}B_1 + \frac{1}{4}B_2 + \frac{1}{6}B_3 + \frac{1}{8}B_4 - 4A_3 - 12A_4 + \frac{1}{2}Ra_A \quad (2.36)
\end{aligned}$$

where for Eqs. (2.35) and (2.36)

$$A_1 = \alpha$$

$$A_2 = -6\alpha - \frac{1}{24}\frac{\alpha^2}{Pr} - \frac{1}{24}Ra_L^a + \frac{1}{24}Ra_A$$

$$A_3 = 9\alpha + \frac{1}{8}\frac{\alpha^2}{Pr} + \frac{1}{8}Ra_L^a - \frac{1}{8}Ra_A$$

$$A_4 = -4\alpha - \frac{1}{12}\frac{\alpha^2}{Pr} - \frac{1}{12}Ra_L^a + \frac{1}{12}Ra_A$$

$$B_1 = -Ra_L^a$$

$$B_2 = -\frac{1}{4}\alpha Ra_L^a$$

$$B_3 = \frac{9}{5}Ra_L^a - \frac{9}{5}Ra_A + \frac{2}{5}\alpha Ra_L^a$$

$$B_4 = -\frac{4}{5}Ra_L^a + \frac{4}{5}Ra_A - \frac{3}{20}\alpha Ra_L^a$$

Since Lighthill found, for a similarity solution in the laminar case, the difference between assuming $\text{Pr} = \infty$ or unity is small, the $\text{Pr} = \infty$ case is assumed here for simplicity. An expression for α in terms of only Ra_L^a is thus obtained by eliminating Ra_A between Eqs. (2.35) and (2.36):

$$\alpha = \frac{144000 - 375.8 Ra_L^a}{-0.0052(Ra_L^a)^2 + 8.4(Ra_L^a) - 5343.6} \quad (2.37)$$

Eq. (2.37) is plotted in Fig. 2.2. Also, α can be eliminated between Eqs. (2.35) and (2.36), and the expression for Ra_A can be obtained in terms of Ra_L^a :

$$Ra_A = \frac{-0.0052(Ra_L^a)^3 + 35.8(Ra_L^a)^2 - 3839.4(Ra_L^a) + 8640000}{-0.0052(Ra_L^a)^2 - 8.4(Ra_L^a) - 5343.6} \quad (2.38)$$

Eq. (2.38) is plotted in Fig. 2.3. On this plot, the Ra_L^a domain is divided into four parts as indicated. Since the main interest of the temperature variation along the cylinder wall is that of a linear increase in the direction of body force, Ra_A is always positive valued, thus the two regions I and III can be eliminated

from the possible applicable range on Ra_L^a . In range IV on Ra_L^a , the relationship between Ra_L^a and Ra_A becomes linear as seen in the figure and at any point on this curve the value of Ra_L^a is always larger than Ra_A by approximately 5500. Since by definition, Ra_A is representative of the linear temperature gradient along the wall of the cylinder and Ra_L^a is that for the centerline axis, at any level (i.e., at any choice of x) along the cylinder the temperature at the centerline is always higher than that at the wall. It is expected that in such a situation the induced convective flow is rising along the centerline axis, and thus down along the wall (see Fig. 2.4). However, the flow parameter (which also indicates the velocity at $r = 0$, centerline) is always positive (see Fig. 2.2 for the Ra_L^a values marked as region IV in Fig. 2.3) indicating its direction to be in the positive x sense (downward). For this reason the Ra_L^a range indicated by IV is also eliminated from the possible applicable range on Ra_L^a .

Thus, the applicable range has been narrowed down to region II alone and for this region a more detailed examination of temperature distributions is necessary to determine which portion of this curve may still be applicable.

In Fig. 2.5, values from Figs. 2.2 and 2.3 are cross plotted for the Ra_L^a range from zero to 1000, and in Fig. 2.6 several temperature profiles are plotted according to Eq. (2.34) choosing the necessary values from Fig. 2.5. Starting at $Ra_L^a \approx 310$ along the Ra_A curve in Fig. 2.5, as Ra_L^a increases the temperature profile flattens (which is depicted in Fig. 2.6) indicating less movement of fluid in the cylinder caused by the small difference in Ra_L^a

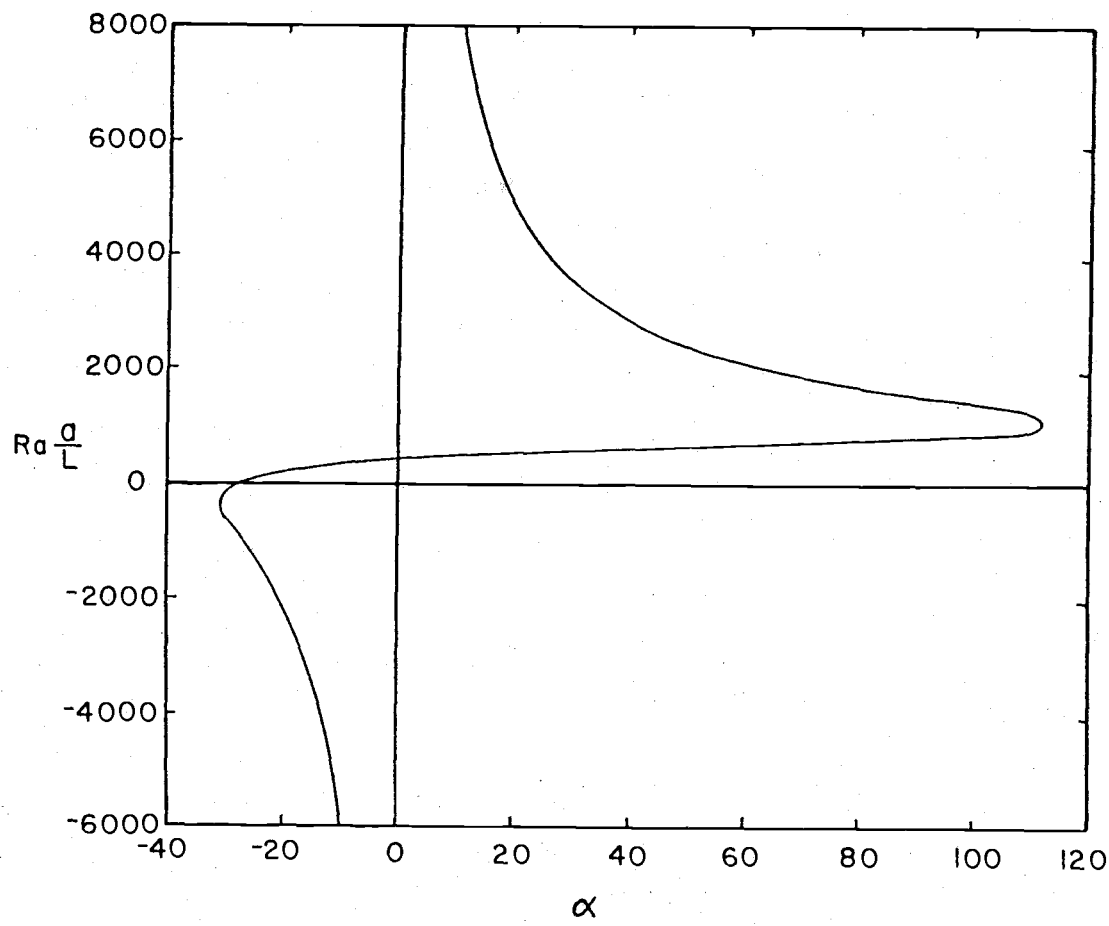


Figure 2.2 Relationship between Ra_L^α and α . (Eq. 2.37)

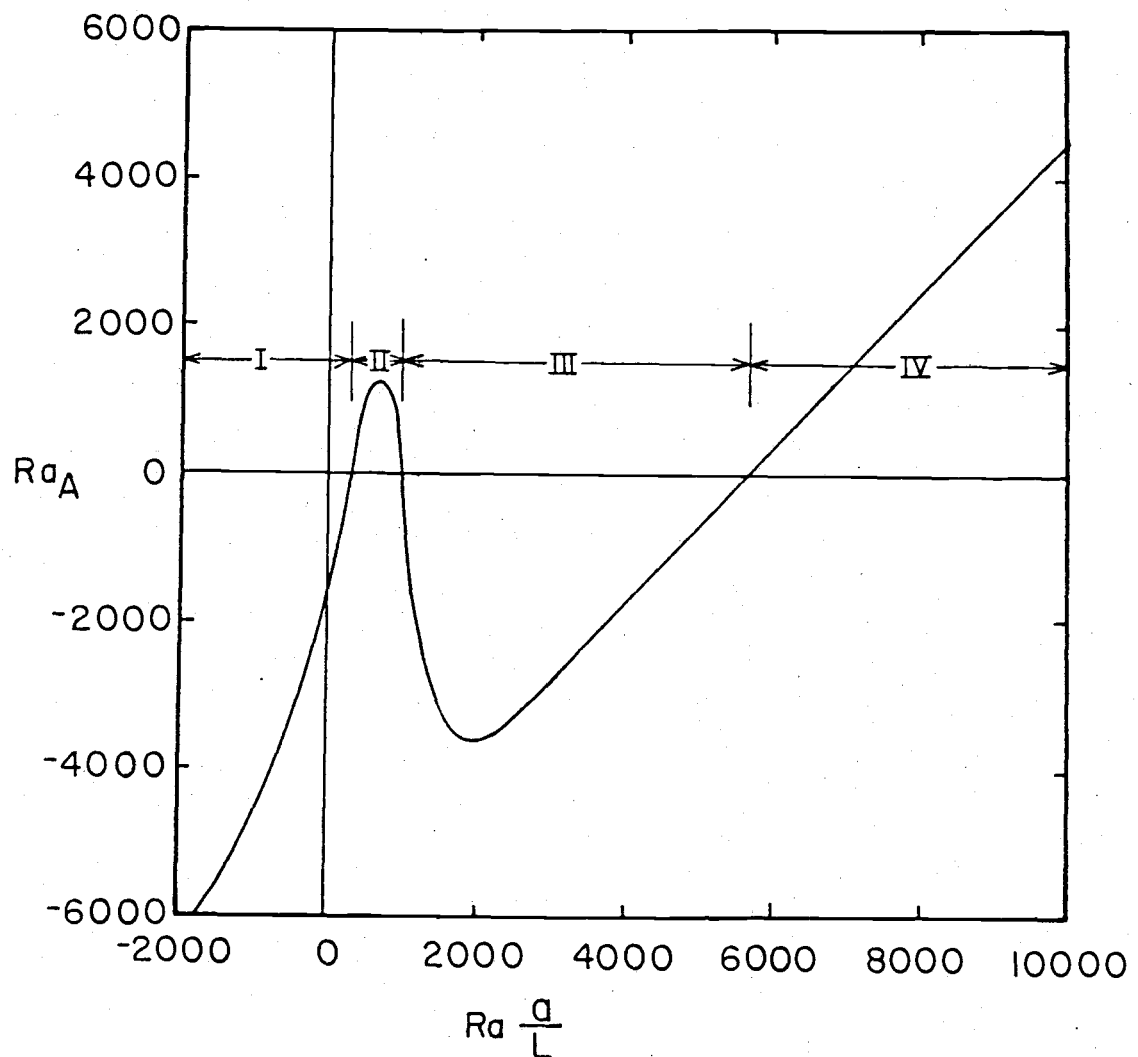
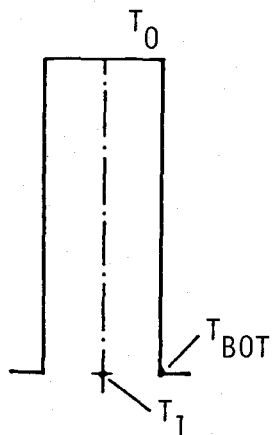


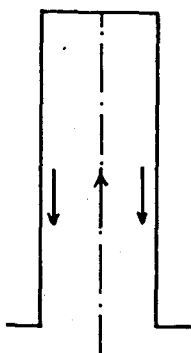
Figure 2.3 Relationship between Ra_L^a and Ra_A . (Eq. 2.38)



$$Ra_L^a \sim (T_1 - T_0)$$

$$Ra_A \sim (T_{BOT} - T_0)$$

a) Temperature and Rayleigh number relations

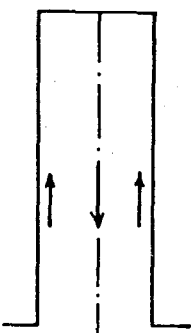


$$Ra_L^a > Ra_A$$

or

$$T_1 > T_{BOT}$$

b) Flow up along the centerline



$$Ra_L^a < Ra_A$$

or

$$T_1 < T_{BOT}$$

c) Flow down along the centerline

Figure 2.4 Two kinds of flow direction predicted by Ra_L^a and Ra_A relations.

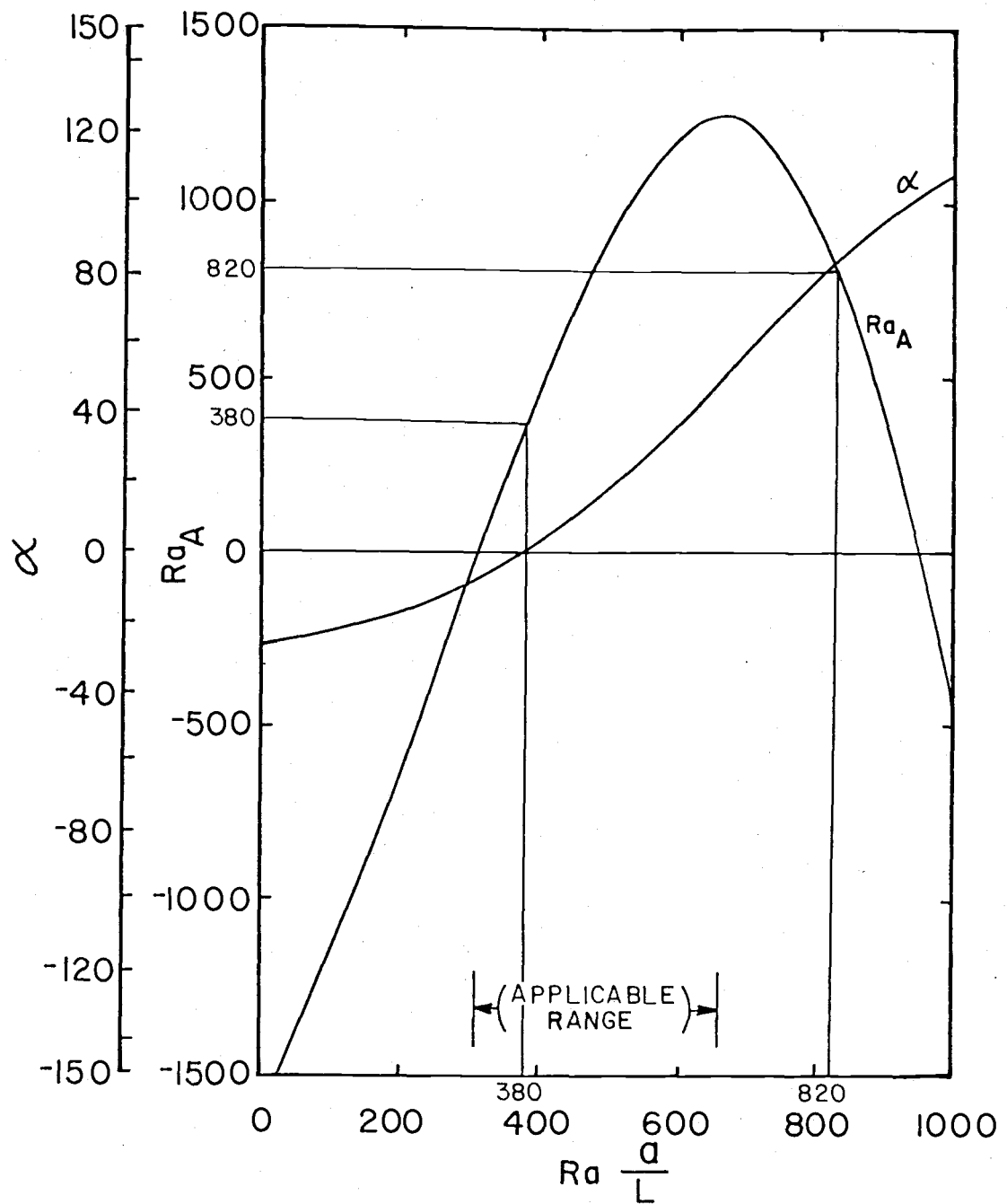


Figure 2.5 Cross plot of Figs. 2.2 and 2.3 in the range $0 < Ra \frac{a}{L} < 1000$.

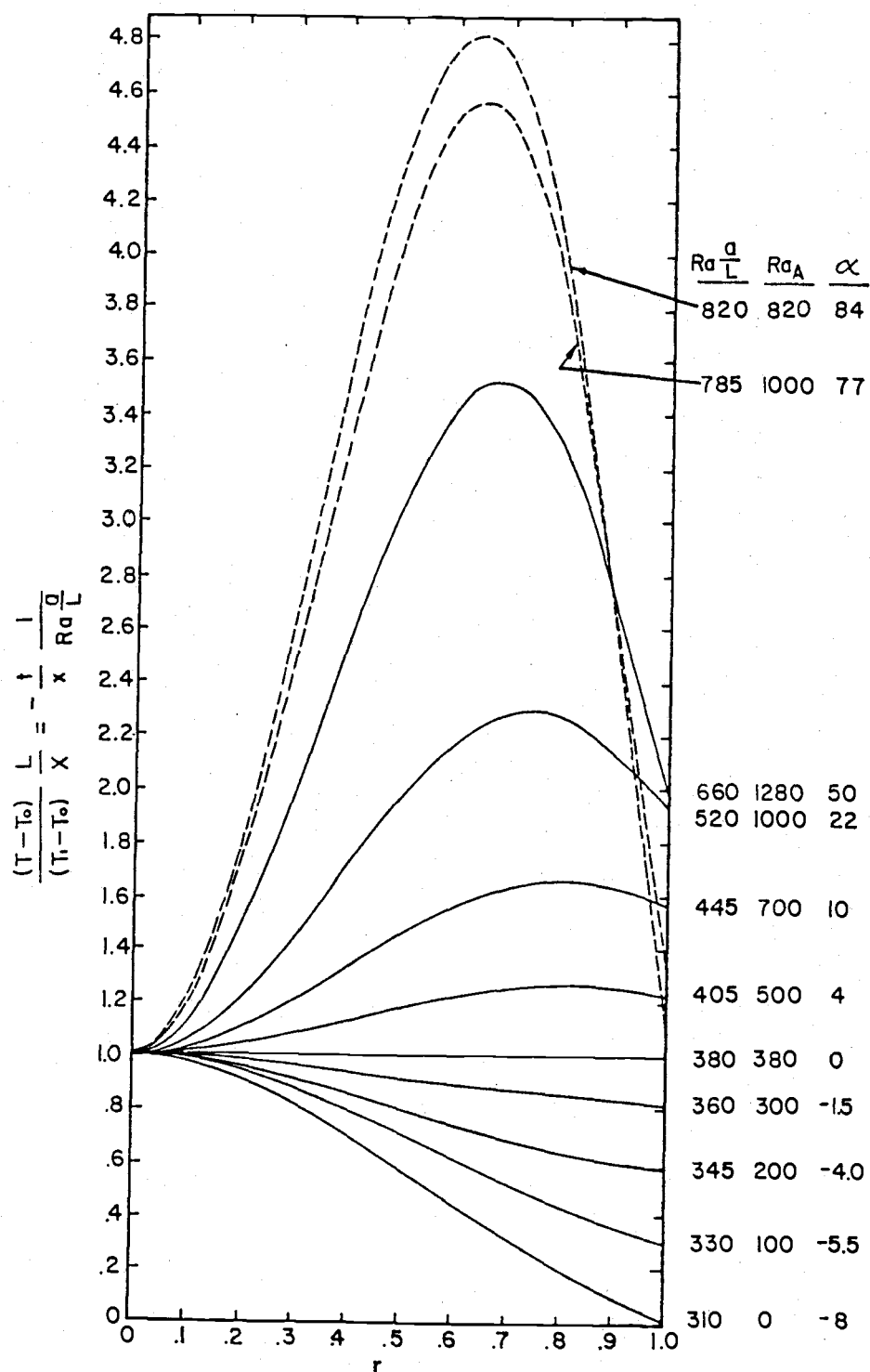


Figure 2.6 Temperature profiles.

and Ra_A^a values. At $Ra_L^a = 380$, Ra_A^a also reaches the same value which causes the flow to become stationary indicated by $\alpha = 0$ (see Fig. 2.5). As soon as this Ra_L^a value is increased further (more than 380), the convective flow is again induced but its direction is reversed as depicted by the α curve in Fig. 2.5. Beyond this point as seen in Fig. 2.6, the temperature profile holds a similar shape except the peak of the profile tends to move away from the wall.

At $Ra_L^a = 660$ in Fig. 2.5, Ra_A^a attains its peak value and further increase in Ra_L^a results in decreased values of Ra_A^a . For such a situation it is reasonable to expect the magnitude of the center-line velocity, α , to decrease since the temperature difference between the center-line and the wall (both at the orifice) is decreasing indicated by the decreasing difference between Ra_A^a and Ra_L^a (see also Fig. 2.4). However this situation is contradicted as indicated by the increasing α in Fig. 2.5 for $Ra_L^a > 660$. It is suspected, as argued by Ostrach and Thornton, that beyond $Ra_L^a = 660$ the temperature gradient along the center-line axis may become so large that the similarity solution does not apply any longer.

Therefore, the most applicable range for this particular problem appears to correspond to Ra_L^a values between 310 and 660. Along the Ra_A^a curve in Fig. 2.5, seven points are chosen between $Ra_L^a = 310$ and 660, and choosing seven corresponding α values from the same figure on the α -curve, velocity profiles are plotted in Fig. 2.7 using Eq. (2.33).

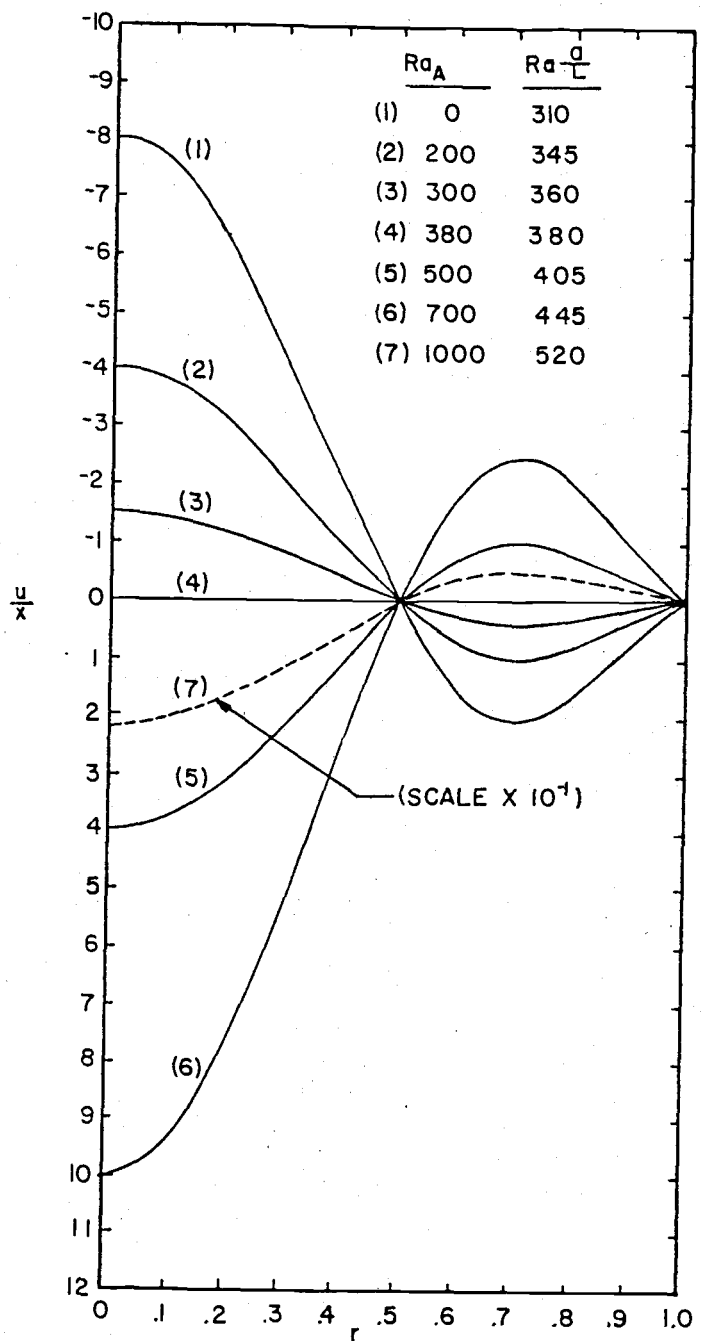


Figure 2.7 Velocity profiles.

2.2.3 Average Heat Transfer

The average heat transfer coefficient Nu_a of this analytical model can be defined as follows:

$$Nu_a \equiv \frac{\text{Net Heat Transfer from the Fluid to the Wall}}{\text{Net Heat Transfer at the Wall}} \quad (2.39)$$

Following the above definition with proper quantities, Nu_a is:

$$Nu_a = \frac{Qa}{k(T_m - T_1)2\pi La} \quad (2.40)$$

where Q is the total heat transfer rate from the fluid to the wall, and T_m is the average temperature of the wall as defined below:

$$T_m \equiv T_0 + (AL/2) \quad (2.41)$$

In Eq. (2.40), a positive Nu_a will indicate the net heat transfer to be from the fluid to the wall. The net heat transfer at the wall can be found by the following expression:

$$Q = 2\pi ak \int_0^L \left. \frac{dT}{dR} \right|_{R=a} dX \quad (2.42)$$

Substitution of Eq. (2.42) into Eq. (2.40) yields:

$$Nu_a = a \int_0^L \left. \frac{dT}{dR} \right|_{R=a} dX / L(T_m - T_1) \quad (2.43)$$

Substituting dimensionless variables, the above expression becomes:

$$Nu_a = \left[\int_0^1 \frac{dt}{dr} \Big|_{r=1} dx \right] / (Ra_L^a - \frac{1}{2} Ra_A) \quad (2.44)$$

Finally, by using the expression for the fluid temperature which is already found in Eq. (2.34) and by solving the integral in Eq. 2.44, a more practical Nu_a equation is found as follows:

$$Nu_a = [2.4(Ra_L^a - Ra_A) + 0.2\alpha Ra_L^a] / (2Ra_L^a - Ra_A) \quad (2.45)$$

The parameters used in the above equation are all dimensionless.

Choosing several values of Ra_A from the applicable range in Fig. 2.5, corresponding Nu_a values are computed using Eq. (2.45), and the results are listed in Table 2.1 and plotted in Fig. 2.8.

2.3 Result of Analytical Study

Among the previous works mentioned in the introduction, Ostrach and Thorntons' investigation is most like the problem in this work. The difference is that in their investigation, the cold reservoir is located at the open top of the closed-bottom cylinder, while in this work the cold fluid is located at the closed-top portion of the open-bottom cylinder. In addition, although a linear temperature gradient is imposed on the wall in the both cases, they are oppositely directed.

For these situations, it is not surprising that correlations among Ra_L^a , Ra_A , and α (see Figs. 2.2 and 2.3) in both cases produced

Table 2.1 Average Heat Transfer Coefficient Eq. (2.45) .

<u>Ra_A</u>	<u>Ra_L^a</u>	<u>α</u>	<u>Nu_a</u>
0	310	- 8	0.40
100	330	- 5.5	0.34
300	360	- 1.5	0.09
380	380	0	0
500	405	4	0.31
700	445	10	1.46
1000	520	22	28.40
1280	660	50	128.80
1000*	780	77	20.30
820*	820	85	16.80

(* Beyond the applicable range)

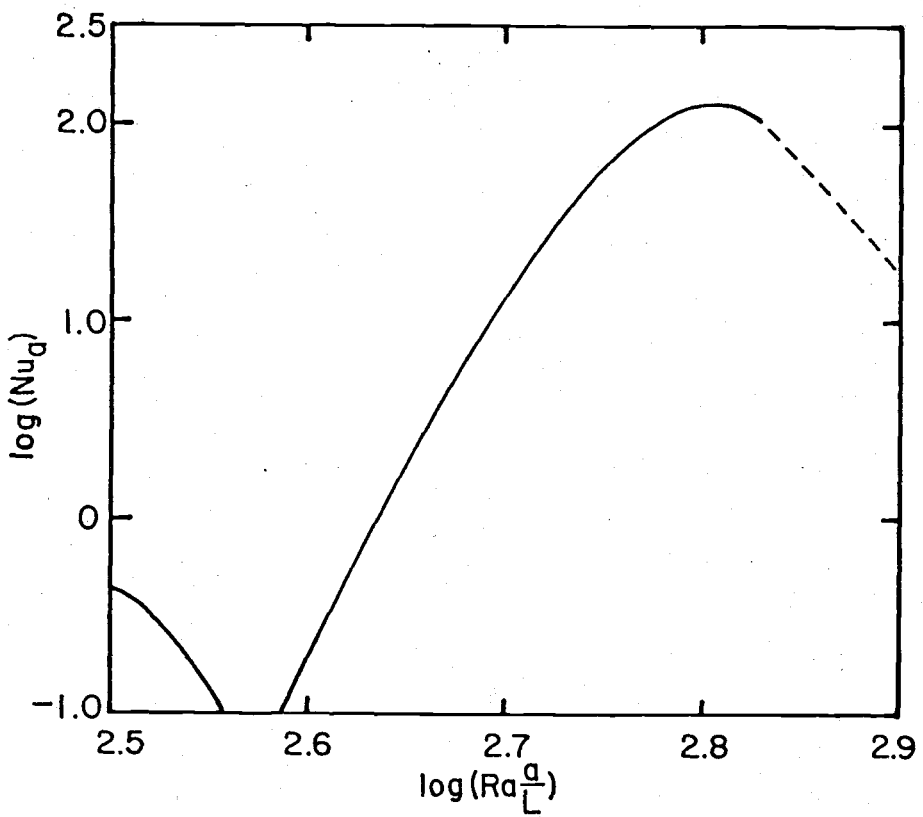


Figure 2.8 Average heat transfer coefficient within the applicable range. (see Table 2.1)

virtually identical results except for the difference caused by the sign change of the coordinate system. The choice of an applicable range is different from Ostrach and Thorntons' temperature and velocity results. In Ostrach and Thorntons' work, the convective flow may be in one direction considering the nature of the imposed wall-temperature and of the location of the cold-fluid reservoir, while in this problem the direction cannot be predetermined without examining the nature of all parameters. For this reason, a lengthy and careful evaluation of the applicable range is required.

In the applicable range, it is found that the convective flow may be zero at a certain combination of Ra_L^a and Ra_A values, namely $Ra_L^a = Ra_A = 380$, and with increasing or decreasing Ra_L^a values from this point (see Fig. 2.5) the flow will rise or fall along the center-line of the cylinder.

In Hasegawa's analysis which is, to a degree, an extension of Ostrach and Thornton's analysis, the average dimensionless heat transfer coefficient, Nu_a is calculated for the applicable range defined by Ostrach and Thornton. A similarity between Hasegawa's result and this work is the significant variation of Ra_A corresponding to a rather small change of Ra_L^a ; while a greater variation of Nu_a is more noticeable in this result than their case. Apparently, this large variation of Nu_a within the applicable range is caused by the flow parameter α . The influence of α in the calculation of Nu_a is seen in Eq. (2.45) where α is a multiplier to Ra_L^a in the numerator, and it is, because of this particular term, that such a large variation in Nu_a occurs as indicated in Table 2.1. Also, values in Table 2.1 and Fig. 2.8 indicate that the direction of

the average heat transfer is always from the fluid to the wall regardless of whether the flow along the wall is up or down. This is a reasonable result since the highest temperature of the system is assumed to be located at $x = 1$ and $r = 0$ (center of the orifice).

III. NUMERICAL STUDY

In this chapter the governing equations, (2.5) through (2.8), are modified in such a way that the system of equations contains three dependent variables, namely temperature, vorticity, and stream function. The modified equations are then converted to a set of difference equations by applying the finite difference technique, followed by writing the Fortran computer code.

3.1 Modification of Governing Equations

The major modification made in the system of governing equations is the combining of the two momentum equations. This is accomplished by, first, differentiating Eq. (2.6) with respect to the radial coordinate, R , and Eq. (2.7) with respect to the axial coordinate, X , and then the two equations are combined by using the common term $\partial^2 P / \partial R \partial X$. At this point, the modified vorticity term:

$$\Xi \equiv \frac{1}{R} \left(\frac{\partial U}{\partial R} - \frac{\partial V}{\partial X} \right) \quad (3.1)$$

is introduced to the combined equation, Ref. [24], yielding

$$\begin{aligned} & \Xi \left(\frac{\partial U}{\partial X} + \frac{\partial V}{\partial R} + \frac{V}{R} \right) + U \frac{\partial \Xi}{\partial X} + V \frac{\partial \Xi}{\partial R} \\ &= \frac{1}{R} \left(\frac{\partial P}{\partial R} \frac{\partial}{\partial X} \left(\frac{1}{\rho} \right) - \frac{\partial P}{\partial X} \frac{\partial}{\partial R} \left(\frac{1}{\rho} \right) \right) + V \left(\frac{\partial^2 \Xi}{\partial X^2} + \frac{3}{R} \frac{\partial \Xi}{\partial R} + \frac{\partial^2 \Xi}{\partial R^2} \right) \end{aligned} \quad (3.2)$$

The bracketed terms in the left hand side of Eq. (3.2) are zero because of the conservation of mass, Eq. (2.5), and the

pressure term $\partial P / \partial R$ can also be made to zero by assuming $|\partial P / \partial R| \ll |\partial P / \partial X|$. The density changes in R- and in X-directions are assumed to be of the same order of magnitude for the configuration of this problem. The other pressure term, $\partial P / \partial X$, in Eq. (3.2) is considered hydrostatic and written as $-\rho_0 g$ where ρ_0 is a density at some reference temperature, T_0 . Then, applying the definition of thermal expansion coefficient (see Eq. (2.15) and the footnote below), the combined equations of Eqs. (2.6) and (2.7) finally takes the following form:

$$U \frac{\partial \Xi}{\partial X} + V \frac{\partial \Xi}{\partial R} = \frac{g \beta_0}{R} \frac{\partial T}{\partial R} + v \left(\frac{\partial^2 \Xi}{\partial X^2} + \frac{3}{R} \frac{\partial \Xi}{\partial R} + \frac{\partial^2 \Xi}{\partial R^2} \right) \quad (3.3)$$

where vorticity is defined by Eq. (3.1).

Introduction of stream function becomes necessary in order for two velocity components to be found. The stream function is defined as:

By Taylor series, specific volume v is expanded about v_0 of at some reference temperature:

$$v = \frac{1}{\rho} \approx v(T_0) + \frac{(T-T_0)}{1!} \frac{\partial v_0(T_0)}{\partial T} + \frac{(T-T_0)^2}{2!} \frac{\partial^2 v(T_0)}{\partial T^2} + \dots$$

Approximating it by using the first two terms of the above series and incorporating the definition of the thermal expansion coefficient, $\beta(T_0) \equiv [\partial v(T_0)/\partial T]/v(T_0)$, the expression for v becomes:

$$v(T) \approx v_0 + (T-T_0)\beta_0 v_0$$

where v_0 and β_0 are at the reference temperature T_0 . Now, differentiating this with respect to the radial coordinate, R , it becomes:

$$\frac{\partial v(T)}{\partial R} = \frac{\partial}{\partial R} \left(\frac{1}{\rho} \right) \approx \beta_0 v_0 \frac{\partial T}{\partial R} = \frac{\beta_0}{\rho_0} \frac{\partial T}{\partial R}$$

$$U \equiv \frac{1}{R} \frac{\partial \Psi}{\partial R}, \quad V \equiv - \frac{1}{R} \frac{\partial \Psi}{\partial X} \quad (3.4)$$

Differentiating the first equation of Eqs. (3.4) with respect to R , the second with respect to X , and substituting them into Eq. (3.1) gives the following expression:

$$\Xi R^2 = - \frac{1}{R} \frac{\partial \Psi}{\partial R} + \frac{\partial^2 \Psi}{\partial R^2} + \frac{\partial^2 \Psi}{\partial X^2} \quad (3.5)$$

which relates the stream function and the vorticity. Thus, solving Eq. (3.5) for Ψ and substituting it into Eq. (3.4) yields the two velocity values.

Therefore, in summing up, the equations to be solved numerically are as follows:

$$U \frac{\partial T}{\partial X} + V \frac{\partial T}{\partial R} = \kappa \left(\frac{\partial^2 T}{\partial R^2} + \frac{1}{R} \frac{\partial T}{\partial R} + \frac{\partial^2 T}{\partial X^2} \right) \quad (2.8)$$

$$U \frac{\partial \Xi}{\partial X} + V \frac{\partial \Xi}{\partial R} = \frac{g\beta_0}{R} \frac{\partial T}{\partial R} + \nu \left(\frac{\partial^2 \Xi}{\partial X^2} + \frac{3}{R} \frac{\partial \Xi}{\partial R} + \frac{\partial^2 \Xi}{\partial R^2} \right) \quad (3.3)$$

$$\Xi R^2 = - \frac{1}{R} \frac{\partial \Psi}{\partial R} + \frac{\partial^2 \Psi}{\partial R^2} + \frac{\partial^2 \Psi}{\partial X^2} \quad (3.5)$$

$$U \equiv \frac{1}{R} \frac{\partial \Psi}{\partial R}, \quad V \equiv - \frac{1}{R} \frac{\partial \Psi}{\partial X} \quad (3.4)$$

The substitution of the following relationships: $X = xL$, $R = ra$, $U = u\kappa L/a^2$, $V = v\kappa/a$, $T - T_0 = t\nu\kappa L/\beta ga^4$, $\Xi = \xi\kappa L/a^4$, and $\Psi = \psi\kappa L$, into these equations yields the following dimensionless expressions:

$$u \frac{\partial t}{\partial x} + v \frac{\partial t}{\partial r} = \frac{\partial^2 t}{\partial r^2} + \frac{1}{r} \frac{\partial t}{\partial r} + \frac{1}{(L/a)^2} \frac{\partial^2 t}{\partial x^2} \quad (2.8a)$$

$$u \frac{\partial \xi}{\partial x} + v \frac{\partial \xi}{\partial r} = Pr \left(\frac{1}{r} \frac{\partial t}{\partial r} + \frac{1}{(L/a)^2} \frac{\partial^2 \xi}{\partial x^2} + \frac{3}{r} \frac{\partial \xi}{\partial r} + \frac{\partial^2 \xi}{\partial r^2} \right) \quad (3.3a)$$

$$\xi r^2 = - \frac{1}{r} \frac{\partial \psi}{\partial r} + \frac{\partial^2 \psi}{\partial r^2} + \frac{1}{(L/a)^2} \frac{\partial^2 \psi}{\partial x^2} \quad (3.5a)$$

$$u \equiv \frac{1}{r} \frac{\partial \psi}{\partial r}, \quad v \equiv - \frac{1}{r} \frac{\partial \psi}{\partial x} \quad (3.4a)$$

where the two dimensionless parameters arising in this process are $Pr (=v/\kappa)$ and L/a , Prandtl number and aspect ratio respectively.

The first equation is of course the energy equation; the second one is the vorticity equation converted from the two-directional momentum equations, coupled to the first one by T ; the third one relates the vorticity and the stream function, coupled to the second by Ξ ; and the last two are the velocity expressions.

3.2 Finite Difference Formulation

The basic numerical formulas used for the partial differential equations mentioned in the last section are; forward, backward, and central difference formulas as listed below Ref's. [35,36,37]:

$$\frac{\partial f}{\partial x} = \frac{f_{i+1,j} - f_{i,j}}{\Delta x} + O(\Delta x) \quad (\text{Forward}) \quad (3.6)$$

$$\frac{\partial f}{\partial x} = \frac{f_{i,j} - f_{i-1,j}}{\Delta x} + O(\Delta x) \quad (\text{Backward}) \quad (3.7)$$

$$\frac{\partial f}{\partial x} = \frac{f_{i+1,j} - f_{i-1,j}}{2\Delta x} + O[(\Delta x)^2] \quad (\text{Central}) \quad (3.8)$$

and

$$\frac{\partial^2 f}{\partial x^2} = \frac{f_{i-1,j} - 2f_{i,j} + f_{i+1,j}}{(\Delta x)^2} + O[(\Delta x)^2] \quad (3.9)$$

For non-standard cases, however, such as at boundaries or the cases which require a higher-than-usual order of approximation, special formulas are needed. These numerical expressions will be derived and noted as this section progresses.

3.2.1 Energy Equation

The energy equation to be written in a finite difference form is Eq. (2.8). Those terms with velocities in this equation require special consideration. When the velocity is positive (or in the direction of scan) or equal to zero, the backward formula is applied to those applicable terms. This technique is termed "upwind" method and is known to accelerate the program for convergence. Those terms which do not involve velocities are approximated by the central finite difference formula for the first and second derivatives [38].

Therefore, the numerical expression for energy becomes:

$$U \frac{\partial T}{\partial X} + V \frac{\partial T}{\partial R} = \kappa \left[\frac{T_{i,j-1} - 2T_{i,j} + T_{i,j+1}}{(\Delta R)^2} + \frac{T_{i,j+1} - T_{i,j-1}}{2R(\Delta R)} + \frac{T_{i-1,j} - 2T_{i,j} + T_{i+1,j}}{(\Delta X)^2} \right] \quad (3.10)$$

where $(U \frac{\partial T}{\partial X} + V \frac{\partial T}{\partial R})$ takes one of the following four forms depending on the direction of the velocity:

$$U \left(\frac{T_{i,j} - T_{i-1,j}}{\Delta X} \right) + V \left(\frac{T_{i,j} - T_{i,j-1}}{\Delta R} \right) \text{ for } U \geq 0 \text{ and } V \geq 0,$$

$$U \left(\frac{T_{i,j} - T_{i-1,j}}{\Delta X} \right) + V \left(\frac{T_{i,j+1} - T_{i,j}}{\Delta R} \right) \text{ for } U \geq 0 \text{ and } V < 0,$$

$$U \left(\frac{T_{i+1,j} - T_{i,j}}{\Delta X} \right) + V \left(\frac{T_{i,j+1} - T_{i,j}}{\Delta R} \right) \text{ for } U < 0 \text{ and } V < 0,$$

and

$$U \left(\frac{T_{i+1,j} - T_{i,j}}{\Delta X} \right) + V \left(\frac{T_{i,j} - T_{i,j-1}}{\Delta R} \right) \text{ for } U < 0 \text{ and } V \geq 0.$$

Eq. (3.10) together with these four different forms of convection terms are applicable for internal nodes.

For those nodes along system boundaries, a modification to Eq. (2.8) must be made. At the centerline or the line of symmetry of the system, the radial velocity approaches zero and the temperature gradient can be assumed zero. Because of these conditions and applying L'Hospital's rule to $\frac{1}{R} \frac{\partial T}{\partial R}$, Eq. (2.8) becomes as follows:

$$\left[U \frac{\partial T}{\partial X} = \kappa \left(2 \frac{\partial^2 T}{\partial R^2} + \frac{\partial^2 T}{\partial X^2} \right) \right]_{R=0}$$

and its finite difference form is,

$$U \frac{\partial T}{\partial X} = \kappa \left(\frac{2T_{i,j-1} - 4T_{i,j} + 2T_{i,j+1}}{(\Delta R)^2} + \frac{T_{i-1,j} - 2T_{i,j} + T_{i+1,j}}{(\Delta X)^2} \right) \quad (3.11)$$

where

$$U \frac{\partial T}{\partial X} = U \left(\frac{T_{i,j} - T_{i-1,j}}{\Delta X} \right) \text{ for } U \geq 0$$

and

$$U \frac{\partial T}{\partial X} = U \left(\frac{T_{i+1,j} - T_{i,j}}{\Delta X} \right) \text{ for } U < 0.$$

In the actual use of the above equations, $T_{i,j+1} = T_{i,j-1}$ is assumed because of the symmetry of the temperature profile about the centerline of the system.

For insulated boundaries, the following conditions apply:

$U = V = 0$ (no slip condition), $\partial T / \partial X = 0$ (when the wall perpendicular to X-axis is insulated), and $\partial T / \partial R = 0$ (when the wall perpendicular to R-axis is insulated). Applying these conditions to the energy equation, Eq. (2.8) becomes:

$$\frac{\partial^2 T}{\partial R^2} + \frac{\partial^2 T}{\partial X^2} = 0 \quad (3.12)$$

for the wall normal to R-axis, and

$$\frac{\partial^2 T}{\partial R^2} + \frac{1}{R} \frac{\partial T}{\partial R} + \frac{\partial^2 T}{\partial X^2} = 0 \quad (3.13)$$

for the wall normal to X-axis. These in the finite difference form are, respectively:

$$\frac{T_{i,j+1} - 2T_{i,j} + T_{i,j-1}}{(\Delta R)^2} + \frac{T_{i+1,j} - 2T_{i,j} + T_{i-1,j}}{(\Delta X)^2} = 0 \quad (3.14)$$

and

$$\begin{aligned} & \frac{T_{i,j+1} - 2T_{i,j} + T_{i,j-1}}{(\Delta R)^2} + \frac{T_{i,j+1} - T_{i,j-1}}{2R\Delta R} \\ & + \frac{T_{i+1,j} - 2T_{i,j} + T_{i-1,j}}{(\Delta X)^2} = 0 \end{aligned} \quad (3.15)$$

where $T_{i,j+1} = T_{i,j-1}$ for Eq. (3.14) and $T_{i+1,j} = T_{i-1,j}$ for Eq. (3.15) can be assumed.

Nodes located at corners require different forms of finite difference expressions, however, these can be derived easily from the last two equations with proper assumptions.

3.2.2 Vorticity Equation

The finite difference form of the vorticity equation is derived from Eq. (3.3). As was done with the energy equation, those terms with velocity coefficients take the backward difference form

when the velocity is positive or equal to zero, and take the forward form when it is negative. Thus, for the internal nodes the finite difference form of Eq. (3.3) can be written as:

$$\begin{aligned} U \frac{\partial \bar{\varepsilon}}{\partial X} + V \frac{\partial \bar{\varepsilon}}{\partial R} &= \frac{g\beta_0}{R} \left(\frac{T_{i,j+1} - T_{i,j-1}}{2\Delta R} \right) \\ &+ V \left[\frac{\bar{\varepsilon}_{i-1,j} - 2\bar{\varepsilon}_{i,j} + \bar{\varepsilon}_{i+1,j}}{(\Delta X)^2} + \frac{3}{R} \left(\frac{\bar{\varepsilon}_{i,j+1} - \bar{\varepsilon}_{i,j-1}}{2\Delta R} \right) \right. \\ &\left. + \frac{\bar{\varepsilon}_{i,j-1} - 2\bar{\varepsilon}_{i,j} + \bar{\varepsilon}_{i,j+1}}{(\Delta R)^2} \right] \end{aligned} \quad (3.16)$$

where $(U \frac{\partial \bar{\varepsilon}}{\partial X} + V \frac{\partial \bar{\varepsilon}}{\partial R})$ takes one of the following four forms depending on the direction of the velocity:

$$U \left(\frac{\bar{\varepsilon}_{i,j} - \bar{\varepsilon}_{i-1,j}}{\Delta X} \right) + V \left(\frac{\bar{\varepsilon}_{i,j} - \bar{\varepsilon}_{i,j-1}}{\Delta R} \right) \text{ for } U \geq 0 \text{ and } V \geq 0,$$

$$U \left(\frac{\bar{\varepsilon}_{i,j} - \bar{\varepsilon}_{i-1,j}}{\Delta X} \right) + V \left(\frac{\bar{\varepsilon}_{i,j+1} - \bar{\varepsilon}_{i,j}}{\Delta R} \right) \text{ for } U \geq 0 \text{ and } V < 0,$$

$$U \left(\frac{\bar{\varepsilon}_{i+1,j} - \bar{\varepsilon}_{i,j}}{\Delta X} \right) + V \left(\frac{\bar{\varepsilon}_{i,j+1} - \bar{\varepsilon}_{i,j}}{\Delta R} \right) \text{ for } U < 0 \text{ and } V < 0,$$

and

$$U \left(\frac{\bar{\varepsilon}_{i+1,j} - \bar{\varepsilon}_{i,j}}{\Delta X} \right) + V \left(\frac{\bar{\varepsilon}_{i,j} - \bar{\varepsilon}_{i,j-1}}{\Delta R} \right) \text{ for } U < 0 \text{ and } V \geq 0.$$

For the centerline (or the line of symmetry), a limit is taken on Eq. (3.3) as the radius, R , approaches zero, and its result is:

$$U \frac{\partial \Xi}{\partial X} = g\beta \frac{\partial T^2}{\partial R^2} + v \left(\frac{\partial^2 \Xi}{\partial X^2} + 4 \frac{\partial^2 \Xi}{\partial R^2} \right) \quad (3.17)$$

This can be expressed in finite difference form as follows:

$$U \frac{\partial \Xi}{\partial X} = g\beta \frac{T_{i,j-1} - 2T_{i,j} + T_{i,j+1}}{(\Delta R)^2} \quad (3.18)$$

$$+ v \left(\frac{\Xi_{i+1,j} - 2\Xi_{i,j} + \Xi_{i-1,j}}{(\Delta X)^2} + 4 \frac{\Xi_{i,j+1} - 2\Xi_{i,j} + \Xi_{i,j-1}}{(\Delta R)^2} \right)$$

where

$$U \frac{\partial \Xi}{\partial X} = U \left(\frac{\Xi_{i,j} - \Xi_{i-1,j}}{\Delta X} \right) \text{ for } U \geq 0,$$

and

$$U \frac{\partial \Xi}{\partial X} = U \left(\frac{\Xi_{i+1,j} - \Xi_{i,j}}{\Delta X} \right) \text{ for } U < 0.$$

For the top ($X = L$) and bottom ($X = 0$) boundaries at the centerline ($R = 0$), Eq. (3.17) is used with the following conditions:

$$U(L,0) = U(0,0) = 0, T(L,0) = \text{constant}, T(0,0) = \text{constant},$$

$$\frac{\partial T(L,0)}{\partial R} = 0, \frac{\partial T(0,0)}{\partial R} = 0, \text{ and } \frac{\partial^2 T(L,0)}{\partial R^2} = \frac{\partial^2 T(0,0)}{\partial R^2} = 0.$$

Thus, we have:

$$\left(\frac{\partial^2 \Xi}{\partial X^2} + 4 \frac{\partial^2 \Xi}{\partial R^2} = 0 \right) \text{ at } X=0 \text{ or } L \quad (3.19)$$

Numerical expressions for $\partial^2 \Xi / \partial X^2$ and $\partial^2 \Xi / \partial R^2$ are:

$$\left. \frac{\partial^2 \Xi}{\partial X^2} \right|_{X=0} = \frac{-5\Xi_{i+1,j} + 4\Xi_{i+2,j} - \Xi_{i+3,j} + 2\Xi_{i,j}}{(\Delta X)^2} \quad (3.20)$$

$$\left. \frac{\partial^2 \Xi}{\partial X^2} \right|_{X=L} = \frac{-5\Xi_{i-1,j} + 4\Xi_{i-2,j} - \Xi_{i-3,j} + 2\Xi_{i,j}}{(\Delta X)^2} \quad (3.21)$$

and

$$\left. \frac{\partial^2 \Xi}{\partial R^2} \right|_{R=0} = \frac{2(\Xi_{i,j+1} - \Xi_{i,j})}{(\Delta R)^2} \quad (3.22)$$

Eq. (3.20) and (3.21) are derived by expanding Taylor series around node (i,j) at three consecutive nodes; $(i+1,j)$, $(i+2,j)$, and $(i+3,j)$, generating three Taylor series expressions about (i,j) , and each of these is multiplied by a factor such that upon summing the three expressions the second-and third-order derivative terms drop out. An example of this procedure is shown below.

$$\left[\Xi_{i+1} = \Xi_i + \Delta X \frac{\partial \Xi_i}{\partial X} + \frac{(\Delta X)^2}{2!} \frac{\partial^2 \Xi_i}{\partial X^2} + \frac{(\Delta X)^3}{3!} \frac{\partial^3 \Xi_i}{\partial X^3} + \dots \right] (-15)$$

$$\left[\Xi_{i+2} = \Xi_i + 2\Delta X \frac{\partial \Xi_i}{\partial X} + \frac{(2\Delta X)^2}{2!} \frac{\partial^2 \Xi_i}{\partial X^2} + \frac{(2\Delta X)^3}{3!} \frac{\partial^3 \Xi_i}{\partial X^3} + \dots \right] (12)$$

$$\left[\Xi_{i+3} = \Xi_i + 3\Delta X \frac{\partial \Xi_i}{\partial X} + \frac{(3\Delta X)^2}{2!} \frac{\partial^2 \Xi_i}{\partial X^2} + \frac{(3\Delta X)^3}{3!} \frac{\partial^3 \Xi_i}{\partial X^3} + \dots \right] (-3)$$

and the sum of these is:

$$-5\Xi_{i+1} + 4\Xi_{i+2} - \Xi_{i+3} = -2\Xi_i + (\Delta X)^2 \frac{\partial^2 \Xi_i}{\partial X^2} + 0 [(\Delta X)^3]$$

or

$$\frac{\partial^2 \Xi_i}{\partial X^2} = \frac{-5\Xi_{i+1} + 4\Xi_{i+2} - \Xi_{i+3} + 2\Xi_i}{(\Delta X)^2}$$

which is Eq. (3.20). Eq. (3.22) is obtained from the ordinary central difference formula with $\Xi_{i,j+1} = \Xi_{i,j-1}$ is applied.

The other option for deriving a boundary condition for the vorticity at ($X=L$, $R=0$) and ($X=0$, $R=0$) is to use Eq. (3.1). The reduction of Eq. (3.1) for these two corner boundaries leads us to somewhat complicated situations due to the limiting values of $\partial U / \partial R$, $\partial V / \partial X$, and $1/R$. Under the presumption that velocity derivatives become zero as R and X approach these two boundary points and, further, their second derivatives with respect to R are also zero at these two points, the reasonable value one can obtain from Eq. (3.1) for $\Xi(L,0)$ and $\Xi(0,0)$ is zero. This method has been successfully applied by Ref.'s [24, 28, and 29], however, this optional boundary value for the vorticity at these particular corners will be further discussed in Sec. 3.3.6.

For the solid boundaries we examine Eq. (3.5):

$$\Xi R^2 = -\frac{1}{R} \frac{\partial \Psi}{\partial R} + \frac{\partial^2 \Psi}{\partial R^2} + \frac{\partial^2 \Psi}{\partial X^2}$$

Evaluating the right hand side of this equation, we find that the first term is zero since $\Psi = \text{constant}$ at solid boundaries ($X=0$ and $X=L$). To evaluate the second term, the definition of the stream function, $U \equiv (1/R)(\partial \Psi / \partial R)$, is once differentiated with

respect to R and $\partial\Psi/\partial R = 0$ is applied. Thus, it yields

$$\frac{\partial U}{\partial R} = \left(\frac{1}{R}\right) \left(\frac{\partial^2 \Psi}{\partial R^2}\right) \quad (3.23)$$

However, the axial velocity, U , becomes zero at $X=0$ and $X=L$, thus we can safely say $\partial U / \partial R = 0$ (this reasoning is illustrated in Fig. 3.1). This, with Eq. (3.23), implies that $\partial^2 \Psi / \partial R^2$ is also zero at the solid boundaries. The last term, $\partial^2 \Psi / \partial X^2$, in Eq. (3.5) is not explainable at this point, and thus, it remains in the equation without change. Therefore, Eq. (3.5) is reduced to follows:

$$\Xi = \frac{1}{R^2} \frac{\partial^2 \Psi}{\partial X^2} \quad (3.24)$$

which is valid at the solid boundaries, $X=0$ and $x=L$. By applying a similar procedure as stipulated above, the vorticity boundary condition at $R=a$ (also a solid boundary) can be reduced from Eq. (3.5) to

$$\Xi = \frac{1}{a^2} \frac{\partial^2 \Psi}{\partial R^2} \quad (3.25)$$

These solid-boundary conditions for the vorticity are expressed in difference form as

$$\Xi_{i,j} = \frac{1}{R^2} \left(\frac{8\Psi_{i-1,j} - \Psi_{i-2,j}}{2(\Delta X)^2} \right) \quad (3.26)$$

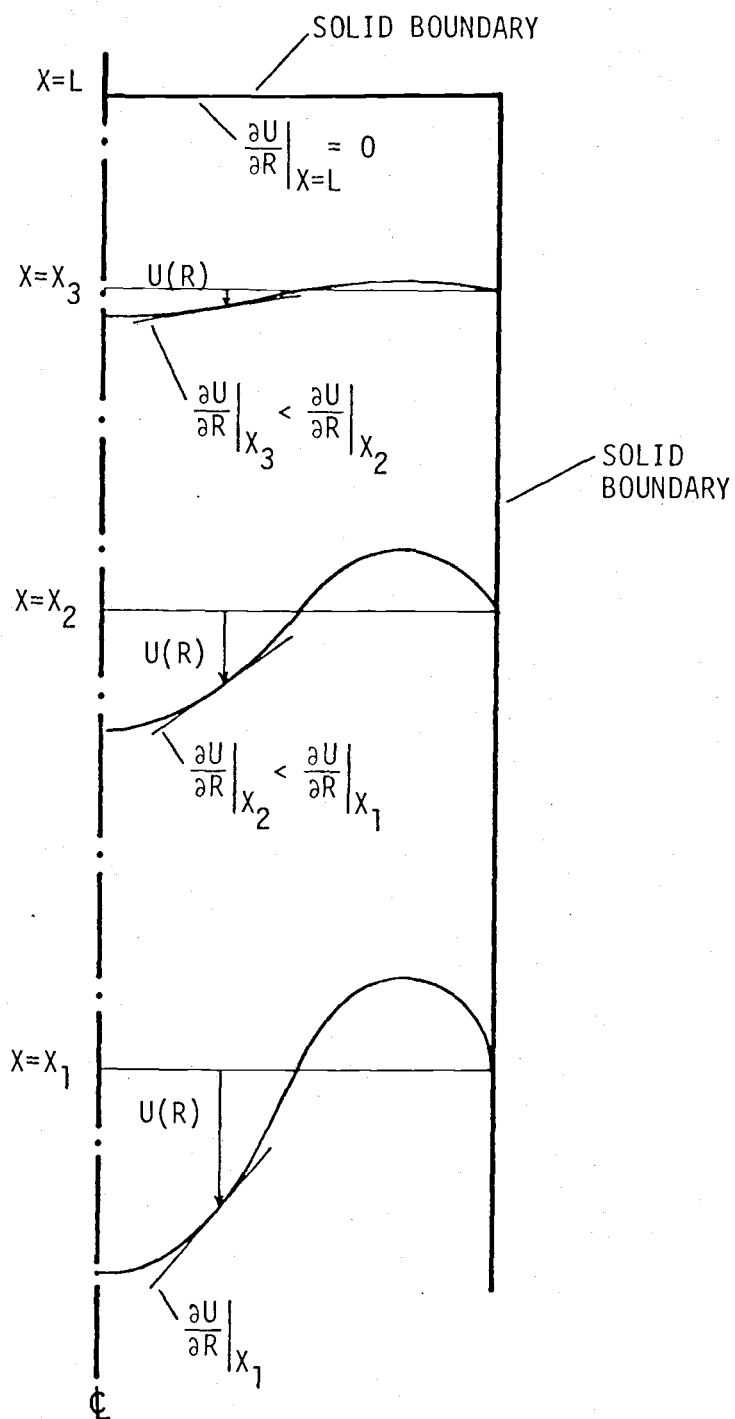


Figure 3.1 The axial velocity gradient illustration; the $\partial U / \partial R$ approaches zero as X approaches $X=L$.

for the top boundary ($X=L$),

$$\Xi_{i,j} = \frac{1}{R^2} \left(\frac{8\Psi_{i+1,j} - \Psi_{i+2,j}}{2(\Delta X)^2} \right) \quad (3.27)$$

for the bottom boundary ($X=0$), and

$$\Xi_{i,j} = \frac{1}{a^2} \left(\frac{8\Psi_{i,j-1} - \Psi_{i,j-2}}{2(\Delta R)^2} \right) \quad (3.28)$$

for the vertical wall boundary ($R=a$). Development of these expressions is illustrated by the following example derivation (see also Fig. 3.2):

$$\left[\Psi_2 = \Psi_1 + \Delta X \frac{\partial \Psi_1}{\partial X} + \frac{1}{2!} (\Delta X)^2 \frac{\partial^2 \Psi_1}{\partial X^2} + \frac{1}{3!} (\Delta X)^3 \frac{\partial^3 \Psi_1}{\partial X^3} + \dots \right] (8)$$

$$\left[\Psi_3 = \Psi_1 + 2\Delta X \frac{\partial \Psi_1}{\partial X} + \frac{1}{2!} (2\Delta X)^2 \frac{\partial^2 \Psi_1}{\partial X^2} + \frac{1}{3!} (2\Delta X)^3 \frac{\partial^3 \Psi_1}{\partial X^3} + \dots \right] (-1)$$

$$8\Psi_2 - \Psi_3 = 7\Psi_1 + 6(\Delta X) \frac{\partial \Psi_1}{\partial X} + 2(\Delta X)^2 \frac{\partial^2 \Psi_1}{\partial X^2} + 0 [(\Delta X)^4]$$

Since $\Psi_1=0$ (assigned value) and $\partial \Psi_1 / \partial X = 0$ (by the symmetry of stream function with respect to the solid boundary), the above expression reduces to

$$\frac{\partial^2 \Psi_i}{\partial X^2} = \frac{8\Psi_{i+1} - \Psi_{i+2}}{2(\Delta X)^2} \quad (3.29)$$

For the nodes located at corners as shown in Fig. 3.3-(a), -(b),

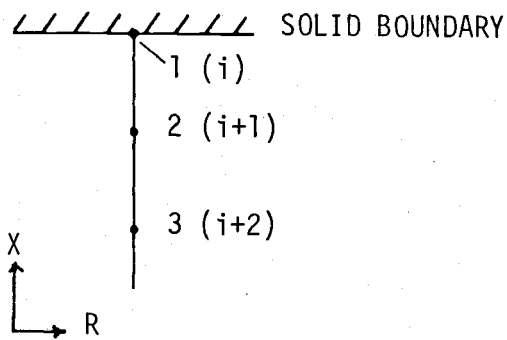


Figure 3.2 Nodal structure used for derivation of Eq. 3.29.

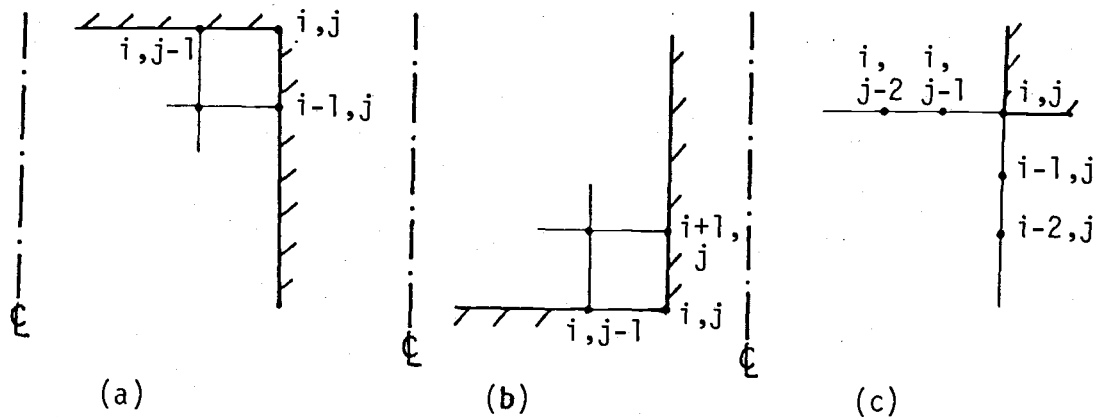


Figure 3.3 Nodal structure used for derivation of Eqs. 3.30 and 3.31.

and -(c), the following numerical expressions are used:

$$\Xi_{i,j} = 0 \quad (3.30)$$

for the nodes shown in Fig. 3.3-(a) and -(b), and

$$\Xi_{i,j} = \frac{1}{4R^2} \left(\frac{8\Psi_{i-1,j} - \Psi_{i-2,j}}{(\Delta X)^2} + \frac{8\Psi_{i,j-1} - \Psi_{i,j-2}}{(\Delta R)^2} \right) \quad (3.31)$$

for the nodes shown in Fig. 3.3-(c). The reason behind Eq. (3.30) is that, since Eqs. (3.26), (3.27), or (3.28) are applied for these corner nodes, Ψ -terms become zero since they are zero at solid walls. Eq. (3.31) is an average of Eqs. (3.26) and (3.28).

3.2.3 Vorticity and Stream Function Relation

Eq. (3.5) expresses the relationship between the vorticity and the stream function within the system. This equation is used to calculate stream function values at each node, provided that the vorticity values for all nodes have been previously calculated.

The conversion of Eq. (3.5) is rather straightforward. The second and third terms on the right hand side of this equation are expressed using the second order central difference equation, Eq. (3.7), and the first term by a first order central difference formulation, Eq. (3.8). The converted equation takes the following form:

$$\Xi_{i,j} R^2 = \frac{1}{R} \left(\frac{\Psi_{i,j-1} - \Psi_{i,j+1}}{2(\Delta R)} \right) + \frac{\Psi_{i,j+1} - 2\Psi_{i,j} + \Psi_{i,j-1}}{(\Delta R)^2} + \frac{\Psi_{i+1,j} - 2\Psi_{i,j} + \Psi_{i-1,j}}{(\Delta X)^2} \quad (3.32)$$

Since this equation is used for calculating stream function values at each node, it is, in actual use, rearranged to give $\Psi_{i,j}$.

The boundary values for $\Psi_{i,j}$ are set to zero which indicates that the boundaries involved here are all solid or symmetric types.

3.2.4 Stream Function Equations

Eq. (3.4) which is used to calculate two-component velocities at each node, is numerically expressed here.

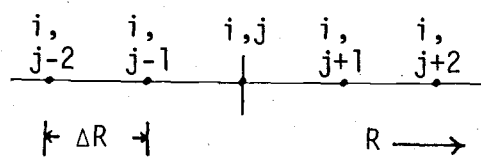
For internal nodes, a four-point Taylor series expansion about the node (i,j) , (see Fig. 3.4) is used to arrive at the following numerical expressions for axial and radial velocities, respectively:

$$U_{i,j} = \frac{\Psi_{i,j-2} - 8\Psi_{i,j-1} + 8\Psi_{i,j+1} - \Psi_{i,j+2}}{12R(\Delta R)} \quad (3.33)$$

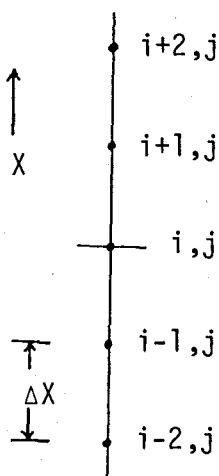
and

$$V_{i,j} = \frac{\Psi_{i+2,j} - 8\Psi_{i+1,j} + 8\Psi_{i-1,j} - \Psi_{i-2,j}}{12R(\Delta X)} \quad (3.34)$$

For nodes adjacent to boundaries, three-point Taylor series expansions are made about node (i,j) and the expressions obtained are:



a) For axial velocity



b) For radial velocity

Figure 3.4 Internal node arrangements for the velocity difference-equations.

$$U_{i,j} = \frac{\Psi_{i,j-2} - 6\Psi_{i,j-1} + 3\Psi_{i,j} + 2\Psi_{i,j+1}}{6R(\Delta R)} + \textcircled{c} \quad (3.35)$$

$$U_{i,j} = \frac{-2\Psi_{i,j-1} - 3\Psi_{i,j} + 6\Psi_{i,j+1} - \Psi_{i,j+2}}{6R(\Delta R)} \quad (3.36)$$

$$V_{i,j} = \frac{-\Psi_{i-2,j} + 6\Psi_{i-1,j} - 3\Psi_{i,j} - 2\Psi_{i+1,j}}{6R(\Delta X)} \quad (3.37)$$

and

$$V_{i,j} = \frac{2\Psi_{i-1,j} + 3\Psi_{i,j} - 6\Psi_{i+1,j} + \Psi_{i+2,j}}{6R(\Delta X)} \quad (3.38)$$

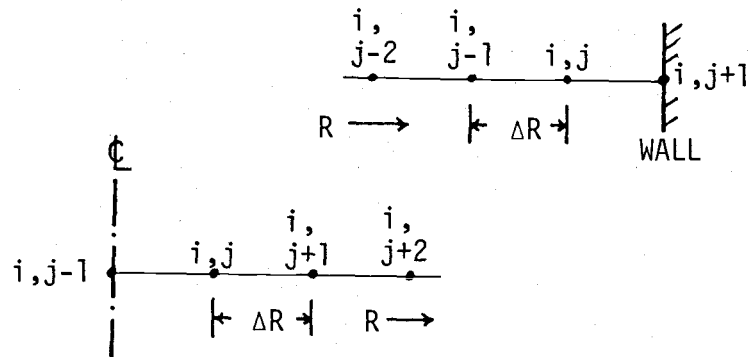
Eq. (3.35) is used at the nodes adjacent to the vertical wall and Eq. (3.36) at nodes adjacent to the center line. Eqs. (3.37) and (3.38) are used at nodes adjacent to the top and the bottom walls, respectively (see Fig. 3.5).

The method used in deriving the above six equations are very similar to those applied in obtaining Eqs. (3.20) and (3.21).

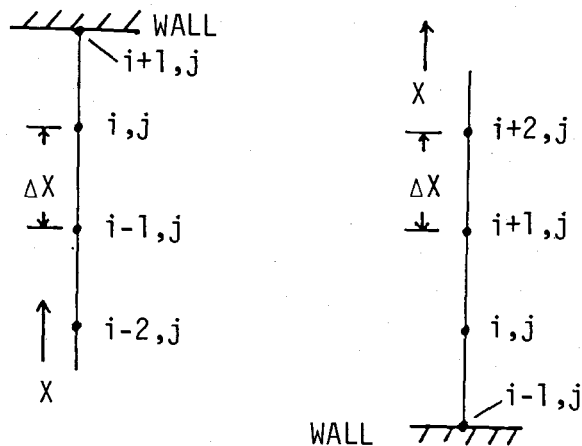
Due to the no-slip condition, both velocity components become zero at the solid boundaries. At the centerline the axial velocity can be calculated using Eq. (3.33) with the conditions, $\Psi_{i,j-1} = \Psi_{i,j+1}$ and $\Psi_{i,j-2} = \Psi_{i,j+2}$, due to the symmetrical nature of the stream lines. The radial velocity at the centerline is assumed zero which is also due to the symmetry of the stream lines about the centerline.

3.2.5 Average Heat Transfer Coefficient

The derivation of the average heat transfer coefficient has



a) For axial velocity



b) For radial velocity

Figure 3.5 Node adjacent to boundaries for velocity calculation.

been discussed earlier in Sec. 2.2.3, where Eq. (2.43) was derived, expressing the average Nusselt number, Nu_a . In the analytical part of this thesis, in Eq. (2.43), the cylinder wall temperature was the average of the top and bottom temperatures, as given by Eq. (2.41). However, in numerical work the average wall temperature can be easily calculated even though the wall temperature varies non-linearly. Thus, T_w, ave is not necessarily the mean of the top and bottom wall temperatures.

For this reason, Eq. (2.43) in Sec. 2.2.3 is written in the following manner:

$$Nu_a = \frac{a}{L} \int_0^L \frac{\left. \frac{\partial T}{\partial R} \right|_w}{T_w, ave - T_1} dX \quad (3.39)$$

where $\left. \frac{\partial T}{\partial R} \right|_w$ is the slope of temperature variation in the radial direction at the cylinder wall, T_w, ave is the mean wall temperature, and T_1 is the orifice temperature (see Fig. 1.1) which was established as a boundary condition in the theoretical solution, but, here, it is calculated prior to the Nu_a computation.

The integration in Eq. (3.39) is done by Simpsons' one-third rule which requires an odd number of nodes; this result in numerical form is as follows:

$$\int_0^L \frac{\left. \frac{\partial T}{\partial R} \right|_w}{T_w, ave - T_1} dX = \frac{\Delta X}{3(T_w, ave - T_1)} \left[\left. \frac{\partial T}{\partial R} \right|_{i,j} + 4 \left. \frac{\partial T}{\partial R} \right|_{i+1,j} + 2 \left. \frac{\partial T}{\partial R} \right|_{i+2,j} + \dots + 4 \left. \frac{\partial T}{\partial R} \right|_{m-1,j} + \left. \frac{\partial T}{\partial R} \right|_{m,j} \right] \quad (3.40)$$

where $\frac{\partial T}{\partial R}|_{i,j}$ are approximated by the following:

$$\frac{\partial T}{\partial R}|_{i,j} = \frac{11T_{i,j} - 18T_{i,j-1} + 9T_{i,j-2} - 2T_{i,j-3}}{6(\Delta R)} \quad (3.41)$$

Eq. (3.41) is the result of the four-node expansion, and the nodal structure for the above two equations is described in Fig. 3.6.

Eq. (3.41) approximates the temperature gradient at the wall in the radial direction, however, it requires that the four nodes be located very close to the wall. This means that, for a good approximation, the radius need be divided into at least 12 to 16 increments depending on the temperature profile. If, in case this many nodes cannot be accommodated, the following equation in place of Eq. (3.41) may provide a better approximation of the temperature gradient at the wall:

$$\frac{\partial T}{\partial R}|_{i,j} = \frac{T_{i,j} - T_{i,j-1}}{\Delta R} \quad (3.41a)$$

which is simply the backward difference equation at the cylinder wall.

Eqs. (3.39) through (3.41) are used in a computation in the following order: 1) first Eq. (3.41) or (3.41a) is used to compute $\frac{\partial T}{\partial R}|_{i,j}$ at each level of i with values of $T_{i,j}$ available from the three conservation equations, 2) $\frac{\partial T}{\partial R}|_{i,j}$ values are substituted into Eq. (3.40), and finally 3) the Nu_a value is computed by Eq. (3.39).

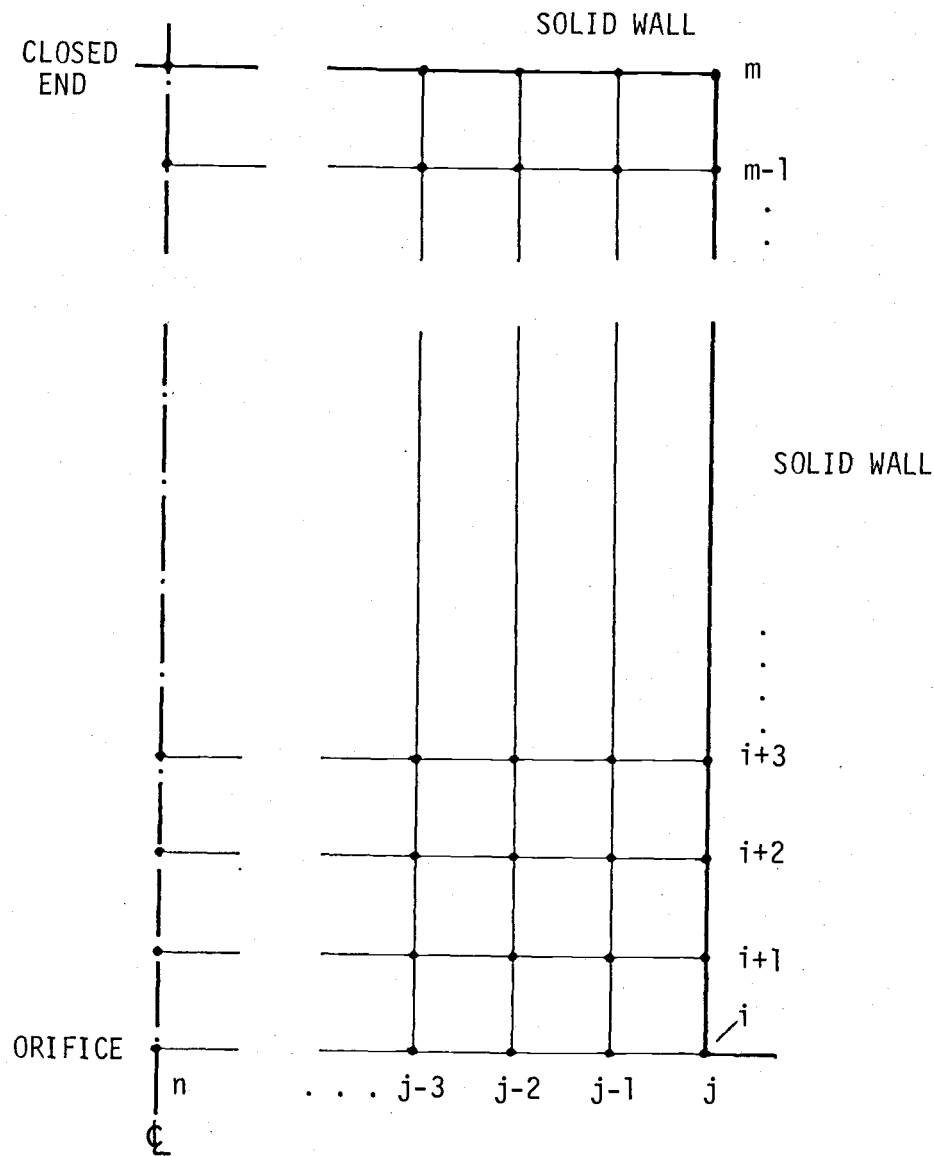


Figure 3.6 Nodal structure used for Eqs. 3.40, 3.41, and 3.41a.

If a local heat transfer coefficient, $h(x)$, is desired at each node along the wall the following expression can be used:

$$h(x) = \frac{k}{(T_{w,\text{ave}} - T_1)} \left. \frac{\partial T}{\partial R} \right|_W$$

where $\left. \frac{\partial T}{\partial R} \right|_W$ is again approximated by Eq. (3.41). The mean heat transfer coefficient, \bar{h} , is simply $\bar{h} = Nu_a k/a$, after having Nu_a calculated.

3.3 Programming Consideration

The finite difference equations discussed in Sec. 3.2 form n linear equations for n unknowns where n is the number of nodes.

For this type of problem, there are basically two numerical solution methods: 1) a matrix-inversion method (e.g. Gauss-Jordan elimination), and 2) an iterative method (e.g. Gauss-Seidel iteration). Depending on the size of program, the matrix-inversion method generally requires a computer with a large memory capacity, however, it may take much shorter computation time than the iteration method. On the other hand, the iteration method may require less memory capacity, but requires a large computation time. The matrix-inversion method involves more complex programming, but can yield a more accurate computed result than the other. A relatively simple computer program is associated with the iteration method, from which one may obtain some results on each run although it may be not so accurate as that of the matrix-inversion method.

After considering the above factors associated with the two methods, the author chose to apply Gauss-Seidel method (iterative

method) for this problem. The reasons for this choice were;

a) availability of PDP-11/10 computer in the Department of Mechanical Engineering at Oregon State University with a rather limited memory capacity, b) modification in the number of nodes or the shape of the domain to be analyzed by the computer program may be easily accomplished and c) each iteration step can be approximated as a time change of the system such that transient results can be obtained, even though the program is written for the case of a steady-state problem.

3.3.1 Gauss-Seidel Iteration Method

The first step in applying the Gauss-Seidel Method to this problem was to modify the numerical equations which were developed in Sec. 3.2 so that the variables of interest were equated to the rest of the variables and constants; that is to re-write each of the equations developed in Sec. 3.2 to the following form (p. 300 of Ref. [35]):

$$x_{i,k} = \sum_{j=1}^{i-1} a_{i,j} x_{j,k} + \sum_{j=i+1}^n a_{i,j} x_{j,k-1} + v_i \quad (3.42)$$

for $1 \leq i \leq n$ and $1 \leq k$. In this equation a 's are the coefficients and v_i are the constants. When $i=1$, $\sum_{j=1}^{i-1} a_{i,j} x_{j,k}$ is interpreted as zero and when $i = n$, $\sum_{j=i+1}^n a_{i,j} x_{j,k-1}$ likewise interpreted as zero.

All numerical equations in this form are expressed in Appendix A, also each equation is explained with its source, applicable nodes, and some restrictions.

The basic idea in the Gauss-Seidel iterative method is that, at each node, the variable of interest is calculated using values of that variable at adjoining nodes, then this newly calculated value replaces the previous value at this node in all subsequent calculations. This is done successively. Because of this feature, Gauss-Seidel iterative method is very often called the successive displacement method as opposed to the simultaneous displacement method of Jacobi's iteration. This procedure is repeated for all nodes until a satisfactory convergence is met. A detailed description of this method can be found in Refs. [35,36,39,40].

A sufficient condition for the convergence of this method is that the coefficient matrix is strictly (row) diagonally dominant or is positive definite [36,35]. The coefficient matrix of this problem is the matrix whose elements consist of coefficients, a's, in Eq. (3.42), or the coefficients, b's, when Eq. (3.42) is applied to n node and is re-written in the following form [41]:

$$\begin{aligned}
 & b_{1,1}x_{1,1} + b_{1,2}x_{1,2} + \dots + b_{1,n}x_{1,n} = c_1 \\
 & b_{2,1}x_{2,1} + b_{2,2}x_{2,2} + \dots + b_{2,n}x_{2,n} = c_2 \\
 & \vdots \\
 & b_{n,1}x_{n,1} + b_{n,2}x_{n,2} + \dots + b_{n,n}x_{n,n} = c_n
 \end{aligned} \tag{3.42}$$

Thus, in order to satisfy the above convergence condition for this problem, the first row elements, for example, must satisfy the following condition:

$$b_{1,1} > b_{1,2}, b_{1,3}, b_{1,4} \dots \text{ or } b_{1,n}$$

and for the second row,

$$b_{2,2} > b_{2,1}, b_{2,3}, b_{2,4} \dots \text{ or } b_{2,n}$$

and so on. It is also important that no element in the principal diagonal of the above matrix have a value of zero.

Torrance [26] and Barakat [24] state that the following inequality conditions ensure the stability of their system:

$$\Delta X \leq \frac{8K}{|U|}, \quad \Delta R \leq \frac{8K}{|V|} \quad \text{Ref. [26]} \quad (3.43)$$

$$\Delta X \leq \frac{2K}{|U|}, \quad \Delta R \leq \frac{2K}{|V|} \quad \text{Ref. [21]} \quad (3.44)$$

Both Refs. [21] and [26] applied the above inequalities to a transient case of natural convection in cylindrical enclosures. The only difference between these two sets of conditions is that in Ref. [21] the result was obtained empirically and the latter set was derived by examining central difference equations for non-linear terms.

3.3.2 Mesh Configuration and Calculation Sequence

The mesh configuration used for this numerical problem is shown in Fig. 3.7. Each node is specified by (M,N) where M and N specify axial and radial directions, respectively. The reservoir

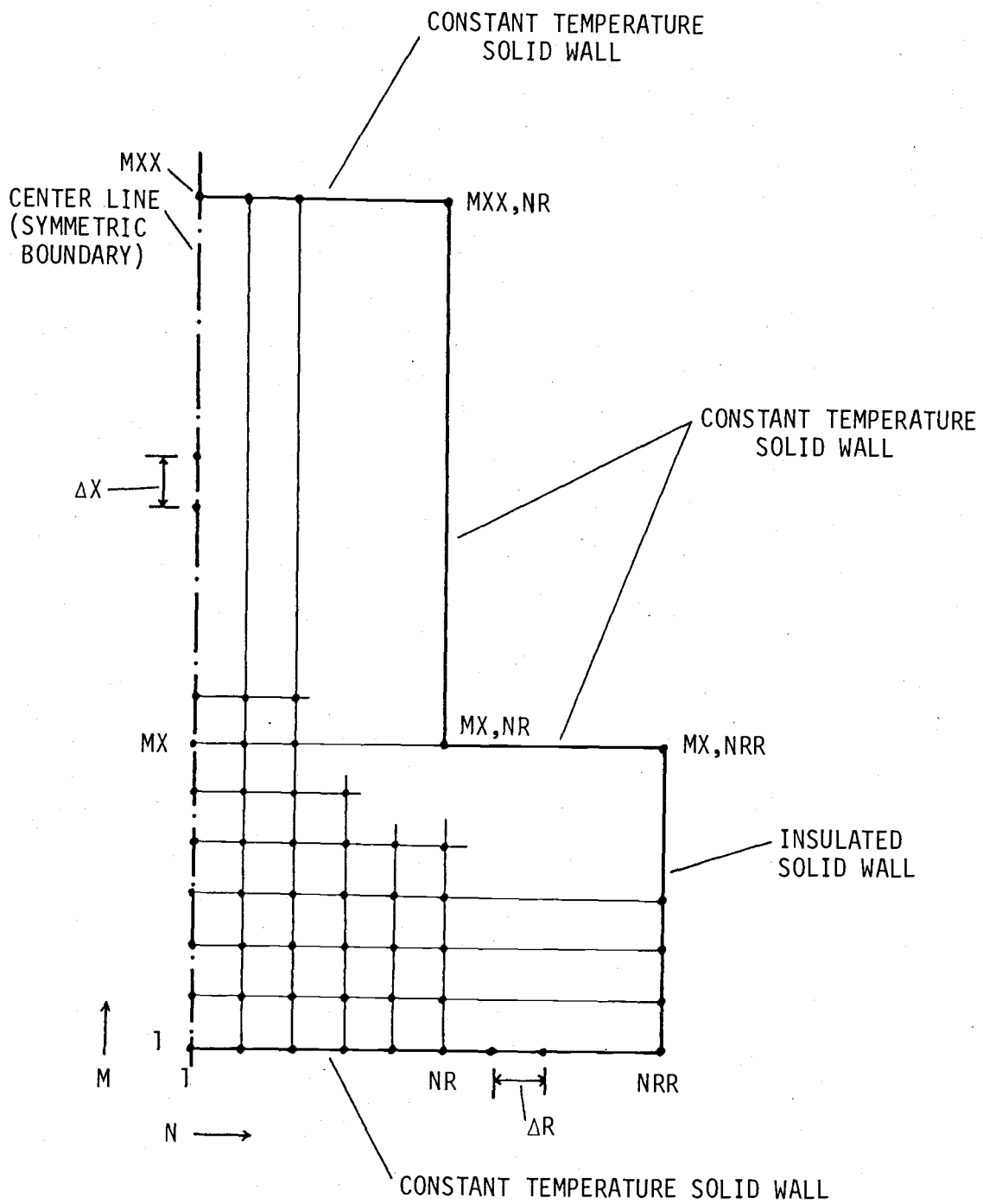


Figure 3.7 Mesh configuration.

section is considered to be $1 \leq M < MX$ and $1 \leq N \leq NRR$, while the fluid column (or cylinder) is defined by $MX < M \leq MXX$ and $1 \leq N \leq NR$. The total number of nodes used is, thus, $(MXX)(NR) + (MX)(NRR - NR)$. The magnitudes of MX, MXX, NR, and NRR must be specified by the user before each run of the program. The limits of MXX and NRR that one can specify depend on two factors: 1) the amount of computation time that the user can afford, and 2) the storage capacity of the machine being used. In the present numerical work values of MXX and NRR were limited by storage capacity, and it was found that the largest (MXX, NRR) that PDP-11/10 can tolerate was (35, 10). If a larger than 35×10 node size were required, one might either shorten the program to create extra storage area, or use a larger machine.

The computation sequence which was applied over the aforementioned nodal system is as follows (see Fig. 3.8 for the program flow chart and Appendix B for the Fortran coded program):

- 1) Boundary conditions and necessary constants are specified, and all nodes are given initial values.
- 2) The temperature calculation is performed for all nodes using the most recent values of T, U, V.
- 3) The vorticity calculation is performed for all nodes using the temperature values from step ②).
- 4) Stream function values are approximated at each node using the vorticity values calculated at the last step (an acceleration method is applied at this step).
- 5) The axial and radial velocities are approximated at each node using the stream function values calculated in the last step.

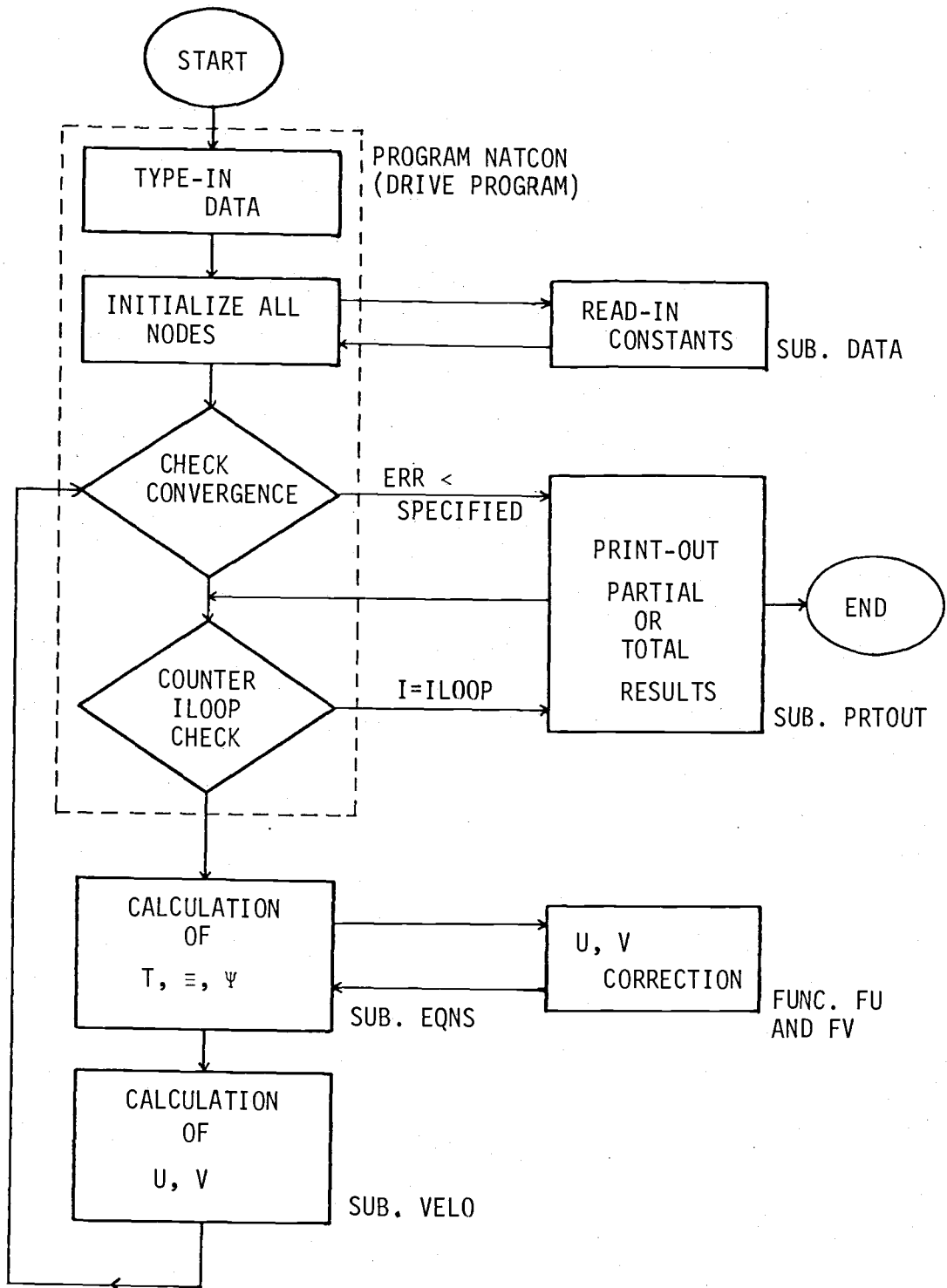


Figure 3.8 Flow chart of the program NATCON.

- 6) The error in each variable is calculated by comparing the previously calculated value and the current value at one specified node - currently which is at node (MX, 3) representing the orifice section, and if the error of any one of the variables exceeds the specified maximum error, ERR, the program returns to step (2).
- 7) If either the convergence check in Step (6) is acceptable, or the specified number of iterations, ILOOP, have been carried out, program execution stops.

Each step of the above computation sequence is guided by the driving program (main program, NATCON). Steps (2) through (4) are carried out in SUBROUTINE EQNS, and step (5) is in SUBROUTINE VELO. The acceleration scheme for fast convergence applied at step (4) is that of Successive Over Relaxation, SOR.

3.3.3 Nusselt Number Calculation

After the variables were calculated by the program NATCON as described in the previous section, one can use the program NUSSLT (see Appendix B for the Fortran coded program of NUSSLT) to compute the local heat transfer coefficients, H(I); the average heat transfer coefficient, HAV; and the average Nusselt number based on the cylinder radius, ANU.

The numerical formulation for this program was explained in Sec. 3.2.5. As described in Sec. 3.2.5, since the Simpson's rule is used for the integration scheme, one must use an odd number of nodes (which must be typed in by the user) along the cylinder wall. Other necessary information to execute this program is explained

in the comment section of the program NUSSLT.

This program was originally written as a sub-program within NATCON. However, as the number of nodes increased in NATCON, the computer was unable to accept the program because of its limited storage capacity. The sub-program was then separated from NATCON and made into an independent program, NUSSLT. The storage problem was thus alleviated, however, the user must now transfer necessary information from the output of NATCON to the input of NUSSLT manually, and it must be executed separately.

3.3.4 Validation of Numerical Method

In order to investigate the validity of this particular numerical method, the numerical solution was compared with that of Ref. [26]. In Ref. [26], several numerical procedures suited for natural convection were presented and their results were compared with experimental results.

For comparison purposes, the numerical program was run using identical boundary conditions to those applied by Ref. [26].

The example problem for this purpose was natural convection within a cylindrical enclosure with a circular heat source located at the center of the bottom boundary. Half of a vertically-cut cross section of the cylinder was divided into an equal-size grid creating total of 121 nodes. A unit temperature was assigned to the bottom center node for the heat source, while the rest of the boundary nodes were assigned zero temperature. Thus, natural convection was induced by the temperature (or potential) difference between the heat-source and that of the rest of the boundary (see

Fig. 3.9). When the air was used as a medium, established condition represents $\text{Gr} (=g\beta(T_1 - T_0)a^3/\nu^2) \approx 1 \times 10^5$.

Solution of the problem described above was obtained after 91 iterations. Then the steady-state streamline and temperature fields were compared with those of Ref. [26] as shown in Figs. 3.10 and 3.11. As seen in these two plots, the results of the current numerical scheme yielded a solution almost identical to those of Torrance. The most obvious difference is in the general shape of the isotherms.

In discussing different methods, Torrence remarked that the solution of Method I turned out to be the least accurate among the four methods he examined. The difference between isotherms of Method I compared with those from other methods including the current work was partially due to the treatment of the vorticity boundary condition for the center line (or line of symmetry) nodes. Method I of Torrence simply assigned zero vorticity to these nodes, however, more precise vorticity values were applied in the other methods, as given by Eq. (3.18).

3.3.5 Effects of Reservoir Boundary Condition and Size

Although the main objective of this work was to investigate natural convection within a circular cylinder standing above a cylindrical reservoir, the effect of the reservoir boundary condition and size compared with that of the column of fluid within the cylinder must not be ignored. Thus, in order to specify a reservoir whose influence on the fluid column situated above it is independent of its boundary conditions and relative

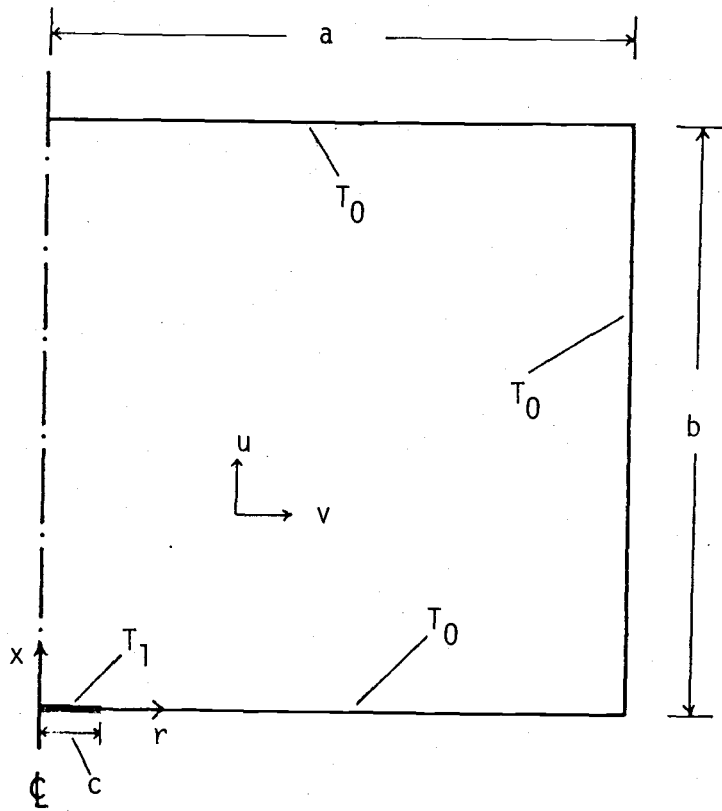
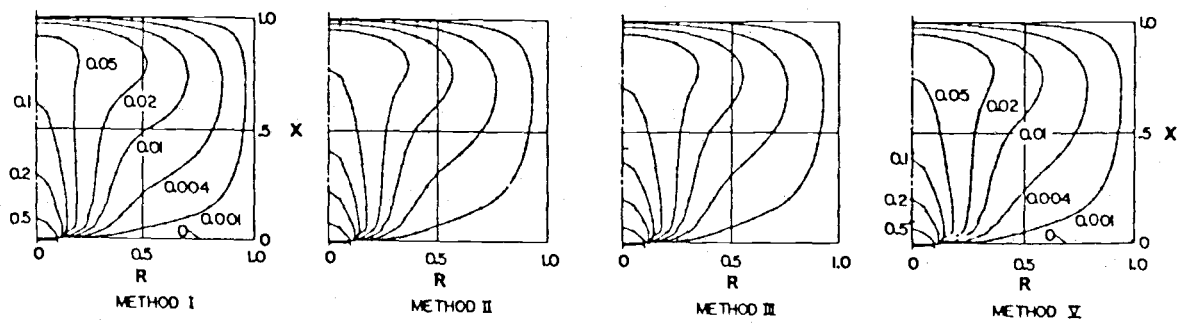
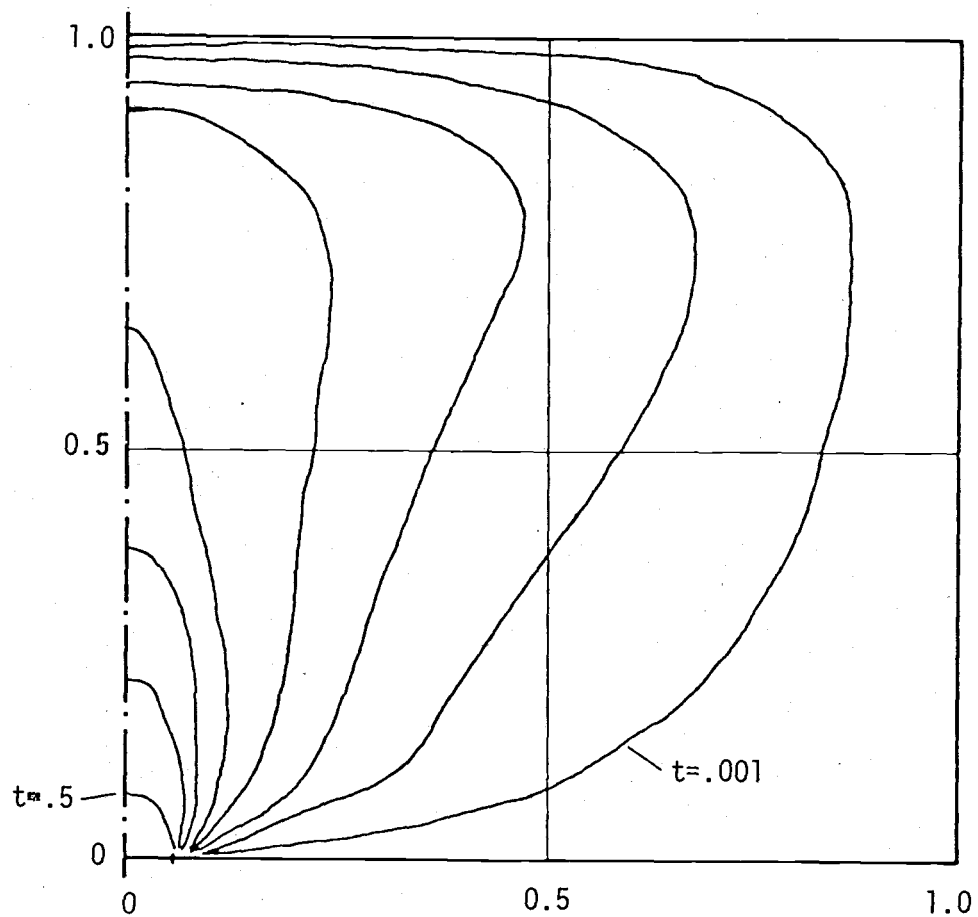


Figure 3.9 The configuration of the problem used by Ref. [26] where $a=b$, $c/a=0.1$, and $T_1 > T_0$.

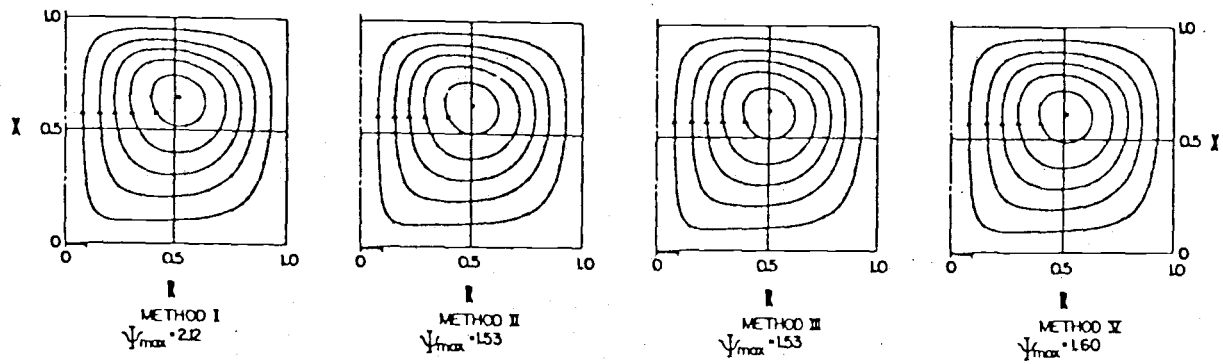


a) Torrance



b) Present Study

Figure 3.10 Isotherms of (a) Ref. [26] and (b) the current study.



a) Torrance

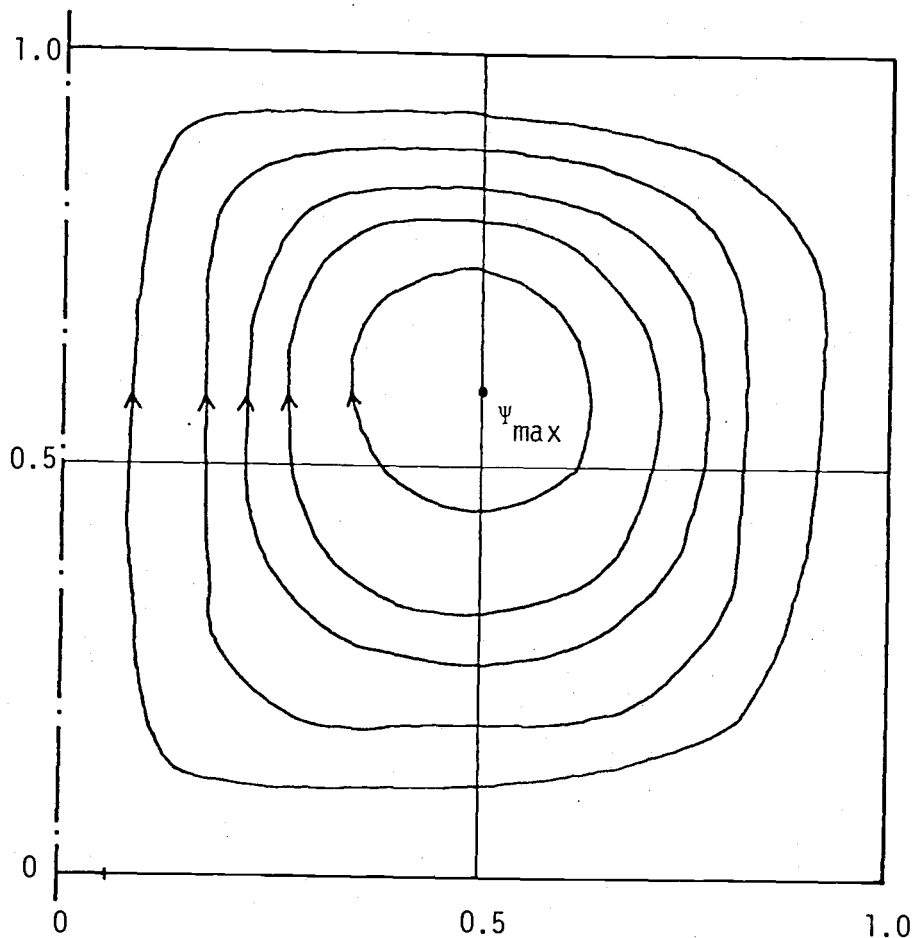
b) Present Study ($\Psi_{\max} \sim 1.45$)

Figure 3.11 Streamlines of (a) Ref. [26] and (b) the current study.

size, three kinds of temperature boundary conditions were compared. Next, the dimensions of the reservoir having no effect on behavior within the cylinder was determined. In the course of this evaluation, and efficiency of the numerical program was also considered.

For the evaluation of temperature boundary conditions in the reservoir, the following three cases were examined:

Case I - All boundaries at uniform and constant temperatures.

Case II - The vertical wall insulated, the rest same as above.

Case III - The top boundary at uniform and constant temperature, the rest insulated.

Isotherms and streamlines resulting for the above three cases were obtained using the current numerical program and are plotted in Figs. 3.12 and 3.13. As seen in these figures, the first two cases yielded similar trends for both isotherms and streamlines within the test section (or the top cylinder), Case III being least like the rest. The reason for this was that the two insulated boundaries of Case III likely generated the most complex flow pattern as seen in Fig. 3.13. Case II required the least number of iterations to reach steady state, indicating it to be the most stable boundary condition among the three cases. For this reason, the boundary condition of Case II was chosen for the all subsequent runs of the current numerical program. The program, NATCON, given in App. B-1, is still provided with these three options for reservoir boundary conditions.

To evaluate the effect of reservoir size on fluid behavior in the cylinder, the first case tried was to find the correlation between the radius and length of the reservoir to those dimensions

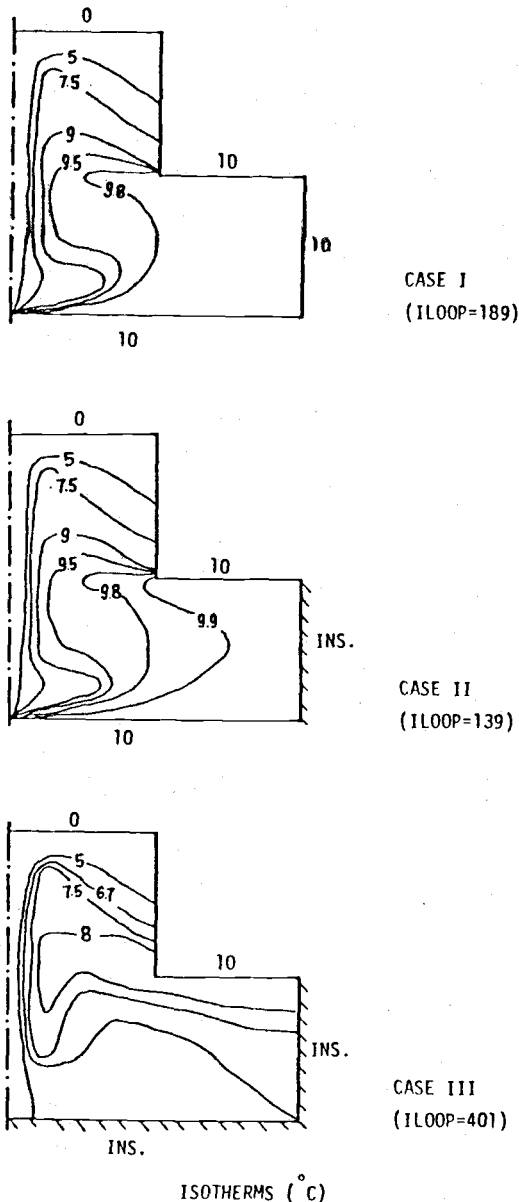


Figure 3.12 Comparison of the three temperature boundary conditions.

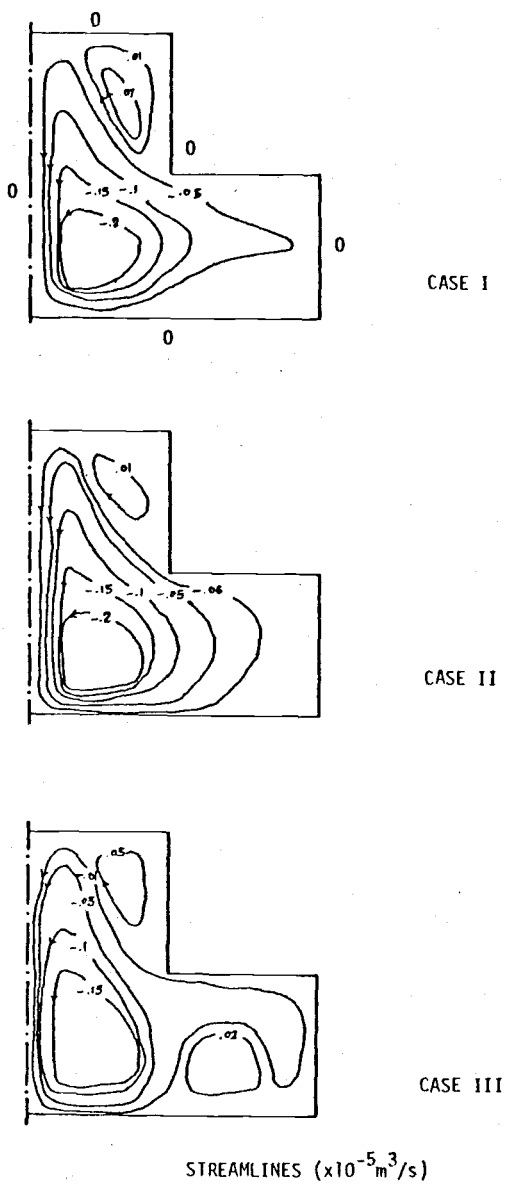


Figure 3.13 Comparison of the three temperature boundary conditions of the reservoir (see Fig. 3.12)

of the cylinder for a constant reservoir wall temperature (see the related variables in the diagram described at the top portion of Fig. 3.14). The radius-ratio, a_{RES}/a , and the length-ratio, L/L_{RES} , were varied from 1.33 to 2.67 and from 1.0 to 3.5, respectively, while the reservoir Grashof number, Gr_{RES} , was maintained at the constant value of 1800. (The reservoir Grashof number is indicative of the reservoir wall temperature relative to the cylinder boundary temperature.) Results of these runs are shown in the three curves plotted in the bottom portion of Fig. 3.14. The indication is that the orifice temperature represented by Gr_{RES} is no longer influenced by the change in reservoir size when L/L_{RES} is 1.0 or greater. For a constant L/L_{RES} a change in a_{RES}/a did affect the orifice temperature slightly.

The next case examined was to determine if the same result would be obtained with the reservoir wall temperature increased at $a_{RES} = 2a$. Results of these runs are described by the remaining curves in Fig. 3.14, indicated by $Gr_{RES} = 11000, 33000$, and 88000 . These three curves indicate that the orifice temperature becomes insensitive to the change of L/L_{RES} when L/L_{RES} is larger or equal to 1.0.

Therefore, when the $L/L_{RES} > 1$ and the cylinder wall is assigned a uniform and constant temperature, one can expect a very small effect of reservoir size for a fixed reservoir wall temperature.

The last test of reservoir-size effects was to examine the situation where the cylinder-wall temperature increased linearly from the cylinder-top temperature of T_0 to the reservoir wall

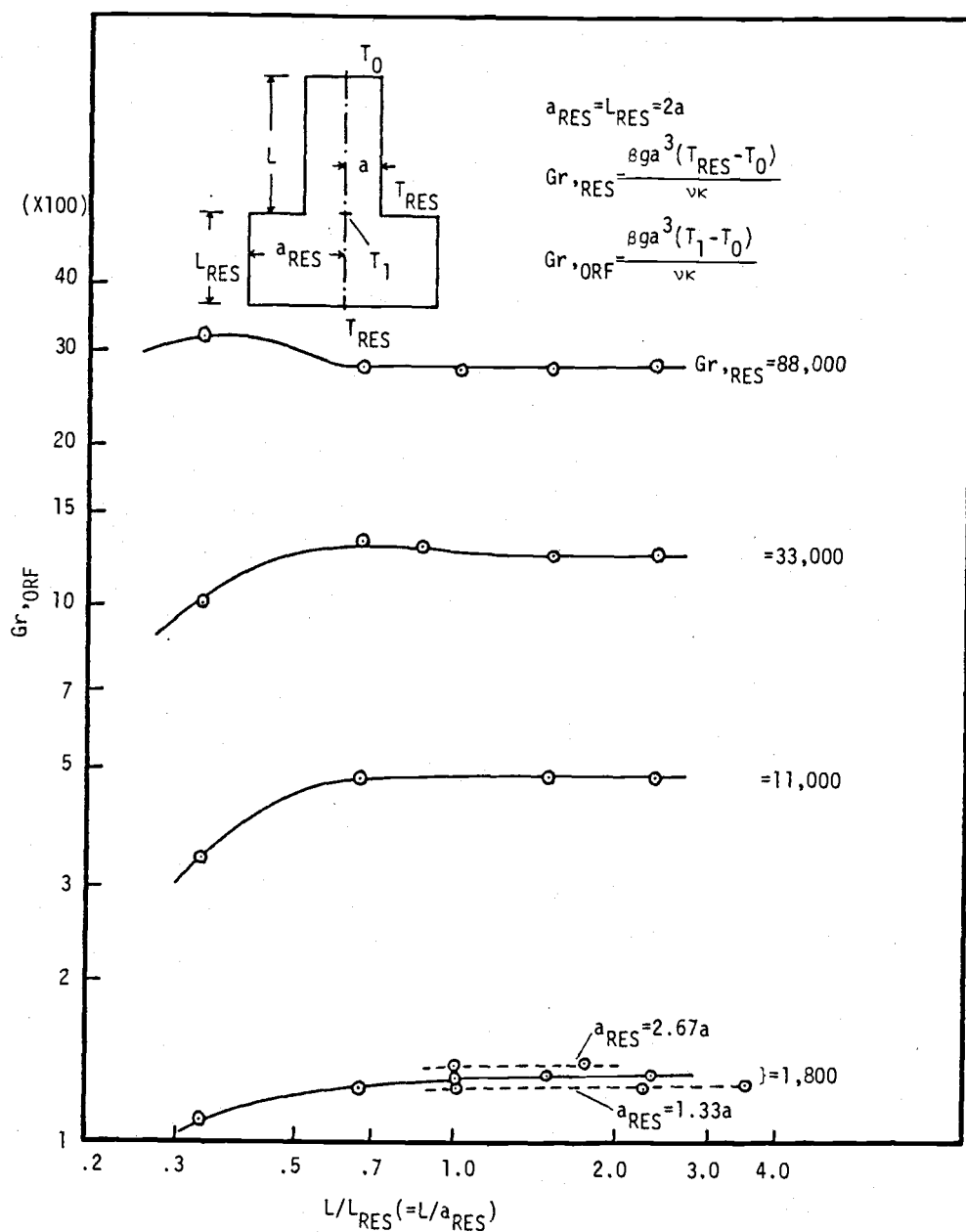


Figure 3.14 Effect of L/L_{RES} at $Ra_A=0$.

temperature of T_{RES} as illustrated by the diagram in Fig. 3.15. Again, the radius-ratio, a_{RES}/a , was held constant at a value of 2.0. The new variable considered in this case was the temperature-gradient parameter, A , which is included in the non-dimensional parameter, Ra_A . The results of this test are plotted in Fig. 3.15. This plot indicates the general variation of Gr_{ORF} with L/L_{RES} to be very similar to the case of constant cylinder-wall temperature. Also, values of Gr_{ORF} each Gr_{RES} approach zero indicating that the orifice temperature, T_1 , is approaching the cylinder-top temperature, T_0 . The major difference between this case and the previous one was that a cylinder with a temperature gradient along its wall required a much large value of L/L_{RES} for Gr_{ORF} to reach its asymptotic value. Also, for this case the orifice velocity never reached a constant value. In the previous case where the cylinder wall was at the constant temperature, the orifice velocity reached a constant value before Gr_{ORF} did.

Another important fact shown in Fig. 3.15 is that when $Gr_{RES} = 11,000$ was tried for several L/L_{RES} values, the numerical solution failed to converge for Gr_{ORF} larger than approximately 8000 and L/L_{RES} larger than 1.0. Studying every 100th iteration from the computer indicated that two similar, but not identical, flow configurations to exist after a number of iterations. Two questions come to mind at this point; 1) Is this phenomenon due to a numerically caused instability within the computer program? or 2) In actuality does this situation exist and the numerical program simply simulated it? This situation will be discussed further in the latter part of this chapter.

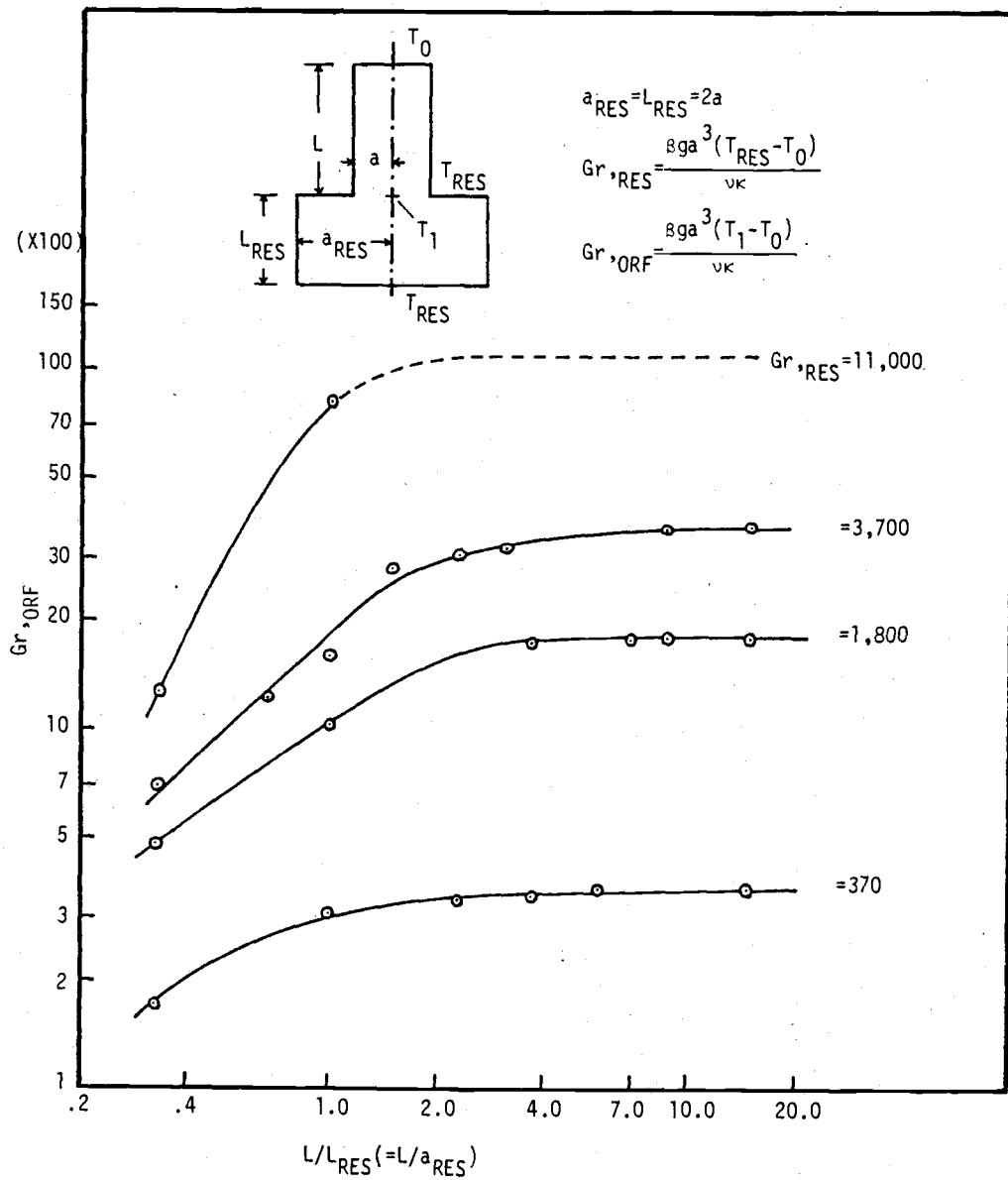


Figure 3.15 Effect of L/L_{RES} at $Ra_A \neq 0$.

3.3.6 Convergence of the Numerical Solution

The major convergence criterion for the numerical solution method employed here is, as discussed in Sec. 3.3.1, to have the coefficient matrix be diagonally dominant. This condition was examined for all nodal equations derived in Secs. 3.2.1 through 3.2.4; two boundary vorticity equations were found to be violating the above convergence criterion. Those are the two equations generated by Eq. (3.19) for the following two corner nodes; ($X=0, R=0$) and ($X=L, R=0$). For this reason, these two equations were replaced by the second option as discussed in Sec. 3.2.2, that is $\Xi(0,0) = \Xi(L,0) = 0$, which in turn satisfied the convergence criterion. Several test runs were carried out with these supposedly converging and non-converging coefficient matrices, and their solutions were compared. The result was that the both matrices did converge, and no significant differences were found between the two solutions. The probable reason for this unexpected result was that the non-converging equations were confined to the two equations which were written for the vorticity at $(0,0)$ and $(L,0)$, thus their effect was suppressed by the remaining stable equations. Although no clear difference between the two were found in the test runs, the supposedly converging boundary conditions, $\Xi(0,0) = \Xi(L,0) = 0$, were employed here rather than the boundary conditions generated by Eq. (3.19).

The mesh size (or the distance between two nodes) is another parameter influencing convergence of a finite-difference numerical solution. This matter was briefly discussed in Sec. 3.3.1 and two

sets of expressions for estimating the maximum ΔX and ΔR for the convergence were given. If the inequality expressions given in Sec. 3.3.1 (Eqs. (3.43) and (3.44)) are converted to give the following equations:

$$C_U = \Delta X |U_{\max}| / \kappa \quad (3.45)$$

$$C_V = \Delta R |V_{\max}| / \kappa \quad (3.46)$$

where C_U and C_V are the mesh sizing factors then, according to Eq. (3.43), the maximum C_U or C_V one can use for the maximum mesh size, ΔX or ΔR , is 8.0. After making six runs with the current numerical program, however, (see Table 3.1), it was found that C_U could be as large as 1277.7 and the system would still converge within the cylinder. The inequalities given by Eqs. (3.43) and (3.44) which are essentially derived or empirically obtained for transient conditions, apparently do not apply to steady state cases. Nevertheless, the author continued this investigation and found an interesting result. That is, under the assumption that C_U and C_V are also functions of some temperature variables, Eqs. (3.45) and (3.46) are divided by the square root of the modified Rayleigh number, $Ra_L^{\frac{a}{L}}$, to give:

$$C'_U = C_U / \sqrt{Ra_L^{\frac{a}{L}}} \quad (3.47)$$

$$C'_V = C_V / \sqrt{Ra_L^{\frac{a}{L}}} \quad (3.48)$$

Table 3.1 Numerical result of mesh sizing factors C_U and C_V for
 $\Delta x = .333$ and $\Delta r = .25$

$\Delta X (= \Delta R)$, cm	$ U_{max} $, cm/s	$ V_{max} $, cm/s	Ra_L^{α}	C_U	C'_U	C_V	C'_V
0.05	0.00962	0.00983	2.1×10^2	.334	.023	.342	.023
0.1	0.201	0.0558	4.1×10^3	13.99	.22	3.883	.061
0.3	1.03	0.22	1.5×10^5	215.0	.559	45.93	.119
0.6	1.64	0.372	1.2×10^6	684.8	.617	155.3	.140
0.9	2.04	0.485	4.2×10^6	1277.7	.624	303.8	.148
1.2	0.655	0.56	1.9×10^6	547.0	.393	467.6	.336

The result of using these equations is given in Table 3.1 showing that all six converging runs required C_U' and C_V' values to be less than unity. This finding indicates that, for a better estimation of maximum converging mesh size for steady-state natural convection, one may need to consider temperature variables as well as flow variables.

In order to accelerate the convergence of the current numerical solution, the successive-over-relaxation method (or often called S.O.R.) was applied strictly to the calculation of stream function, Eq. (3.5). The way the above method was used, can be illustrated by the following expression:

$$\psi^{n+1} = \bar{\alpha}\psi^n + (1-\bar{\alpha})\psi^{n-1} \quad (3.49)$$

where α is the relaxation factor, and ψ^{n+1} , ψ^n , and ψ^{n-1} represent, respectively, the stream function value to be used for the immediately following calculation, the current value, and the value from the preceding calculation. When $\bar{\alpha} = \frac{1}{2}$, Eq. (3.49) approximates the subsequent value to be the average of the current and the old values. When $\bar{\alpha} = 1$, it is the same as not applying the S.O.R. at all. When $\bar{\alpha} < 1$ or $\bar{\alpha} > 1$, future values assume a weighted average of the current and old values. The two states, $\bar{\alpha} < 1$ and $\bar{\alpha} > 1$, are often termed "under-relaxation" and "over-relaxation", respectively [36,40].

To investigate the effectiveness of the successive over-relaxation method applied here, the following nodal structure was used (see also the node information given in Fig. 3.7): 5 nodes

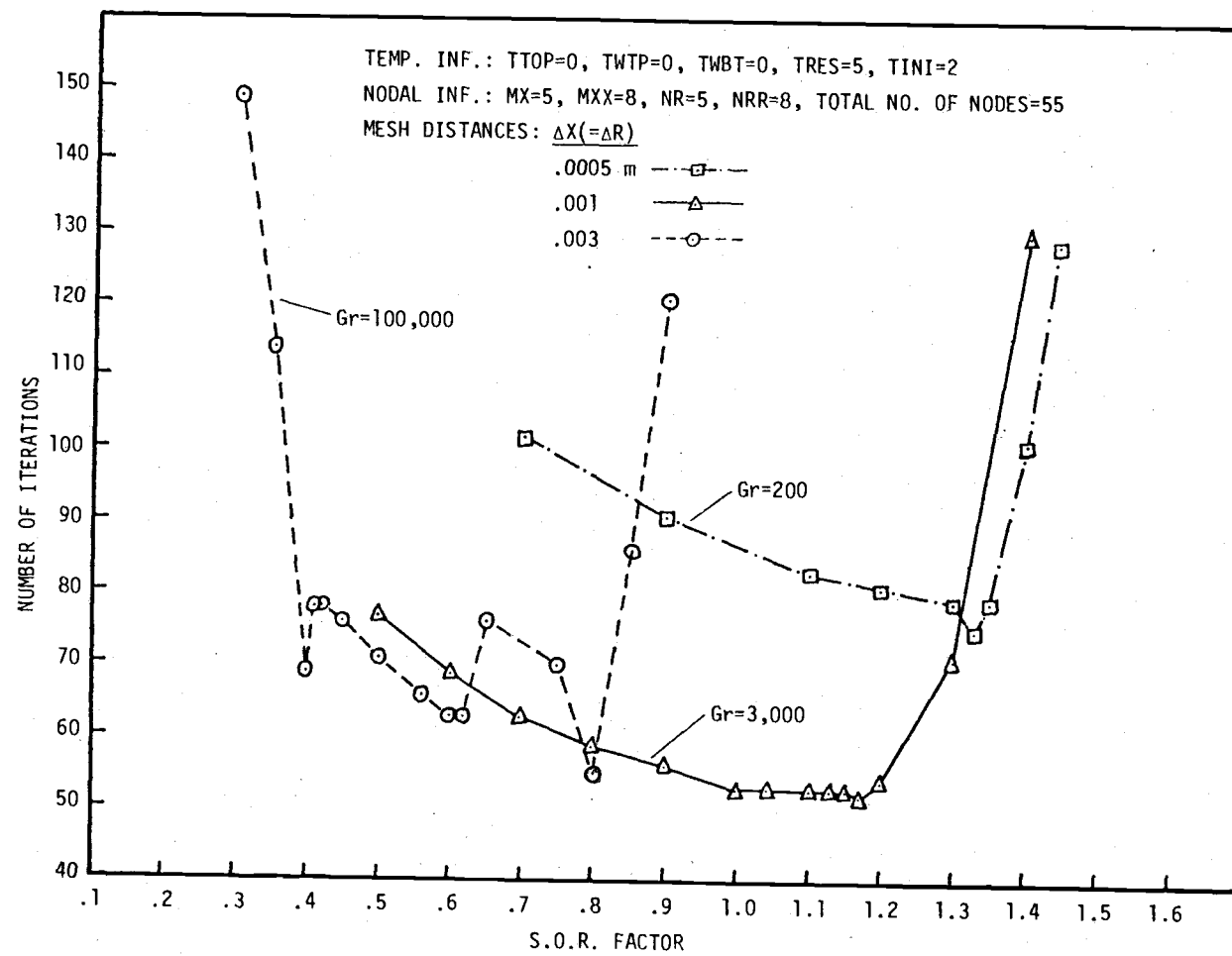


Figure 3.16 Required number of iterations for various S.O.R. factors and mesh sizes for the same nodal structure.

from Ref. [40],

$$\bar{\alpha} = 2/\left(1 + \sqrt{1 - \cos^2 \frac{\pi}{h}}\right) \quad (3.51)$$

which estimates the optimum relaxation factor for a square domain where h represents the mesh divisions. The domain of the current problem is neither square nor rectangular; however, when $p = 5$ and $q = 7$ (which is the approximate configuration tested here) are used in Eq. (3.50), it estimates the largest optimum relaxation factor to be 1.23 and the smallest to be 0.31. When $h=(5+7)/2$ is used in Eq. (3.51), the estimated optimum relaxation factor is 1.33. Therefore, the empirically found optimum-relaxation factors agree quite well with the theoretically estimated values as above. Hwang and Cheng [30], also applied the S.O.R. method in a natural convection study and their optimum relaxation factor ranged from 0.25 to 1.8 for a circular domain.

To show that the optimum relaxation factor is independent of the number of nodes (or how finely the domain is meshed) used three additional runs were made with the total number of nodes varying from 55 to 119. This result is plotted in Fig. 3.17 which clearly substantiates the point stated above. It also indicates that, although the optimum relaxation factor stays unchanged, more iterations are required for convergence as the domain is divided into a finer grid. This observation is logical since, with a finer mesh the total number of nodes on which the convergence must be made is increased.

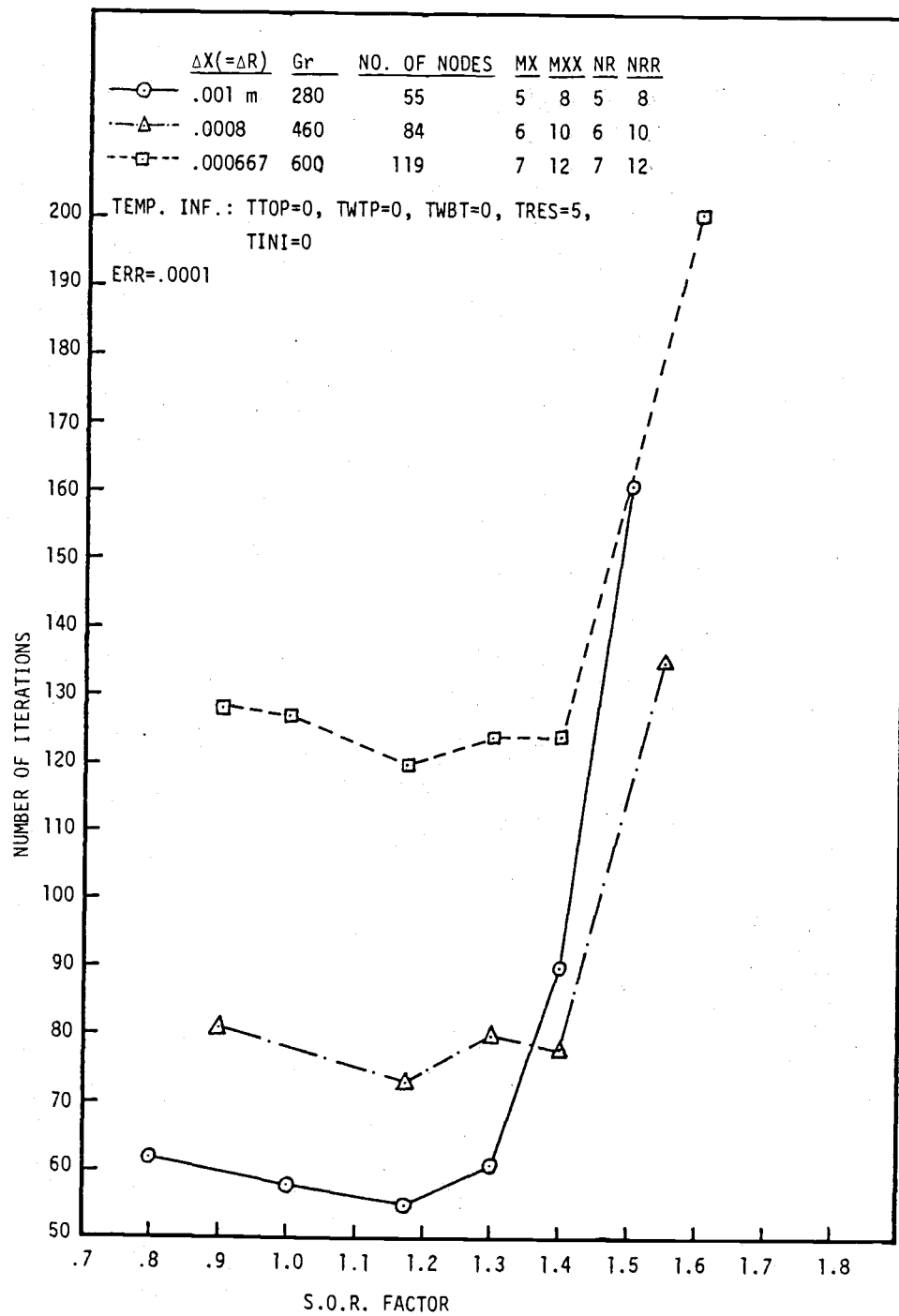


Figure 3.17 Required number of iterations for various mesh sizes and number of nodes for approximately the same G_r .

Finally, results are shown in Fig. 3.18 for S.O.R. factors; a) larger than, b) equal to, and c) smaller than optimum. In this case the temperature variation at a certain node is plotted against number of iterations. Also shown in Fig. 3.19 is a typical example of variations of the three variables when a too-large mesh distance is used and, in Fig. 3.20, the case is shown when an acceptable mesh distance is used.

3.4 Result of Numerical Study

We now present the results of a numerical study using the program which has been discussed in the previous portions of this chapter.

The three basic dimensionless parameters that are used for evaluating computated results, are; a) the aspect ratio of the cylinder, $AR=L/a$, b) a Rayleigh number based on the cylinder-wall temperature gradient, $Ra_A = \beta g a^4 A / \nu k$, and c) a modified Rayleigh number which is a product of Grashof number and the reciprocal of AR , $Ra_L^a = \beta g a^4 (T_1 - T_0) / \nu k L$. Here, Ra_A and AR are used as input variables, and Ra_L^a thus becomes the computed result or the output. The aspect ratio is one of the two dimensionless parameters found by non-dimensionalizing the governing equations (see Eqs. (2.8a), (3.3a), (3.5a), and (3.4a)). The other dimensionless parameter found in the above process is Prandtl number, which is maintained constant at 7.0 (comparable to that of water) throughout this work. To compare the results of this numerical work to the similarity solution (Chapter II), the boundary-temperature configuration of the cylinder is restricted to the one shown in Fig. 3.21.

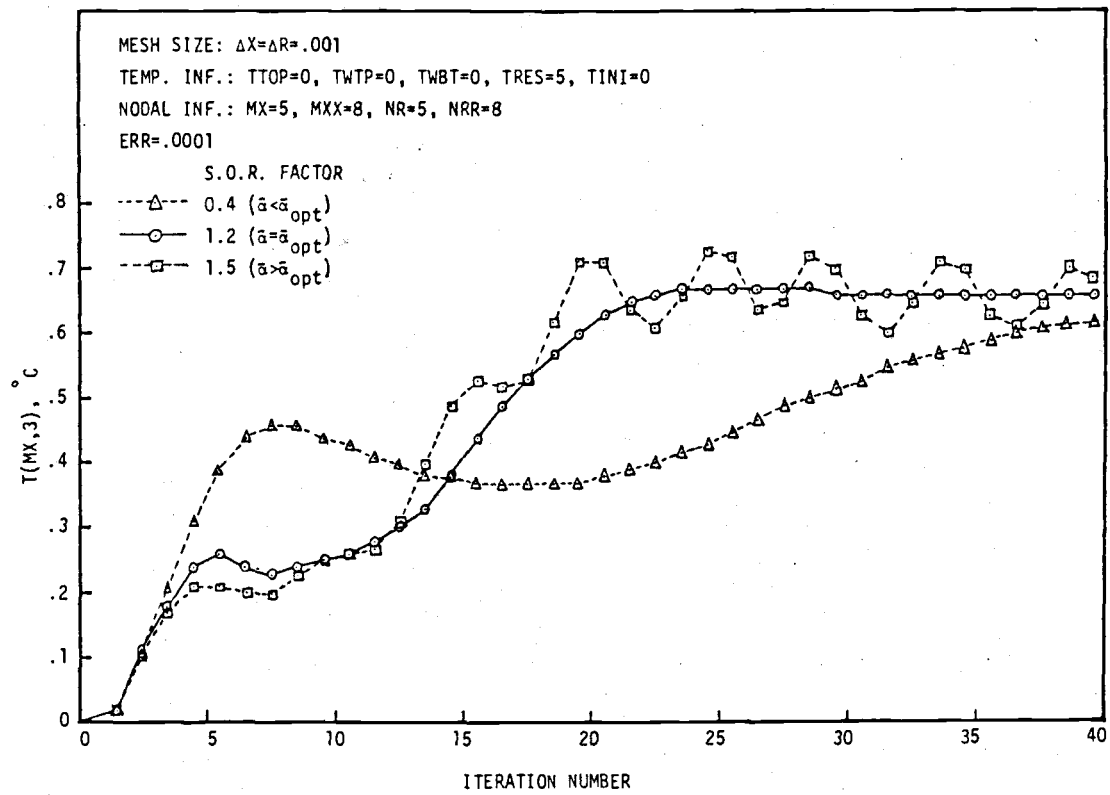


Figure 3.18 Comparison of the variation of temperature at a certain node when S.O.R. factor is larger, or smaller than the optimum FAC, or when it is equal to the optimum FAC.

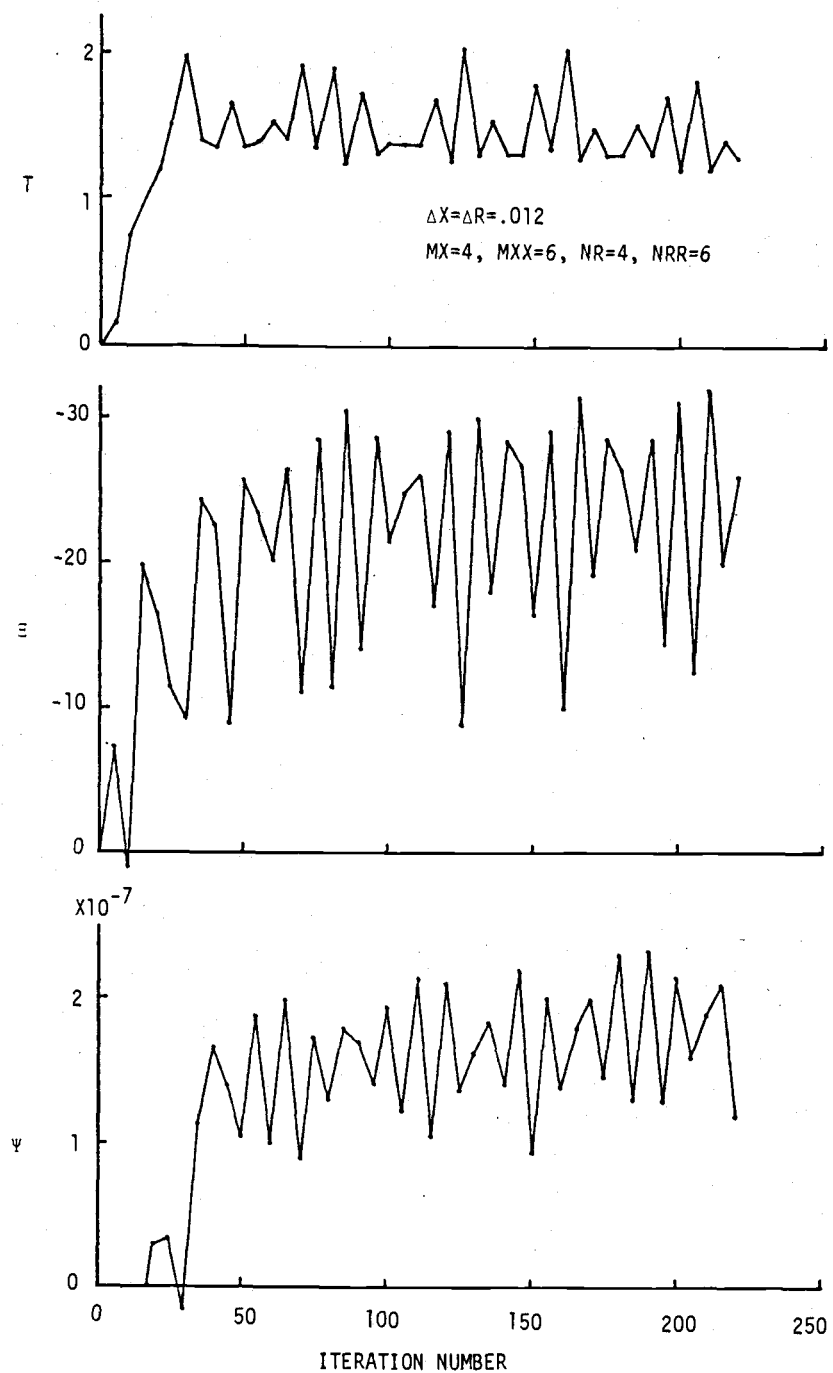


Figure 3.19 Typical variations of T , E , and Ψ when the numerical solution fails to converge due to excessively large mesh distances are used.

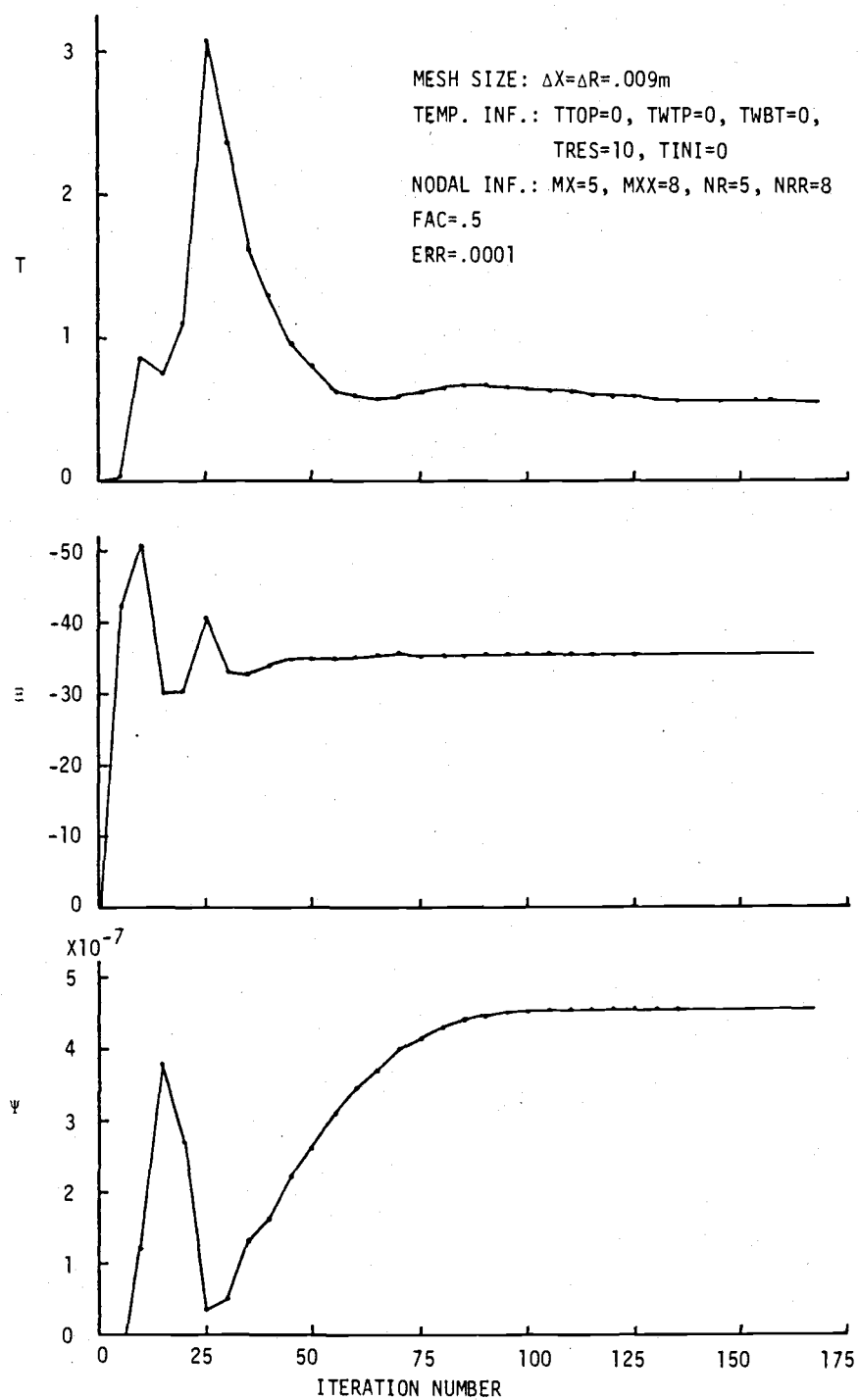


Figure 3.20 Typical variations of T , ϵ , and Ψ when the numerical solution converges.

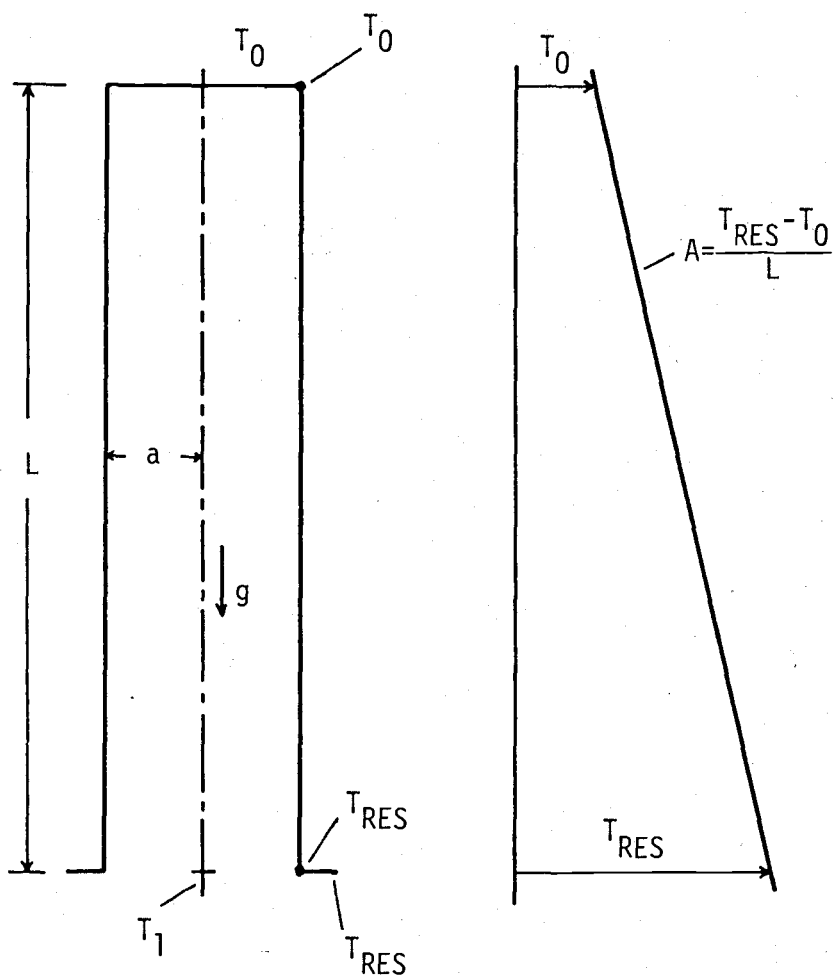


Figure 3.21 The boundary temperature configuration applied to the numerical study where T_0 is the coldest and T_{RES} is the hottest temperature of the system.

By doing so, one can ensure that the temperature of the top surface and that of the top of the cylinder are equal (no temperature jump is created); the same is true at the lower corner where the bottom of the cylinder joins the top horizontal wall of the reservoir. In this configuration, T_0 is always the coldest and T_{RES} is the hottest temperatures of the system, and thus the resulting orifice temperature, T_1 , must be $T_0 < T_1 < T_{RES}$. Also, because of the above restriction, Ra_A and Ra_L^a simply become the dimensionless representations of the wall temperature difference and the axial (or centerline) temperature difference relative to the coldest temperature, T_0 .

3.4.1 Flow Characterization

With the configuration described above, approximately 100 computer runs (see Table 3.2) were made using the PDP-11/10. Some representative computed results are plotted as Ra_A vs. Ra_L^a for several different AR's as shown in Fig. 3.22a through 3.22h. Also plotted on these figures is the superimposed curve for the similarity solution.

By inspecting each of these plots and comparing the results with the similarity solution, one can see that for AR = 4 through 35 within the Ra_A range of from 400 to 1300, the solutions are virtually the same. Although the plot of AR = 40 shows some agreement with that of the similarity solution, an inspection of the flow structure indicates otherwise; this is discussed in detail later. The aspect ratio is roughly divided into the

Table 3.2 Summary of Computer Runs

Run No.	AR	Ra _A	Ra _L ^a	FAC	I
01	.25	896	501	.3	115
02	.5	339	202	.3	141
03	.5	883	507	.3	153
04	.67	550	256	.5	62
05	.83	28200	3260	.6	114
06	1.0	13600	2280	.7	94
07	1.0	643	349	.3	158
08	1.0	99	70	1.0	145
09	1.0	418	260	1.15	153
10	1.0	895	427	1.2	101
11	1.0	1290	536	1.3	99
12	1.0	1990	703	1.3	111
13	1.3	275	198	.5	62
14	2.0	43	37	1.0	134
15	2.0	217	180	.55	151
16	2.0	434	325	.8	116
17	2.0	869	493	.8	106
18	2.0	1300	622	.8	124
19	2.0	2170	879	.7	116
20	2.0	6520	4470	.3	485
21	3.0	122	110	.5	91
22	4.0	199	183	.3	217
23	4.0	424	365	.5	331
24	4.0	993	541	1.3	148
25	4.0	1290	625	1.2	183
26	6.0	145	137	.5	181
27	6.0	434	379	.5	177
28	6.0	1010	556	.5	98
29	6.0	1590	750	.5	160
30	7.3	50	48	.5	65
31	12.0	109	106	.5	297
32	12.0	434	390	.5	175

Table 3.2 Summary of Computer Runs (continued)

Run No.	AR	Ra _A	Ra _L ^a	FAC	I
33	12.0	724	476	.5	97
34	12.0	1160	608	.5	109
35	12.0	1450	710	.5	135
36	15.0	438	398	1.1	265
37	15.0	849	511	.7	133
38	15.0	1190	610	.5	147
39	15.0	1390	673	.3	143
40	15.0	100	98	1.2	429
41	15.0	226	221	1.2	361
42	15.0	1580	738	.3	180
43	17	998	553	.5	130
44	18	990	551	.5	131
45	20	1020	559	.3	129
46	24	145	143	.5	652
47	24	290	284	.5	539
48	24	406	392	1.25	1985
49	24	1000	555	1.3	140
50	30	1000	556	.3	151
51	35	436	399	.3	1145
52	35	895	525	.3	155
53	35	1290	641	.3	150
54	40	1000	556	.3	148
56	40	199	198	.8	1943
57	40	437	405	.3	423
58	40	696	501	.3	290
59	40	1290	642	.3	191
60	45	1000	616	.3	160
61	50	1000	616	.3	160
62	54	1010	616	.3	298
63	60	1000	616	.3	348
64	70	1000	612	.3	216

Table 3.2 Summary of Computer Runs (continued)

Run No.	AR	Ra _A	Ra _L ^a	FAC	I
65	80	1000	615	.3	160
66	15	338	328	.3	549
67	15	566	435	.3	276
68	15	498	416	.3	357
69	15	1100	582	.3	161
70	15	696	470	.3	178
71	40	398	386	.3	1873
72	60	707	506	.3	227
73	60	849	557	.3	130
74	60	1150	670	.3	154
75	70	1090	648	.3	156
76	4	2970	2010	.3	1143
77	16	1510	702	.3	132

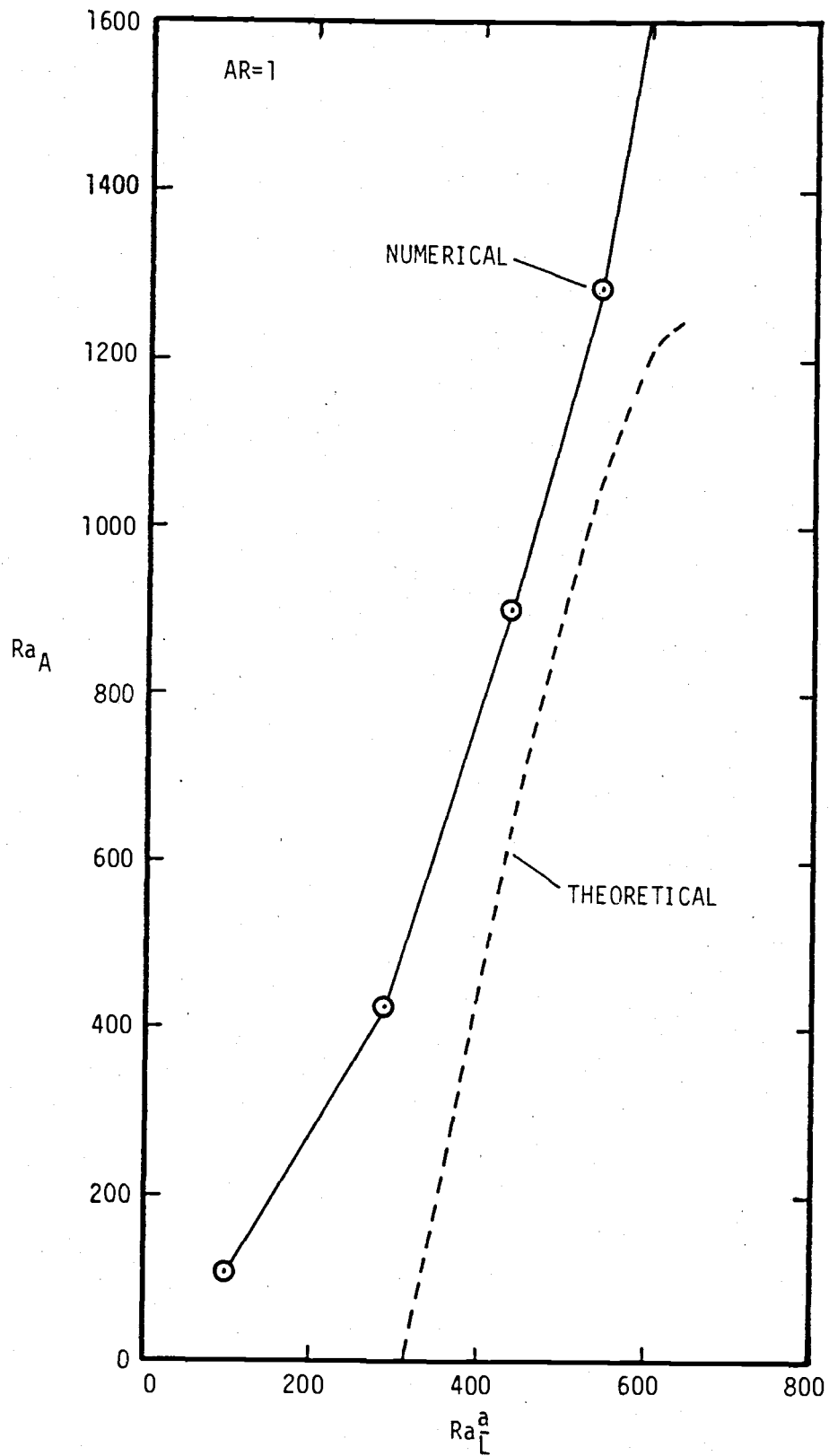


Figure 3.22a Ra_A vs. Ra_L^a for various AR's.

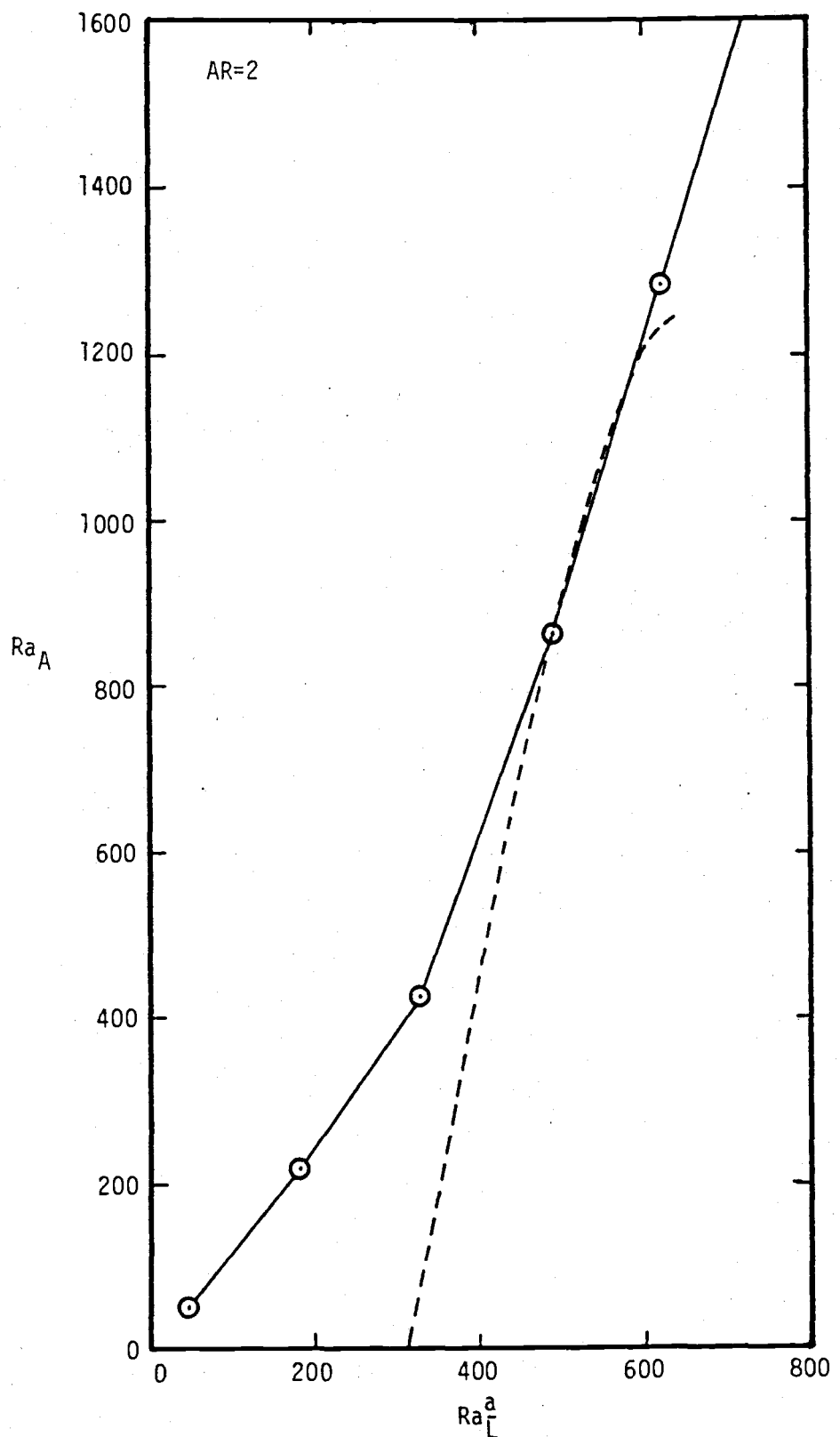


Figure 3.22b

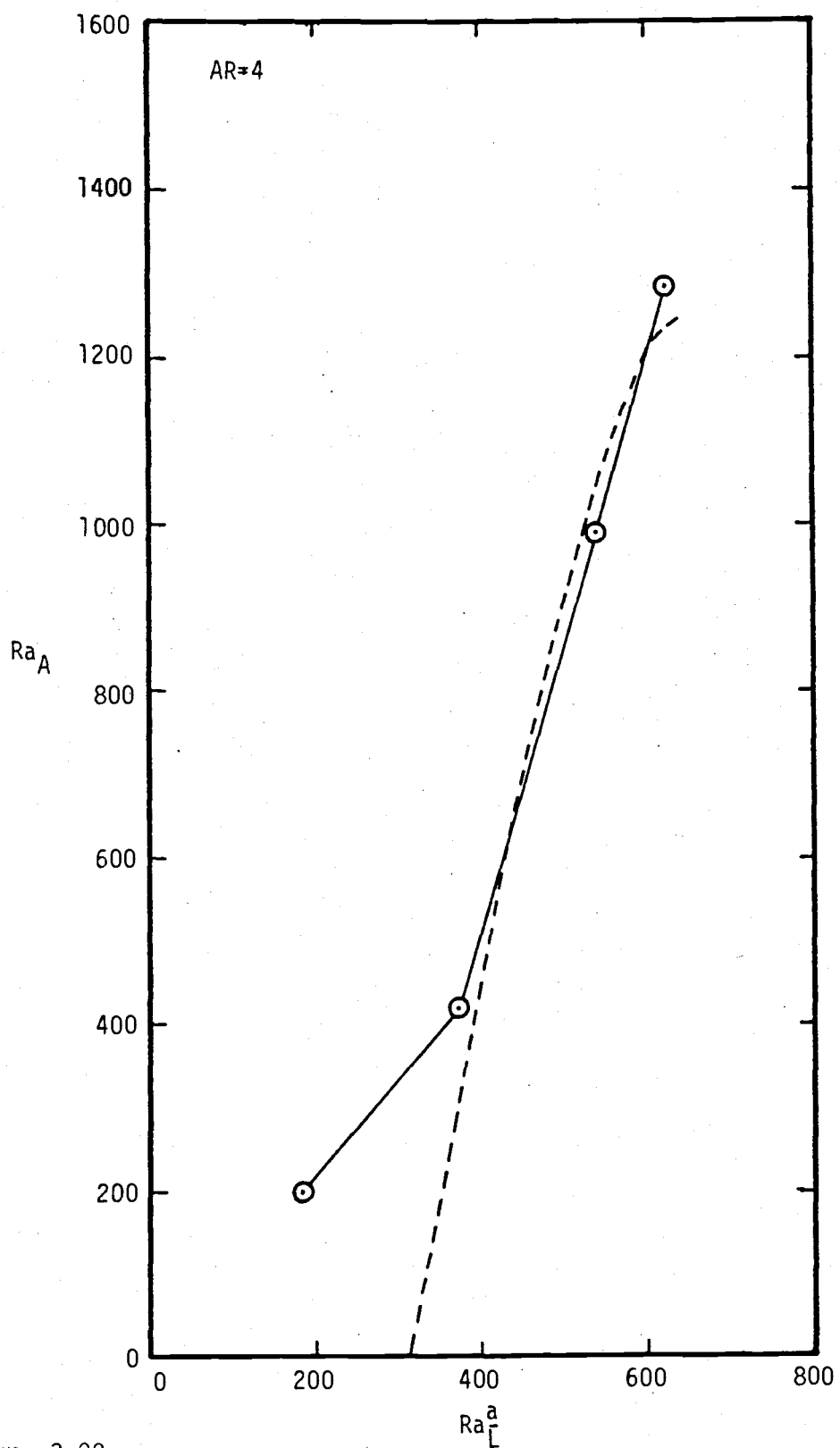


Figure 3.22c

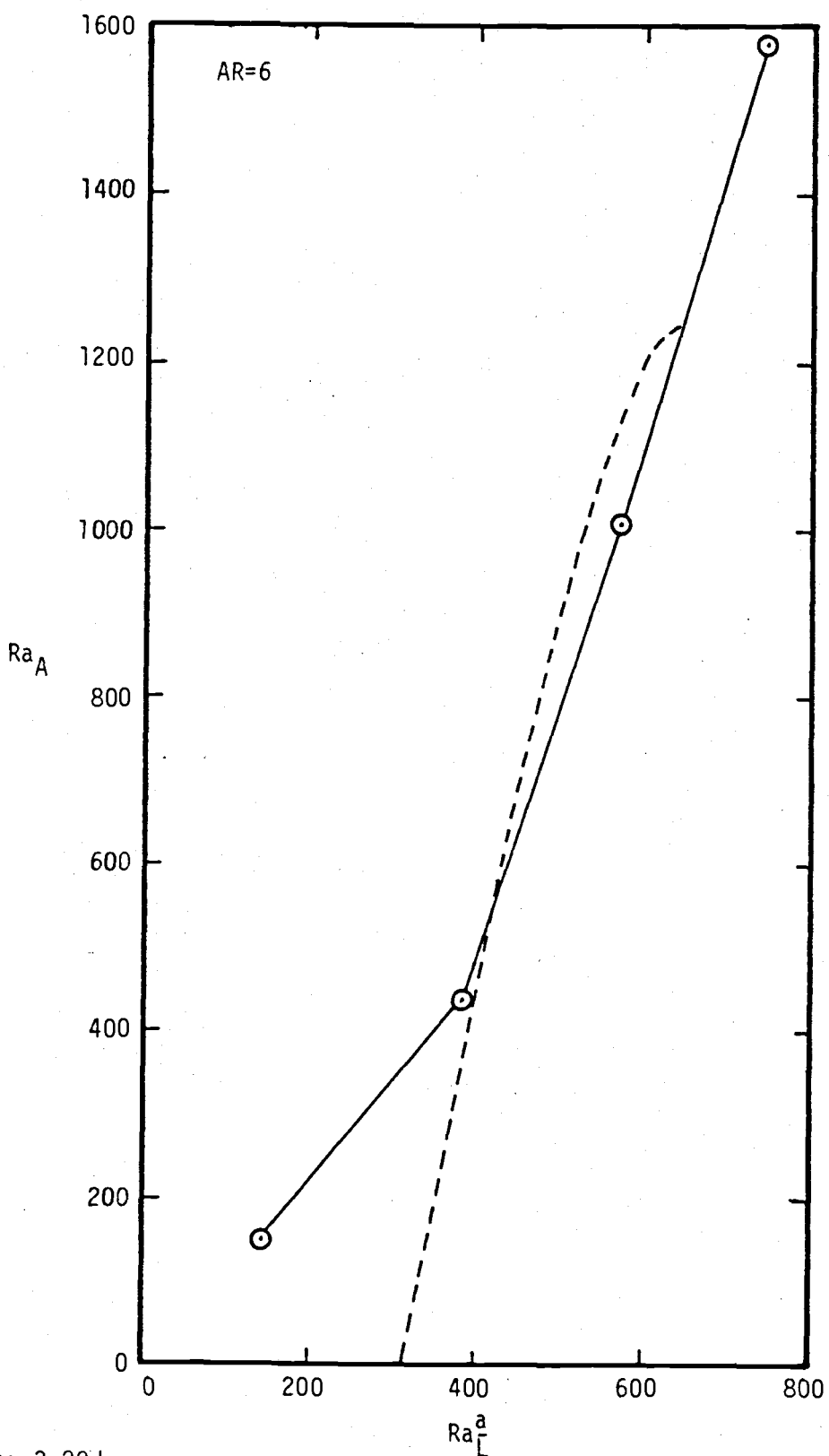


Figure 3.22d

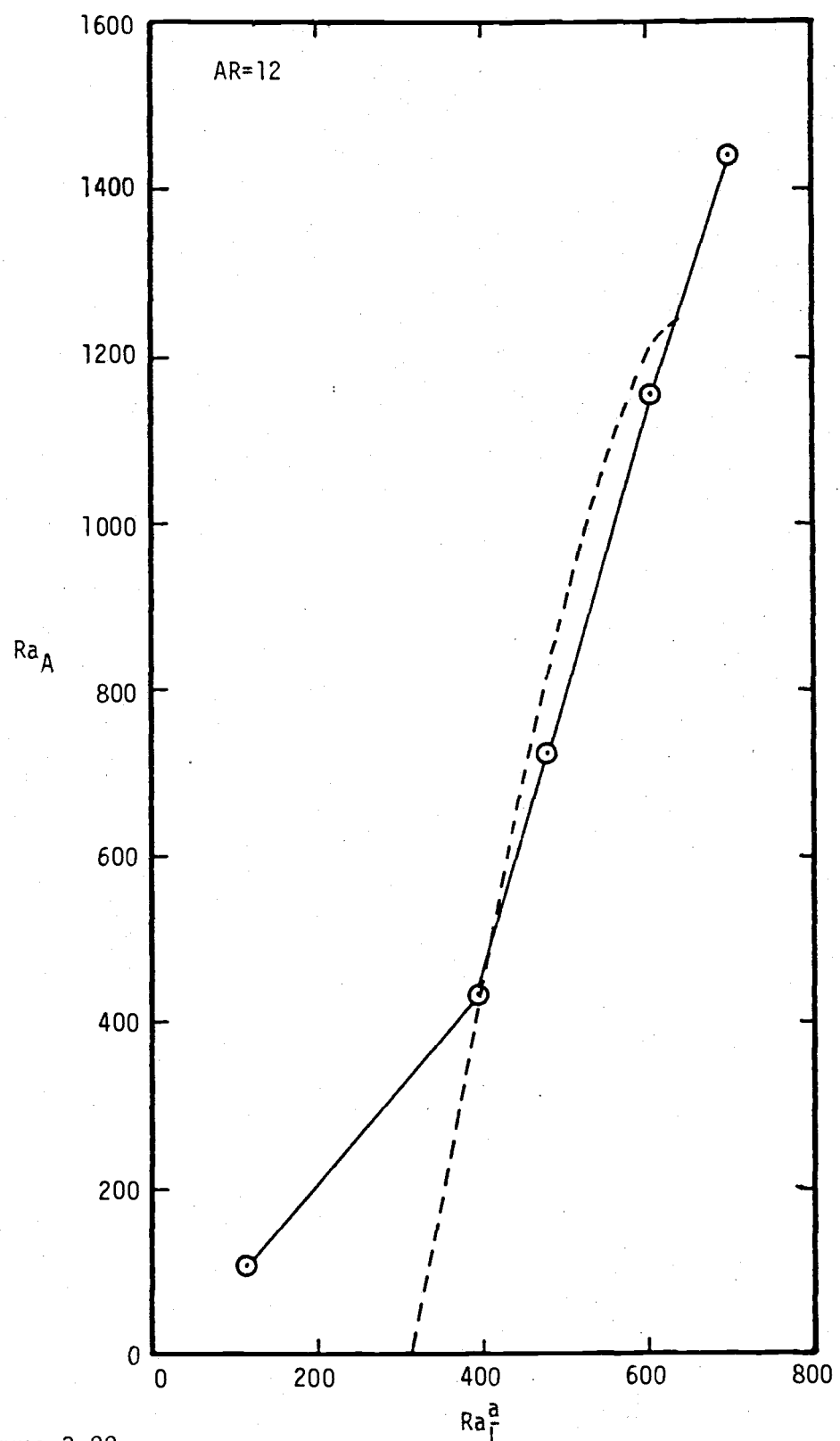


Figure 3.22e

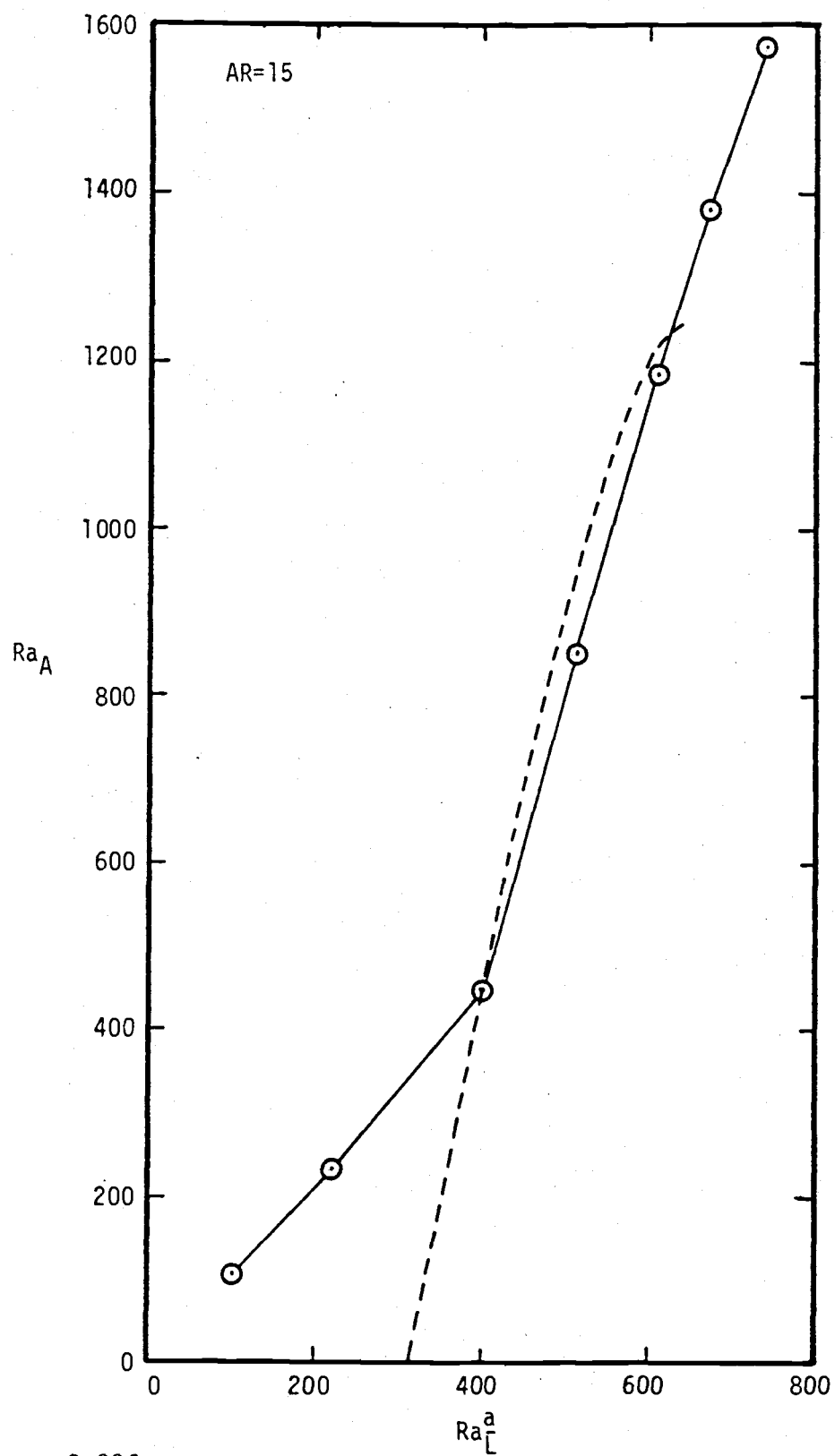


Figure 3.22f

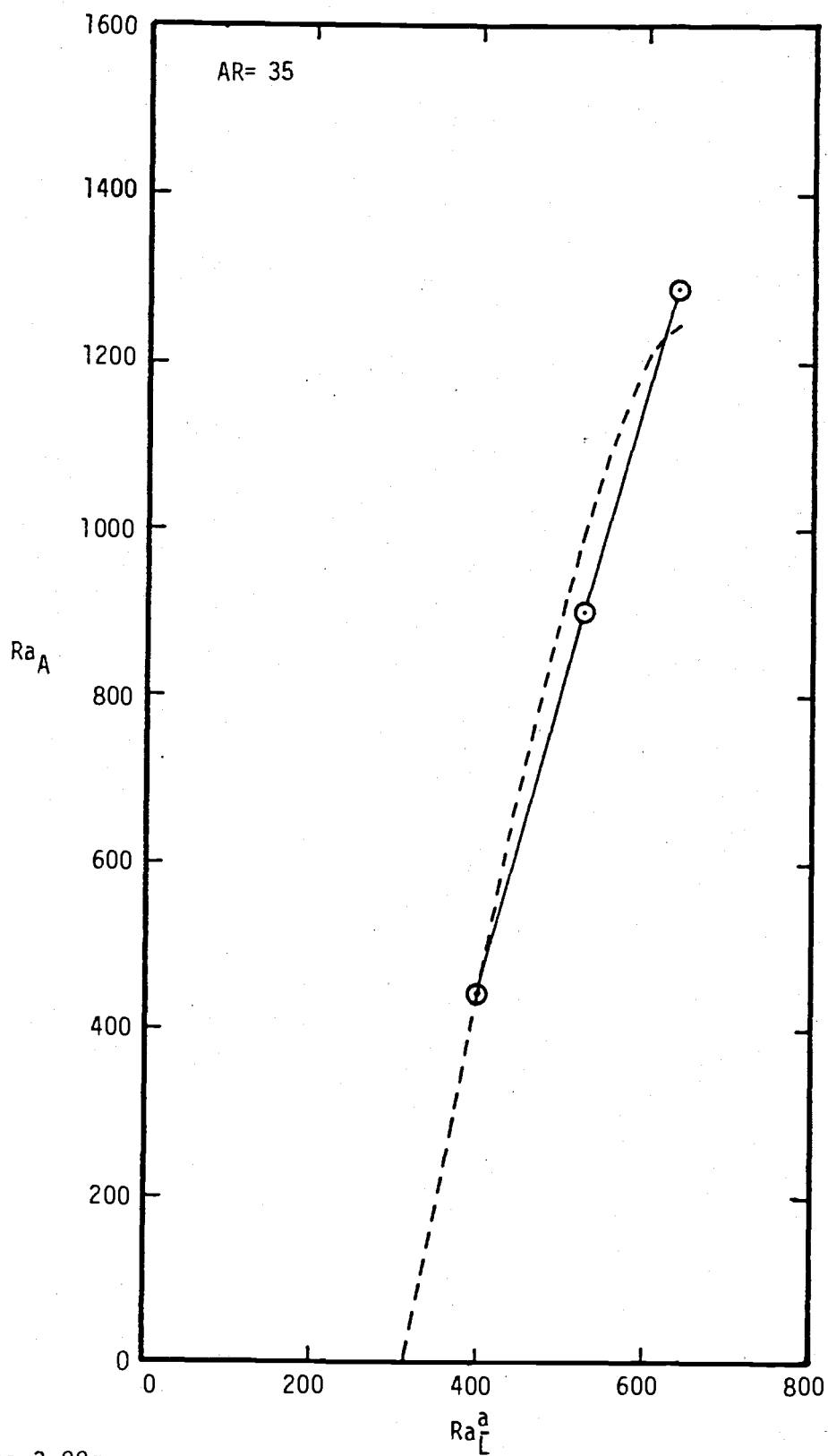


Figure 3.22g

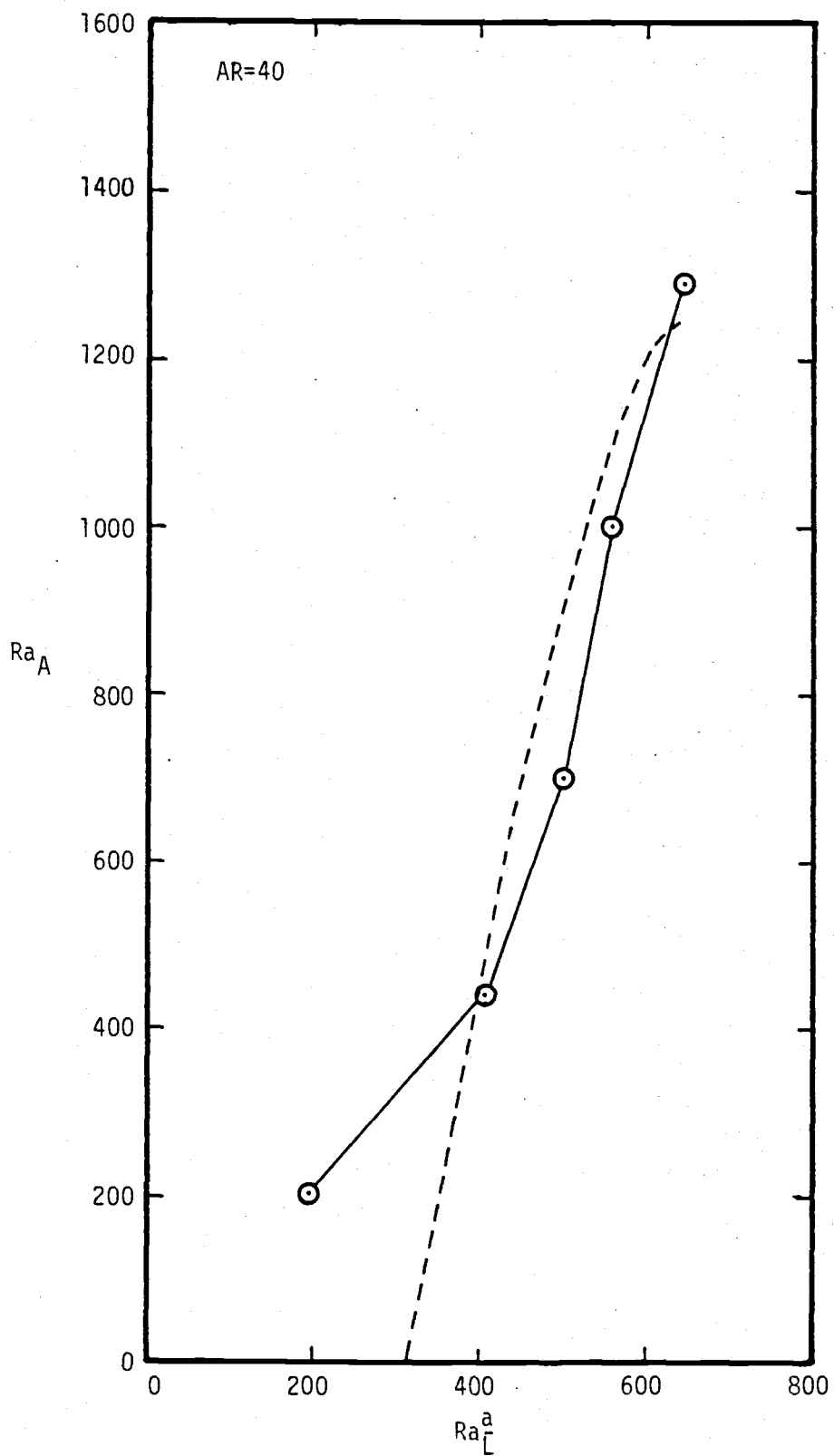


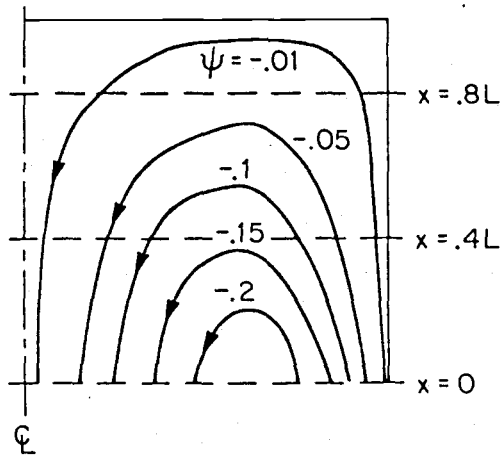
Figure 3.22h

following three ranges: 1) $AR < 4$, 2) $4 \leq AR \leq 35$, and 3) $AR > 35$. In each range of AR, its characteristics will be presented.

1) $AR < 4$: According to Lighthill [11], who theoretically studied the case with the cold reservoir located above the cylinder and a constant temperature established along the tube wall at the value equal to the hottest temperature of the system, two critical aspect ratios exist; the first defining the smallest AR of the similarity flow regime, and the second defining the largest AR, beyond which value the similarity flow breaks down. Although the physical model of the current study differs somewhat from that of Lighthill's, the results are similar. As seen in Fig. 3.23 where the velocity profiles and streamlines are plotted for $AR = 1$ and $Ra_A = 400$, the axial velocity profile at the open end of the cylinder, $x = 0$, indicates an undeveloped flow region around the centerline, $r < .2$. At the wall side, $r > .8$, boundary layer flow is indicated while a shear flow occurs between the above two radii. In Fig. 3.24, the development of the boundary layer along the wall is shown as the AR is increased from .25 to 1.0. This figure shows that when AR is small, the major shear flow occurs for $.2 < r < .9$ (dotted portion is approximated by the mass conservation); this is indicated by the case of $AR = .25$. As AR increases, the boundary-layer type flow grows in extent and eventually fills the entire section, which would be the case at $AR = 1.0$, although the profile still shows some flatness at $r < .2$. Another way to show whether similarity flow is present or not is by checking to see if the flow parameter, α , is constant along the centerline of the tube. The flow parameter at $r = 0$ is defined as $\alpha = u/x$ from

RUN NO. 09

$AR = 1$
 $Ra_A \cong 400$



$$\psi, (= \Psi / \kappa L)$$

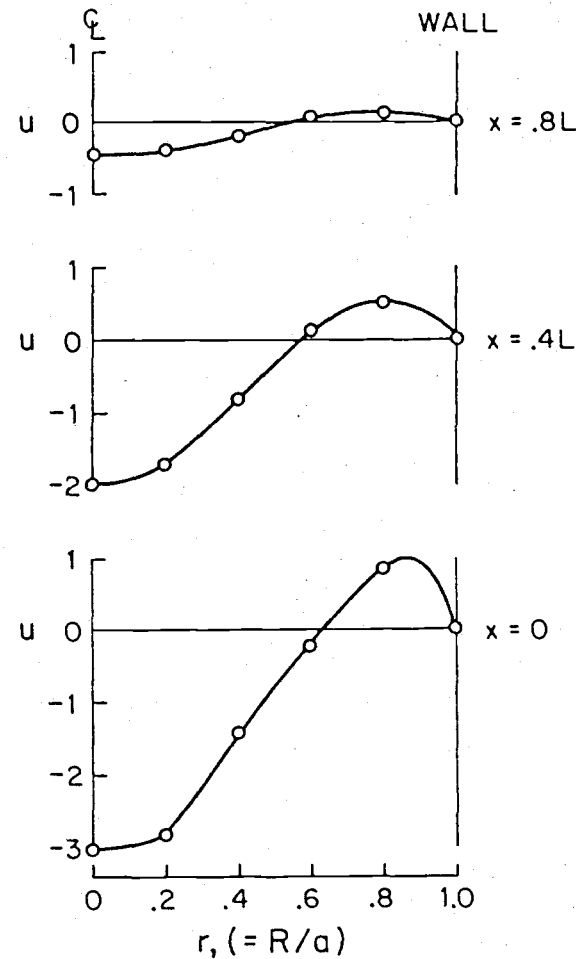


Figure 3.23 Streamlines and axial velocity profiles of Run No. 09.

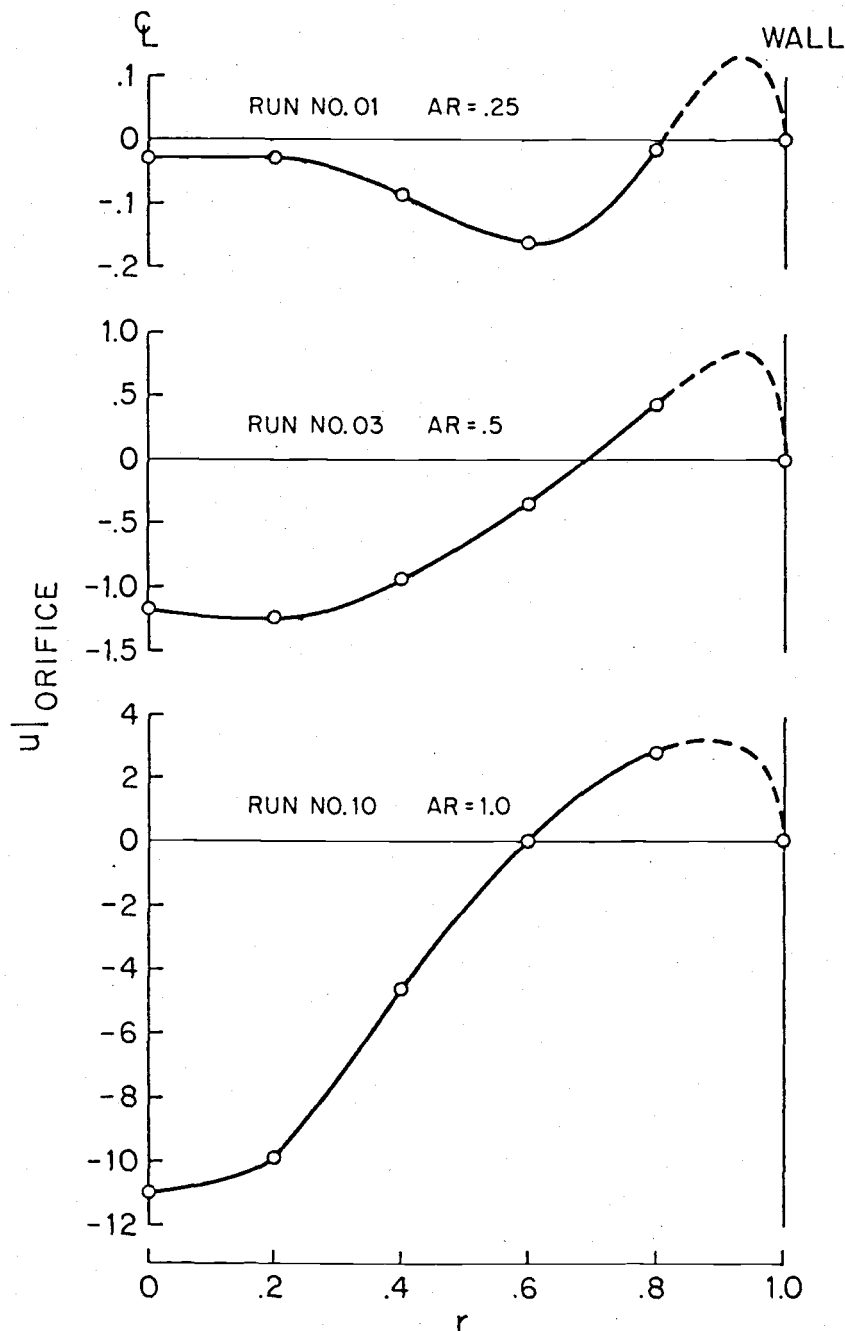


Figure 3.24 Development of axial velocity profiles at the orifice section for $\text{AR} = .25, .5$, and 1.0 at $\text{Ra}_A \approx 900$.

Eq. (2.33). For similarity flow, this parameter has only one value which theoretically applies at any x , x being measured from the closed-end. To determine the variation in the flow parameter, α/α_{\max} is plotted vs. x/L for $AR = 2$ and $AR = 15$ at $Ra_A \frac{a}{L} = 350, 500$, and 600 in Fig. 3.25. From this figure, it is evident that the variation of α/α_{\max} at $AR = 2$ is much larger than that at $AR = 15$, indicating the flow for $AR = 15$ to be more of a similarity type than for $AR = 2$.

These characteristics are typical of the flow patterns generated in the cylinders with $AR < 4$, thus, $AR = 4$ is comparable to the first critical aspect ratio of Lighthill.

2) $4 \leq AR \leq 35$: Within this range for aspect ratio the numerical results agreed best with the similarity solution. This was indicated previously by the constant value of the flow parameter, α , in Fig. 3.25 when compared with that for $AR = 2$. In this figure α is not observed to be absolutely constant, however, deviation is seen only at the orifice section in all three plots for $AR = 15$. This deviation is probably due to the finite size of the reservoir used in this numerical study, whereas in the theoretical study the similarity solution was derived up to the orifice section from the closed-end of the cylinder. A break-down in the similarity flow is seen to occur within this aspect-ratio range for values of Ra_A outside the range $400 < Ra_A < 1300$ which corresponds to $400 < Ra_A \frac{a}{L} < 600$, respectively. To illustrate this point, isotherms and streamlines for $AR = 15$ (refer to Fig. 3.22f) at $Ra_A = 230, 850$, and 1580 are plotted in Fig. 3.26, 3.27, and 3.28. Fig. 3.26 shows

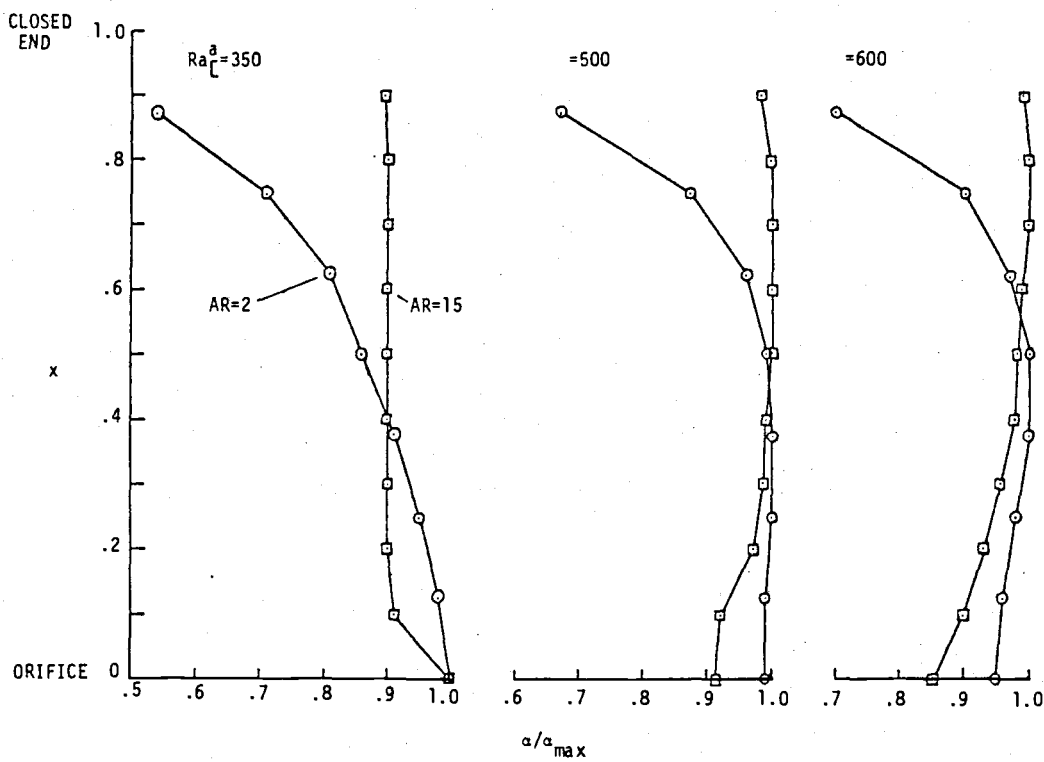


Figure 3.25 Variation of the flow parameter α along the cylinder length for $AR=2$ and 15, and $\text{Ra}^{\frac{a}{L}}=350, 500$, and 600.

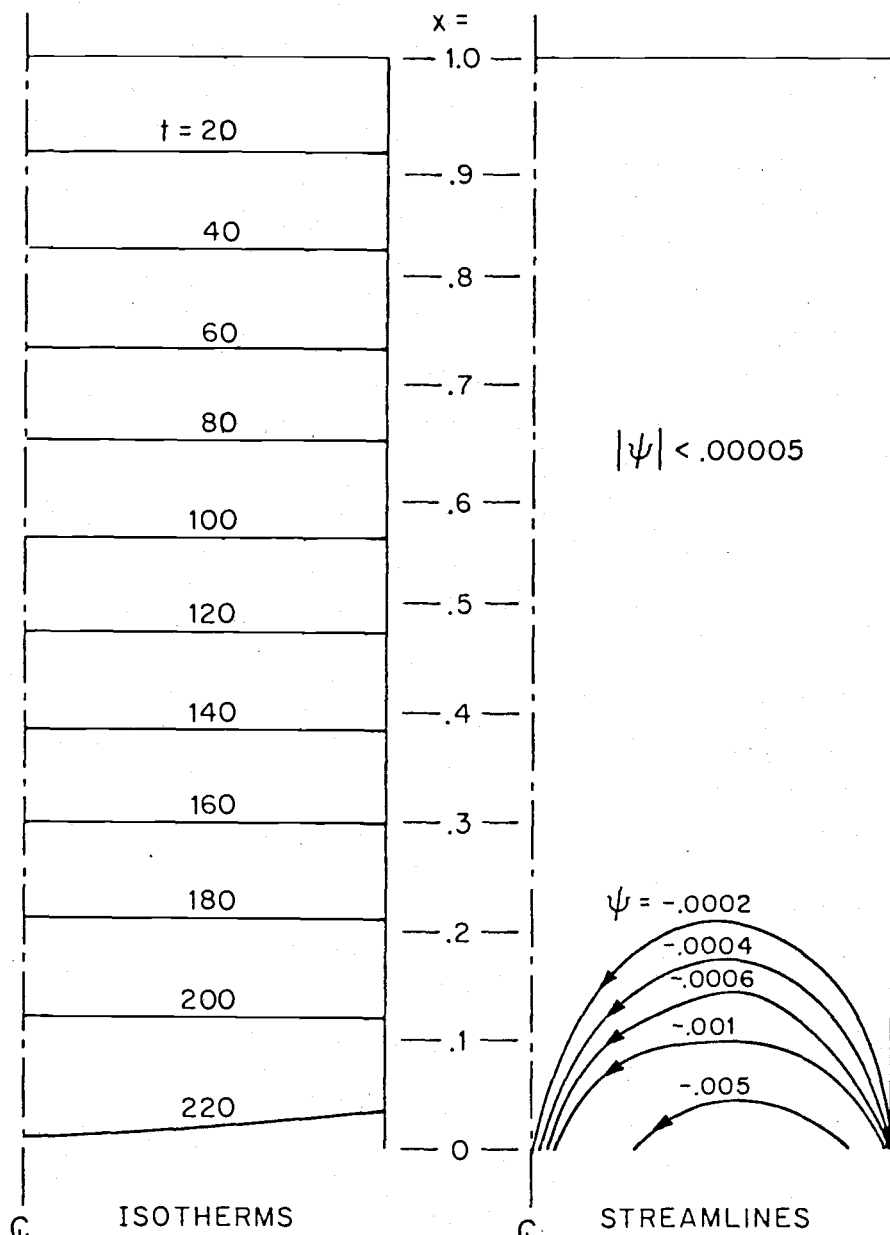
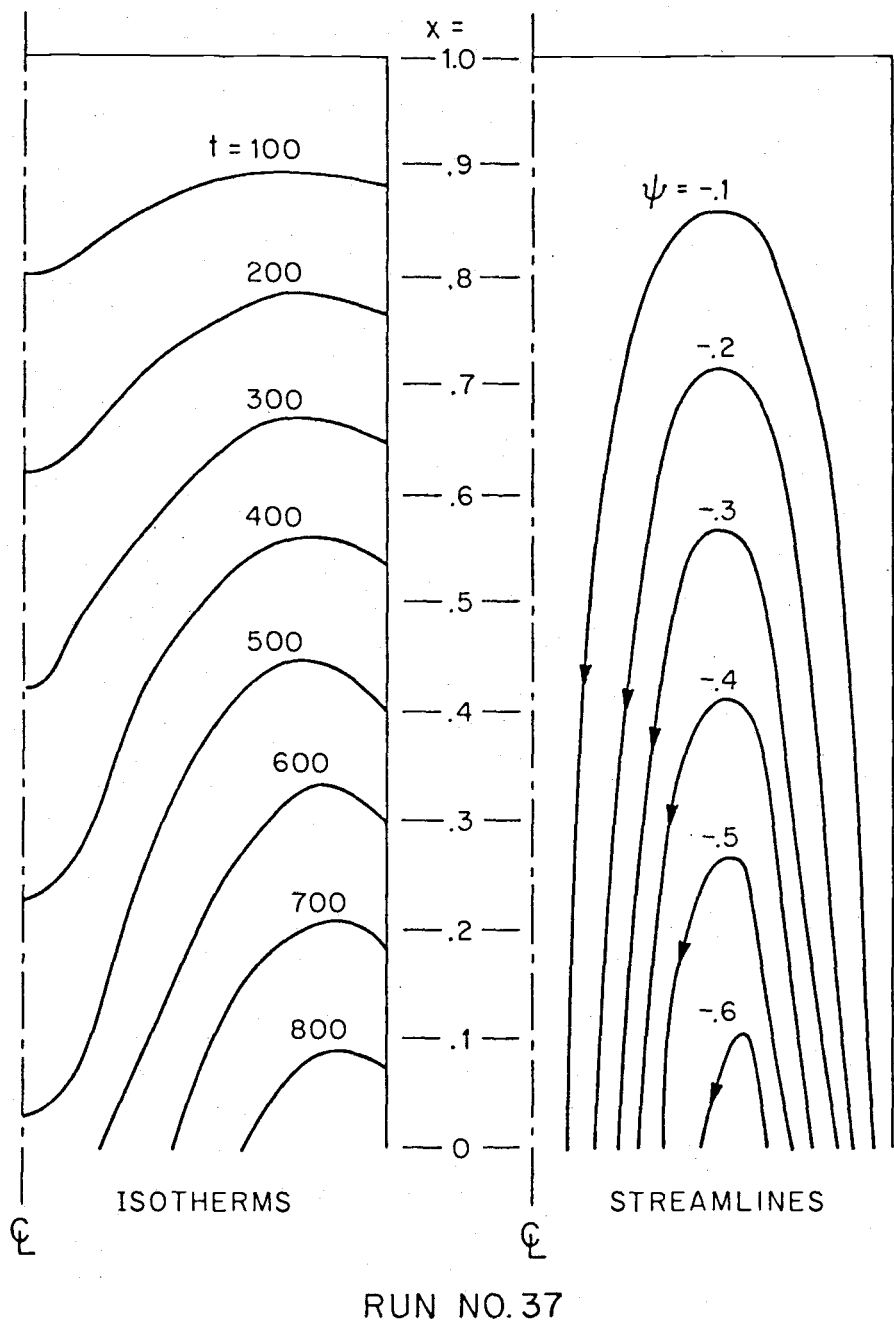
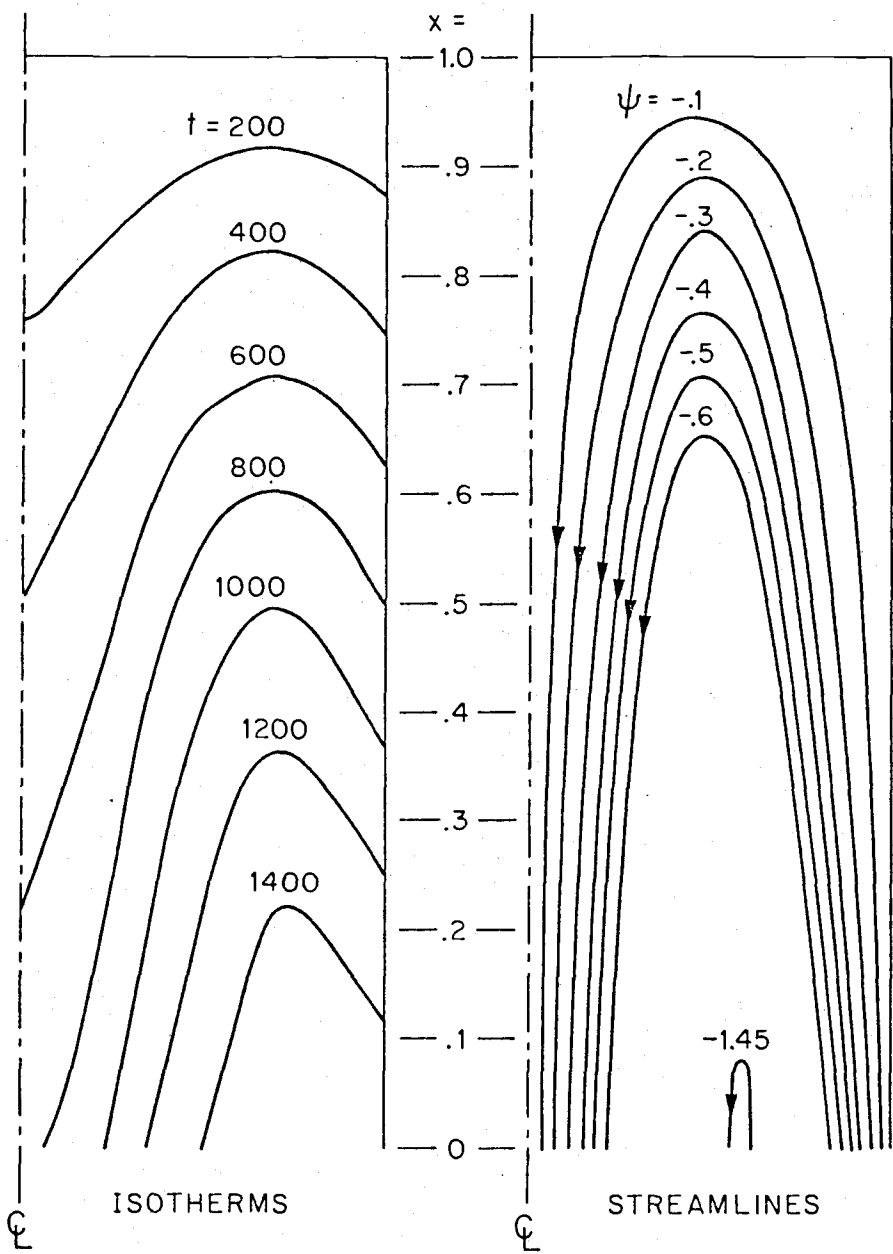


Figure 3.26 Isotherms and streamlines of $AR=15$ at $R_A=230$.



RUN NO. 37

Figure 3.27 Isotherms and streamlines of $AR=15$ at $Ra_A=850$.



RUN NO. 42

Figure 3.28 Isotherms and streamlines of AR=15 at $Ra_A=1580$.

that heat transfer is mainly dominated by conduction rather than by convection. Very weak convection is seen only in the fluid below $x = .3$ as indicated both by the streamlines, and by the u/u_{\max} plot in Fig. 3.29, where u/u_{\max} along the centerline is plotted for the same three cases. Fig. 3.29 also indicates that the fluid from $x = .3$ up to the top is very nearly stationary along the centerline for $Ra_A = 230$. Fig. 3.27 shows typical isotherms and streamlines when flow within the entire cylinder is of a similarity nature, and in Fig. 3.29 the axial velocity profile along the centerline is shown, which indicates the linear variation of the axial velocity with the distance measured from the top. When $Ra_A = 1580$, a condition outside the similarity regime, streamlines and isotherms are as shown in Fig. 3.28. As seen in this figure, strong convective flow reaching the top of the cylinder is found for $Ra_A > 1300$ within the range of AR discussed here. This becomes more evident when the streamlines of Fig. 3.28 are compared with those plotted in Fig. 3.27 (note that the six streamlines range from $\Psi = .1$ to $.6$ in the both cases).

Thus it is within this range of AR that similarity flow is most likely to exist, the range being $400 < Ra_A < 1300$. Outside of this range of Ra_A convective flow rate fails to reach the closed-top end leaving some portion of the fluid nearly stagnant when $Ra_A < 400$, and an extremely strong convective flow fills the entire cylinder when $Ra_A > 1300$.

3) AR > 35: When the AR exceeds 35, a typical convective-flow pattern found is as shown in Fig. 3.30, where a newly formed convection cell is seen at the top portion of the cylinder.

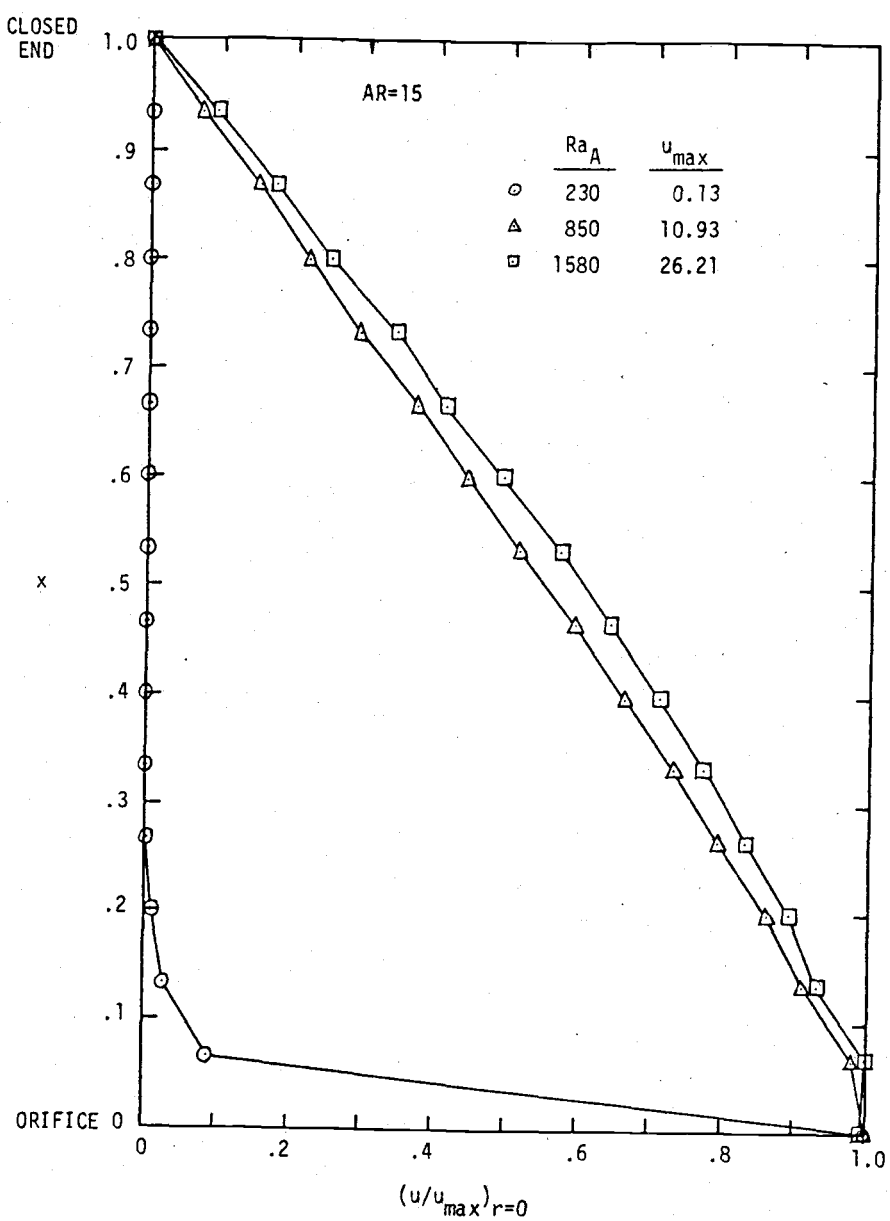


Figure 3.29 Axial velocity profiles along the centerline of the cylinder.

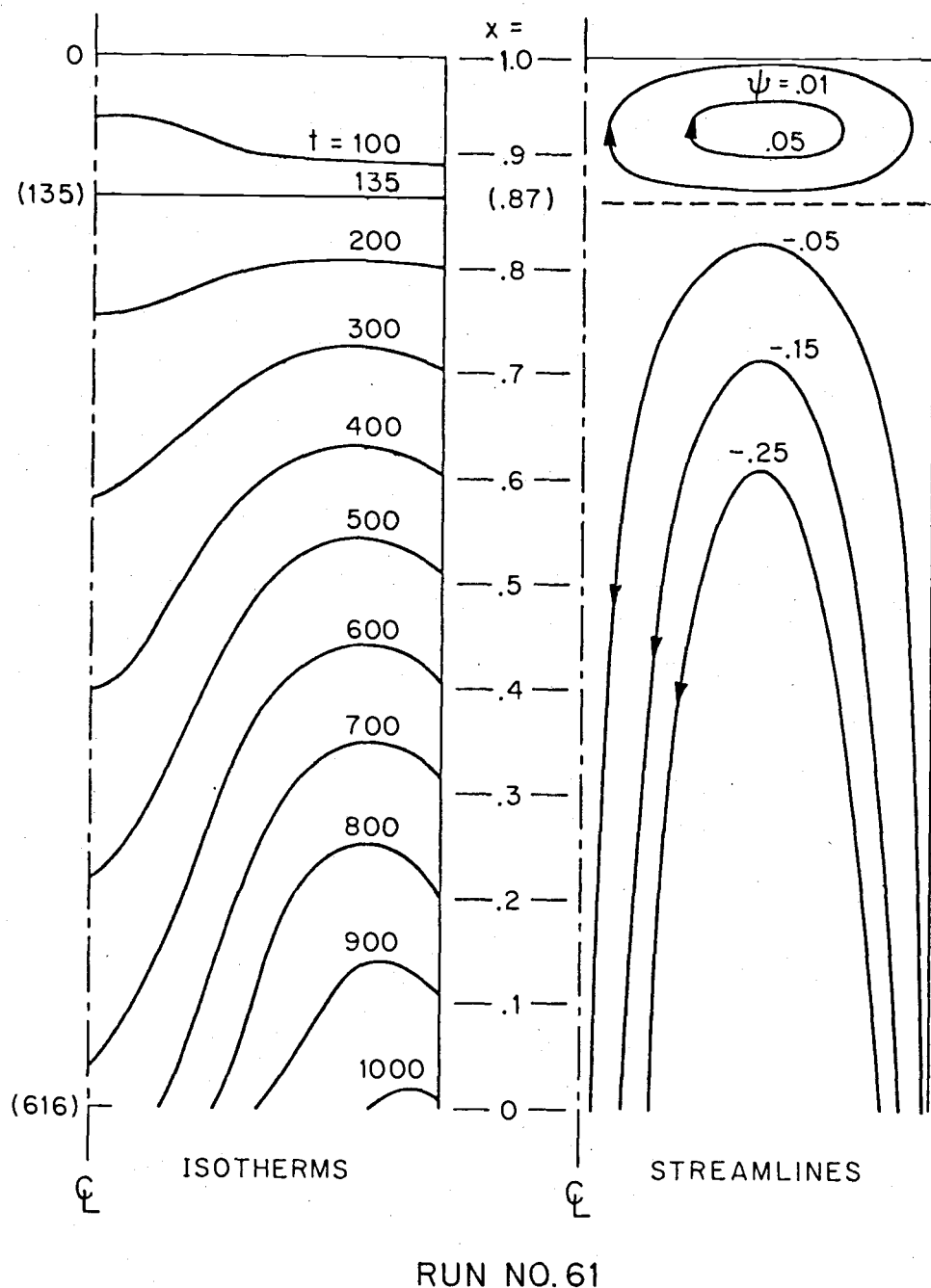


Figure 3.30 Isotherms and streamlines at $AR=50$ and $Ra_A=1000$.

Because of this cell formation the isotherms take on a different configuration than previously seen at $AR < 35$ (for comparison see Fig. 3.27). A rather interesting isotherm pattern that one can notice in Fig. 3.30 is the formation of an interface-like surface at about $x = .87$, about which surface the two isotherms, $t = 100$ and 200, look to be symmetric. Also, an examination of the radial velocity indicates that its maximum occurs at this surface at all radial positions. Although the flow pattern depicted in Fig. 3.30 is typical of the range $AR > 35$, if an AR is chosen close to 35, one would expect to see no cell formation at all for certain ranges of Ra_A ; this condition is illustrated in Fig. 3.31. In this figure, axial velocity profiles along the centerline are plotted for $199 \leq Ra_A \leq 1290$ at $AR = 40$, where one can see that for $Ra_A = 437$ and 696, a cell is forming at the top portion ($x > .85$) of the cylinder which is indicated by $u(r = 0)$ going into the positive side. However, the cell is replaced by a stagnant fluid layer like that of Fig. 3.26 when $Ra_A < 437$, and by continuous convection flow when $Ra_A > 696$.

Therefore, when $AR > 35$, the flow is characterized as having an independent convection cell toward the closed-end of the cylinder for $Ra_A > 400$, flow in the rest of the cylinder is of a similarity nature.

3.4.2 Flow Regimes

To summarize what was presented in the previous subsection and considering Lighthill's two critical aspect ratios, a flow-regime map, as shown in Fig. 3.32 was constructed with additional data

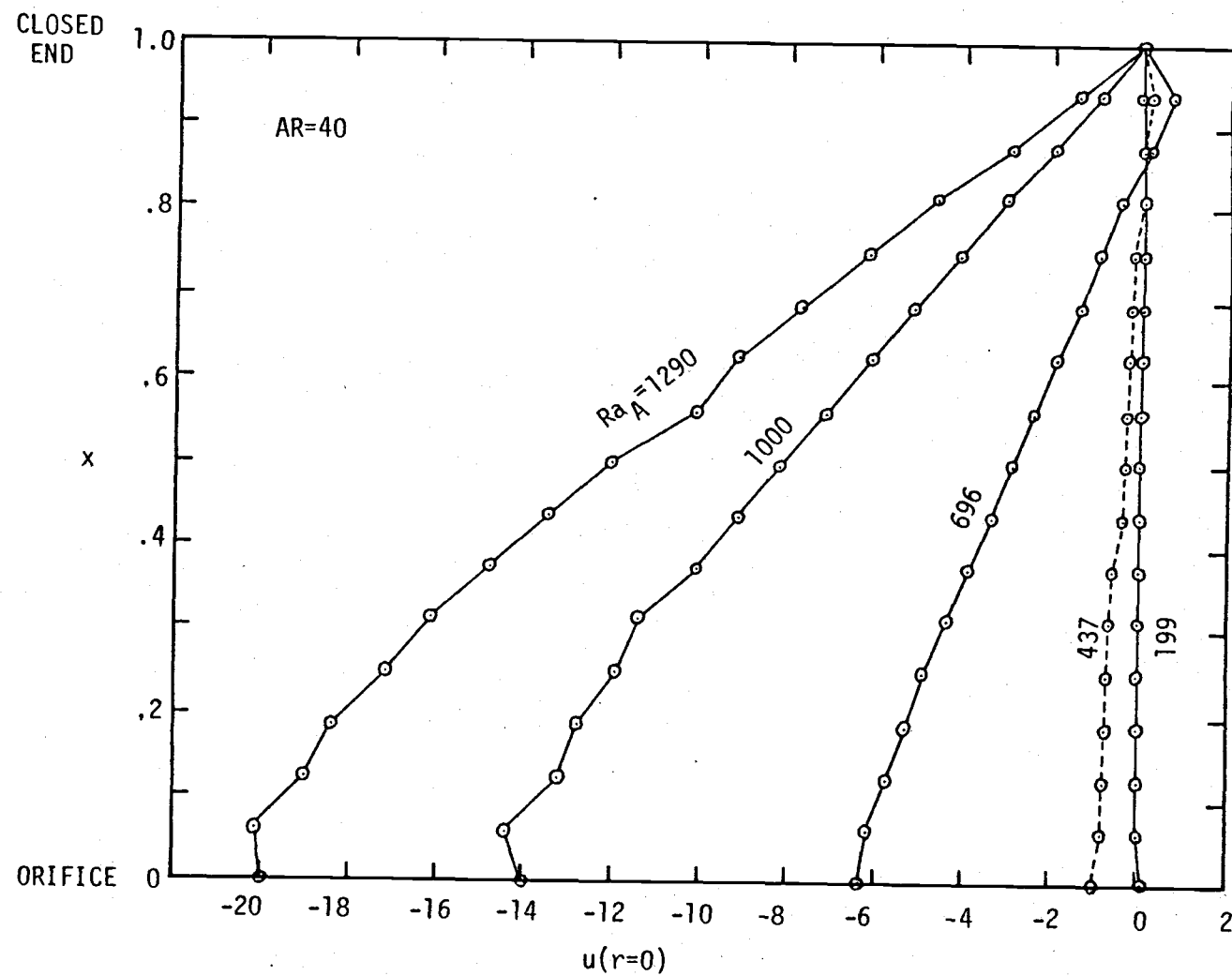


Figure 3.31 Axial velocity profiles along the centerline of the cylinder at $AR=40$ for various Ra_A .

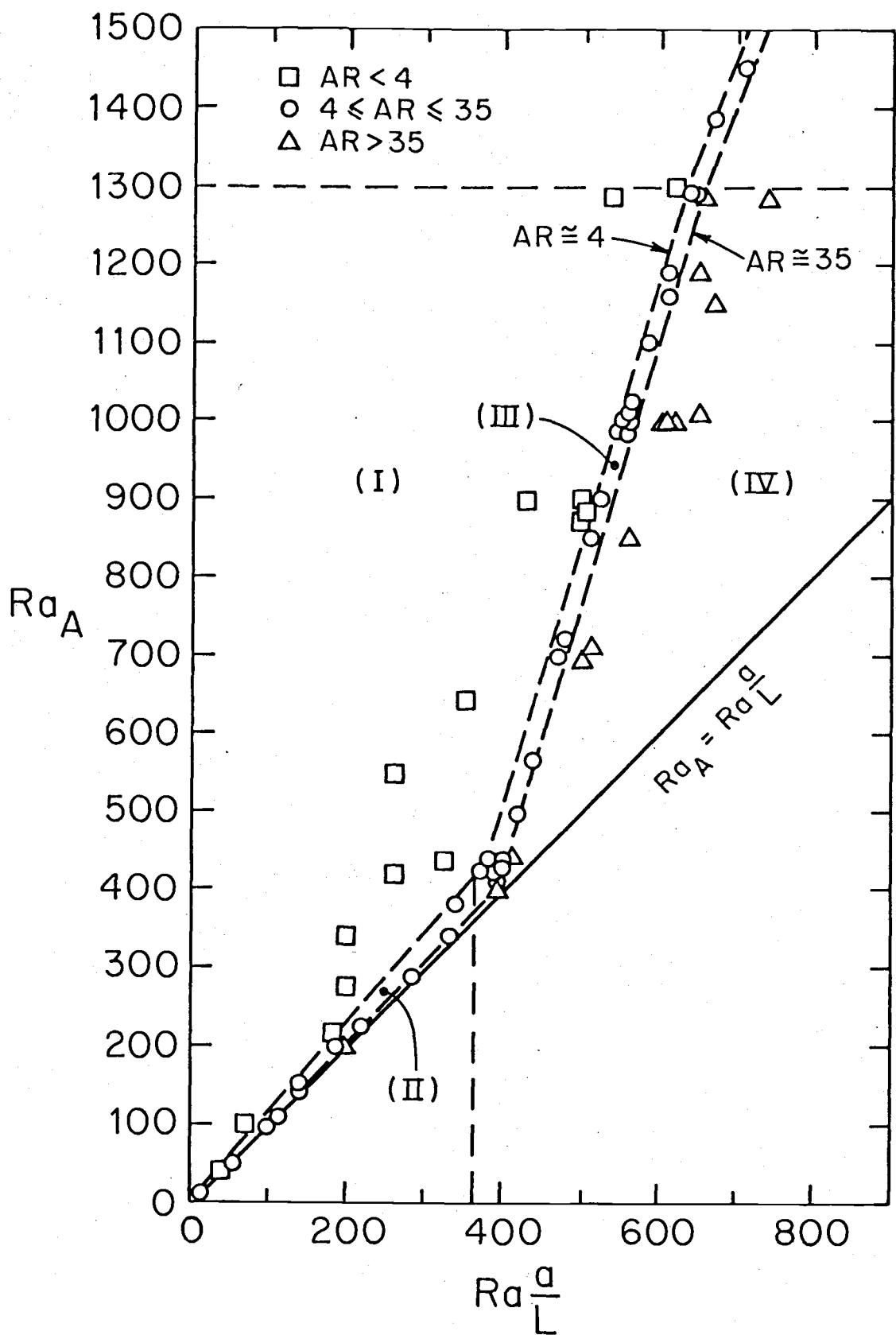


Figure 3.32 Flow regime map.

from the numerical solution to that already presented in the Sec. 3.4.1. Referring to Fig. 3.32, the two critical AR as mentioned above are found to be, approximately, $AR = 4$ and 35 . As Lighthill predicted, the difference between these two is approximately a factor of order ten. Thus, $AR = 4$ can be considered as the lower limit and $AR = 35$ as the upper limit such that only within these limits similarity flow exist. (This region is labelled III in the figure). In the adjoining regions, three different flow regimes are found within the two Ra_A boundaries; namely from the line of $Ra_A = Ra_L^{\alpha}$ up to $Ra_A = 1300$. Each of these four regimes is discussed below (see Fig. 3.32):

Regime I -- This regime is bounded by $Ra_A = 1300$ and $AR = 4$. The most distinctive aspect of the convective flow of this regime is that, along the wall, flow is of the boundary-layer type while in the central portion of the cylinder flow is undeveloped (see Fig. 3.23 and 3.24).

Regime II -- This regime lies within the region defined by $Ra_A = Ra_L^{\alpha}$, $AR = 4$, and $Ra_L^{\alpha} = 360$. Within this flow regime, only a weak convective flow can be seen at the open end of the cylinder, while the rest of the fluid remains nearly stationary (see Fig. 3.26).

Regime III -- This is the similarity flow regime which is defined by values of $AR = 4$, $AR = 35$, $Ra_L^{\alpha} = 360$, and $Ra_A = 1300$. The principal characteristic of similarity flow is that the axial velocity is proportional to the distance measured from the closed-end of the cylinder with the proportionality constant designated α (flow parameter) which is related to the combination of Ra_A and

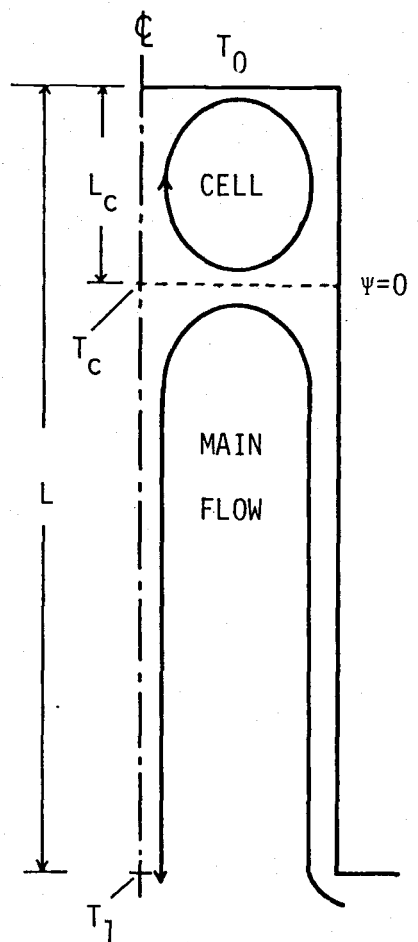
$\frac{Ra}{L}^a$ as described previously. In the theoretical study, the applicable part of the similarity solution (see Fig. 2.5) began at $Ra_A = 0$ and extended to $Ra_A = 1300$, however, in the numerical study no similarity flow was found for values of Ra_A less than approximately 440. Thus, it may be proper to redefine the applicable range of the similarity solution here to $400 < Ra_A < 1300$ and $380 < \frac{Ra}{L}^a < 650$.

Regime IV -- This regime is defined by $Ra_A = \frac{Ra}{L}^a$, $\frac{Ra}{L}^a = 360$, and $AR = 35$, and $Ra_A = 1300$. Within this region an independent convection cell is formed within a certain distance from the closed-end, and below it a similarity flow exists throughout the rest of the cylinder (see Fig. 3.30). After the cell formation became evident within this flow regime, 21 additional computer runs were made in order to characterize the conditions of cell-formation and their dimensions.

A summary of the results of the computer runs made for this purpose is listed in Table 3.3, where L_C/L is the ratio of the cell length to the cylinder length; L_C/a is the cell aspect ratio which is the product of AR and L_C/L ; $(Ra_L^a)_C$ is the corrected modified-Rayleigh number which is, as explained in Fig. 3.33, the modified Rayleigh number of a main flow (or a continuous convection from reservoir); and $(AR)_M$ is the AR of the main flow. Values of Ra_A are shown as functions of $\frac{Ra}{L}^a$ and L_C/L in Fig. 3.34, and extrapolated values of L_C/L from Fig. 3.34 are graphed in Figs. 3.35 and 3.36 as functions $\frac{Ra}{L}^a$ and Ra_A . These results basically indicate the following; (a) for a constant L_C/L the relationship between $\frac{Ra}{L}^a$ and Ra_A is linear, (b) for a constant Ra_A , L_C/L increases almost

Table 3.3 Computer runs made for the evaluation
of cell formation in Regime IV

Run No.	AR	Ra_A	Ra_L^a	L_C/L	L_C/a	$(Ra_L^a)_C$	$(AR)_M$
78	13.6	770	490	0	0	490	13.6
79	21.8	777	569	.273	5.95	493	15.8
80	30.0	1000	614	.140	4.20	552	25.8
81	32.5	489	467	.753	24.47	395	8.0
82	40.0	1000	676	.272	10.88	554	29.1
83	40.3	1290	639	0	0	639	40.3
84	45.0	991	669	.267	12.02	548	33.0
85	52.0	598	502	.377	19.60	444	32.4
86	54.3	996	780	.505	27.40	559	26.9
87	60.0	1300	713	.116	6.96	656	50.4
88	60.0	707	499	.104	6.24	475	53.8
89	70.0	1020	622	.135	9.45	560	60.6
90	71.4	1300	732	.143	10.21	649	61.2
91	73.7	995	833	.628	46.28	559	27.4
92	80.0	1180	757	.242	19.36	621	60.6
93	94.3	1290	724	.139	13.11	641	46.4
94	110.3	1190	910	.508	56.03	620	54.3
95	115.3	996	780	.504	58.11	561	57.2
96	121.7	1270	719	.133	16.19	633	105.5
97	122.0	796	649	.503	61.37	501	60.6
98	125.7	1190	910	.508	63.86	620	61.8



$$Ra_L^a = \frac{\beta g a^4 (T_1 - T_0)}{v k L}$$

$$(Ra_L^a)_c = \frac{\beta g a^4 (T_1 - T_c)}{v k (L - L_c)}$$

$$(AR)_M = \frac{L - L_c}{a}$$

Figure 3.33 Illustration of the corrected modified-Rayleigh number when a cell is formed.

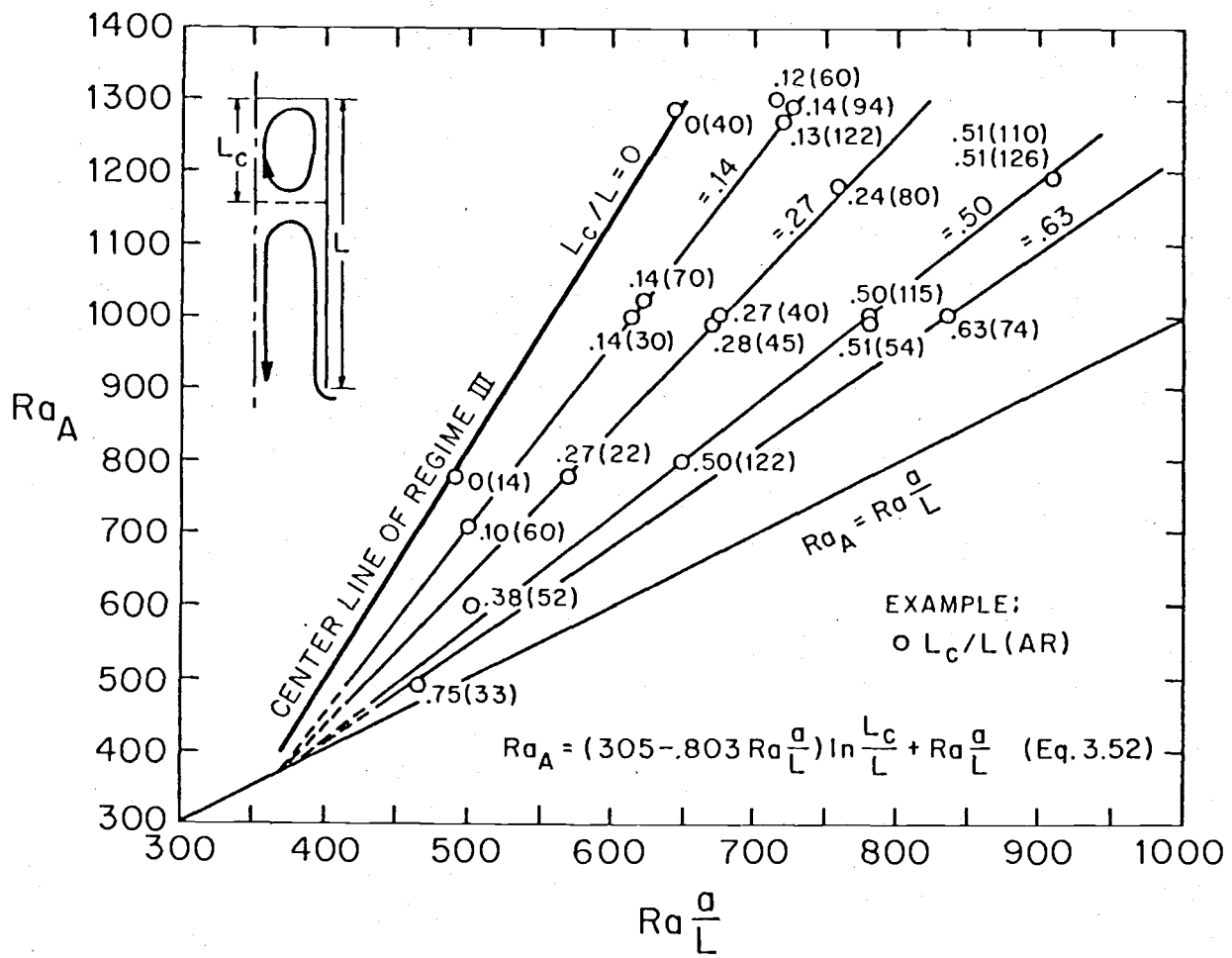


Figure 3.34 Correlation of Ra_A , Ra_L^a , and L_c/L in Regime IV.

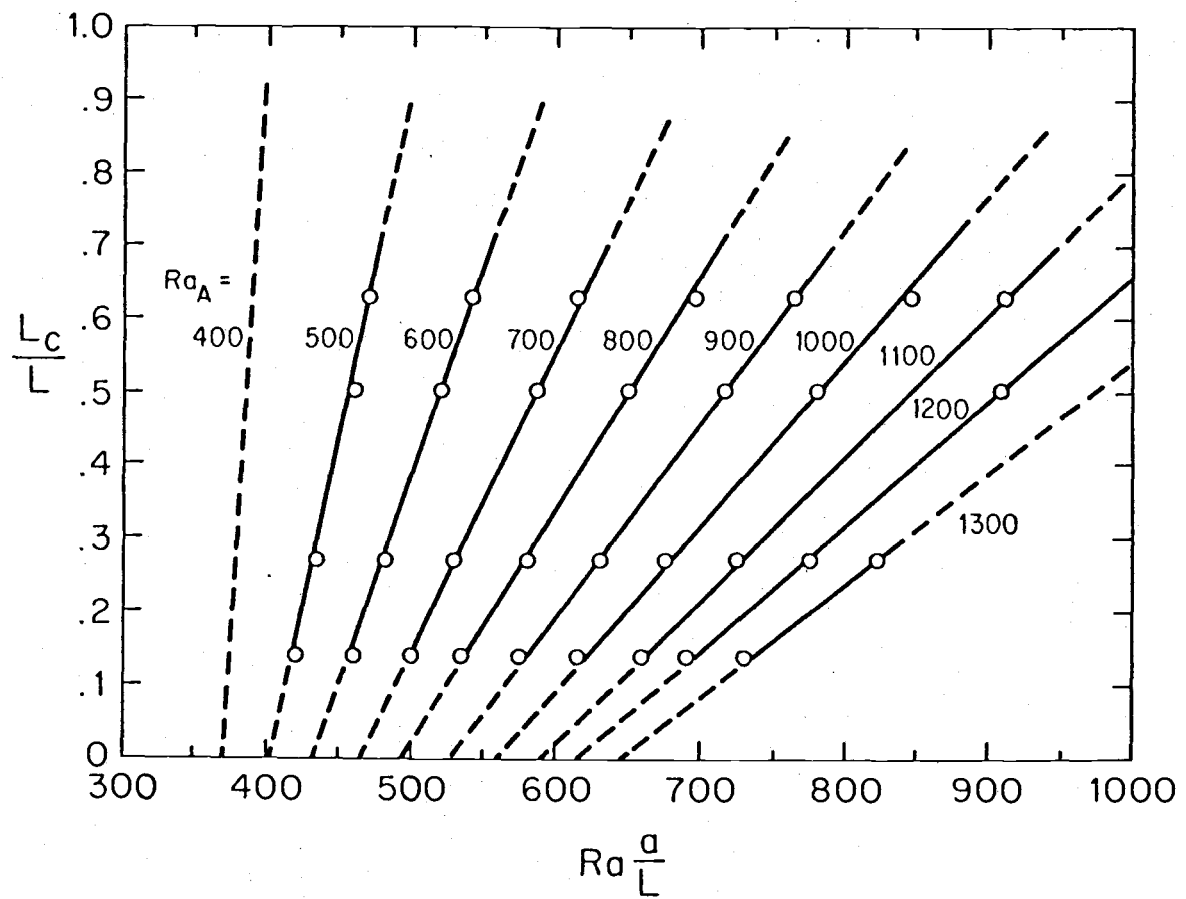


Figure 3.35 L_c/L vs. Ra^a/L for various Ra_A (extrapolated from Fig. 3.34).

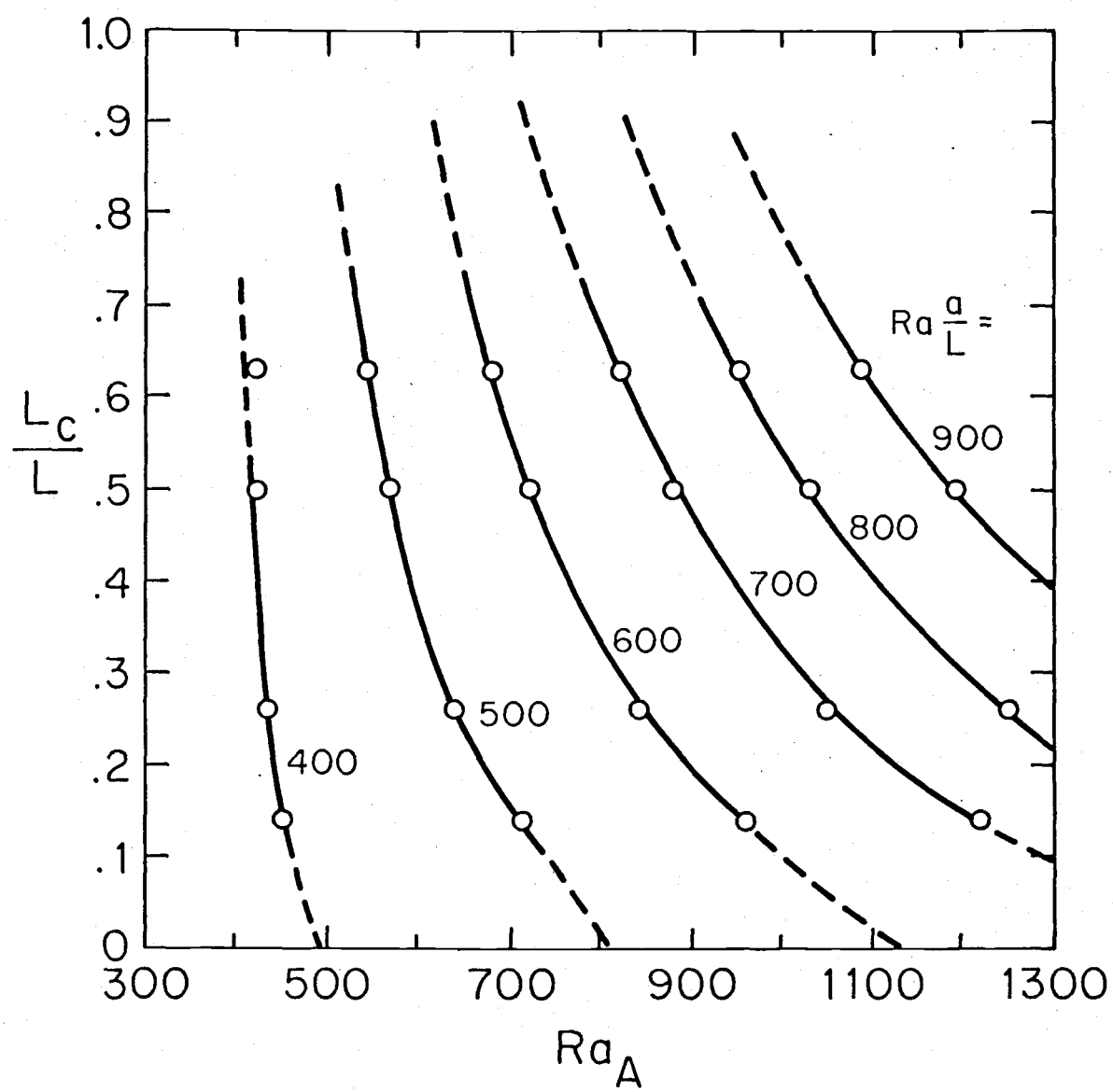


Figure 3.36 L_c/L vs. Ra_A for various $Ra \frac{a}{L}$ (extrapolated from Fig. 3.34).

linearly with Ra_L^a , and (c) for a constant Ra_L^a , L_C/L decreases non-linearly with Ra_A . In addition Fig. 3.34 also suggests that, if extrapolated, L_C/L -lines will converge to the common value of $Ra_A = Ra_L^a = 380$, a value which interestingly was earlier defined as the approximate lower-limit of Ra_L^a for Regime III (the similarity flow regime), as indicated in Fig. 3.32, and was also the value at which flow reversal was predicted to take place in the similarity solution (see the variation of α in Fig. 2.5). Also, in Fig. 3.34 the aspect ratios do not appear to give any specific trend, however, those aspect ratios which were known to be within the similarity flow regime ($4 \leq AR \leq 35$), are also amenable to cell formation when the combination of Ra_A and Ra_L^a is appropriate. Thus, it is important to emphasize here that although the similarity-flow regime has been defined rather specifically by the aspect-ratio range ($4 \leq AR \leq 35$), the aspect-ratio alone is not sufficient to identify any flow regime. Next, the corrected Ra_L^a , $(Ra_L^a)_C$, is plotted in Fig. 3.37 which indicates that all $(Ra_L^a)_C$ fall on the similarity-flow line which is represented by the dotted line. This means that flow between the cylinder and the reservoir is of the similarity type, while above it an independent convection cell is generated. This interpretation was reinforced by calculating α and noting its being constant at $r = 0$ within the continuous flow region. A surprising result from the α calculation is that, although the $(AR)_M$ is very large, such as that of RUN NO. 96 in Table 3.3, α remained nearly constant along the center-line; for the case of RUN NO. 96, the maximum deviation was about 15%. This indicates that when the main flow is bounded by a free surface or

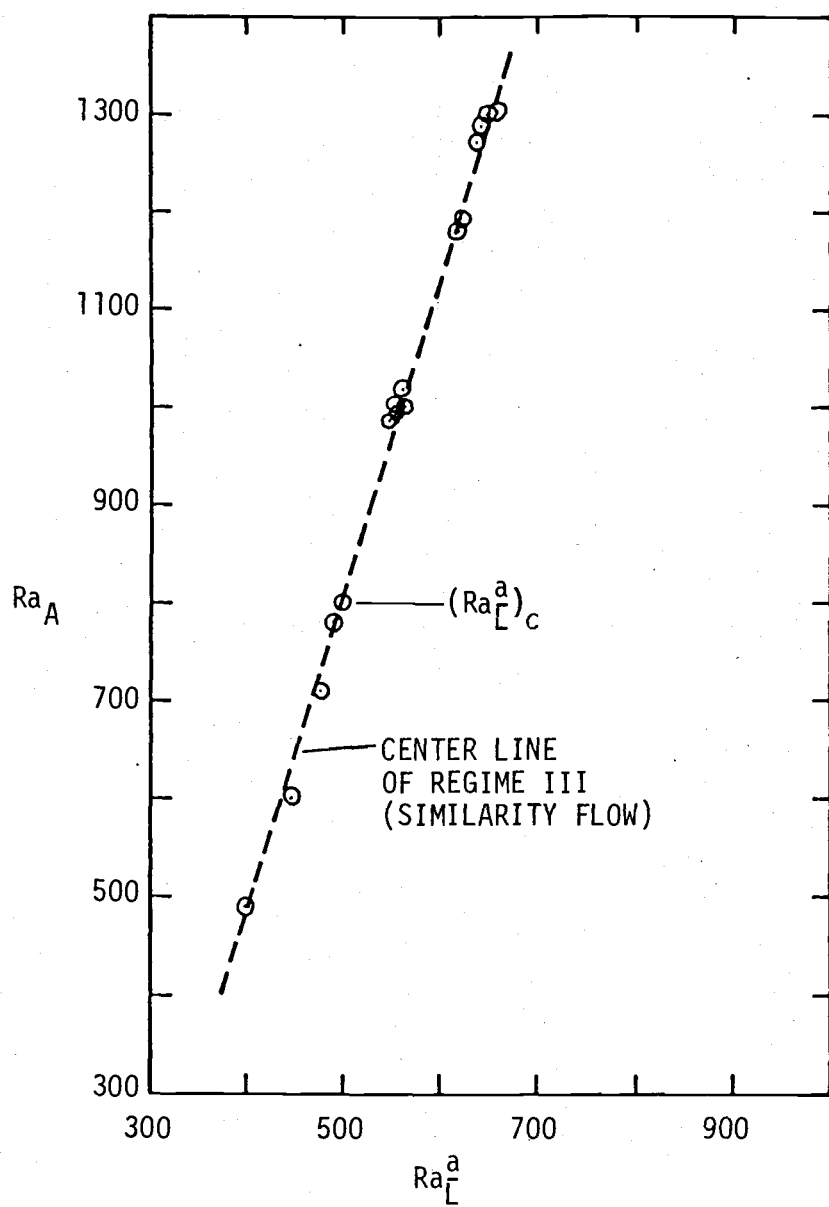


Figure 3.37 Corrected Ra_A^a for the flows in Regime IV (see also Fig. 3.33).

an interface of $\Psi = 0$ rather than a solid boundary, similarity flow tends to exist even for values of AR larger than 35. Finally, an equation expressing the relationship between Ra_A , Ra_L^a and L_C/L was derived from the data shown in Fig. 3.34 as follows: (a) first, a general expression for L_C/L lines was found as,

$$(\text{SLOPE}) = (Ra_A - 380)/(Ra_L^a - 380)$$

where (SLOPE) is a variable and represents slopes of L_C/L lines;

(b) then, (SLOPE) was related to L_C/L as,

$$(\text{SLOPE}) = 1.0 - 0.803 \ln(L_C/L)$$

where HP - 67 Curve Fitting routine was used and the coefficient of determination was found to be nearly unity [42,43]; and (c) the above two expressions were combined by (SLOPE) to obtain the following final expression,

$$Ra_A = (305 - .803 Ra_L^a) \ln \frac{L_C}{L} + Ra_L^a \quad (3.52)$$

where Ra_L^a lies between 380 and 1300, and L_C/L is from 0.05 (effectively zero) to 1.0. This equation was tested with all Ra_A values listed in Table 3.3 and the maximum error was found to be 1.6% which resulted with RUN NO. 84. Eq. (3.52) can also be written as follows to make L_C/L as a dependent variable,

$$L_C/L = \text{EXP}[(Ra_A - Ra_L^a)/(305 - .803 Ra_L^a)] \quad (3.53)$$

In Eqs. (3.52) and (3.53), $\text{Ra}_{\frac{a}{L}}$ can be replaced by,

$$\text{Ra}_{\frac{a}{L}} = (\text{Ra}_{\frac{a}{L}})_C \left(1 - \frac{L_C}{L} \frac{(T_1 - T_0)}{(T_1 - T_C)}\right) \quad (3.54)$$

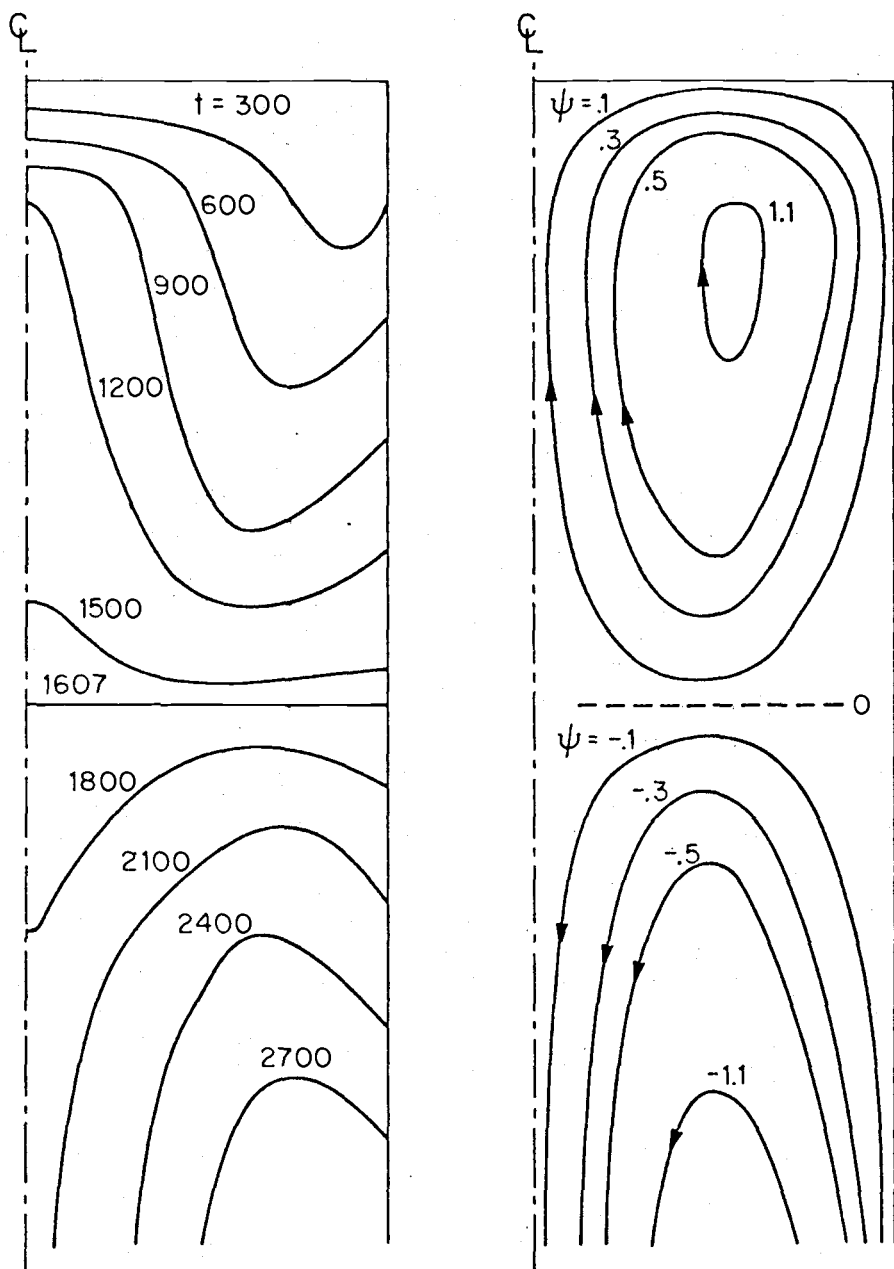
where $(\text{Ra}_{\frac{a}{L}})_C$ is the corresponding $\text{Ra}_{\frac{a}{L}}$ of the similarity-flow regime at the same Ra_A , and L_C/L in Eq. (3.54) can be replaced by,

$$\frac{L_C}{L} = (L_C/a)/AR \quad (3.55)$$

where L_C/a is the aspect-ratio of the cell.

Not many tests are made for the case where $\text{Ra}_A > 1300$, however, when values of $AR = 15$ at $\text{Ra}_A = 1580$ were specified, a strong continuous convection flow was found to fill the entire tube, as was already described in Fig. 3.28. When Ra_A was increased to about 3000 with $AR = 4$, a cell was found to form (see Fig. 3.38) within the upper portion of the cylinder. The noticeable difference between this cell and those found in Regime IV (see Fig. 3.30) is that the intensity of the cell found in this case is as strong as that of the continuous convection current beneath it; this was not the case in the previously found cells where $\text{Ra}_A < 1300$. A possible reason for the formation of a cell in the case of $\text{Ra}_A < 1300$ is that convection currents originating in the reservoir increasingly loses their momentum due to the decrease in the temperature difference between the fluid and the wall (or a corresponding decrease in the buoyancy force) while flowing up along the cylinder wall, thus before reaching the top of the cylinder the fluid reaches a condition of equilibrium at which point the fluid starts flowing

down to the reservoir along the axis of the cylinder. Meanwhile, the fluid within the top portion of the cylinder where fluid from the reservoir did not reach, forms its own weak circulation (or a convection cell), its direction being determined by that of the continuous convection fluid at the interface. In the case of cell formation with $Ra_A > 1300$, this same reasoning does not apply since both the cell and the continuous flow below it are of approximately equal strength as shown in Fig. 3.38. For this reason, streamlines are plotted in Fig. 3.39 at eight sequential stages before converging to the steady state case of Fig. 3.38. Referring to Fig. 3.39, at $I = 30$ (or after 30 iterations) flow originating in the reservoir does reach the top of the cylinder, however, a small cell of $\psi = .1$ has formed at the top corner of the cylinder. A possible reason for cell formation to originate at this particular place would be that the strong flow moving up along the wall responds to 90° corner such that when it suddenly meets the closed-end surface of the cylinder, part of the fluid is bent to the wall side creating a vortex at the corner with the rest traveling back to the reservoir. After the creation of this small vortex (or cell), it continues to grow (as in $I = 60$ and 90) by extracting heat from the main flow at the interface ($\psi = 0$) until the interface temperature becomes constant along a horizontal line as seen in Fig. 3.38. Meanwhile, the main flow, from which energy was lost to the cell, decreases in size and its region moves downward as the cell grows. Before reaching steady state the $\psi = 0$ line shifts vertically many times like a "border dispute" as seen in $I = 150$ through 700 . Finally when reaching steady state, the $\psi = 0$



RUN NO. 76

Figure 3.38 Cell formation in $AR=4$ at $Ra_A=2970$ and $Ra_L^a=2010$.

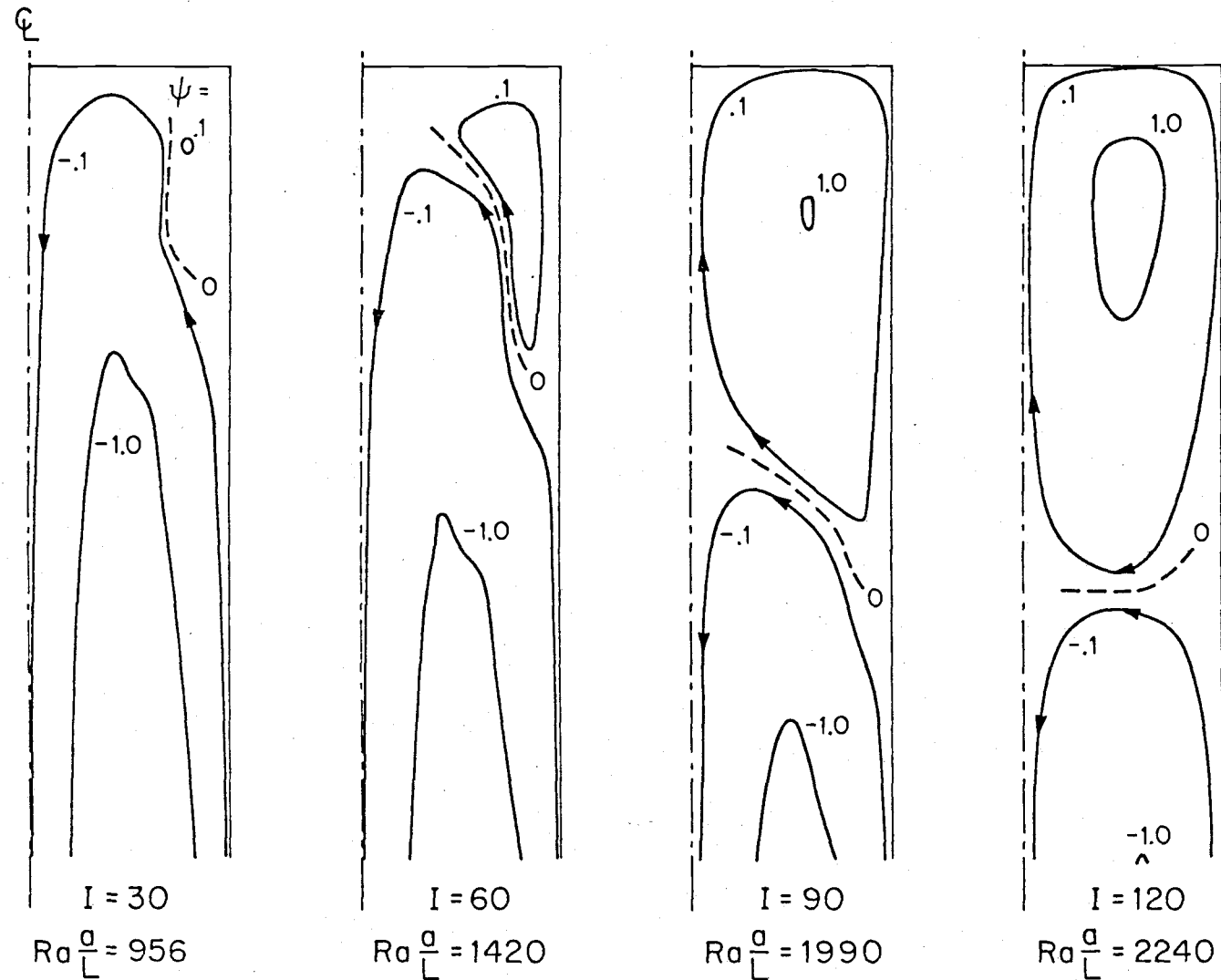


Figure 3.39 Development of a cell in $\text{AR}=4$ at $\text{Ra}_A=2970$ where I represents the number of iterations.

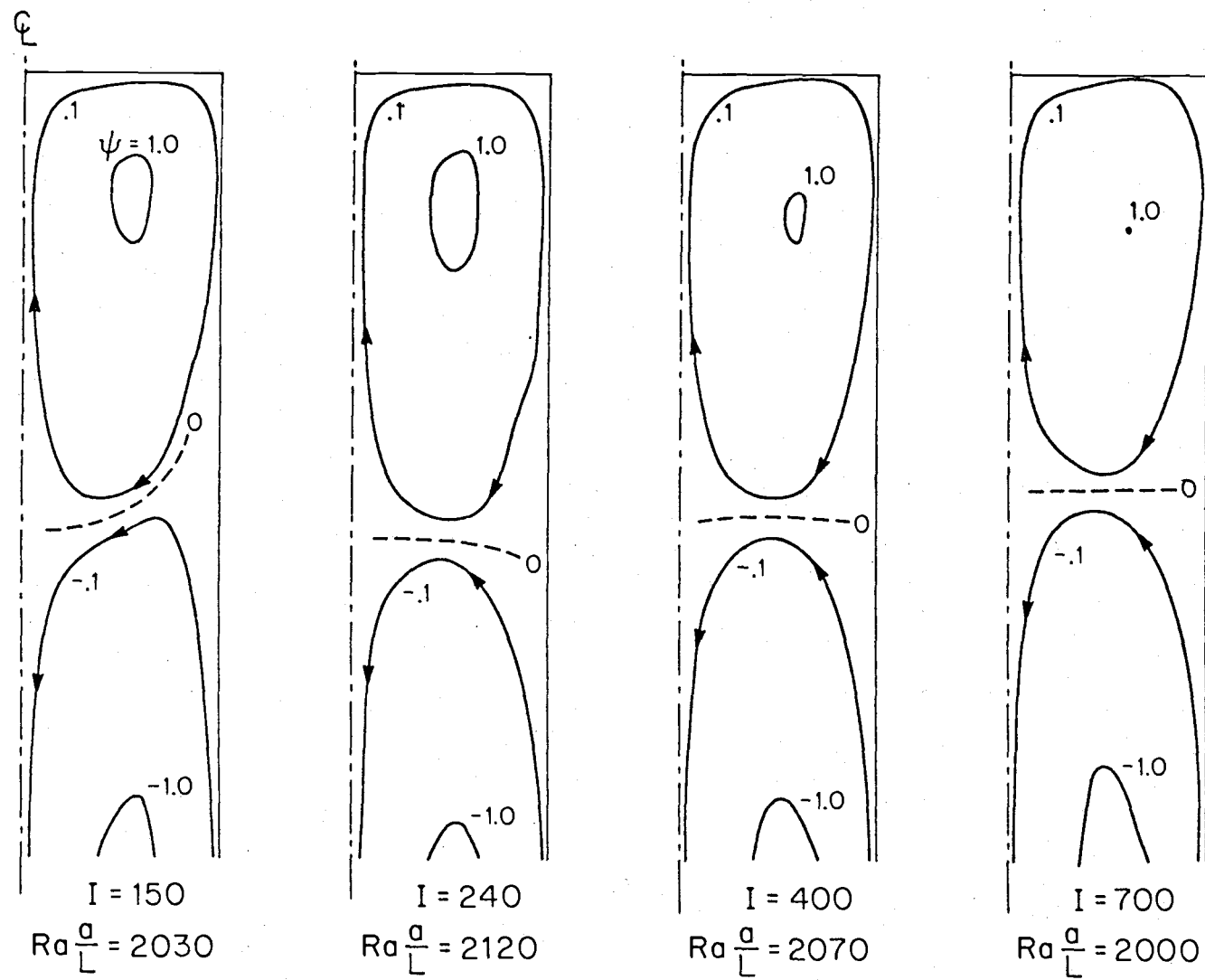


Figure 3.39 (continued).

line becomes horizontal and maintains this position.

All reasoning is done under the assumption that each iteration step in this steady-state numerical solution approximately equal to the time step of a transient solution, which is reasonable since the current numerical solution uses the iteration method rather than the matrix inversion method, as was true for both cases discussed in the earlier section of this chapter. The major difference between the steady-state and transient numerical solutions would be that in the latter case, the time increment (or step) can be controlled, whereas this is not possible in the steady-state numerical solution.

When Ra_A was increased beyond a value of 3000 at $AR = 4$, the numerical solution did not converge to a steady state limit, rather it became periodic with a near identical flow pattern occurring after a number of iteration steps. This is a periodic instability, similar to that experienced by Elder [18] who applied a similar iterative solution to a natural convection problem with two vertical parallel plates at different temperatures. Later, de Vahl Davis and Thomas [19] experienced a similar situation with their numerical solution for natural convection in a vertical annulus.

Several additional computer runs were made with different aspect ratios, at approximately the largest Ra_A for which instability would not occur; results of these runs are plotted against AR in Fig. 3.40 (also see Table 3.4). This plot indicates the existence of periodic instability to be strongly related to AR and Ra_A for $AR \leq 6$. For $AR > 6$ an increase in AR does not seem

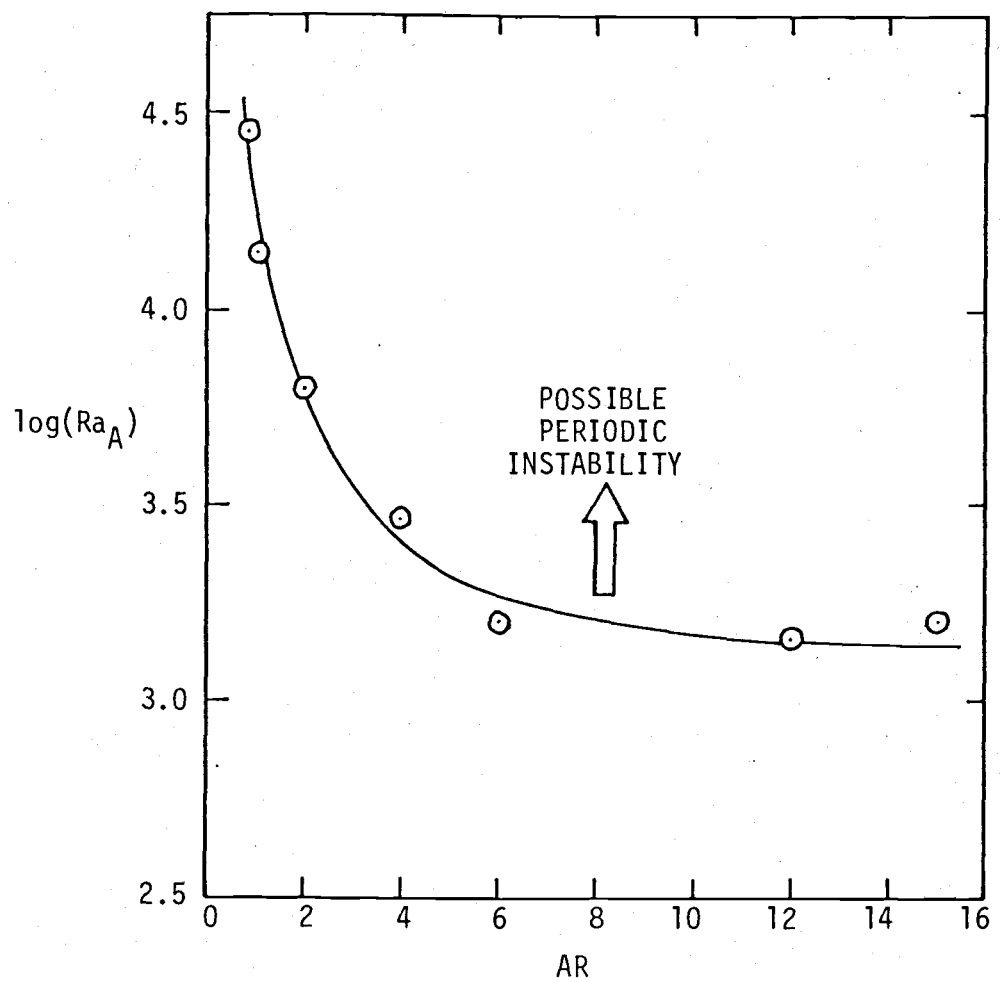


Figure 3.40 Region of periodic instability for $AR=.83$ to 15
(see also Table 3.4).

Table 3.4 The largest Ra_A without a periodic instability

Run No.	AR	Ra_A	$\log(Ra_A)$
05	.83	28,000	4.45
06	1.0	13,600	4.13
20	2.0	6,520	3.81
76	4.0	2,970	3.47
29	6.0	1,590	3.20
35	12.0	1,450	3.16
42	15.0	1,580	3.20

to influence the largest value of Ra_A .

Finally, within the similarity flow regime it is possible to compare numerical vs. theoretical values for the flow parameter, α ; axial velocity profiles; and temperature profiles. The cases specified in these comparisons are listed in Table 3.5, and the results are plotted in Figs. 3.41, 3.42, and 3.43. In Fig. 3.41, the numerically determined flow parameter, α , is compared with that obtained theoretically by Eq. (2.37). The greater difference between the two as $Ra_L^{\frac{1}{2}}$ increases may be due to a combination of the finite size of reservoir used and the linearization of terms in the momentum equations applied in this numerical solution. Probably, the linear variation α in Fig. 3.41 is an indication of a linear input specification while the theoretical α suggests a non-linear variation. This seems to be a reasonable explanation if one assumes the increase in $Ra_L^{\frac{1}{2}}$ (or Ra_A , at least, in the similarity flow regime) to cause a proportional change in the momentum, since momentum is non-linearly related to any of the flow variables. The author feels that the resulting difference in α may be caused by the use of a finite-size reservoir more than by the linearization, where the fluid traveling back into the reservoir must face the reservoir-bottom located within a finite distance from the orifice, which in turn influences the fluid within the cylinder.

In Figs. 3.42 and 3.43 the theoretically obtained velocity and temperature profiles using Eqs. (2.33) and (2.34) are plotted for comparison with numerically obtained profiles. The plots in these two figures indicate that, within the similarity flow regime, the general shapes of temperature and velocity profiles are

Table 3.5 Temperature and Velocity Profiles from Numerical and Theoretical Studies within the Similarity Flow Regime at AR = 15.

A) Cases

RUN No.	Ra_A	Ra_L^{α}	α_{ave}	St.D.	α_{max}	α_{min}
36	438	398	1.14	.03	1.26	1.11
37	849	511	11.78	.31	12.08	10.95
39	1190	610	21.00	1.05	22.00	18.38

B) Velocity Profile at $x = .533$ from the closed-end (Numerical results are in the first row and the similarity-solution values from Eq. (2.33) are in the second row of each case)

RUN No.	$u(x = .533)$					
	$r = 0$.2	.4	.6	.8	1.0
36	- .608	- .51	- .19	.07	.14	0
	- .608	- .47	- .15	.11	.12	0
37	- 6.40	-5.22	-1.75	.9	1.41	0
	- 6.28	-4.86	-1.6	1.13	1.27	0
39	-11.44	-9.16	-2.83	1.77	2.39	0
	-11.20	-8.67	-2.84	2.02	2.26	0

C) Temperature Profiles at $x = .533$ from the closed-end (Numerical results are in the first row and the similarity-solution values from Eq. (2.34) are in the second row of each case)

RUN No.	$t(x = .533)$					
	$r = 0$.2	.4	.6	.8	1.0
36	216	218	225	231	234	234
	212	215	221	227	232	234
37	278	312	390	461	481	455
	273	303	378	453	482	453
39	341	412	572	704	722	640
	325	390	546	694	731	635

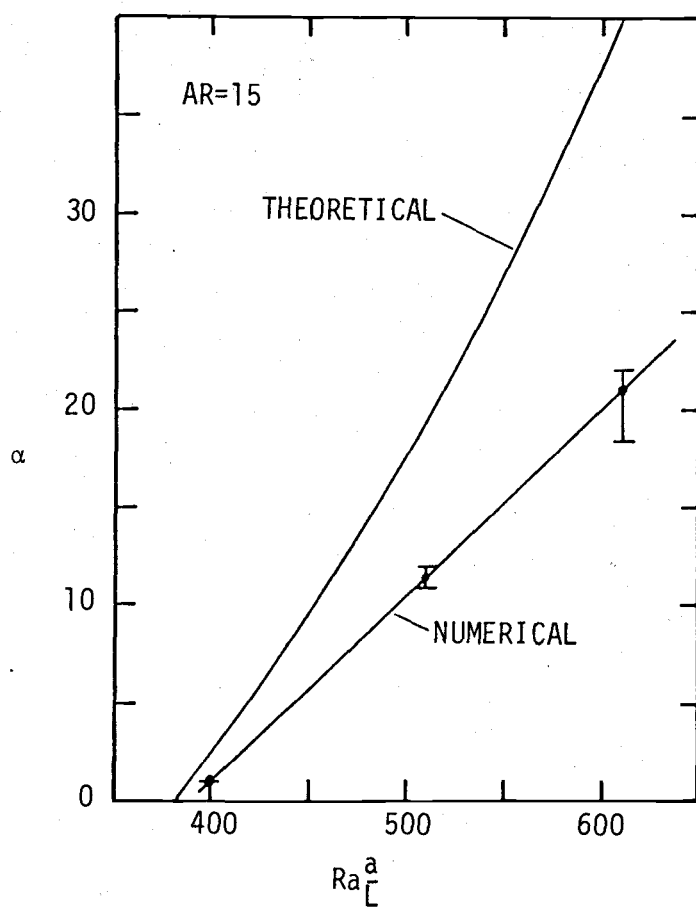


Figure 3.41 Theoretical and numerical flow parameter variations over the applicable Ra_L^a range.

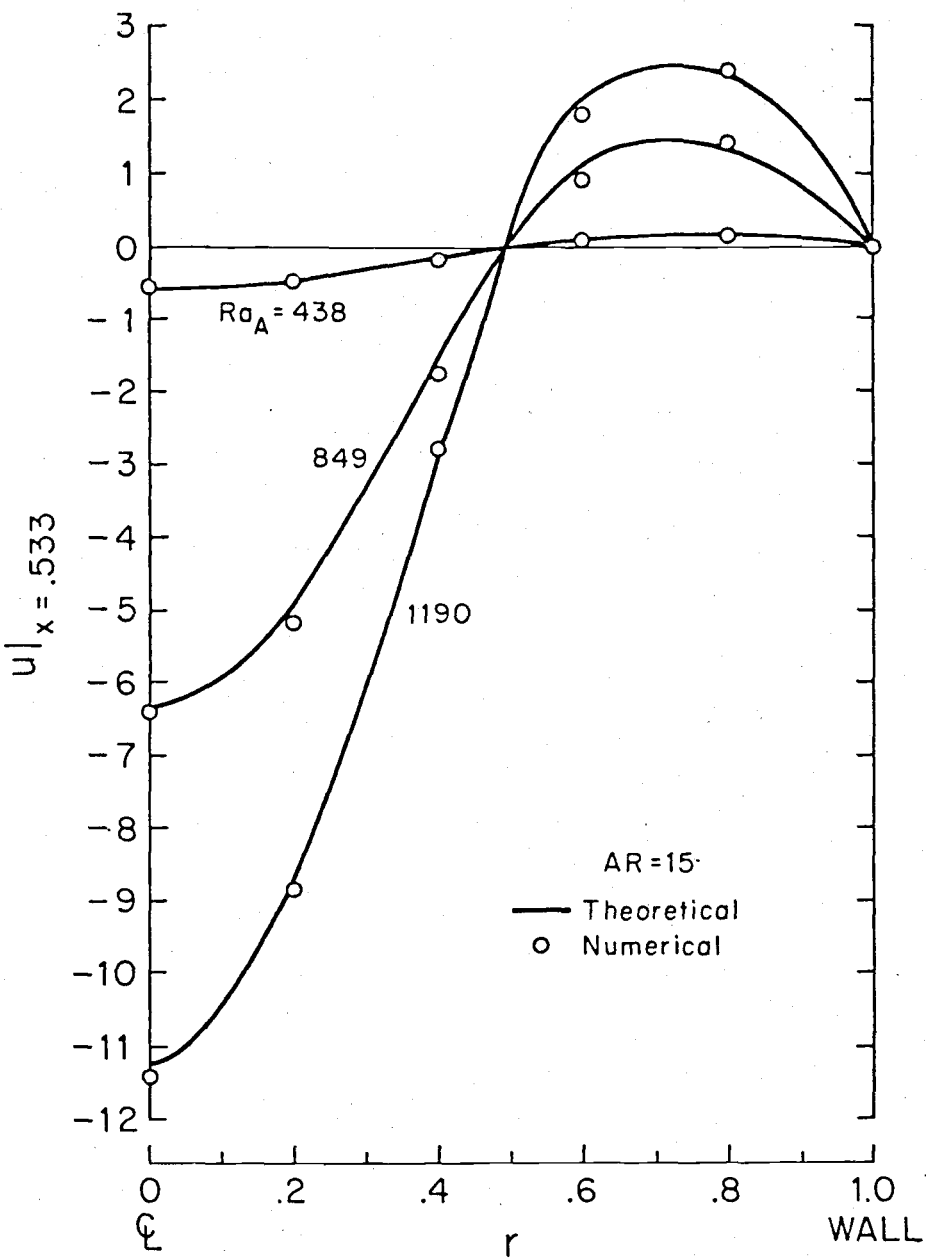


Figure 3.42 Theoretical and numerical velocity profiles within the similarity flow regime (see Table 3.5).

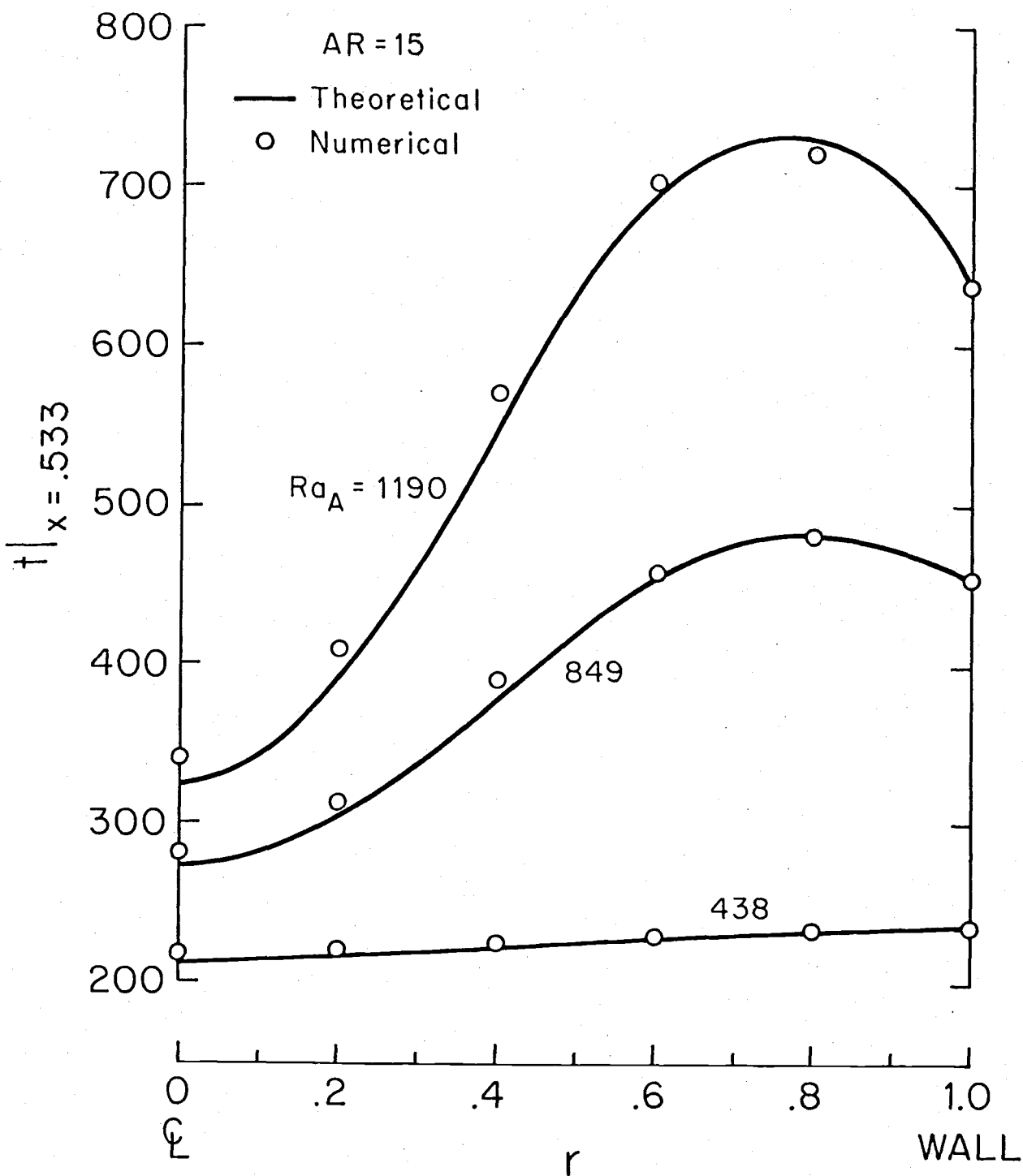


Figure 3.43 Theoretical and numerical temperature profiles within the similarity flow regime (see Table 3.5).

predicted with some precision by the current numerical solution. This very good comparison is further evidence that the numerical solution of this work does, indeed, yield physically meaningful results.

3.4.3 Nusselt Number and Heat Transfer Coefficient

The computer program, NUSSLT which is listed in App.-B, is used to calculate Nusselt number and local heat transfer coefficients along the cylinder wall.

First, in Fig. 3.44 (see Table 3.6) the mean Nusselt number is plotted as a function of Ra_A for $AR = 2, 15$, and 40 which represent the aspect ratios of Regimes I, III, and IV respectively. As seen in the figure, when $AR = 2$, much of the heat transfer appears to be from the fluid to the wall. However, for $AR = 15$ and 40 relatively little heat transfer takes place for $Ra_A \leq 400$ where very little convective flow occurs (Regime II). As soon as Ra_A increases to that of the similarity flow regime ($Ra_A > 400$) heat transfer sharply increases from the wall to the fluid.

To show the variation in heat transfer coefficients within Regimes I, III, and IV, local coefficients presented as $h/|h_{\max}|$ are plotted along the length of the cylinder in Fig. 3.45 for $AR = 2$ (Regime I), 15 (Regime III), and 70 (Regime IV). In this figure, most wall-to-fluid heat transfer is seen to occur when $AR = 15$, that is when similarity flow exists. When a cell is formed, as is typical in Regime IV, the direction of the heat transfer reverses to being from the fluid to the wall as indicated by the curve of $AR = 70$. Convection heat transfer is more balanced

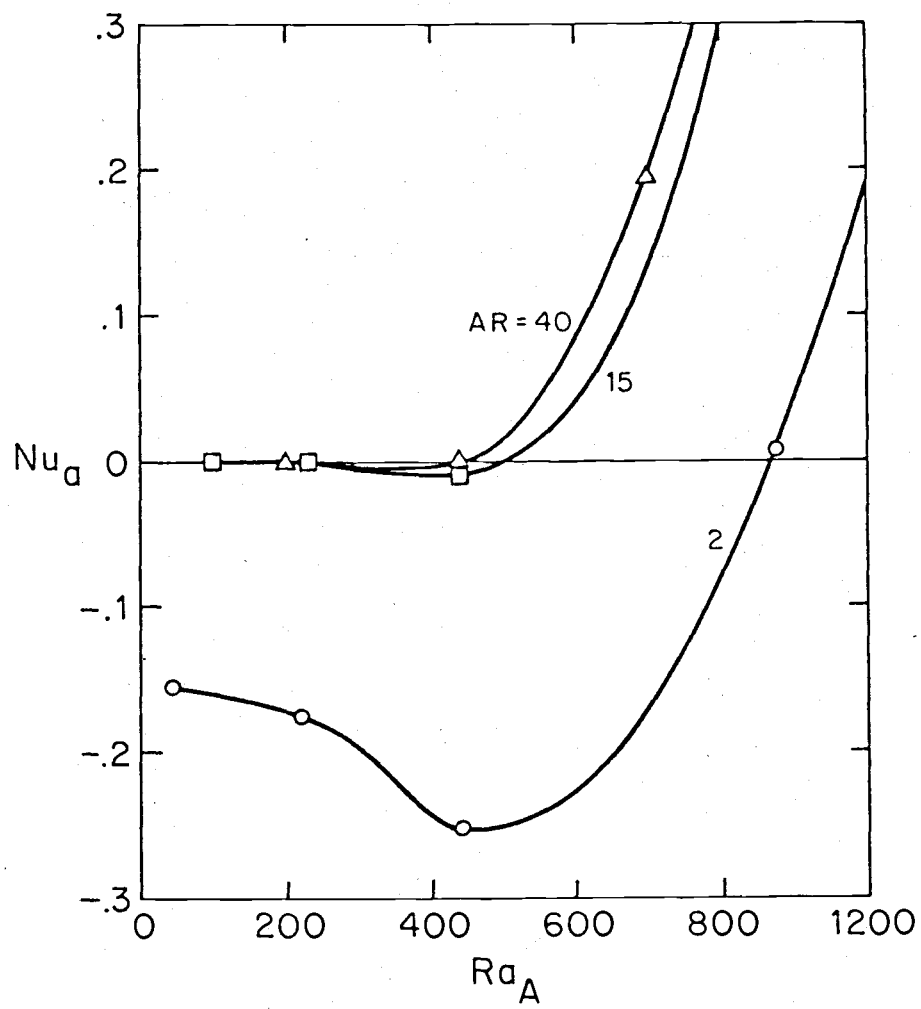


Figure 3.44 Net Nu_A vs. Ra_A for $AR=2$, 15 , and 40 (a negative Nu_A indicates the net heat transfer from the fluid to the cylinder wall).

Table 3.6 Nusselt Numbers for Various AR's

No.	Ra_A	Ra_L^a	Nu_a
<u>AR = 2</u>			
14	43.4	37.3	- .155
15	217	180	- .1767
16	434	325	- .253
17	869	493	.00714
18	1300	622	3.917
<u>AR = 15</u>			
40	99.6	98.0	- .0015
41	226	221	- .00133
36	438	398	- .0144
37	849	511	3.257
39	1190	610	10.56
<u>AR = 40</u>			
56	199	198	.002257
57	437	405	- .006719
58	696	501	.1886
54	1000	556	3.385
59	1290	642	88.27

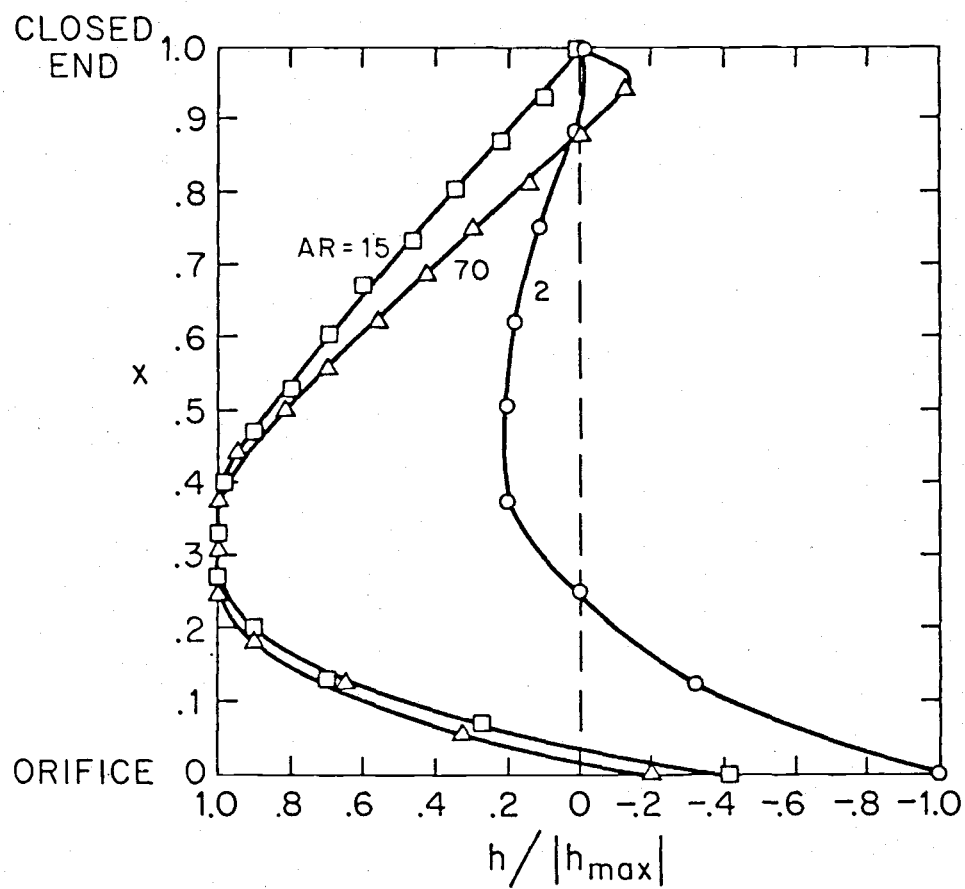


Figure 3.45 Variation of local heat transfer coefficients along the cylinder length at $Ra_A \approx 1000$ for $AR=2, 15, 70$.

between the two directions when $AR = 2$, which apparently is typical for Regime I. The similarity of the two curves for $AR = 15$ and 70 up to $x = .5$ is due to the formation of similarity flow in both cases.

3.4.4 Cases of Lighthill and Ostrach

A minor change was made in the current numerical program such that it could accept the configurations that were previously investigated by Lighthill [11] for $Ra_A = 0$ and by Ostrach and Thornton [14] for negative Ra_A (indicating that the wall temperature increases in the direction opposite to the applied body force, see Fig. 3.46). With this modified program, several additional computer runs (see Table 3.7) were made with $AR = 15$ which was chosen because it was well within the similarity flow regime. The results of this investigation are presented in Fig. 3.47.

Fig. 3.47 indicates that the theoretically derived applicable range of Ostrach and Thornton ($-1600 < Ra_A < 0$ and $0 < Ra_{\frac{d}{L}} < 310$) for similarity flow agrees with the numerical solution up to $Ra \geq -300$ for $AR = 15$. When Ra_A is assigned larger negative values, the similarity-flow curves resulting from the numerical solution deviates from that of the theoretical solution, and becomes increasingly divergent as Ra_A takes on larger negative values. To assist in explaining this deviation, the streamlines of the data points indicated in Fig. 3.47 were plotted and are presented in Figs. 3.48 and 3.49. The streamline plot indicates that a vigorous flow exists toward the open-end of the cylinder but does not penetrate far toward the closed-end. What this means, is that for the

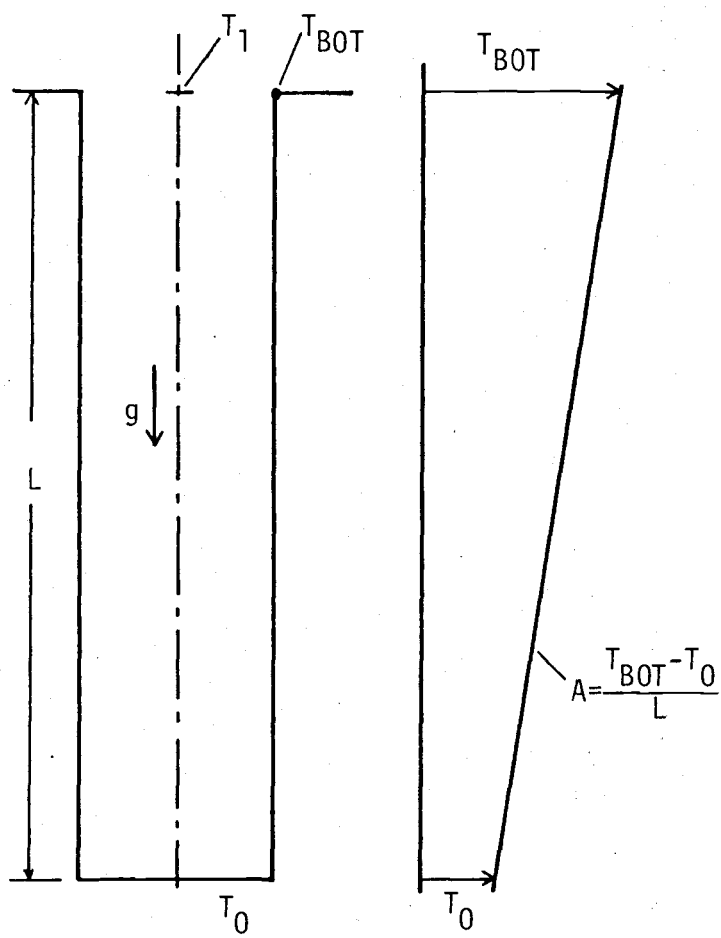


Figure 3.46 Configuration of the model investigated by Lighthill when $A=0$, and later by Ostrach and Thornton when $A\neq 0$.

Table 3.7 Computer Runs made for the Cases of Lighthill
and Ostrach (S - Similarity flow; N - no)

Run No.	AR	Ra _A	Ra _L ^a	I	S/N
99	15	-792	169	112	N
100	15	-792	256	111	S
101	15	-407	250	116	S
102	15	-407	272	115	N
103	15	-306	255	118	S
104	15	-91	277	120	N
105	15	-91	288	120	S
106	15	0	293	116	N
107	15	0	400	119	N
108	15	0	241	116	N
109	15	0	304	116	S
110	15	0	507	118	N
111	15	0	193	158	N
112	15	113	301	112	N
113	15	113	322	117	S
114	15	113	407	116	N
115	15	260	355	84	S
116	15	260	344	101	N
117	15	396	605	117	N
118	15	396	424	91	N
119	15	453	430	911	N
120	15	453	431	936	N
121	15	679	627	1011	N

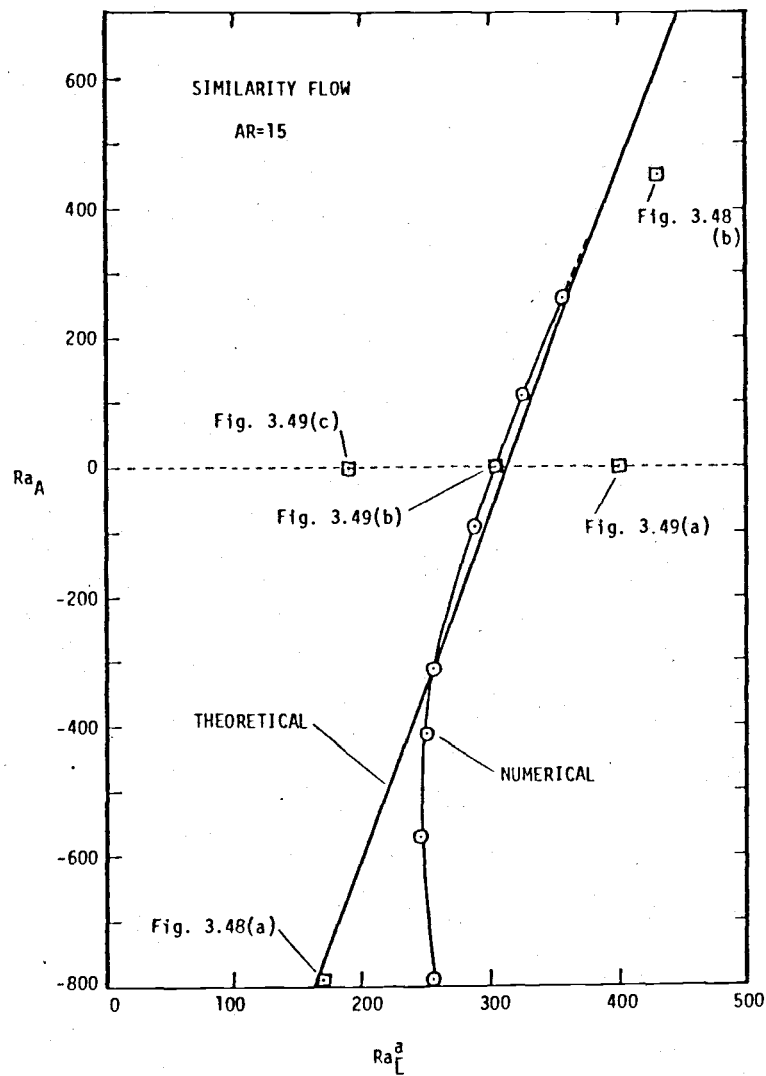


Figure 3.47 Comparison of similarity flows resulted from the theoretical and from the numerical analysis at AR=15.

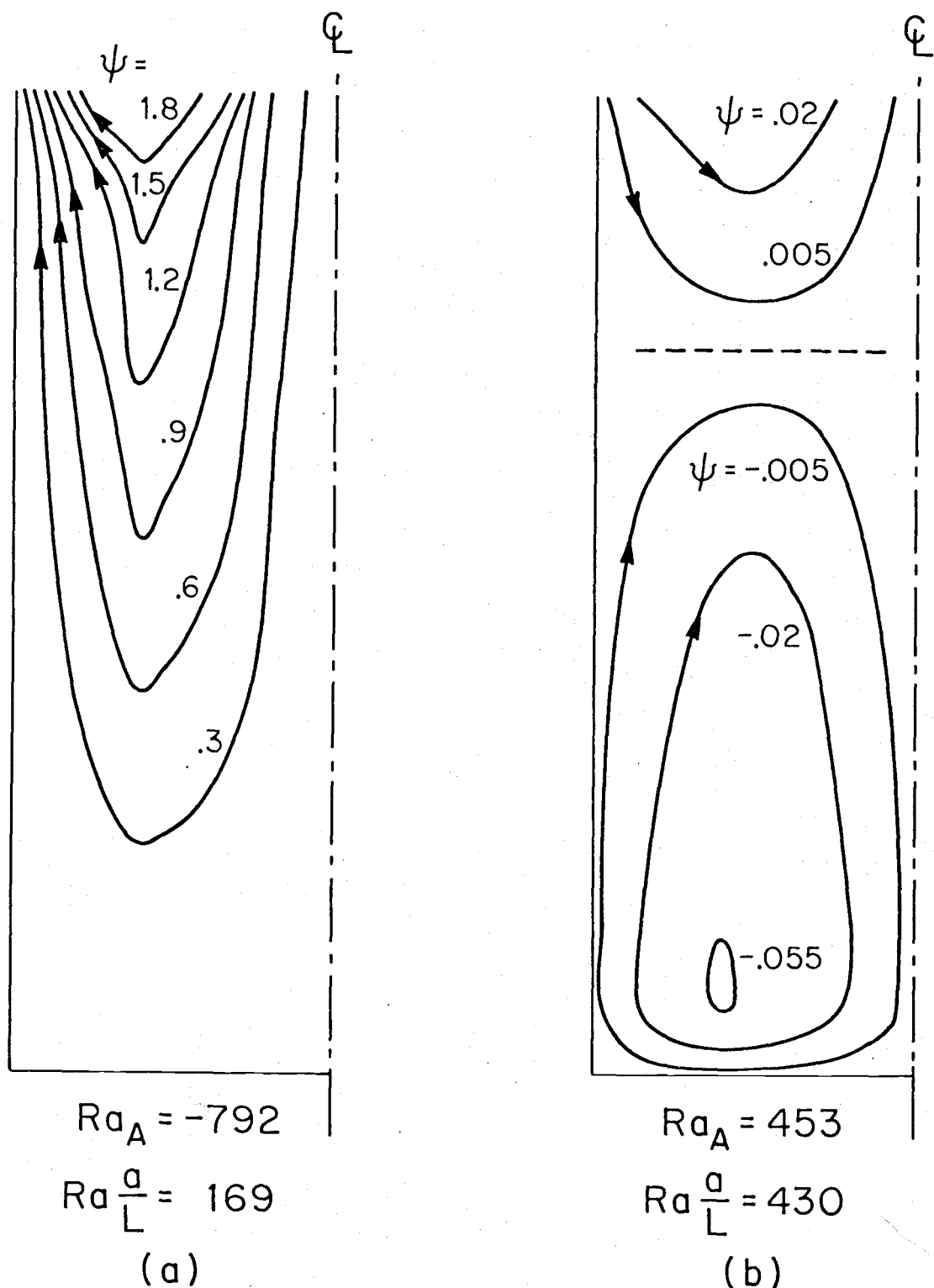


Figure 3.48 Streamlines of non-similarity flows in the Ostrach's configuration at $AR=15$.

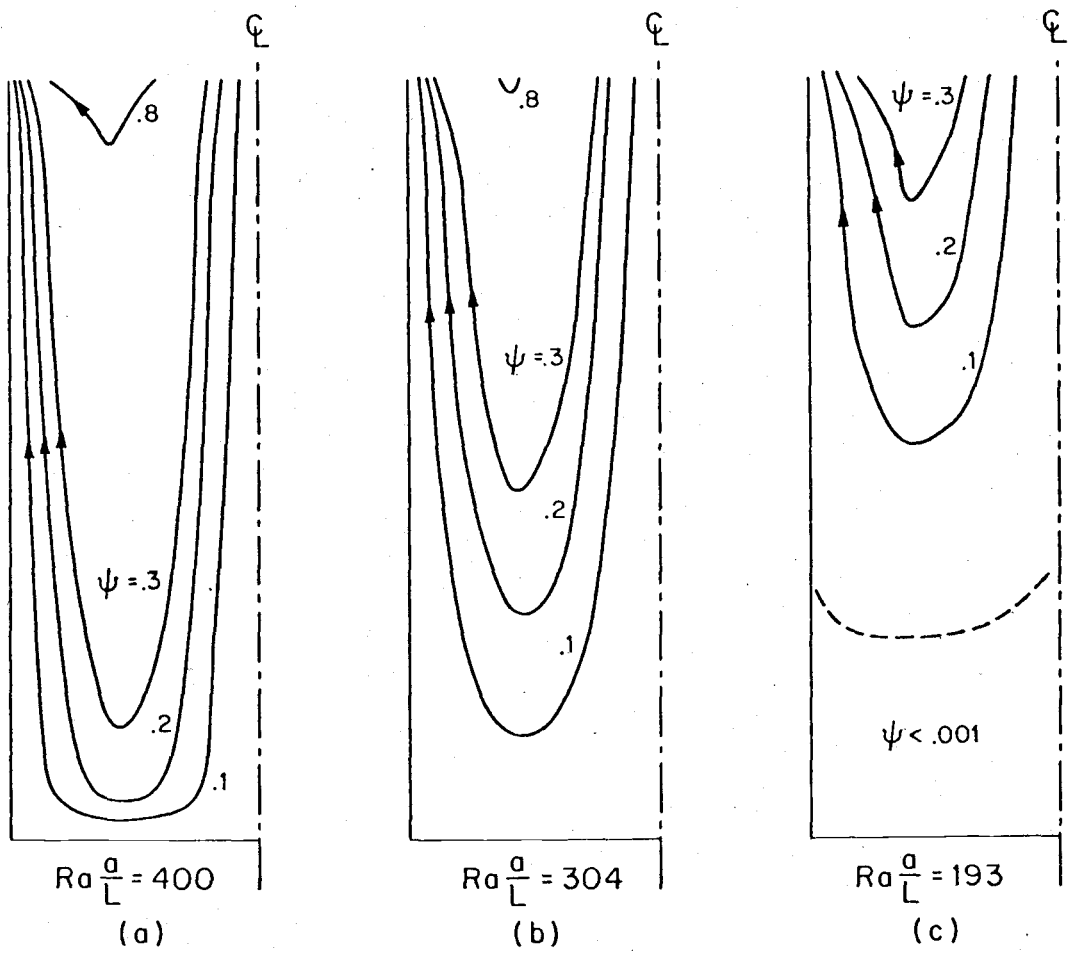


Figure 3.49 The case of Lighthill where $R_A=0$ at $AR=15$ for various $\frac{Ra}{L}$.

imposed $Ra_A = -800$, the theoretically predicted value of $Ra_L^a = 170$ was not sufficiently large to produce a strong flow far toward the closed region of the cylinder. It appears that to form a similarity flow at $Ra_A = -800$, Ra_L^a must be as large as 250, which is the value shown in Fig. 3.47.

Again referring to Fig. 3.47, similarity flow resulting from the numerical solution exists for positive values of Ra_A which was not predicted by Ostrach and Thornton. The upper limit for $AR = 15$ is found to be near $Ra_A = 350$ which is interestingly, the approximate Ra_A value where similarity flow for the previous case begins (see the flow regime map, Fig. 3.32). This is also the point where flow reversal is theoretically predicted (see Fig. 2.5). For this case, the reason that similarity flow is not achieved is that a cell is formed as Fig. 3.48(b) illustrates. The formation of the cell is probably due to the excessively large temperature gradient decreasing from the bottom (hottest) to the open-end. It was also found that in the vicinity of the theoretically-predicted similarity-flow curve for $Ra_A > 350$, the numerical solution required more iterations to reach convergence than when $Ra_A < 350$. This seems to indicate that the nature of the flow described above is very similar to that of the previous configuration where cell formation was indicated when Ra_A was larger than 1300 (compare Fig. 3.48(b) with Fig. 3.38), also, in the latter case, some indication of instability was detected.

The Lighthill case is for $Ra_A = 0$. He predicted that if the flow is similar, the modified Rayleigh number, Ra_L^a , should have a value near 311. This was also predicted by Ostrach and Thornton

and by the theoretically determined result in Chap. II. In the present numerical study, it was computed to be $Ra_L^{\alpha} = 305$ as seen in Fig. 3.47, thus good agreement is also obtained here. To show further the differences in flow characteristics at $Ra_A = 0$, three conditions with data points indicated by figure numbers along the $Ra_A = 0$ line were examined; their streamlines are plotted in figure numbers, Fig. 3.49(a), (b) and (c). The streamline pattern in Fig. 3.49(a) occurs when Ra_L^{α} is larger than that of similarity flow, which indicates that the non-similarity flow is formed due to an excessively strong convection current from the reservoir reaching the closed-end. This trend was found to be true as well for the region to the right side of the numerically obtained similarity-flow curve. Also, this situation compares well with flow results obtained in the previous case when Ra_A was about 1300 or larger (see Fig. 3.28). The streamlines in Fig. 3.49(b) are typical of similarity flow a case already discussed when similarity flow was obtained (see Fig. 3.27). and as seen in these two figures, they are very much alike. Fig. 3.49(c) shows the streamlines for the situation where Ra_A is smaller than that of similarity flow at $Ra_A = 0$. The reason for not able to achieve similarity flow here is that the temperature difference between the fluid in the reservoir and the cylinder wall was too small thus Ra_L^{α} did not reach a large enough value such that the flow originating within the reservoir then moving down along the axis of the cylinder achieved temperature equilibrium before reaching the bottom portion of the cylinder. Thus, the fluid within a certain distance from the closed-end appeared to remain stagnant.

By examining the temperature field of this particular run it is seen that, within about 0.27 L from the closed-end of the cylinder, the fluid temperature remained the same as that at the wall. Again comparing this situation with that of the previous configuration, this result agrees well with what was discussed for the resulted flow when $Ra_A < 380$ and $4 < AR < 35$ or it was named Flow Regime II in Fig. 3.32.

Finally, the theoretical and numerical flow parameter α is compared in Fig. 3.50 for this particular configuration where the reservoir is located on top of the cylinder and the body force is directed downward. In Fig. 3.50, each numerically obtained α is the average of those along the centerline nodes with AR again restricted to a value of 15. In this figure, we see again the deviation of the numerically determined α from the theoretical one as was seen in Fig. 3.41 of the previous configuration. However, the type of deviation in this case is different from that in Fig. 3.41, in that the numerically estimated α is larger than the theoretical value over a wide range in Ra_L^{α} as seen in Fig. 3.50, while Fig. 3.41 indicated the opposite. The reason for this deviation is again due to the finite size of reservoir used in the numerical solution. In this case the reservoir was located on top of the cylinder, and similarity flow was downward along the cylinder-axis. Thus, the reasoning used for Fig. 3.41 does not apply here. Instead the reason would be that, since the cold reservoir wall at the top of the system was located sufficiently near such that the returning fluid from the cylinder was intensely cooled by the nearby cold reservoir-wall and which, in turn, returned into

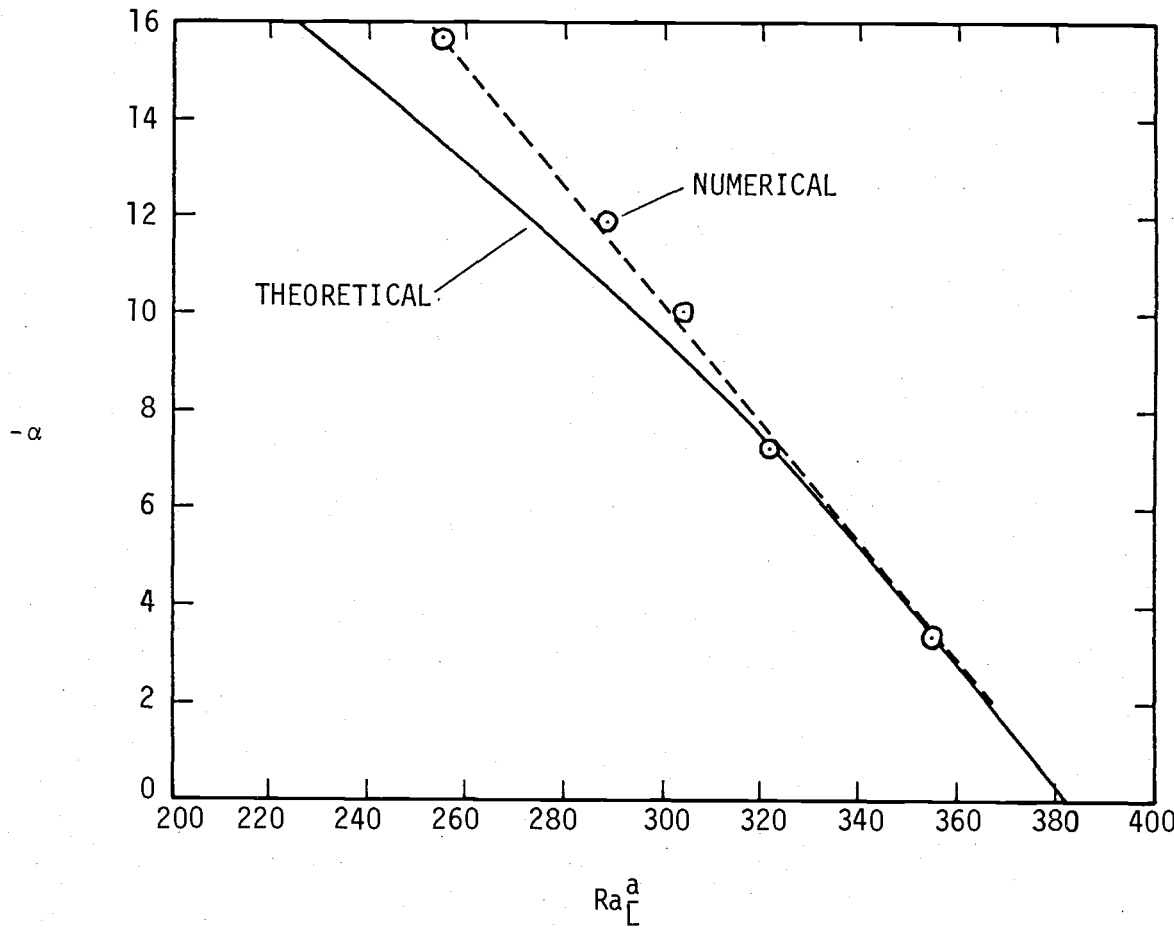


Figure 3.50 Comparison of the theoretical and numerical flow parameters for the cases of Lighthill and Ostrach; $-306 < Ra_A^a < 260$, and $255 < Ra_A^a < 355$.

the cylinder down along the axis at a much faster rate than when there was no restriction made on the reservoir size.

IV. CONCLUSIONS AND RECOMMENDATIONS

A closed-form solution was developed and solved for similarity flow in Chap. II, and the finite-difference solution was developed in Chap. III to obtain the information for non-similarity flow regimes not predicted by the above closed-form solution. Based upon the results reported in these respective chapters, the following conclusions can be listed:

- 1) The analytically defined similarity-flow regime was well predicted by the numerical solution for $380 < Ra_A < 1200$ and $380 < Ra_L^a < 660$.
- 2) The result given by the numerical solution further defined three other flow regimes within the approximate Rayleigh-number ranges of $0 < Ra_A < 1300$ and $0 < Ra_L^a < 1000$. One may thus identify the convection flow upon specifying Ra_A , Ra_L^a , and AR of such geometries (see Fig. 3.32).
- 3) Flow regime IV (see Fig. 3.32) in which a secondary-flow cell formed, was further investigated to define the geometric characteristics of cells. Again by specifying two of the three parameters within this flow regime, one can identify the convection flow as well as cell sizes, parametrically, either by Fig. 3.34 or by Eq. (3.52).
- 4) The theoretically determined similarity flow of Lighthill's configuration was duplicated by the numerical solution with $Ra_A = 0$ and $Ra_L^a = 310$, and further, two flow patterns, one for $Ra_L^a < 310$ and the other for $Ra_L^a > 310$, were characterized for $AR = 15$. Also, the case of Ostrach and Thornton was run

for $AR = 15$ and it was subsequently demonstrated that the numerically predicted similarity flow by the current solution agreed reasonably well with that of Ostrach and Thornton. The current numerical solution, however, was also capable of generating isotherms and streamlines for this case, which enabled the author to explain the above partial agreement of the similarity flow in detail as well as to describe the non-similarity flows of their configuration (see Sec. 3.4.4).

- 5) With regard to the application of the current results to a typical geothermal well where $Ra_A \approx 10^7$ and $AR > 150$, a direct correlation is not possible for such large values of Ra_A . However, based on the conclusion presented so far it would be safe to assume that in such geometries one can expect at least a break-down of continuous convection flow originating in the reservoir, such that the top portion of the well would be occupied either by secondary flow (or cell), or by periodically unstable convection flow.

Overall, as was proposed originally, the fundamental problem was solved mainly by means of the numerical solution, with results yielding sufficient information for one to understand the convection flows in such geometries at least for $0 < Ra_A < 1300$ and $0 < Ra_L^a < 1000$, and in lesser degree for $Ra_A > 1300$. Thus to define other possible flow regimes in a region with Ra_A much larger than 1300, any solution must account for turbulent effects. By doing so and having the current result for the case of laminar flows, one may also be able to determine the transitional Rayleigh numbers. Finally, the validation of both cases by experiment will complete the current problem.

V. BIBLIOGRAPHY

1. Benard, H., "Les Tourbillons Cellulaires dans Une Nappe Liquide Transportant de la Chaleur par Convection en Régime Permanent," Annales de Chimie et de Physique, Vol. 23, 1901, pp. 62-144.
2. Rayleigh, Lord, "On Convective Currents in a Horizontal Layer of Fluid When the Higher Temperature is on the Underside," Phil. Mag., Vol. 32, 1916, pp. 529-546.
3. Jeffreys, H., The Earth, Its Origin, History and Physical Condition, 2nd Ed., Cambridge, England, Univ. Press, 1929.
4. Hales, A. L., "Convection Currents in Geysers," Royal Astron. Soc. Geophys. Suppl., Vol. 4, No. 1, 1937, pp. 122-131.
5. Pellew, A., and R. V. Southwell, "On Maintained Convective Motion in a Fluid Heated From Below," Proceedings, Royal Society, Series A, Vol. 176, 1940, pp. 312-343.
6. Krige, L. J., "Borehole Temperatures in the Transvaal and Orange Free State," Royal Soc. London Proc., Ser. A, Vol. 173, 1939, pp. 450-474.
7. Diment, W. H., "Thermal Regime of a Large Diameter Borehole: Instability of the Water Column and Comparison of Air- and Water-Filled Conditions," Geophysics, Vol. 32, No. 4, 1967, pp. 720-726.
8. Gretener, P., "On the Thermal Stability of Large Diameter Wells - An Observational Report," Geophysics, Vol. 32, No. 4, 1967, pp. 727-738.
9. Sammel, E. A., "Convective Flow and Its Effect on Temperature Logging in Small-Diameter Wells," Geophysics, Vol. 33, No. 6, December 1968, pp. 1004-1012.
10. Donaldson, I. G., "Free Convection in a Vertical Tube with a Linear Wall Gradient," Aust. J. Phys., Vol. 14, 1961, pp. 529-539.
11. Lighthill, M. J., "Theoretical Considerations of Free Convection in Tubes," Quarterly Journal of Mech. and App. Math., Vol. 6, 1953, pp. 398-439.
12. Martin, B. W., and H. Cohen, "Heat Transfer by Free Convection in an Open Thermosyphon Tube," Brit. J. Appl. Phys., Vol. 5, 1954, pp. 91-96.
13. Martin, B. W., "Free Convection in an Open Thermosyphon with Special Reference to Turbulent Flow," Proc. of the Royal

Society, Ser. A, Math. and Phys., Vol. 230, No. 1183, July 1955, pp. 502-530.

14. Ostrach, S., and P. R. Thornton, "On the Stagnation of Natural-Convection Flows in Closed-End Tubes," Trans. ASME, Vol. 80, 1958, pp. 363-366.
15. Hasegawa, S., "Heat Transfer in an Open Thermosyphon," Japan Soc. Mech. Engrs. Trans., Vol. 28, No. 192, August 1962, pp. 930-960.
16. Elder, J. W., "Laminar Free Convection in a Vertical Slot," J. Fluid Mech., Vol. 23, Part I, 1965, pp. 77-98.
17. Elder, J. W., "Turbulent Free Convection in a Vertical Slot," J. Fluid Mech., Vol. 23, Part I, 1965, pp. 99-111.
18. Elder, J. W., "Numerical Experiments with Free Convection in a Vertical Slot," J. Fluid Mech., Vol. 24, Part 4, 1966, pp. 823-843.
19. Vahl Davis, G. de, and R. W. Thomas, "Natural Convection between Concentric Vertical Cylinders," High Speed Computing in Fluid Dynamics, The Physics of Fluid Supplement II, 1969, pp. II-198 - II-207.
20. Vahl Davis, G. de, and G. D. Mallinson, "A Note on Natural Convection in a Vertical Slot," J. Fluid Mech., Vol. 72, part 1, 1975, pp. 87-93.
21. Batchelor, G. K., "Heat Transfer by Free Convection across a Closed Cavity between Vertical Boundaries at Different Temperatures," Quarterly of Applied Mathematics, Vol. XII, No. 3, Oct., 1954, pp. 209-233.
22. Vest, C. M., and V. S. Arpacı, "Stability of Natural Convection in a Vertical Slot." J. Fluid Mech., Vol. 36, Part 1, 1969, pp. 1-15.
23. Ostrach, S., and C. Raghavan, "Effect of Stabilizing Thermal Gradients on Natural Convection in Rectangular Enclosure," Presented at the AIAA-ASME Thermophysics and Heat Transfer Conference, Palo Alto, Calif., May 24-26, 1978.
24. Barakat, H. Z., and J. A. Clark, "Analytical and Experimental Studies of the Transient Laminar Natural Convection Flows in Partially Filled Liquid Containers," Third International Heat Transfer Conference Proceeding, 1966, pp. 152-162.
25. Kee, R. J., C. S. Landram, and J. C. Miles, "Natural Convection of a Heat Generated Fluid within Closed Vertical Cylinders and Spheres," J. of Heat Transfer, Feb. 1976, pp. 55-61.

26. Torrance, K. E., "Comparison of Finite-Difference Computations of Natural Convection," J. of Research of the National Bureau of Standards - B, Mathematical Sciences, Vol. 72B, No. 4, Oct.-Dec. 1968, pp. 281-301.
27. Powe, R. E., and R. M. Comfort, "Numerical Solution of Two-Dimensional Natural Convection in Enclosed Spaces," Presented at the Winter Annual ASME Meeting, San Francisco, Calif., Dec. 10-15, 1978.
28. Newell, M. E., and F. W. Schmidt, "Heat Transfer by Laminar Natural Convection within Rectangular Enclosures," J. of Heat Transfer, Feb. 1970, pp. 159-168.
29. Ozoe, H., K. Yamamoto, S. W. Churchill, and H. Sayama, "Three-Dimensional, Numerical Analysis of Laminar Natural Convection in a Confined Fluid Heated from Below," J. of Heat Transfer, ASME, Vol. 98, Series C, n2, May 1976, pp. 202-207.
30. Hwang, G. J., and K. C. Cheng, "Boundary Vorticity Method for Convection Heat Transfer with Secondary Flow-Application to the Combined Free and Forced Laminar Convection in Horizontal Tubes," Fourth International Heat Transfer Conference Proceeding, Vol. IV, 1970, NC3.5, pp. 1-12.
31. Pepper, D. W., and S. D. Harris, "Numerical Solution of Three Dimensional Natural Convection by the Strongly Implicit Procedure," Presented at the Winter Annual ASME Meeting, San Francisco, Calif., Dec. 10-15, 1978.
32. Mallinson, G. D., and G. de Vahl Davis, "The Method of the False Transient for the Solution of Coupled Elliptic Equations," J. of Computational Physics, Vol. 12, 1973, pp. 435-461.
33. White, F. M., Viscous Fluid Flow, McGraw-Hill Book Co., 1974.
34. Kays, W. M., Convective Heat and Mass Transfer, McGraw-Hill Book Co., 1966.
35. Carnahan, B., H. A. Luther, and J. O. Wilkes, Applied Numerical Method, John Wiley and Sons, Inc., New York, 1969.
36. Gerald, C. F., Applied Numerical Analysis Addison-Wesley Publishing Co., Massachusetts, 1970.
37. James, M. L., G. M. Smith, and J. C. Wolford, Applied Numerical Methods for Digital Computation, Second Edition, IEP-ADun-Donnelley Publisher, New York, 1977.
38. Patankar, S. V., Numerical Heat Transfer and Fluid Flow, Hemisphere Publishing Co., Washington, 1980.

39. Conte, S. D., and C. de Boar, Elementary Numerical Analysis, 2nd ed., McGraw-Hill Book Co., New York, 1972.
40. Forsythe, G. E., and W. R. Wasow, Finite-Difference Methods for Partial Differential Equations, John Wiley and Sons, Inc., New York, 1960.
41. Forsythe, G. E., and C. B. Moler, Computer Solution of Linear Algebraic Systems, Prentice-Hall, Inc., New Jersey, 1967.
42. Neter, J., and W. Wasserman, Applied Linear Statistical Methods, Regression, Analysis of Variance, and Experimental Designs, Richard D. Irwin Inc., Illinois, 1974.
43. Hewlett-Packard, HP-67, Standard Pac, Cupertino, California, 1976.

APPENDICES

VI. APPENDICES

- A. Modified Numerical Equations
- B. Computer Codes
 - B-1 Program NATCON
 - B-2 Example Input-Output Listing of NATCON
 - B-3 Program NUSSLT

Appendix A

Modified Numerical Equations

This appendix is referred first time in Section 3.3.1, and contains the modified form of the numerical equations developed in Sec. 3.2. This modification was necessitated by the application of Gauss-Seidel iterative method to this problem.

Energy Equations:

- 1) for the internal nodes when $U \geq 0$ and $V \geq 0$ (from Eq. (3.10))

$$T_{i,j} = \left[\left(\frac{U}{\alpha \Delta X} + \frac{1}{(\Delta X)^2} \right) T_{i-1,j} + \left(\frac{V}{\alpha \Delta R} + \frac{1}{(\Delta R)^2} - \frac{1}{2R(\Delta R)} \right) T_{i,j-1} \right. \\ \left. + \left(\frac{1}{(\Delta R)^2} + \frac{1}{2R(\Delta R)} \right) T_{i,j+1} + \frac{T_{i+1,j}}{(\Delta X)^2} \right] \\ \left[\frac{1}{\alpha} \left(\frac{U}{\Delta X} + \frac{V}{\Delta R} \right) + 2 \left(\frac{1}{(\Delta R)^2} + \frac{1}{(\Delta X)^2} \right) \right]$$

- 2) for the internal nodes when $U \geq 0$ and $V < 0$ (from Eq. (3.10))

$$T_{i,j} = \left[\left(\frac{1}{(\Delta R)^2} - \frac{1}{2R(\Delta R)} \right) T_{i,j-1} + \left(\frac{1}{(\Delta R)^2} + \frac{1}{2R(\Delta R)} - \frac{V}{\alpha \Delta R} \right) T_{i,j+1} \right. \\ \left. + \left(\frac{1}{(\Delta X)^2} + \frac{U}{\alpha \Delta X} \right) T_{i-1,j} + \frac{T_{i+1,j}}{(\Delta X)^2} \right] \\ \left[\frac{1}{\alpha} \left(\frac{U}{\Delta X} - \frac{V}{\Delta R} \right) + 2 \left(\frac{1}{(\Delta R)^2} + \frac{1}{(\Delta X)^2} \right) \right]$$

3) for the internal nodes when $U < 0$ and $V < 0$ (from Eq. (3.10))

$$T_{i,j} = \left[\left(\frac{1}{(\Delta R)^2} - \frac{1}{2R(\Delta R)} \right) T_{i,j-1} + \left(\frac{1}{(\Delta R)^2} + \frac{1}{2R(\Delta R)} - \frac{V}{\alpha \Delta R} \right) T_{i,j+1} \right. \\ \left. + \left(\frac{1}{(\Delta X)^2} - \frac{U}{\alpha \Delta X} \right) T_{i+1,j} + \frac{T_{i-1,j}}{(\Delta X)^2} \right] \\ \left[- \frac{1}{\alpha} \left(\frac{U}{\Delta X} + \frac{V}{\Delta R} \right) + 2 \left(\frac{1}{(\Delta R)^2} + \frac{1}{(\Delta X)^2} \right) \right]$$

4) for the internal nodes when $U < 0$ and $V \geq 0$ (from Eq. (3.10))

$$T_{i,j} = \left[\left(\frac{1}{(\Delta R)^2} - \frac{1}{2R(\Delta R)} + \frac{V}{\alpha \Delta R} \right) T_{i,j-1} + \left(\frac{1}{(\Delta R)^2} + \frac{1}{2R(\Delta R)} \right) T_{i,j+1} \right. \\ \left. + \left(\frac{1}{(\Delta X)^2} - \frac{U}{\alpha \Delta X} \right) T_{i+1,j} + \frac{T_{i-1,j}}{(\Delta X)^2} \right] \\ \left[\frac{1}{\alpha} \left(\frac{V}{\Delta R} - \frac{U}{\Delta X} \right) + 2 \left(\frac{1}{(\Delta X)^2} + \frac{1}{(\Delta R)^2} \right) \right]$$

5) for the centerline nodes when $U \geq 0$ (from Eq. (3.11))

$$T_{i,j} = \left[\left(\frac{1}{(\Delta X)^2} + \frac{U}{\alpha \Delta X} \right) T_{i-1,j} + \frac{T_{i+1,j}}{(\Delta X)^2} + \frac{4T_{i,j+1}}{(\Delta R)^2} \right] \\ \left(\frac{U}{\alpha \Delta X} + \frac{4}{(\Delta R)^2} + \frac{2}{(\Delta X)^2} \right)$$

6) for the centerline nodes when $U < 0$ (from Eq. (3.11))

$$T_{i,j} = \left[\left(\frac{1}{(\Delta X)^2} - \frac{U}{\alpha \Delta X} \right) T_{i+1,j} + \frac{4T_{i,j+1}}{(\Delta R)^2} + \frac{T_{i-1,j}}{(\Delta X)^2} \right] / \left(\frac{4}{(\Delta R)^2} - \frac{U}{\alpha \Delta X} + \frac{2}{(\Delta X)^2} \right)$$

7) for the insulated vertical boundary nodes (from Eq. (3.14))

$$T_{i,j} = \left(\frac{T_{i,j-1}}{(\Delta R)^2} + \frac{T_{i+1,j} + T_{i-1,j}}{2(\Delta X)^2} \right) / \left(\frac{1}{(\Delta R)^2} + \frac{1}{(\Delta X)^2} \right)$$

8) for the insulated horizontal boundary nodes (from Eq. (3.15))

$$T_{i,j} = \left(\frac{T_{i,j+1} + T_{i,j-1}}{(\Delta R)^2} + \frac{T_{i,j+1} - T_{i,j-1}}{2R(\Delta R)} + \frac{2T_{i+1,j}}{(\Delta X)^2} \right) / \left(\frac{2}{(\Delta R)^2} + \frac{2}{(\Delta X)^2} \right)$$

9) for the insulated bottom center node

$$T_{i,j} = \left(\frac{2T_{i,j+1}}{(\Delta R)^2} + \frac{T_{i+1,j}}{(\Delta X)^2} \right) / \left(\frac{2}{(\Delta R)^2} + \frac{1}{(\Delta X)^2} \right)$$

for the insulated bottom corner nodes

$$T_{i,j} = \left(\frac{T_{i+1,j}}{(\Delta X)^2} + \frac{T_{i,j-1}}{(\Delta R)^2} \right) / \left(\frac{1}{(\Delta X)^2} + \frac{1}{(\Delta R)^2} \right)$$

Vorticity Equations:

1) for the internal nodes when $U \geq 0$ and $V \geq 0$ (from Eq. (3.16))

$$\begin{aligned} \Xi_{i,j} = & \left[\left(\frac{U}{v\Delta X} + \frac{1}{(\Delta X)^2} \right) \Xi_{i-1,j} + \left(\frac{V}{v\Delta R} - \frac{3}{2R(\Delta R)} + \frac{1}{(\Delta R)^2} \right) \Xi_{i,j-1} \right. \\ & \left. + \left(\frac{3}{2R(\Delta R)} + \frac{1}{(\Delta R)^2} \right) \Xi_{i,j+1} + \frac{\Xi_{i+1,j}}{(\Delta X)^2} + \frac{g\beta_0}{vR} \left(\frac{T_{i,j+1} - T_{i,j-1}}{2\Delta R} \right) \right] / \\ & \left[\frac{1}{v} \left(\frac{U}{\Delta X} + \frac{V}{\Delta R} \right) + 2 \left(\frac{1}{(\Delta X)^2} + \frac{1}{(\Delta R)^2} \right) \right] \end{aligned}$$

2) for the internal nodes when $U \geq 0$ and $V < 0$ (from Eq. (3.16))

$$\begin{aligned} \Xi_{i,j} = & \left[\left(\frac{1}{(\Delta X)^2} + \frac{U}{v\Delta X} \right) \Xi_{i-1,j} + \frac{\Xi_{i+1,j}}{(\Delta X)^2} + \left(\frac{3}{2R\Delta R} + \frac{1}{(\Delta R)^2} - \frac{V}{v\Delta R} \right) \Xi_{i,j+1} \right. \\ & \left. + \left(\frac{1}{(\Delta R)^2} - \frac{3}{2R\Delta R} \right) \Xi_{i,j-1} + \frac{g\beta_0}{vR} \left(\frac{T_{i,j+1} - T_{i,j-1}}{2\Delta R} \right) \right] / \\ & \left[\frac{1}{v} \left(\frac{U}{\Delta X} - \frac{V}{\Delta R} \right) + 2 \left(\frac{1}{(\Delta X)^2} + \frac{1}{(\Delta R)^2} \right) \right] \end{aligned}$$

3) for the internal nodes when $U < 0$ and $V < 0$ (from Eq. (3.16))

$$\begin{aligned} \Xi_{i,j} = & \left[\frac{\Xi_{i-1,j}}{(\Delta X)^2} + \left(\frac{1}{(\Delta X)^2} - \frac{U}{v\Delta X} \right) \Xi_{i+1,j} + \left(\frac{1}{(\Delta R)^2} - \frac{3}{2R\Delta R} \right) \Xi_{i,j-1} \right. \\ & \left. + \left(\frac{3}{2R\Delta R} + \frac{1}{(\Delta R)^2} - \frac{V}{v\Delta R} \right) \Xi_{i,j+1} + \frac{g\beta_0}{vR} \left(\frac{T_{i,j+1} - T_{i,j-1}}{2\Delta R} \right) \right] / \\ & \left[- \frac{1}{v} \left(\frac{U}{\Delta X} + \frac{V}{\Delta R} \right) + 2 \left(\frac{1}{(\Delta X)^2} + \frac{1}{(\Delta R)^2} \right) \right] \end{aligned}$$

4) for the internal nodes when $U < 0$ and $V \geq 0$ (from Eq. (3.16))

$$\begin{aligned} \Xi_{i,j} = & \left[\frac{\Xi_{i-1,j}}{(\Delta X)^2} + \left(\frac{1}{(\Delta X)^2} - \frac{U}{v\Delta X} \right) \Xi_{i+1,j} + \left(\frac{1}{(\Delta R)^2} - \frac{3}{2R\Delta R} + \frac{V}{v\Delta R} \right) \Xi_{i,j-1} \right. \\ & \left. + \left(\frac{3}{2R\Delta R} + \frac{1}{(\Delta R)^2} \right) \Xi_{i,j+1} + \frac{g\beta_0}{vR} \left(\frac{T_{i,j+1} - T_{i,j-1}}{2\Delta R} \right) \right] / \\ & \left[\frac{1}{v} \left(\frac{V}{\Delta R} - \frac{U}{\Delta X} \right) + 2 \left(\frac{1}{(\Delta X)^2} + \frac{1}{(\Delta R)^2} \right) \right] \end{aligned}$$

5) for the centerline nodes when $U \geq 0$ (from Eq. (3.18))

$$\begin{aligned} \Xi_{i,j} = & \left[\left(\frac{U}{v\Delta X} + \frac{1}{(\Delta X)^2} \right) \Xi_{i-1,j} + \frac{\Xi_{i+1,j}}{(\Delta X)^2} + \frac{4}{(\Delta R)^2} \Xi_{i,j-1} \right. \\ & \left. + \frac{4}{(\Delta R)^2} \Xi_{i,j+1} + \frac{g\beta_0}{v} \left(\frac{T_{i,j-1} - 2T_{i,j} + T_{i,j+1}}{(\Delta R)^2} \right) \right] / \\ & \left(\frac{U}{v\Delta X} + \frac{2}{(\Delta X)^2} + \frac{8}{(\Delta R)^2} \right) \end{aligned}$$

6) for the centerline nodes when $U < 0$ (from Eq. (3.18))

$$\begin{aligned} \Xi_{i,j} = & \left[\frac{\Xi_{i-1,j}}{(\Delta X)^2} + \left(\frac{1}{(\Delta X)^2} - \frac{U}{v\Delta X} \right) \Xi_{i+1,j} + \frac{4}{(\Delta R)^2} \Xi_{i,j-1} \right. \\ & \left. + \frac{4}{(\Delta R)^2} \Xi_{i,j+1} + \frac{g\beta_0}{v} \left(\frac{T_{i,j-1} - 2T_{i,j} + T_{i,j+1}}{(\Delta R)^2} \right) \right] / \\ & \left(- \frac{U}{v\Delta X} + \frac{2}{(\Delta X)^2} + \frac{8}{(\Delta R)^2} \right) \end{aligned}$$

7) for the bottom center node (from Eq. (3.20))

$$\Xi_{i,j} = \left[\left(5\Xi_{i+1,j} - 4\Xi_{i+2,j} + \Xi_{i+3,j} \right) / (\Delta X)^2 - \frac{8}{(\Delta R)^2} \Xi_{i,j+1} \right] \left[\left(\frac{2}{(\Delta X)^2} - \frac{8}{(\Delta R)^2} \right) \right]$$

8) for the top center node (from Eq. (3.21))

$$\Xi_{i,j} = \left[\left(5\Xi_{i-1,j} - 4\Xi_{i-2,j} + \Xi_{i-3,j} \right) / (\Delta X)^2 - \frac{8}{(\Delta R)^2} \Xi_{i,j+1} \right] \left[\left(\frac{2}{(\Delta X)^2} - \frac{8}{(\Delta R)^2} \right) \right]$$

9) for the solid boundary nodes Eqs. (3.26) through (3.28) are used.

10) for the various corner nodes Eqs. (3.30) through (3.31) are used except, for the centerline Eq. (3.17) is used.

Vorticity and Stream Function Relation:

1) for the all internal nodes (from Eq. (3.32))

$$\begin{aligned} \Psi_{i,j} = & \left[-\frac{\Psi_{i-1,j}}{(\Delta X)^2} - \frac{\Psi_{i+1,j}}{(\Delta X)^2} + \left(-\frac{1}{(\Delta R)^2} - \frac{1}{2R(\Delta R)} \right) \Psi_{i,j-1} \right. \\ & \left. + \left(\frac{1}{2R\Delta R} - \frac{1}{(\Delta R)^2} \right) \Psi_{i,j+1} + \Xi_{i,j} R^2 \right] \left[\left(-\frac{2}{(\Delta X)^2} - \frac{2}{(\Delta R)^2} \right) \right] \end{aligned}$$

2) for the all solid boundary nodes

$$\psi_{i,j} = 0$$

Stream Function Equations:

Eqs. (3.33) through (3.38) were used without any modification.

Appendix B
Computer Codes

B-1 Program NATCON: The Fortran coded program NATCON is included in the following 11 pages. This numerical program is developed and used in Chap. III. The first stage of the coded-program development was done by the use of the CDC CYBER-75 computer at Oregon State University with the unsponsored research fund provided by the OSU Computer Center. Upon the completion of the first stage development which also included the debugging, the total coded-program was transferred to the PDP-11/10 computer of the mechanical engineering department of OSU. Thereafter, all computer runs were made by the above computer, except the last approximately 40 runs out of about 250 total runs, were made by the PDP-11/10 of the chemistry department of the above institution.

Most of the explanation of the program were already done in Chap. III, however, the pertinent coded-variables are as follows:

(in program) (in analysis)

U	U	Axial velocity, m/s
V	V	Radial velocity, m/s
S	Ψ	Stream function, m^3/s
T	T	Temperature, $^{\circ}C$
W	Ξ	Vorticity, $1/s \cdot m$
G	g	Gravitational constant, m/s^2
BET	β	Thermal expansion coefficient, $1/{}^{\circ}C$
THRCON	k	Thermal conductivity, $kJ/s \cdot m \cdot K$

(in program) (in analysis)

VIS	ν	Kinematic viscosity, m^2/s
DENS	ρ	Density, kg/m^3
SPHT	c_p	Specific heat, $kJ/kg\cdot K$

Other related variables are also listed in Appendix B-2.

```

C      PROGRAM NATCON
COMMON/A/U(30,10),V(30,10),S(30,10),T(30,10),W(30,10)
COMMON/B/G,BET,A,THRCON,VIS,DXS,DR,DRS,AL,DXR,
1      XD,RD
COMMON/C/OLD,FAC,FACH
COMMON/D/MX,MXX,NR,NRR,IFLUID
COMMON/E/TTOP,TWTP,TWBT,TRTP,TRBT
IRES=2
*****
C FOLLOWING 11 CONSTANTS ARE FREQUENTLY CHANGED
C TO OBTAIN A SUITABLE GN, RA, OR RM.
*****
TYPE 1
1 FORMAT(' LIMIT ON ITERATION, ILLOOP=',$)
ACCEPT 100,ILLOOP
100 FORMAT(I4)
TYPE 10
10 FORMAT(' WATER-0; GLYCERINE-1: ',$)
ACCEPT 100,IFLUID
TYPE 2
2 FORMAT(' IF RESERVOIR PRINTOUT DESIRED TYPE "1", IF NOT "0":',$)
ACCEPT 100,IRESV
TYPE 110
110 FORMAT(' IF EVERY N TH ITERATION PRINTOUT DESIRED, TYPE IN
1THAT NUMBER, IF NOT "0", IPRNT=',$)
ACCEPT 100,IPRNT
TYPE 3
3 FORMAT(' MESH DISTANCES: DX=',$)
ACCEPT 101,DX
101 FORMAT(G20.6)
TYPE 4
4 FORMAT(' DR=',$)
ACCEPT 101,DR
TYPE 5
5 FORMAT(' BOUNDARY TEMPERATURES:') 
TYPE 6
6 FORMAT(' TOP OF THE FLUID, TTOP=',$)
ACCEPT 101,TTOP
TYPE 8
8 FORMAT(' TOP OF THE WALL, TWTP=',$)
ACCEPT 101,TWTP
TYPE 9
9 FORMAT(' BOT OF THE WALL, TWBT=',$)
ACCEPT 101,TWBT
TYPE 11
11 FORMAT(' WALLS OF THE RES, TRTP=',$)
ACCEPT 101,TRTP
TYPE 20
20 FORMAT(' TRBT=',$)

```

```

ACCEPT 101,TRBT
TYPE 111
111 FORMAT(' INITIAL FLUID TEMP., TINI=',$)
ACCEPT 101,TINI
TYPE 12
12 FORMAT(' NO. OF NODE FROM THE RES BOT CENTER:')*
TYPE 13
13 FORMAT('          TO THE RESERVOIR TOP, MX=',$)
ACCEPT 100,MX
TYPE 14
14 FORMAT('          TO THE CYLINDER TOP, MXX=',$)
ACCEPT 100,MXX
TYPE 15
15 FORMAT('          TO THE CYLINDER WALL, NR=',$)
ACCEPT 100,NR
TYPE 16
16 FORMAT('          TO THE RESERVOIR WALL,NRR=',$)
ACCEPT 100,NRR
TYPE 17
17 FORMAT(' RELAXATION FACTOR, FAC=',$)
ACCEPT 101,FAC
TYPE 18
18 FORMAT(' SUCCESSIVE TOLERANCE, ERR=',$)
ACCEPT 101,ERR

```

```

MCK=MX
NCK=(NR+1)/2
CHKT=0.
CHKS=0.
CHKV=0.
CHKW=0.
CHKU=0.
OLD=0.
FACM=1.-FAC
CALL DATAS
DO 1000 M=1,MXX
IR=NR
IF(M.LE.MX)IR=NRR
DO 1000 N=1,IR
U(M,N)=0.
V(M,N)=0.
S(M,N)=0.
T(M,N)=TINI
W(M,N)=0.

```

1000 CONTINUE

C NON-LINEAR WALL TEMP. TYPE-IN PROCEDURE

TYPE 103

103 FORMAT(' IF WALL TEMP IS NON-LINEAR, TYPE IN "0"; IF LINEAR, "1":
1',\$)

ACCEPT 104,LINER

104 FORMAT(I2)

```

IF(LINER.EQ.1)GO TO 300
ISTRT=MX+1
IEND=MXX-1
DO 200 I=ISTRT,IEND
TYPE 201,I
201 FORMAT(' AT M=',I3,' :$',)
ACCEPT 202,T(I,NR)
202 FORMAT(F10.3)
200 CONTINUE
300 CONTINUE
C*****CALCULATION STARTS FROM HERE ON*****
C*****CALCULATION STARTS FROM HERE ON*****
JPRNT=IPRNT
DO 2000 I=1,ILoop
CALL EQNS(MX,NR,MXX,NRR,IRES,LINER)
CALL VELO(MX,NR,MXX,NRR)
IF(I.EQ.JPRNT)GO TO 2001
GO TO 2002
2001 JPRNT=JPRNT+IPRNT
C
      WRITE(5,2003)I,T(MCK,NCK),W(MCK,NCK),S(MCK,NCK)
2003 FORMAT(1X,I4,2X,E11.4,2X,E11.4,2X,E11.4)
      GO TO 2002
C
      CALL PRTOUT(I,MX,NR,MXX,NRR,IRESV)
2002 CONTINUE
IF(I.LT.20)GO TO 2000
ABST=ABS((T(MCK,NCK)-CHKT)/T(MCK,NCK))
ABSS=ABS((S(MCK,NCK)-CHKS)/S(MCK,NCK))
ABSV=ABS((V(MCK,NCK)-CHKV)/V(MCK,NCK))
ABSW=ABS((W(MCK,NCK)-CHKW)/W(MCK,NCK))
ABSU=ABS((U(MCK,NCK)-CHKU)/U(MCK,NCK))
CHKT=T(MCK,NCK)
CHKS=S(MCK,NCK)
CHKV=V(MCK,NCK)
CHKW=W(MCK,NCK)
CHKU=U(MCK,NCK)
IF(ABST.GT.ERR)GO TO 2000
IF(ABSS.GT.ERR)GO TO 2000
IF(ABSV.GT.ERR)GO TO 2000
IF(ABSW.GT.ERR)GO TO 2000
IF(ABSU.GT.ERR)GO TO 2000
GO TO 2100
2000 CONTINUE
2100 CALL PRTOUT(I,MX,NR,MXX,NRR,IRESV)
CALL EXIT
END
      SUBROUTINE DATAS
COMMON/A/U(30,10),V(30,10),S(30,10),T(30,10),W(30,10)
COMMON/B/G,BET,A,THRCN,VIS,BX,DXS,DR,DRS,AL,BXDR,
1           XD,RD
COMMON/C/OLD,FAC,FACH
COMMON/D/MX,MXX,NR,NRR,IFLUID

```

COMMON/E/TTOP,TWTP,TWBT,TRTP,TRBT
 G=-9.8065
 IF(IFLUID.EQ.1)GO TO 1000

C
 ✓ C ---WATER---
 C

SPHT=4.182
 DENS=998.2
 THRCON=.0006
 VIS=10.05E-7
 BET=.0002
 GO TO 2000

1000 CONTINUE

C
 ✓ C ---GLYCERINE---
 C

SPHT=2.62
 DENS=1259.
 THRCON=.00029
 VIS=7.54E-4
 BET=.00054

2000 CONTINUE

DXS=DX*DX
 DRS=DR*DR
 XD=1./DXS
 RD=1./DRS
 AL=THRCON/(DENS*SPHT)
 DXDR=1./DXS+1./DRS
 A=(TWBT-TWTP)/(FLDAT(MXX-MX)*DX)

RETURN

END

SUBROUTINE EQNS(MX,NR,MXX,NRR,IRES,LINER)
 COMMON/A/U(30,10),V(30,10),S(30,10),T(30,10),W(30,10)
 COMMON/B/G,BET,A,THRCON,VIS,DX,DXS,DR,DRS,AL,DXR,

1 XD,RD

COMMON/C/OLD,FAC,FACH

COMMON/E/TTOP,TWTP,TWBT,TRTP,TRBT

✓ C***ENERGY EQUATION*****

DO 9000 M=1,MXX
 IR=NR
 IF(M.LE.MX)IR=NRR
 DO 9000 N=1,IR
 IF(M.EQ.1)GO TO 2000
 IF(M.GT.1.AND.M.LT.MX)GO TO 1000
 IF(M.EQ.MX)GO TO 2004
 IF(M.GT.MX.AND.M.LT.MXX)GO TO 200
 IF(M.EQ.MXX)GO TO 300
 1000 IF(N.EQ.1)GO TO 2001
 IF(N.GT.1.AND.N.LT.NRR)GO TO 2002
 IF(N.EQ.NRR)GO TO 2003
 2000 GO TO(101,101,103),IRES
 101 T(M,N)=TRBT
 GO TO 9000
 103 IF(N.EQ.1)GO TO 104

```

IF(N.GT.1.AND.N.LT.NRR)GO TO 105
IF(N.EQ.NRR)GO TO 106
104 T(M,N)=(2.*T(M,N+1)*RD+T(M+1,N)*XD)/(2.*RD+XD)
GO TO 9000
105 T(M,N)=((T(M,N+1)+T(M,N-1))*RD+(T(M,N+1)-T(M,N-1))/_
1 (2.*FLOAT(N-1)*DRS)+2.*T(M+1,N)*XD)/(2.*DXDR)
GO TO 9000
106 T(M,N)=(T(M+1,N)*XD+T(M,N-1)*RD)/DXDR
GO TO 9000
2001 IF(U(M,N).GE.0.)GO TO 2100
T(M,N)=((XD-FU(M,N)/(AL*DX))*T(M+1,N)_
1 +4.*T(M,N+1)*RD+T(M-1,N)*XD)/_
2 (4.*RD-FU(M,N)/(AL*DX)+2.*XD)
GO TO 9000
2100 T(M,N)=((XD+FU(M,N)/(AL*DX))*T(M-1,N)_
1 +T(M+1,N)*XD+4.*T(M,N+1)*RD)/_
2 (FU(M,N)/(AL*DX)+4.*RD+2.*XD)
GO TO 9000
2002 IF(U(M,N).GE.0..AND.V(M,N).GE.0.)GO TO 2101
IF(U(M,N).GE.0..AND.V(M,N).LT.0.)GO TO 2102
IF(U(M,N).LT.0..AND.V(M,N).LT.0.)GO TO 2103
GO TO 2104
2003 GO TO(107,108,108),IRES
107 T(M,N)=TRES
GO TO 9000
108 T(M,N)=(T(M,N-1)*RD+(T(M+1,N)+T(M-1,N))/(2.*DXS))/DXDR
GO TO 9000
2004 IF(N.EQ.1)GO TO 2001
IF(N.GT.1.AND.N.LT.NR)GO TO 2002
IF(N.EQ.NR)GO TO 2105
T(M,N)=TRTP
GO TO 9000
2101 T(M,N)=((FU(M,N)/(AL*DX)+XD)*T(M-1,N)_
1 +(FU(M,N)/(AL*DR)+RD-1./(2.*FLOAT(N-1)*DRS))*T(M,N-1)_
2 +(RD+1./(2.*FLOAT(N-1)*DRS))*T(M,N+1)_
3 +T(M+1,N)*XD)/_
4 ((FU(M,N)/DX+FV(M,N)/DR)/AL+2.*DXDR)
GO TO 9000
2102 T(M,N)=((RD-1./(2.*FLOAT(N-1)*DRS))*T(M,N-1)_
1 +(RD+1./(2.*FLOAT(N-1)*DRS)-FV(M,N)/(AL*DR))*T(M,N+1)_
2 +(XD+FU(M,N)/(AL*DX))*T(M-1,N)+T(M+1,N)*XD)/_
3 ((FU(M,N)/DX-FV(M,N)/DR)/AL+2.*DXDR)
GO TO 9000
2103 T(M,N)=((RD-1./(2.*FLOAT(N-1)*DRS))*T(M,N-1)_
1 +(RD+1./(2.*FLOAT(N-1)*DRS)-FV(M,N)/(AL*DR))*T(M,N+1)_
2 +(XD-FU(M,N)/(AL*DX))*T(M+1,N)+T(M-1,N)*XD)/_
3 ((FU(M,N)/DX+FV(M,N)/DR)/(-AL)+2.*DXDR)
GO TO 9000
2104 T(M,N)=((RD-1./(2.*FLOAT(N-1)*DRS)+FV(M,N)/(AL*DR))*T(M,N-1)_
1 +(RD+1./(2.*FLOAT(N-1)*DRS))*T(M,N+1)_
2 +(XD-FU(M,N)/(AL*DX))*T(M+1,N)+T(M-1,N)*XD)/_
3 ((FV(M,N)/DR-FU(M,N)/DX)/AL+2.*DXDR)
GO TO 9000

```

```

2105 T(M,N)=TWBT
      GO TO 9000
200 IF(N.EQ.1)GO TO 2001
      IF(N.GT.1.AND.N.LT.NR)GO TO 2002
      IF(LINER.EQ.0)GO TO 9000
      T(M,N)=TWTP+A*DX*FLOAT(MXX-M)
      GO TO 9000
300 T(M,N)=TTOP
      IF(N.EQ.NR)GO TO 350
      GO TO 9000
350 T(M,N)=TWTP
9000 CONTINUE
C***MOMENTUM EQUATION*****  

      DO 9100 M=1,MXX
      IR=NR
      IF(M.LE.MX)IR=NRR } *
      DO 9100 N=1,IR
      IF(M.EQ.1)GO TO 3000
      IF(M.GT.1.AND.M.LT.MX)GO TO 3001
      IF(M.EQ.MX)GO TO 303
      IF(M.GT.MX.AND.M.LT.MXX)GO TO 301
      IF(M.EQ.MXX)GO TO 3002
3000 IF(N.EQ.1)GO TO 4001
      IF(N.GT.1.AND.N.LT.NRR)GO TO 4002
      IF(N.EQ.NRR)GO TO 4003
3001 IF(N.EQ.1)GO TO 4004
      IF(N.GT.1.AND.N.LT.NRR)GO TO 4006
      IF(N.EQ.NRR)GO TO 4011
3002 IF(N.EQ.1)GO TO 4012
      IF(N.GT.1.AND.N.LT.NR)GO TO 4013
      IF(N.EQ.NR)GO TO 4014
301 IF(N.EQ.1)GO TO 4004
      IF(N.GT.1.AND.N.LT.NR)GO TO 4006
      IF(N.EQ.NR)GO TO 4011
303 IF(N.EQ.1)GO TO 4004
      IF(N.GT.1.AND.N.LT.NR)GO TO 4006
      IF(N.EQ.NR)GO TO 310
      IF(N.GT.NR.AND.N.LT.NRR)GO TO 4013
      IF(N.EQ.NRR)GO TO 4014
310 W(M,N)=((8.*S(M-1,N)-S(M-2,N))*XD+(8.*S(M,N-1)-S(M,N-2))*RD)/
1     (4.*FLOAT(N-1)*FLOAT(N-1)*DRS)
      GO TO 9100
4001 W(M,N)=0.
C4001 W(M,N)=((5.*W(M+1,N)-4.*W(M+2,N)+W(M+3,N))*XD-
C   1     -8.*W(M,N+1)*RD)/(2.*XD-8.*RD)
      GO TO 9100
4002 W(M,N)=(8.*S(M+1,N)-S(M+2,N))/(2.*DXS*FLOAT(N-1)*FLOAT(N-1)*DRS)
      GO TO 9100
4003 W(M,N)=0.
      GO TO 9100
4004 IF(U(M,N).GE.0.)GO TO 4005
      U(M,N)=(W(M-1,N)*XD+(XD-EU(M,N)/(VIS*DX))*W(M+1,N)
1     +(8.*RD)*W(M,N+1))

```

```

2      +G*BET*(2.*T(M,N+1)-2.*T(M,N))/(VIS*DRS))/  

3      (-FU(M,N)/(VIS*DX)+2.*XD+8.*RD)
GO TO 9100
4005 W(M,N)=((FU(M,N)/(VIS*DX)+XD)*W(M-1,N)+W(M+1,N)*XD  

1      +(8.*RD)*W(M,N+1))
2      +G*BET*(2.*T(M,N+1)-2.*T(M,N))/(VIS*DRS))/  

3      (FU(M,N)/(VIS*DX)+2.*XD+8.*RD)
GO TO 9100
4006 IF(U(M,N).GE.0..AND.V(M,N).GE.0.)GO TO 4007
IF(U(M,N).GE.0..AND.V(M,N).LT.0.)GO TO 4008
IF(U(M,N).LT.0..AND.V(M,N).LT.0.)GO TO 4009
GO TO 4010
4007 W(M,N)=((FU(M,N)/(VIS*DX)+XD)*W(M-1,N)  

1      +(FV(M,N)/(VIS*DR)-3./(2.*FLOAT(N-1)*DRS)+RD)*W(M,N-1)
2      +(3./(2.*FLOAT(N-1)*DRS)+RD)*W(M,N+1)
3      +W(M+1,N)*XD
4      +G*BET*(T(M,N+1)-T(M,N-1))/(2.*FLOAT(N-1)*DRS*VIS))/  

5      ((FU(M,N)/DX+FV(M,N)/DR)/VIS+2.*DXDR)
GO TO 9100
4008 W(M,N)=((XD+FU(M,N)/(VIS*DX))*W(M-1,N)+W(M+1,N)*XD  

1      +(3./(2.*FLOAT(N-1)*DRS)+RD-FV(M,N)/(VIS*DR))*W(M,N+1)
2      +(RD-3./(2.*FLOAT(N-1)*DRS))*W(M,N-1)
3      +G*BET*(T(M,N+1)-T(M,N-1))/(2.*VIS*FLOAT(N-1)*DRS))/  

4      ((FU(M,N)/DX-FV(M,N)/DR)/VIS+2.*DXDR)
GO TO 9100
4009 W(M,N)=(W(M-1,N)*XD+(XD-FU(M,N)/(VIS*DX))*W(M+1,N)  

1      +(RD-3./(2.*FLOAT(N-1)*DRS))*W(M,N-1)
2      +(3./(2.*FLOAT(N-1)*DRS)+RD-FV(M,N)/(VIS*DR))*W(M,N+1)
3      +G*BET*(T(M,N+1)-T(M,N-1))/(2.*VIS*FLOAT(N-1)*DRS))/  

4      ((-FU(M,N)/DX-FV(M,N)/DR)/VIS+2.*DXDR)
GO TO 9100
4010 W(M,N)=(W(M-1,N)*XD  

1      +(XD-FU(M,N)/(VIS*DX))*W(M+1,N)
2      +(RD-3./(2.*FLOAT(N-1)*DRS)+FV(M,N)/(VIS*DR))*W(M,N-1)
3      +(3./(2.*FLOAT(N-1)*DRS)+RD)*W(M,N+1)
4      +G*BET*(T(M,N+1)-T(M,N-1))/(2.*FLOAT(N-1)*VIS*DRS))/  

5      ((FV(M,N)/DR-FU(M,N)/DX)/VIS+2.*DXDR)
GO TO 9100
4011 W(M,N)=(B.*S(M,N-1)-S(M,N-2))/(2.*FLOAT(N-1)*FLOAT(N-1)*DRS*DRS)
GO TO 9100
4012 W(M,N)=0.
C4012 W(M,N)=((5.*W(M-1,N)-4.*W(M-2,N)+W(M-3,N))*XD  

C     1      -8.*W(M,N+1)*RD)/(2.*XD-8.*RD)
GO TO 9100
4013 W(M,N)=(B.*S(M-1,N)-S(M-2,N))/(2.*DXS*FLOAT(N-1)*FLOAT(N-1)*DRS)
GO TO 9100
4014 W(M,N)=0.
9100 CONTINUE
****STREAM FUNCTIONS*****  

DO 9200 M=1,MXX
IR=NR
IF(M.LE.MX)IR=NRR
DO 9200 N=1,IR

```

```

IF(M.EQ.1)GO TO 5100
IF(M.GT.1.AND.M.LT.MX)GO TO 5101
IF(M.EQ.MX)GO TO 403
IF(M.GT.MX.AND.M.LT.MXX)GO TO 401
IF(M.EQ.MXX)GO TO 5100
401 IF(N.EQ.1.OR.N.EQ.NR)GO TO 5100
IF(N.GT.1.AND.N.LT.NR)GO TO 5102
403 IF(N.EQ.1.OR.N.EQ.NR)GO TO 5100
IF(N.GT.1.AND.N.LT.NR)GO TO 5102
IF(N.GT.NR)GO TO 5100
5100 S(M,N)=0.
GO TO 9200
5101 IF(N.EQ.1)GO TO 5100
IF(N.GT.1.AND.N.LT.NRR)GO TO 5102
IF(N.EQ.NRR)GO TO 5100
5102 OLD=S(M,N)
S(M,N)=((-S(M-1,N)-S(M+1,N))*XD)
1      +(-RD-1./(2.*FLOAT(N-1)*DRS))*S(M,N-1)
2      +(-RD+1./(2.*FLOAT(N-1)*DRS))*S(M,N+1)
3      +W(M,N)*FLOAT(N-1)*FLOAT(N-1)*DRS)/
4      (-2.*DXDR)
S(M,N)=FAC*S(M,N)+FACM*OLD
9200 CONTINUE
RETURN
END
SUBROUTINE VELO(MX,NR,MXX,NRR)
COMMON/A/U(30,10),V(30,10),S(30,10),T(30,10),W(30,10)
COMMON/B/G,BET,A,THRCON,VIS,DX,DXS,DR,DRS,AL,DXDR,
1      XD,RD
COMMON/C/OLD,FAC,FACM,
MMNUS=MXX-1
NNNUS=NRR-1
NRMNUS=NR-1
MXMNUS=MX-1
***AXIAL VELOCITY (U)*****
DO 7000 M=1,MXX
IR=NR
IF(M.LE.MX)IR=NRR
DO 7000 N=1,IR
IF(M.EQ.1)GO TO 1000
IF(M.GT.1.AND.M.LT.MX)GO TO 1001
IF(M.GE.MX.AND.M.LT.MXX)GO TO 100
IF(M.EQ.MXX)GO TO 1000
100 IF(N.EQ.1)GO TO 2000
IF(N.EQ.2)GO TO 2001
IF(N.GT.2.AND.N.LT.NRMNUS)GO TO 2002
IF(N.EQ.NRMNUS)GO TO 2003
1000 U(M,N)=0.
GO TO 7000
1001 IF(N.EQ.1)GO TO 2000
IF(N.EQ.2)GO TO 2001
IF(N.GT.2.AND.N.LT.NMNUS)GO TO 2002
IF(N.EQ.NMNUS)GO TO 2003

```

```

      IF(N.EQ.NRR)GO TO 1000
C2000 OLD=U(M,N)
2000 U(M,N)=2.*S(M,N+1)*RD
C     U(M,N)=FAC*U(M,N)+FACM*OLD
     GO TO 7000
C2001 OLD=U(M,N)
2001 U(M,N)=(-3.*S(M,N)+6.*S(M,N+1)-S(M,N+2))/1
     (6.*FLOAT(N-1)*DRS)
C     U(M,N)=FAC*U(M,N)+FACM*OLD
     GO TO 7000
C2002 OLD=U(M,N)
2002 U(M,N)=(S(M,N-2)-8.*S(M,N-1)+8.*S(M,N+1)-S(M,N+2))/1
     (12.*FLOAT(N-1)*DRS)
C     U(M,N)=FAC*U(M,N)+FACM*OLD
     GO TO 7000
C2003 OLD=U(M,N)
2003 U(M,N)=(S(M,N-2)-6.*S(M,N-1)+3.*S(M,N))/(6.*FLOAT(N-1)*DRS)
C     U(M,N)=FAC*U(M,N)+FACM*OLD
7000 CONTINUE
***RADIAL VELOCITY (V)*****
DO 8000 M=1,MXX
IR=NR
IF(M.LE.MX)IR=NRR
DO 8000 N=1,IR
IF(M.EQ.1)GO TO 1100
IF(M.EQ.2)GO TO 1101
IF(M.GT.2.AND.M.LT.MXMNUS)GO TO 200
IF(M.EQ.MXMNUS)GO TO 201
IF(M.EQ.MX)GO TO 202
  IF(M.GT.MX.AND.M.LT.MMNUS)GO TO 1102
IF(M.EQ.MMNUS)GO TO 1103
IF(M.EQ.MXX)GO TO 1100
200 IF(N.EQ.1.OR.N.EQ.NRR)GO TO 1100
IF(N.GT.1.AND.N.LT.NRR)GO TO 2102
201 IF(N.EQ.1.OR.N.EQ.NRR)GO TO 1100
IF(N.GT.1.AND.N.LT.NR)GO TO 2102
IF(N.GE.NR.AND.N.LT.NRR)GO TO 2103
202 IF(N.EQ.1.OR.N.GE.NR)GO TO 1100
IF(N.GT.1.AND.N.LT.NR)GO TO 2102
1100 V(M,N)=0.
GO TO 8000
1101 IF(N.EQ.1)GO TO 1100
IF(N.GT.1.AND.N.LT.NRR)GO TO 2101
IF(N.EQ.NRR)GO TO 1100
1102 IF(N.EQ.1)GO TO 1100
IF(N.GT.1.AND.N.LT.NR)GO TO 2102
IF(N.EQ.NR)GO TO 1100
1103 IF(N.EQ.1)GO TO 1100
IF(N.GT.1.AND.N.LT.NR)GO TO 2103
IF(N.EQ.NR)GO TO 1100
C2101 OLD=V(M,N)
2101 V(M,N)=(3.*S(M,N)-6.*S(M+1,N)+S(M+2,N))/1
     (6.*FLOAT(N-1)*DX*DR)

```

```

C      V(M,N)=FAC*V(M,N)+FACM*OLD
      GO TO 8000
C2102 OLD=V(M,N)
2102  V(M,N)=(S(M+2,N)-8.*S(M+1,N)+8.*S(M-1,N)-S(M-2,N))/(
           1     (12.*FLOAT(N-1)*DR*DX)
C      V(M,N)=FAC*V(M,N)+FACM*OLD
      GO TO 8000
C2103 OLD=V(M,N)
2103  V(M,N)=(-S(M-2,N)+6.*S(M-1,N)-3.*S(M,N))/(
           1     (6.*FLOAT(N-1)*DR*DX)
C      V(M,N)=FAC*V(M,N)+FACM*OLD
8000  CONTINUE
      RETURN
      END
      FUNCTION FU(M,N)
COMMON/A/U(30,10),V(30,10)
C      FU=(U(M-1,N)/2.+U(M,N)+U(M+1,N)/2.)/2.
FU=U(M,N)
      RETURN
      END
      FUNCTION FV(M,N)
COMMON/A/U(30,10),V(30,10)
C      FV=(V(M,N-1)/2.+V(M,N)+V(M,N+1)/2.)/2.
FV=V(M,N)
      RETURN
      END
      SUBROUTINE PRTOUT(I,MX,NR,MXX,NRR,IRESV)
COMMON/A/U(30,10),V(30,10),S(30,10),T(30,10),W(30,10)
COMMON/B/G,BET,A,THRCON,VIS,DX,DXS,DR,DRS,AL,DXR,
1      XD,RD
COMMON/C/OLD,FAC,FACH
COMMON/E/TTOP,TWTP,TWBT,TRTP,TRBT
PRN=VIS/AL
RA=A*BET*G*((FLOAT(NR-1)*DR)**4)/(VIS*AL)
GN=BET*G*(T(MX,1)-TTOP)*((FLOAT(NR-1)*DR)**3)/(VIS*AL)
RM=GN*FLOAT(NR-1)*DR/(FLOAT(MXX-MX)*DX)
WRITE(5,4002)
WRITE(5,5000)RA,RM,GN,PRN
WRITE(5,5001)T(MX,1),U(MX,1)
5001 FORMAT(1X,'T(MX,1)=',E10.3,3X,'U(MX,1)=',E10.3)
WRITE(5,1000)I
WRITE(5,1001)
DO 2000 IM=1,MXX
M=MXX-IM+1
IF(M.LE.MX)GO TO 3000
WRITE(5,4000)(T(M,N),N=1,NR)
GO TO 2000
3000 WRITE(5,4001)(T(M,N),N=1,NRR)
IF(M.EQ.(MX-1).AND.IRESV.EQ.0) GO TO 2100
2000 CONTINUE
2100 WRITE(5,1003)
DO 2001 IM=1,MXX
M=MXX-IM+1

```

```

IF(M.LE.MX)GO TO 3001
WRITE(5,4000)(W(M,N),N=1,NR)
GO TO 2001
3001 WRITE(5,4001)(W(M,N),N=1,NRR)
IF(M.EQ.(MX-1).AND.IRESV.EQ.0) GOTO 2200
2001 CONTINUE
2200 WRITE(5,1004)
DO 2002 IM=1,MXX
M=MXX-IM+1
IF(M.LE.MX)GO TO 3002
WRITE(5,4000)(S(M,N),N=1,NR)
GO TO 2002
3002 WRITE(5,4001)(S(M,N),N=1,NRR)
IF(M.EQ.(MX-1).AND.IRESV.EQ.0) GO TO 2300
2002 CONTINUE
2300 WRITE(5,1005)
DO 2003 IM=1,MXX
M=MXX-IM+1
IF(M.LE.MX)GO TO 3003
WRITE(5,4000)(U(M,N),N=1,NR)
GO TO 2003
3003 WRITE(5,4001)(U(M,N),N=1,NRR)
IF(M.EQ.(MX-1).AND.IRESV.EQ.0) GO TO 2400
2003 CONTINUE
2400 WRITE(5,1006)
DO 2004 IM=1,MXX
M=MXX-IM+1
IF(M.LE.MX)GO TO 3004
WRITE(5,4000)(V(M,N),N=1,NR)
GO TO 2004
3004 WRITE(5,4001)(V(M,N),N=1,NRR)
IF(M.EQ.(MX-1).AND.IRESV.EQ.0) GO TO 2500
2004 CONTINUE
2500 CONTINUE
1000 FORMAT(/1X,'I=',I4)
1001 FORMAT(/1X,'TEMPERATURE IN DEGREE C')
1003 FORMAT(/1X,'VORTICITY')
1004 FORMAT(/1X,'STREAM FUNCTION')
1005 FORMAT(/1X,'AXIAL VELOCITY IN METER/SEC')
1006 FORMAT(/1X,'RADIAL VELOCITY IN METER/SEC')
4000 FORMAT(1X,6E10.3)
4001 FORMAT(1X,9E10.3)
4002 FORMAT(//1X,'COMPUTATION RESULTS:')
5000 FORMAT(1X,'RA=',E10.3,5X,'RM=',E10.3,5X,'GN=',E10.3,5X,
1      'FRN=',F9.5)
RETURN
END

```

B-2 Example Input-Output Listing: The example input and output listings of the program NATCON are included in the following six pages. The input portion is listed in the first page where the values of frequently changed constants are set before each run of the program. The output section starts from the line "COMPUTED RESULTS:" at the bottom of the first page and includes following five pages where maps of the temperature, the vorticity, the stream function values, the axial velocity, and the radial velocity are listed. The explanation of input and output variables are as follows:

(in program) (in analysis)

ILOOP	n/a	Maximum number of iterations
DX	ΔX	Axial mesh distance, m
DR	ΔR	Radial mesh distance, m
TTOP	T_0	Cylinder top temperature, °C
TWTP	T_0	Top cylinder-wall temperature, °C
TWBT	T_{BOT}	Bottom cylinder-wall temperature, °C
TRTP	T_{RES}	Reservoir top-wall temperature, °C
TRBT	n/a	Reservoir bottom-wall temperature, °C
MX	n/a	See Fig. 3.7
MXX	n/a	See Fig. 3.7
NR	n/a	See Fig. 3.7
NRR	n/a	See Fig. 3.7
FAC	FAC	Successive-over-relaxation factor
ERR	n/a	Successive iteration error
RA	Ra_A	Modified Rayleigh number based on the wall temperature gradient

(in program) (in analysis)

RM	Ra_L^a	Modified Rayleigh number based on the center line temperature
GN	Ra	Grashof number based on the centerline temperature
PRN	Pr	Prandtl number
I	n/a	Iteration number at the time of print out

RUN CON

LIMIT ON ITERATION, ILOOP=1000

WATER-0; GLYCERINE-1: 0

IF RESERVOIR PRINTOUT DESIRED TYPE "1", IF NOT "0":1

IF EVERY N TH ITERATION PRINTOUT DESIRED, TYPE INTHAT NUMBER, IF NOT "0", IPRNT=0

MESH DISTANCES: DX=.015

DR=.001

BOUNDARY TEMPERATURES:

TOP OF THE FLUID, TTOP=0.

TOP OF THE WALL, TWTP=0.

BOT OF THE WALL, TWBT=46.

WALLS OF THE RES, TRTP=46.

TRBT=46.

INITIAL FLUID TEMP., TINI=5.

NO. OF NODE FROM THE RES BOT CENTER:

TO THE RESERVOIR TOP, MX=5

TO THE CYLINDER TOP, MXX=25

TO THE CYLINDER WALL, NR=6

TO THE RESERVOIR WALL,NRR=9

RELAXATION FACTOR, FAC=.3

SUCCESSIVE TOLERANCE, ERR=.00001

IF WALL TEMP IS NON-LINEAR, TYPE IN "0"; IF LINEAR, "1":1

COMPUTATION RESULTS:

RA= 0.130E+04 RM= 0.713E+03 GN= 0.428E+05 PRN= 6.99224
T(MX,1)= 0.252E+02 U(MX,1)=-0.307E-01

I= 179

TEMPERATURE IN DEGREE C

0.000E+00						
0.386E+01	0.360E+01	0.287E+01	0.211E+01	0.194E+01	0.230E+01	
0.465E+01	0.464E+01	0.461E+01	0.458E+01	0.458E+01	0.460E+01	
0.587E+01	0.617E+01	0.684E+01	0.737E+01	0.735E+01	0.690E+01	
0.709E+01	0.771E+01	0.906E+01	0.101E+02	0.101E+02	0.920E+01	
0.831E+01	0.923E+01	0.113E+02	0.129E+02	0.128E+02	0.115E+02	
0.953E+01	0.107E+02	0.134E+02	0.156E+02	0.155E+02	0.138E+02	
0.107E+02	0.122E+02	0.156E+02	0.182E+02	0.182E+02	0.161E+02	
0.119E+02	0.137E+02	0.177E+02	0.208E+02	0.209E+02	0.184E+02	
0.131E+02	0.152E+02	0.197E+02	0.233E+02	0.235E+02	0.207E+02	
0.143E+02	0.166E+02	0.217E+02	0.258E+02	0.260E+02	0.230E+02	
0.155E+02	0.180E+02	0.237E+02	0.282E+02	0.285E+02	0.253E+02	
0.166E+02	0.194E+02	0.255E+02	0.304E+02	0.309E+02	0.276E+02	
0.177E+02	0.207E+02	0.273E+02	0.326E+02	0.333E+02	0.299E+02	
0.188E+02	0.220E+02	0.290E+02	0.346E+02	0.355E+02	0.322E+02	
0.199E+02	0.232E+02	0.305E+02	0.365E+02	0.377E+02	0.345E+02	
0.210E+02	0.245E+02	0.321E+02	0.382E+02	0.397E+02	0.368E+02	
0.220E+02	0.255E+02	0.332E+02	0.397E+02	0.415E+02	0.391E+02	
0.231E+02	0.268E+02	0.349E+02	0.411E+02	0.431E+02	0.414E+02	
0.240E+02	0.275E+02	0.351E+02	0.418E+02	0.445E+02	0.437E+02	
0.252E+02	0.293E+02	0.384E+02	0.445E+02	0.457E+02	0.460E+02	0.460E+02
0.261E+02	0.305E+02	0.395E+02	0.445E+02	0.456E+02	0.458E+02	0.459E+02
0.273E+02	0.322E+02	0.408E+02	0.447E+02	0.455E+02	0.458E+02	0.459E+02
0.281E+02	0.323E+02	0.395E+02	0.433E+02	0.445E+02	0.457E+02	0.459E+02
0.460E+02						

VORTICITY

0.000E+00	0.252E+02	0.166E+02	0.793E+01	0.186E+01	0.000E+00
-0.108E+04	-0.982E+03	-0.682E+03	-0.257E+03	0.719E+02	0.189E+03
-0.444E+02	-0.378E+02	-0.233E+02	-0.714E+01	0.344E+01	0.500E+01
0.935E+03	0.807E+03	0.501E+03	0.151E+03	-0.718E+02	-0.884E+02
0.190E+04	0.164E+04	0.101E+04	0.305E+03	-0.145E+03	-0.181E+03
0.285E+04	0.246E+04	0.152E+04	0.462E+03	-0.215E+03	-0.277E+03
0.379E+04	0.327E+04	0.203E+04	0.619E+03	-0.284E+03	-0.376E+03
0.471E+04	0.406E+04	0.253E+04	0.778E+03	-0.349E+03	-0.480E+03
0.562E+04	0.484E+04	0.302E+04	0.938E+03	-0.411E+03	-0.589E+03
0.649E+04	0.560E+04	0.350E+04	0.110E+04	-0.469E+03	-0.704E+03
0.734E+04	0.634E+04	0.396E+04	0.126E+04	-0.521E+03	-0.825E+03
0.816E+04	0.704E+04	0.442E+04	0.143E+04	-0.568E+03	-0.955E+03
0.894E+04	0.772E+04	0.485E+04	0.159E+04	-0.607E+03	-0.109E+04
0.967E+04	0.836E+04	0.527E+04	0.176E+04	-0.640E+03	-0.124E+04
0.104E+05	0.896E+04	0.566E+04	0.192E+04	-0.662E+03	-0.139E+04
0.110E+05	0.952E+04	0.605E+04	0.211E+04	-0.675E+03	-0.157E+04
0.116E+05	0.100E+05	0.633E+04	0.224E+04	-0.674E+03	-0.173E+04
0.120E+05	0.105E+05	0.673E+04	0.248E+04	-0.662E+03	-0.198E+04
0.124E+05	0.107E+05	0.677E+04	0.247E+04	-0.626E+03	-0.207E+04
0.127E+05	0.111E+05	0.738E+04	0.300E+04	-0.524E+03	-0.239E+04
0.131E+05	0.112E+05	0.670E+04	0.228E+04	-0.179E+03	-0.141E+04
0.134E+05	0.113E+05	0.688E+04	0.303E+04	0.110E+04	0.302E+03
0.134E+05	0.110E+05	0.635E+04	0.276E+04	0.108E+04	0.325E+03
0.134E+05	0.113E+05	0.737E+04	0.406E+04	0.207E+04	0.690E+03
0.000E+00	-0.375E+03	-0.288E+03	-0.204E+03	-0.131E+03	-0.722E+02
					-0.320E+02
					-0.833E+01
					0.000E+00

STREAM FUNCTION

0.000E+00 0.000E+00 0.000E+00 0.000E+00 0.000E+00 0.000E+00
0.000E+00 0.142E-08 0.375E-08 0.403E-08 0.168E-08 0.000E+00
0.000E+00 0.520E-10 0.130E-09 0.131E-09 0.475E-10 0.000E+00
0.000E+00-0.106E-08-0.263E-08-0.258E-08-0.875E-09 0.000E+00
0.000E+00-0.215E-08-0.534E-08-0.523E-08-0.179E-08 0.000E+00
0.000E+00-0.324E-08-0.803E-08-0.790E-08-0.272E-08 0.000E+00
0.000E+00-0.431E-08-0.107E-07-0.106E-07-0.367E-08 0.000E+00
0.000E+00-0.538E-08-0.134E-07-0.132E-07-0.466E-08 0.000E+00
0.000E+00-0.643E-08-0.160E-07-0.159E-07-0.567E-08 0.000E+00
0.000E+00-0.746E-08-0.186E-07-0.186E-07-0.673E-08 0.000E+00
0.000E+00-0.847E-08-0.212E-07-0.213E-07-0.782E-08 0.000E+00
0.000E+00-0.946E-08-0.238E-07-0.240E-07-0.897E-08 0.000E+00
0.000E+00-0.104E-07-0.262E-07-0.267E-07-0.102E-07 0.000E+00
0.000E+00-0.113E-07-0.287E-07-0.294E-07-0.114E-07 0.000E+00
0.000E+00-0.122E-07-0.309E-07-0.320E-07-0.127E-07 0.000E+00
0.000E+00-0.131E-07-0.333E-07-0.348E-07-0.142E-07 0.000E+00
0.000E+00-0.138E-07-0.352E-07-0.370E-07-0.154E-07 0.000E+00
0.000E+00-0.147E-07-0.378E-07-0.405E-07-0.175E-07 0.000E+00
0.000E+00-0.149E-07-0.382E-07-0.410E-07-0.180E-07 0.000E+00
0.000E+00-0.163E-07-0.429E-07-0.480E-07-0.228E-07 0.000E+00
0.000E+00-0.153E-07-0.390E-07-0.426E-07-0.227E-07 0.000E+00 0.000E+00 0.000E+00 0.000E+00
0.000E+00-0.199E-07-0.570E-07-0.823E-07-0.852E-07-0.691E-07-0.416E-07-0.135E-07 0.000E+00
0.000E+00-0.190E-07-0.540E-07-0.784E-07-0.826E-07-0.680E-07-0.410E-07-0.131E-07 0.000E+00
0.000E+00-0.235E-07-0.716E-07-0.113E-06-0.128E-06-0.110E-06-0.699E-07-0.246E-07 0.000E+00
0.000E+00 0.000E+00 0.000E+00 0.000E+00 0.000E+00 0.000E+00 0.000E+00

AXIAL VELOCITY IN METER/SEC

0.000E+00	0.000E+00	0.000E+00	0.000E+00	0.000E+00	0.000E+00	0.000E+00
0.284E-02	0.237E-02	0.799E-03	-0.419E-03	-0.641E-03	0.000E+00	
0.104E-03	0.822E-04	0.242E-04	-0.169E-04	-0.213E-04	0.000E+00	
-0.212E-02	-0.167E-02	-0.469E-03	0.361E-03	0.425E-03	0.000E+00	
-0.431E-02	-0.339E-02	-0.952E-03	0.729E-03	0.862E-03	0.000E+00	
-0.648E-02	-0.510E-02	-0.144E-02	0.109E-02	0.130E-02	0.000E+00	
-0.863E-02	-0.680E-02	-0.193E-02	0.145E-02	0.174E-02	0.000E+00	
-0.108E-01	-0.849E-02	-0.243E-02	0.179E-02	0.217E-02	0.000E+00	
-0.129E-01	-0.102E-01	-0.293E-02	0.212E-02	0.261E-02	0.000E+00	
-0.149E-01	-0.118E-01	-0.344E-02	0.244E-02	0.304E-02	0.000E+00	
-0.169E-01	-0.134E-01	-0.396E-02	0.274E-02	0.347E-02	0.000E+00	
-0.189E-01	-0.150E-01	-0.448E-02	0.302E-02	0.389E-02	0.000E+00	
-0.208E-01	-0.166E-01	-0.500E-02	0.328E-02	0.431E-02	0.000E+00	
-0.227E-01	-0.181E-01	-0.555E-02	0.352E-02	0.473E-02	0.000E+00	
-0.244E-01	-0.195E-01	-0.606E-02	0.372E-02	0.512E-02	0.000E+00	
-0.262E-01	-0.210E-01	-0.666E-02	0.389E-02	0.555E-02	0.000E+00	
-0.276E-01	-0.221E-01	-0.710E-02	0.400E-02	0.586E-02	0.000E+00	
-0.294E-01	-0.237E-01	-0.787E-02	0.411E-02	0.636E-02	0.000E+00	
-0.299E-01	-0.239E-01	-0.792E-02	0.407E-02	0.639E-02	0.000E+00	
-0.326E-01	-0.268E-01	-0.964E-02	0.402E-02	0.737E-02	0.000E+00	
-0.307E-01	-0.242E-01	-0.813E-02	0.321E-02	0.618E-02	0.000E+00	0.000E+00
-0.398E-01	-0.333E-01	-0.172E-01	-0.489E-02	0.186E-02	0.467E-02	0.500E-02
-0.380E-01	-0.315E-01	-0.164E-01	-0.498E-02	0.146E-02	0.446E-02	0.496E-02
-0.469E-01	-0.410E-01	-0.245E-01	-0.101E-01	0.453E-03	0.625E-02	0.772E-02
0.000E+00	0.000E+00	0.000E+00	0.000E+00	0.000E+00	0.000E+00	0.000E+00

RADIAL VELOCITY IN METER/SEC

0.000E+00 0.000E+00 0.000E+00 0.000E+00 0.000E+00 0.000E+00
0.000E+00 -0.321E-04 -0.435E-04 -0.323E-04 -0.108E-04 0.000E+00
0.000E+00 -0.984E-04 -0.127E-03 -0.882E-04 -0.259E-04 0.000E+00
0.000E+00 -0.721E-04 -0.888E-04 -0.574E-04 -0.143E-04 0.000E+00
0.000E+00 -0.725E-04 -0.899E-04 -0.590E-04 -0.153E-04 0.000E+00
0.000E+00 -0.720E-04 -0.897E-04 -0.593E-04 -0.157E-04 0.000E+00
0.000E+00 -0.714E-04 -0.892E-04 -0.595E-04 -0.162E-04 0.000E+00
0.000E+00 -0.705E-04 -0.885E-04 -0.596E-04 -0.166E-04 0.000E+00
0.000E+00 -0.695E-04 -0.876E-04 -0.598E-04 -0.172E-04 0.000E+00
0.000E+00 -0.682E-04 -0.865E-04 -0.598E-04 -0.179E-04 0.000E+00
0.000E+00 -0.668E-04 -0.853E-04 -0.600E-04 -0.187E-04 0.000E+00
0.000E+00 -0.648E-04 -0.834E-04 -0.597E-04 -0.194E-04 0.000E+00
0.000E+00 -0.631E-04 -0.822E-04 -0.602E-04 -0.206E-04 0.000E+00
0.000E+00 -0.598E-04 -0.784E-04 -0.585E-04 -0.210E-04 0.000E+00
0.000E+00 -0.587E-04 -0.788E-04 -0.611E-04 -0.233E-04 0.000E+00
0.000E+00 -0.515E-04 -0.684E-04 -0.539E-04 -0.220E-04 0.000E+00
0.000E+00 -0.553E-04 -0.790E-04 -0.668E-04 -0.289E-04 0.000E+00
0.000E+00 -0.333E-04 -0.417E-04 -0.340E-04 -0.170E-04 0.000E+00
0.000E+00 -0.630E-04 -0.103E-03 -0.102E-03 -0.496E-04 0.000E+00
0.000E+00 0.107E-04 0.366E-04 0.537E-04 0.428E-04 0.000E+00
0.000E+00 -0.138E-03 -0.269E-03 -0.437E-03 -0.603E-03 0.000E+00 0.000E+00 0.000E+00
0.000E+00 -0.123E-03 -0.255E-03 -0.411E-03 -0.520E-03 -0.201E-03 -0.948E-04 -0.212E-04 0.000E+00
0.000E+00 -0.244E-03 -0.432E-03 -0.534E-03 -0.505E-03 -0.363E-03 -0.210E-03 -0.705E-04 0.000E+00
0.000E+00 0.264E-03 0.292E-03 0.183E-03 0.746E-04 0.196E-04 -0.101E-04 -0.140E-04 0.000E+00
0.000E+00 0.000E+00 0.000E+00 0.000E+00 0.000E+00 0.000E+00 0.000E+00 0.000E+00

B-3 Program NUSSLT: The program NUSSLT is included in the following three pages. This coded program was first developed together with the program NATCON by the CDC CYBER-75 computer of the OSU Computer Center. However, when NATCON was transferred to the PDP-11/10 as mentioned in Appendix B-1, because of the limited memory capacity of the PDP-11/10 the program NUSSLT had to be separated from the program NATCON and thus these two programs were stored in two separate memory discs.

Originally, the approximation of radial temperature gradients $dT(X,R)/dR$ at $R=Wall$ at several different X was done by 4-node approximation (see Sec. 3.2.5). However, it was realized that the 4-node approximation required more number of nodes between $R=0$ and $Wall$ in order to obtain an accurate result. In this aspect, a 2-node approximation, when only five or six nodes in the radial direction (which was the case currently) were assigned, actually gave a better approximation of the temperature gradient at the wall. Thus, the listed program is currently written to apply the 2-node approximation. However, a minor change will modify the program to the 4-node approximation. To make this modification, comment those statements underlined by a solid line and uncomment those statements underlined by a dotted line in the program.

Other explanation is also given in the comment section at the beginning of the program.

C PROGRAM NUSSLT
C
C THIS PROGRAM COMPUTES THE LOCAL HEAT TRANSFER COEFFICIENTS,
C THE AVERAGE H. T. COEFFICIENT, AND THE NUSSELT NUMBER BASED ON
C THE RADIUS OF THE CYLINDER OF THE PROBLEM OF PROGRAM "NATCON".
C
C EXPLANATION OF CONSTANTS:
C M; NO. OF NODES (SHOULD BE ODD SINCE THE SIMPSON'S RULE IS USED
C FOR THE INTEGRATION SCHEME), AND THIS VALUE SHOULD CORRESPOND
C TO (MXX-MX-1) OF NATCON
C DX AND DR; MESH DISTANCES USED IN NATCON
C R; RADIUS OF THE CYLINDER, =DR*(NR-1)
C TORF; ORIFICE TEMPERATURE AT NODE (MX,1)
C TEPM. MAP; T(I,1), T(I,2), T(I,3), T(I,4)
C WHERE T(I,1) IS THE WALL TEMP., AND T(I,4) IS THE
C 4TH NODE'S TEMP. FROM THE WALL. I=1 CORRESPONDS
C TO THE MX AND I=M TO THE MXX OF NATCON.

C
DIMENSION T(25,4),H(25),DTR(25),X(25),Y(25)
TYPE 104
ACCEPT 105,M
TYPE 100
ACCEPT 101,DX
TYPE 102
ACCEPT 101,DR
TYPE 103
ACCEPT 101,R
TYPE 106
ACCEPT 101,TORF
TYPE 301
TYPE 305
DO 300 I=1,M
TYPE 302,I
ACCEPT 303,T(I,1),T(I,2)
C ACCEPT 303,T(I,1),T(I,2),T(I,3),T(I,4)
300 CONTINUE
C
THRCON=.0006
CL=DX*FLOAT(M-1)
C
C** AVERAGE WALL TEMPERATURE ***
C
SUMT=0.
DO 1500 I=1,M
SUMT=SUMT+T(I,1)
1500 CONTINUE
TWAV=SUMT/FLOAT(M)
C
C** LOCAL HEAT TRANSFER COEFFICIENTS ***
C
WRITE(5,1001)
DO 1000 I=1,M
DTR(I)=(T(I,1)-T(I,2))/DR

```

C      DTR(I)=(11.*T(I,1)-18.*T(I,2)+9.*T(I,3)-2.*T(I,4))/(6.*DR)
H(I)=THRCON*DTR(I)/(TWAV-TORF)
WRITE(5,1002)I,H(I)
1000 CONTINUE
C
C** AVERAGE NUSSELT NO. AND ABS. AVE. NU NO. ***
C
      X(1)=DTR(1)
      Y(1)=ABS(DTR(1))
      DO 2000 I=2,M-1
      ODD=FLOAT(I)*.5-FLOAT(I/2)
      IF(ODD.GT.0.)GO TO 2001
      X(I)=DTR(I)*4.
      Y(I)=ABS(X(I))
      GO TO 2000
2001 X(I)=DTR(I)*2.
      Y(I)=ABS(X(I))
2000 CONTINUE
      X(M)=DTR(M)
      Y(M)=ABS(X(M))
C
      XSUM=0.
      YSUM=0.
      DO 2002 I=1,M
      XSUM=XSUM+X(I)
      YSUM=YSUM+Y(I)
2002 CONTINUE
      ANU=(R/CL)*(DX/(3.*(TWAV-TORF)))*XSUM
      ABNU=(R/CL)*(DX/(3.*(TWAV-TORF)))*YSUM
C
C** AVERAGE H. T. COEFFICIENT ***
C
      HAV=ANU*THRCON/CL
C
C** PRINT RESULTS ***
C
      WRITE(5,3000)HAV
      WRITE(5,3001)ANU
      WRITE(5,3003)ABNU
C
      100 FORMAT(' DX(METER)=',:)
      101 FORMAT(F12.6)
      102 FORMAT(' DR(METER)=',:)
      103 FORMAT(' RADIUS, R(METER)=',:)
      104 FORMAT(' NO. OF NODES (MUST BE ODD), M=',:)
      105 FORMAT(I3)
      106 FORMAT(' ORIFICE CENTER TEMP., TORF(C)=',:)
      301 FORMAT(' TYPE-IN 4 TEMPS(C) FROM WALL IN AF6.3:')
      305 FORMAT(10X,'*****-----')
      303 FORMAT(2F6.3)
C      305 FORMAT(10X,'*****-----')
C      303 FORMAT(AF6.3)
      302 FORMAT(' I=',I3,' :',:)
      1001 FORMAT(//1X,'COMPUTED RESULTS:',/2X,

```

```
1'LOCAL H. T. COEFFICIENTS (KJ/SEC.M2.C)--')
1002 FORMAT(12X,'H('',I3,'')=',E12.4)
3000 FORMAT(2X,'THE AVERAGE H. T. COEFFICIENT, (KJ/SEC.M2.C), HAV=',  
     1E12.4)
3001 FORMAT(2X,'THE AVERAGE NUSSELT NO. BASED ON RADIUS, ',  
     1'ANU=',E12.4)
3003 FORMAT(2X,'ABS. ANU=',E12.4)
      CALL EXIT
      END
```